# CYTOSOLIC DELIVERY OF PROTEINS, PEPTIDES AND CELL-IMPERMEABLE SMALL MOLECULES INTO LIVE CELLS UTILIZING VIRUS-INSPIRED MULTIVALENT CELL-PENETRATING PEPTIDES: PRINCIPLES AND MECHANISMS

A Dissertation

by

ALFREDO ERAZO OLIVERAS

Submitted to the Office of Graduate and Professional Studies of
Texas A&M University
in partial fulfillment of the requirement for the degree of

DOCTOR OF PHILOSOPHY

| | |
|---|---|
| Chair of Committee, | Jean-Philippe Pellois |
| Committee Members, | Ryland Young |
| | Thomas Meek |
| | Wenshe Liu |
| Head of Department, | Gregory Reinhart |

December 2014

Major Subject: Biochemistry

# ABSTRACT

Cell-penetrating peptides (CPPs) facilitate the delivery of cell-impermeable macrmolecules across the plasma membrane of live cells. CPPs act as biological Trojan horses by hijacking and inducing endocytosis to enter cells, which leads to entrapment of these peptides inside endocytic organelles. However, the endosomolytic activity displayed by CPPs is very low and cargos/CPP-cargo conjugates typically remain trapped inside endosomes. As a result, cargos often cannot reach their intracellular targets and fail to exert a biological response. A possible solution to this problem is to increase the endosomolytic activity of CPPs by creating multivalent CPPs. This idea is based on the rationale that an increase in the local concentration of CPPs at the sites where CPPs interacts with their cellular components could lead to higher endosomolytic activity. Interestingly, the previous has been observed in nature. For example, viruses display multiple proteins on their surface in order to bind extracellular receptors efficiently, facilitate entry to cells and cause infection. In this work, I report a delivery methodology based on the CPP TAT, a peptide derived from the HIV-1 TAT protein. I demonstrate that a trimeric multivalent CPP, Fl-$TAT_3$, penetrates live cells more efficiently that its dimeric and tetrameric counterparts and delivers different molecules inside cells. Moreover, I describe the generation of an improved multivalent endosomolytic agent, dfTAT. I show that dfTAT endosomolytic activity is highly efficient and can deliver proteins, peptides and cell-impermeable small molecules into the cytosolic space of live cells. I show that dfTAT-mediated delivery can be achieved in multiple cell types. Furthermore, dfTAT

delivered multiple molecules inside cells simultaneously and more than once. Interestingly, the amount of cargo delivered into the cytosolic space of cells could be controlled. Remarkably, I demonstrate that dfTAT-mediated delivery did not significantly affect important cellular processes. In addition, I provide mechanistic insights involved in dfTAT cell penetration. I show that dfTAT escapes the endocytic pathway from late endosomes. Finally, I show that endosomal escape seems to require interactions between dfTAT and BMP, a phospholipid only found inside late endosomes. These collective insights should provide a basis for the development of improved delivery agents.

# DEDICATION

I would like to dedicate this work to my beloved parents and my dear sister, which without their constant support and unconditional love I would not be writing these words.

# ACKNOWLEDGMENTS

I would like to express my most sincere gratitude to Dr. Pellois, my mentor and guide throughout this wonderful odyssey also known as graduate school. For his endless patience, support, motivation, willingness to share his experiences and making his laboratory a nurturing environment to grow as a scientist. I addition, I would like to acknowledge Dr. Ry Young, Dr. Wenshe Liu and Dr. Thomas Meek for serving as my committee members and for all their helpful advice and contributions towards my studies. I would like to thank Dr. Donald Pettigrew, who also served as my committee member, for his valuable guidance. I would like to thank Dr. Alfredo Ángeles-Boza for all his advice, support and dear friendship during the beginning of my graduate years. I would also like to express my deepest gratitude and appreciation to all former and current members of the Pellois laboratory, in particular, Gregory A. Johnson, Ting-Yi Wang and Kristina Najjar, who contributed uniquely to my growth during my time at Texas A&M University.

Finally, I would like to thank all my close friends and my beloved family back home for their support and endless love.

# NOMENCLATURE

| | |
|---|---|
| Antp | antennapedia homeodomain |
| ATCC | American Type Culture Collection |
| BMP | bis(monoacylglycero)phosphate |
| BSA | bovine serum albumin |
| CPP | cell-penetrating peptide |
| DCM | dichloromethane |
| DIC | N,N-diisopropylcarbodiimide |
| DIEA | N,N-Diisopropylethylamine |
| DIGE | Differential in gel electrophoresis |
| DMEM | Dulbecco's modified eagle medium |
| DMF | dimethylformamide |
| EGFP | enhanced green fluorescent protein |
| FBS | fetal bovine serum |
| FITC | fluorescein isothiocyanate |
| Fl | carboxy-fluorescein |
| FRET | Förster resonance energy transfer |
| GTPase | guanosine triphosphate hydrolase |
| HA2 | haemagglutinin protein II |
| HBTU | 2-(1H-Benzotriazole-1-yl)-1,1,3,3-tetramethyluronium hexafluorophosphate |

| | |
|---|---|
| HDF | human dermal fibroblast |
| HEPES | 4-(2-hydroxyethyl)-1-piperazineethanesulfonic acid |
| HIV | Human immunodeficiency virus |
| HPLC | high-performance liquid chromatography |
| HSPG | heparin sulfate proteoglycan |
| IPTG | isopropyl _-D-1-thiogalactopyranoside |
| kDa | kilo Dalton |
| L-15 | Leibovitz's 15 |
| MALDI | matrix-assisted laser desorption/ionization |
| MAP | model amphipathic peptide |
| MPTP | mitochondrial permeability transition pore |
| MTT | 3-(4,5-Dimethylthiazol-2-yl)-2,5-diphenyltetrazolium bromide |
| MVB | multivesicular bodies |
| NLS | nuclear localization signal |
| NMR | nuclear magnetic resonance |
| p53 | protein 53 |
| PAD | pro-apoptotic domain |
| PBS | phosphate buffer saline |
| PCI | photochemical internalization |
| PCR | polymerase chain reaction |
| PNA | peptide nucleic acid |
| Ptd | phosphatidyl |

| | |
|---|---|
| RBC | red blood cell |
| SDS-PAGE | sodium dodecyl sulfate polyacrylamide gel electrophoresis |
| SPPS | solid-phase peptide synthesis |
| TAT | Trans-Activator of Transcription |
| TCEP | tris(2-carboxyethyl)phosphine |
| TFA | Trifluoroacetic acid |
| TMR | 5(6)-carboxytetramethylrhodamine |

TABLE OF CONTENTS

Page

LIST OF FIGURES

# 1. INTRODUCTION

## 1.1 History of macromolecule delivery inside live cells

The plasma membrane of live cells is a biological barrier that controls the passage of molecules in and out of cells[1]. Although this barrier allows some small molecules and ions to cross in and out of the cell directly but not large and/or hydrophilic molecules[2]. The delivery of biologics into the cytosolic space of live cells is, therefore, not a trivial task. Several techniques such as microinjection, electroporation, transfection, chemical "nanoblasts", liposome encapsulation, and virus-like particles have been utilized to allow hydrophilic macromolecules to enter cells[3-5]. However, these methods generally display one or more of the following: high cell toxicity, undesirable immunogenic effects requirement of high expertise and low delivery efficiency[6-13]. The latter makes these methods impractical. The development of a robust delivery methodology that allows macromolecule membrane translocation is, therefore, crucial, since the targets of these macromolecules/biologics are localized in the cytosolic space of cells. A promising approach to solving this problem is using cell-penetrating peptides (CPPs) as delivery vectors.

Back in 1988, the laboratories of Loewenstein and Pabo showed for the first time that a protein, trans-activator of transcription (Tat), from the human immunodeficiency virus type 1 (HIV-1) was able to penetrate live cells[14, 15]. After incubating the 86-amino

*Parts of this chaper are reprinted with permission from "Improving the Endosomal Escape of Cell-Penetrating Peptides and Their Cargos: Strategies and Challenges" by Erazo-Oliveras,A+.; Muthukrishnan, N+.; Baker, R+.; Wang, T.-Y.; Pellois, J.-P. *Pharmaceuticals* **2012**, 5, 1177-1209 doi:10.3390/ph5111177. +authors contributed equally. 

acid Tat protein with HeLa cells for 8 hr, which had been transfected with pHIV-LTRCAT, HIV-LTR (an important HIV-1 gene) was trans-activated. Transactivation of HIV-LTR, in turn, led to the production of RNA. It was not until a few years later that the laboratory of Frankel showed insights about the mechanism involved in Tat cellular penetration. Frankel and coworkers showed that the Tat protein was endocytosed after binding, in a non-specific manner, to the cell surface of live cells[16]. Although it appeared then that Tat cellular translocation was not biologically important, in part due to the lack of a specific receptor for this protein, its ability to penetrate cells made it a potentially useful delivery vehicle. In an attempt to better understand how Tat penetrates live cells, the laboratory of Lebleu discovered the CPP TAT. Lebleu and coworkers demonstrated that out of the 86 amino acids comprising Tat the small region $^{47}$YGRKKRRQRRR$^{57}$ was essential for cellular internalization[17]. Together, all the evidence clearly indicated that a small peptide sequence could potentially be used to deliver macromolecules inside live cells.

Over the past two decades, a number of peptide sequences have been shown to display a similar transduction activity as the CPP TAT. These CPP sequences include: penetratin, a 16-mer peptide derived from the third helix of Drosophila antennapedia homeoprotein (Antp)[18]; the VP22 peptide from the herpes simplex virus VP22 protein[19], MPG, a peptide derived from the fusion of sequence of HIV gp41 and the hydrophilic nuclear localization sequence (NLS) of SV40 T-antigen[20]; transportan (TP), a chimeric peptide derived from the neuropeptide galanin and the wasp venom peptide mastoparan[21]; and the synthetic polyarginine ($R_n$) peptides[22]. Other well-known CPPs include CADY, Pep-1, MAP,

Xentry and PPTG1[23-27]. CPPs usually display 30 or less amino acids and are polycationic or amphipathic in nature[28, 29]. CPPs-based delivery technologies are potentially useful for the delivery of therapeutics and the study of cellular processes both *in cellulo* and *in vivo*[30, 31]. Therefore, it is important to better understand the mechanisms of CPP penetration and the CPP delivery activity.

### 1.2 Development of CPPs as general delivery tools

CPPs possess the ability to carry cell-impermeable macromolecules into live cells. For instance, full-length p53, an important tumor suppressor, and p53-derived peptides were delivered into the cytosolic space and nucleus of cancer cells *in cellulo* using TAT, VP22, penetratin and polyarginines[32-35]. Delivery of the cargos into cells bearing mutations in the p53 gene in their genome restored p53 activity and induced cell apoptosis. A major breakthrough in the field of CPP delivery came from one of the first attempts to establish the potential of utilizing CPPs to deliver macromolecules *in vivo*. The laboratory of Langel delivered a peptide nucleic acid (PNA) molecule (an artificial polymer utilized in antisense therapy) using CPPs[36]. A PNA molecule, complementary to the galanin receptor type 1 mRNA, was delivered by penetratin and transportan into the superficial layers of the dorsal horn in a rat and suppressed the expression of galanin receptors. A year later, Dowdy and coworkers delivered biologically active β-galactosidase, a 120-kilodalton (kDa) protein, into most tissues of a mouse, including the brain[37]. CPPs have also been used to deliver small interfering RNA (siRNA) into live cells[38-40]. This is a prevalent topic in the delivery field, since this technology has the potential to treat multiple diseases in humans. Troy and

coworkers showed that a synthetic siRNA covalently attached to the CPP penetratin is taken up by primary mammalian hippocampal and sympathetic neurons[41]. This, in turn, led to the knockdown of specific genes and a considerable reduction in expression of the targeted protein products. In addition to protein, peptides and nucleic acids CPPs have been shown to deliver drugs, liposomes, quantum dots, fluorophores and magnetic nanoparticles[42-46]. All the current evidence regarding CPP-mediated delivery suggests that this technology is independent of the cell type utilized and the nature of the cargo[47]. This indicates that CPPs can serve as a general delivery tool.

### 1.2.1 Potential problems of CPP-mediated macromolecule delivery

There is strong evidence showing that different cargos can be delivered inside cells. However, while CPP-mediated endocytic uptake of cargos is typically efficient, it appears that the endosomolytic activity (disruption of endosomes and subsequent leakage of its contents) of CPPs is, in the contrary, very poor[48]. For instance, CPP-fluorophores and fluorescent CPP-protein conjugates display a punctate distribution inside cells consistent with endosomal entrapment when observed by fluorescence microscopy[49-51]. In many cases, no fluorescence signal is observed in the cytosolic space indicating that the CPP-cargo did not reached the cytosolic space and it remains trapped inside endosomes[52]. Furthermore, delivery of biologically active cargos inside cells with CPPs often fails to display significant cellular activities[53]. Interestingly, attaching reagents to CPPs that disrupt endosomes leads to a dramatic improvement in the cellular delivery and biological

activity of CPP-cargos[54]. To this day, this issue remains as the bottleneck of the delivery field. Therefore, the current challenge is to increase the endosomolytic activity of CPPs.

### 1.3 Proposed mechanism of macromolecule delivery into live cells using CPPs

Even though CPPs have been used extensively for more than two decades, the mechanism of CPP penetration remains unclear. This lack of understanding can be attributed, in one part, to laboratories utilizing different methodologies that are not comparable to study CPP delivery[48, 55]. Moreover, the use of cell fixation during these mechanistic studies has given rise to several cellular artifacts, which in turn, has caused the reevaluation of some of these findings. Finally, the different influences that affect: cargo size, the stereochemistry of the CPP sequence, the choice of strategy to attach cargo to the CPP (covalent, non-covalent, co-incubation) and the different concentrations of CPP used in delivery assays has on the mechanism of CPP-mediated delivery, making deciphering of these mechanisms a much harder task. However, the current evidence has allowed scientists in the delivery field to narrow down all the possible mechanisms of CPP delivery to two major ones. The first mechanism involves direct translocation of CPPs across the plasma membrane of cells via an energy-independent process[56, 57]. Several models have been proposed to describe the way the CPP interacts with and crosses the plasma membrane of live cells[58, 59]. The second major mechanism of CPP penetration involves a two-step process: endocytosis and endosomal release[58, 60, 61]. In this mechanism, the CPP is taken up by cells into an endocytic vesicle where it stays trapped until the CPP disrupts the endosomal membrane and escapes from the endocytic pathway to enter the

cytosolic space of the cell. The exact molecular details of how CPPs disrupt the endocytic membrane and at what stage it escapes the endocytic pathway remains unclear. The current evidence that have already been established involving these two major mechanisms of CPP penetration will be discussed in detail.

### 1.3.1 Direct membrane translocation of CPPs inside cells

Certain CPPs have the ability to cross the membrane of cells directly. The specific details describing how the CPP crosses the plasma membrane have been described and divided into several different models, which include the carpet model, inverted micelle model and pore formation[62].

In the carpet model, the CPP first binds to the plasma membrane of cells. After the CPP surpasses a threshold concentration (refer to as an "extensive association"), a major destabilization of the plasma membrane allows the CPP to enter the cytosolic space[59, 63, 64]. Destabilization of the plasma membrane takes place as a result of the reorganization of phospholipids and is believed to be only transient.

The inverted micelle model was first described in a study of the cellular internalization of the peptide penetratin by Prochiantz and coworkers[65]. In this model, the interaction of the CPP with the plasma membrane leads to rearrangement of the phospholipids and formation of inverted hexagonal structures refer to as inverted micelles. The CPP localizes in the hydrophilic lumen of the inverted micelle until it destabilizes the membrane and consequently escapes into the cytosolic space. Nuclear magnetic resonance (NMR) studies using the CPP penetratin have shown that, indeed, CPPs can cause the

formation of these inverted micelle structures[66]. The inverted micelle model provides a plausible explanation for direct membrane translocation of small CPP-cargo conjugates since the CPP-cargo is not required to interact with the hydrophobic part of the cell membrane, and, in result, there is no need to overcome the high energetic barrier of such process. This notion is consistent with the idea that high molecular weight CPP-cargo conjugates are most likely not to cross membranes using these mechanisms[67].

The pore formation model is comes in as two different versions the toroidal and the barrel stave models[62, 68]. In both models, the direct translocation of the CPP across the membrane involves formation of a transient pore as a result of the CPP inserting into the membrane. In the toroidal model, the hydrophilic face of the CPP interacts with the phospholipid heads. This interaction leads to distortion and rearrangement of the plasma membrane. On the contrary, in the barrel stave model the hydrophobic face of an amphipathic CPP interacts with the fatty acid chain of the phospholipids and the hydrophilic face orients to the hydrophilic side and forms the pore. In both cases, the CPP reaches the cytosolic space after crossing the plasma membrane through the pore.

All the models previously described display several similarities. The most obvious and probably most important is the requirement of the CPP to become in direct contact with the lipid bilayer of cells and cause disruption and a major reorganization of phospholipids. The latter, in most cases, only occurs after the CPP reaches a specific concentration (usually described as a high peptide/lipid ratio). However, these models share several differences that are important to mention. For example, in the pore formation model, the CPP makes direct contact with both faces of the lipid bilayer (hydrophilic and

hydrophobic) while in the carpet and inverted micelle models the CPP makes contact only with the hydrophilic face. Another example is the dramatic and extensive reorganization of the lipid bilayer that occurs in the case of the toroidal, carpet and inverted micelle models. In the contrary, in the barrel stave model, the CPP is thought not to cause significant membrane perturbations. Finally, the models that display pore formation evoke for the existence of a well-defined CPP structure in the membrane pore. In contrast, the carpet model predicts a highly disorganized CPP structure.

All these models that were described, with exception of the inverted micelle model, can allow the translocation of high molecular CPP-cargo conjugates. Moreover, the requirement of the presence of amphipathic peptides that will allow some of the molecular events in these models to take place is a feature observed in many CPPs[69]. However, the low cell toxicity observed, in most cases, is not on par with the degree of membrane disruption that will need to occur in order for large CPP-cargo conjugates to cross the plasma membrane directly. This clearly indicates that direct membrane translocation is not the only mechanism involve in CPP penetration, especially during delivery of large CPP-cargo conjugates or when CPP-cargo conjugates are present at low concentrations.

### 1.3.2 Entry of CPPs inside live cells by non-direct membrane translocation

To this date, multiple studies have shown that CPPs can enter live cells utilizing several endocytic pathways[70, 71]. Moreover, the same CPPs have been reported to use different endocytic routes to gain access to the cell interior. Even though these

discrepancies have not been resolved, it is well established that all these CPPs share a common model of cellular entry. This model involves four major steps: i) binding of CPPs to the surface of cells, ii) uptake of CPPs by endocytosis into endocytic vesicles (leads to entrapment of CPPs inside vesicles), iii) trafficking of CPPs along the endocytic pathway and iv) escape of CPPs into the cytosolic space of cells (these step involves CPP-mediated disruption of endocytic vesicles) (**Figure 1-1**). This study will focus on this type of cellular translocation using the CPP TAT.

### 1.3.3 Binding of CPPs to the surface of live cells

Highly-positively charged CPPs have the ability to interact with negatively charged macromolecules[72]. As mentioned earlier, CPP-mediated delivery has been shown to be cell type independent. It has been proposed that association of CPPs with the surface of cells does not require interactions with cellular receptors[47]. Several studies have shown that the positively charged arginine residues in CPPs are essential for their activity[73]. The guanidinium group on the side chain of arginine residues can form bidentate hydrogen bonds with carboxylate, phosphate and sulfate anions[74]. On the contrary, the amino groups on the side chain of lysines can only form monodentate hydrogen bonds (one reason as to why polylysines) display a lower delivery efficiency than polyarginines and TAT). Moreover, the higher the number of arginine residues on a CPP (not just their presence, Arg v.s. Lys) increases their activity *in* vitro and *in cellulo*[73, 75, 76].

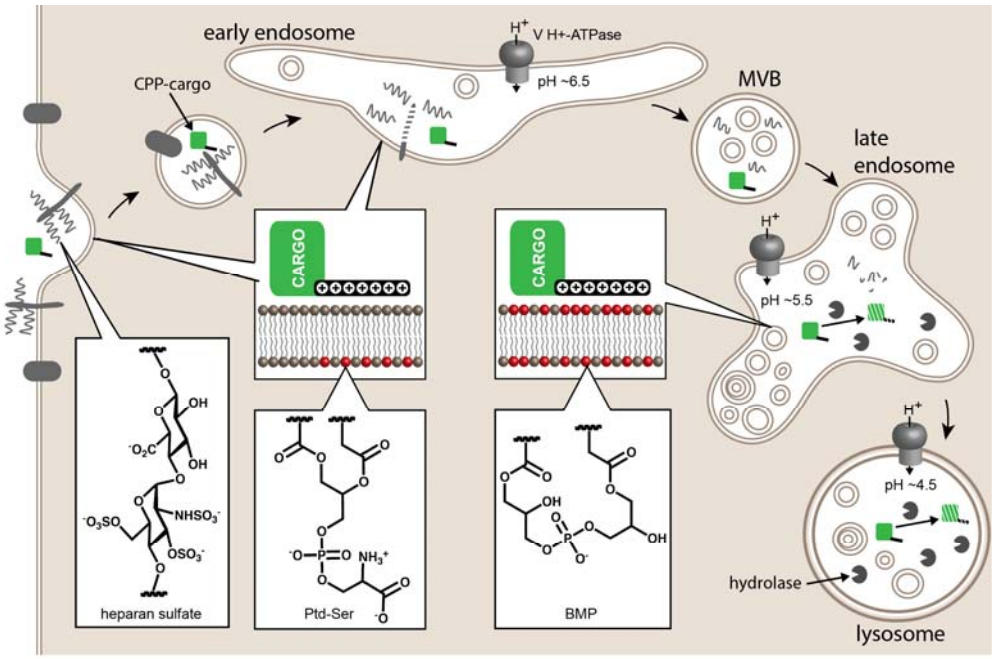


**Figure 1-1. Model of the trafficking of a CPP-cargo conjugate through the endocytic pathway**. From left to right: A CPP-cargo binds to heparin sulfate proteoglycans (HSPGs) on the cell surface and induces endocytosis. Endocytosis leads to uptake and entrapment of the CPP-cargo inside an endocytic vesicle. The endosomal membrane contains the lipid phosphatidylserine (Ptd-Ser) in its outer leaflet. During endosomal maturation, a vacuolar H+-ATPase acidifies the lumen of endocytic organelles. The CPP-cargo reaches early endosomes (pH~6.5). Concurrently, hydrolases partially degrade HSPGs and release HS fragments. Upon further maturation, the CPP-cargo reaches multivesicular bodies, late endosomes (pH~5.5), and lysosomes (pH~4.5). The membrane of the intraluminal vesicles of late endosomes is enriched with BMP. HS is further degraded to smaller fragments. The CPP-cargo is susceptible to degradation due to the low pH and lysosomal hydrolases.

CPPs have also been shown to display strong affinity towards proteoglycans (PGs), a protein-polysaccharide macromolecule hybrid present on the surface of cells [77]. The two major types of PGs in cells are the transmembrane protein syndecans and the membrane lipid-linked glypicans[78]. The linear glycosaminoglycans (GAGs) on these PGs are heavily

substituted with sulfates and, in lesser amount, carboxylates. Binding of CPPs to heparan sulfate PGs (HSPGs) is believe to be, in most part, due to the presence of positively-charged arginine residues in CPPs (**Figure 1-1**). Interestingly, studies have shown that delivery of CPPs depend greatly on HSPGs[79]. For example, the laboratory of Raines and Chernomordik demonstrated that the uptake of nonaarginine ($R_9$) and TAT inside cells was significantly reduced in a cell line deficient in heparan sulfate (HS)[49, 80]. Other peptides have been shown to display similar behavior.

This evidence and that of others has allowed to establish a model that explains the first step involved in CPP penetration (this model does not require the presence of a specific cell receptor). The positively charged arginine residues in CPPs strongly bind to negatively charged HSPGs through electrostatic interactions. These interactions allow the CPPs to dock on the surface of live cells until the second step, endocytosis of CPPs, ensues.

HSPGs are involved in many cellular processes such as: cytokine signaling, lipid metabolism, viral transcription activation, microbe invasiveness, cell growth, wound healing and angiogenesis[81-85]. Interestingly, HSPGs have also been shown to be involved in ligand catabolism[86, 87]. It has been shown that some ligands that bind HSPGs, became endocytosed and are targeted to lysosomes for degradation. In some cases, ligand-mediated clustering at the cell surface precedes ligand internalization (endocytosis)[86, 88]. More importantly, both syndecans and glypicans are known to be actively endocytosed inside cells[89, 90]. This evidence shows a link between the first two steps of CPP penetration: binding of CPPs to HSPGs and CPP endocytosis. Most importantly, it suggests two modes

of CPP internalization. In the first one, CPPs bind to HSPGs, which could then trigger endocytosis and CPP internalization into endocytic vesicles. In the second one, the CPP binds to HSPGs and enters cells in a piggyback manner. The second step of CPP internalization will be discussed in detail next.

### 1.3.4 Endocytic internalization and endosomal trafficking of CPPs

One mechanism by which macromolecules are internalized into cells is endocytosis (**Figure 1-1**). There are various endocytic mechanisms, which can be divided into phagocytosis, a process that occurs only in certain cells (e.g. macrophages) and pinocytosis, an energy-dependent process that occurs in most cells[91, 92]. There is a consensus among the delivery community that CPPs can enter cells by pinocytosis. The most well-known types of pinocytosis include: cavelolae-mediated endocytosis, clathrin-mediated endocytosis and macropinocytosis[93-96]. It has been shown that CPPs have the ability to hijack or induce different pinocytic mechanisms[97, 98].

Several studies have been carried out to better understand the role of pinocytosis and the influence of each different type of pinocytosis in CPP delivery. Pinocytosis is an energy-dependent process. Then, incubation of cells at 4 ºC inhibits every type of pynocytic uptake (cavelolae-mediated endocytosis, clathrin-mediated endocytosis and macropinocytosis). For example, Futaki and coworkers showed that uptake of an arginine-rich CPP decreased significantly in HeLa cells incubated at 4 ºC using flow cytometry[99]. Similar results have been observed for the TAT peptide[100]. This type of experiment is normally carried out to distinguish between pinocytosis and direct membrane translocation

as the route of CPP penetration. Therefore, it is consensus in the delivery field that pinocytosis is a major route used by arginine rich CPPs to enter cells[101].

Other studies have focused on deciphering the exact pathway by which a particular CPP enters cells. However, these experiments are not without disadvantages and are often difficult to interpret. Yet, they have provided insightful mechanistic details involving CPP penetration. Inhibitors of cavelolae-mediated endocytosis, clathrin-mediated endocytosis and macropinocytosis have been used to selectively block a single pathway. It has been shown that uptake of TAT and TAT-cargo conjugates is significantly reduced when cells are incubated with amiloride, an inhibitor of macropinocytosis[102]. Similar results have been observed for polyarginine peptides[103]. While it is important to mention that these inhibitors are not one hundred percent specific[104] and could still block, to a lesser extent, other pathways, they remain a very useful tool for *in cellulo* assays.

Another approach employed to elucidate the route of CPP uptake is colocalization assays. These assays measure colocalization of CPPs with cellular protein markers found only in one specific type of endocytosis or fluorescent cargos known to enter cells by a specific route. Assays perform with penetratin showed colocalization of transferrin, a marker of clathrin-mediated endocytosis, with the peptide at early stages of the endocytic pathway[105]. On the other hand, TAT has been shown to colocalize with fluorescently labeled dextrans, a marker of macropinocytosis[106].

The evidence for CPP endocytosis discussed earlier is part of a large reservoir of data. CPPs have been utilized to deliver numerous cargos inside cells. In multiple cases, the cargo has been delivered in the form of a CPP-cargo conjugate. Covalent attachment

of a cargo to a CPP has been shown to alter the route of endocytosis utilized by the CPP (as mentioned before). Consequently, it is no surprise that multiple endocytic pathways has been shown to be involved for the same CPP. However, the most recognized model of uptake for the CPP TAT (focus of this study) is macropinocytosis[107].

To this date, macropinocytosis remains not fully characterized. Macropinocytosis is a form of fluid-phase endocytosis performed by all mammalian cells[108]. This process occurs at ruffling sites containing newly formed actin filaments[109]. Ruffling takes place in different cells at different extents. This, in turn, contributes to the observed varying rates of macropinocytosis among cell types. It has been shown that effector molecules such as: epidermal growth factor (EGF) and phorbol esters can induce membrane ruffling and, subsequently, macropinocytosis[110, 111]. On the other hand, these processes can be inhibited by amiloride and cytochalasins[112]. It has been shown that TAT can induce structural changes on actin filaments reminiscent of ruffling *in vitro*[113]. Moreover, TAT can induce macropinocytosis and increase the uptake of different cargos inside cells. However, the exact molecular details behind this process are still unknown.

After ruffles take form (circular, cup-shaped or planar folds), they close into large endocytic vesicles called macropinosomes. Due to the unguided nature of this process, formation of vesicles does not always follow ruffling and sometimes the ruffles recede back to the cytosolic space[114]. The vesicles that do form pinch-off the plasma membrane and become intracellular vesicles that range in size from 0.5 - 5 μm in diameter[115, 116]. These vesicles are very large when compared to the vesicles formed by caveolae and clathrin-mediated endocytosis (50 nm and 100 nm, respectively)[117, 118]. This suggests that

cells will display a limit, with macropinocytosis at the top of the range, for the size of a particular cargo that can be internalized by each pathway.

During endocytosis of CPPs, the endocytic vesicle formed, which contains CPPs will undergo a complex maturation process involving multiple synchronized dependent and independent steps[119]. Multiple endocytic vesicles displaying different characteristics will form during the maturation process (**Figure 1-1**). These vesicles have been well characterized and can be distinguish based on their morphology, intracellular localization, the rate with which they accumulate endocytic markers and the presence of specific endocytic protein markers. It is known that newly internalized CPPs and cargos are transported into early endosomes (EEs)[119]. The amount of lipids and proteins that are internalized, along with the CPPs, into EEs is enormous, and some of these materials are recycled back to the plasma membrane[114]. EE readily fuse with and move away from other EE allowing efficient trafficking. EE display a mosaic membrane that allows the recruitment of specialized proteins, like Rab5, and formation of protein-protein, protein-lipid and lipid-lipid domains involve, in part, in the trafficking and maturation of these vesicles[120]. Maturation of EEs lead to formation of another type of endocytic vesicle, multivesicular bodies (MVBs)[121, 122]. These process initiates after EE detaches from tubular structures, and the vesicle moves away from the plasma membrane towards the nucleus along microtubules. Following further fusion events and invagination of the limiting endosomal membrane, intraluminal vesicles are formed within pre-existing EEs. The previous step marks the formation of MVBs. These vesicles, compared to EE, display lesser protein markers and gradually gain hydrolases from the trans-Golgi network

(TGN)[123]. At the end of their maturation process, MVBs sort and segregate protein receptors and lipids to intraluminal or limiting membranes. This last step leads to the formation of late endosomes (LEs)[124, 125]. LEs are morphologically different than MVBs. The population of late endosomes varies in size and contains sac-like and tubular vesicles. The protein and lipid composition of LEs is different than other endocytic organelles. LEs contain important proteins like Lamp1 and Rab7[126, 127]. These vesicles contain bis-monoacylglycerophosphate (BMP), a phospholipid found only in LE[128]. BMP is highly enriched in the intraluminal vesicles of LEs and is thought to be necessary for the entry of some viruses into the cytosolic space of cells by back-fusion[129, 130]. BMP is very important since it has been shown to bind TAT with high affinity[131]. Furthermore, the presence of BMP increases TAT-mediated leakage and lipid mixing *in vitro*. During the final stages of the endocytic pathway, LEs fuse with lysosomes. Lysosomes represent the dead-end of the endocytic pathway[132]. These organelles contain acidic hydrolases, which are essential for lysosome function, that digest macromolecules. In order to reach the cytosolic space of cells and avoid degradation, CPPs have to escape the endocytic pathway (**Figure 1-2**).

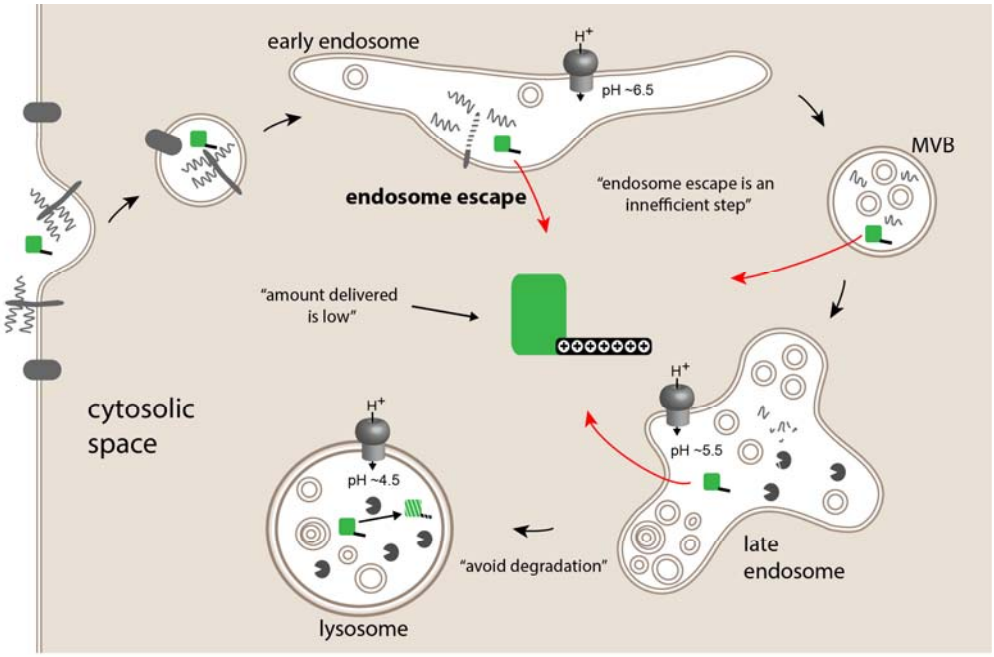


**Figure 1-2. CPP-cargo conjugate endosomal escape**. From left to right: A CPP-cargo binds to HSPGs on the cell surface and enter cells, which leads to entrapment of the CPP-cargo inside an endocytic vesicle. After the CPP-cargo reaches early endosomes, MVBs or late endosomes it can escape from the endocytic pathway (red arrows). This is the preferred point of exit for a CPP-cargo conjugate in order to avoid degradation. The CPP-cargo is susceptible to degradation and, in order to avoid degradation and inactivation, it needs to escape the endocytic pathway before it reaches lysosomes. The endosomolytic activity of CPPs is low and endosomal escape is innefecient. Consequently, the amount of CPP-cargo delivered into the cytosolic space of cells is very low.

### 1.3.5 Escape of CPPs from the endocytic pathway: The limiting step

Because endosomal release might determine the efficiency with which a cargo reaches the cytosol of cells, understanding the mechanisms involved in this step is important. To date, these mechanisms remain poorly defined. Part of the challenge associated with understanding how CPP-cargos escape from the endocytic pathway is that efficiency of endosomal escape is often poor[48, 133]. Cargos that typically require fewer copies to elicit a biological response certainly demonstrate that endosomal escape takes place (as is the case for TAT-Cre). However, cargos that require more copies inside cells for activity often fail to show significant biological effects. Several assays have been developed to assess the endosomal escape efficiency of CPPs. Fluorescence-based methods have revealed that CPPs conjugated to fluorescent cargos typically remain localized within the endocytic pathway[52]. Mass spectrometry approaches have also confirmed these results, though estimates vary widely depending on the conditions used[103, 134, 135]. Maybe the most telling examples are not those in which delivery worked, but the applications where no cytosolic delivery is detected[136-139]. For instance, TAT has been conjugated to an ubiquitin cargo designed to be cleaved by cytosolic deubiquitinating enzymes upon escape from endosomes. However, upon incubation with cells, endocytosis was detected but cleavage of ubiquitin was not[139]. It was therefore concluded that the protein did not access the cytosol to any detectable extent.

While many mechanisms have been proposed to explain plasma membrane translocation[140], fewer have been offered to explain endosomal escape. First, it should be noted that mechanisms that imply the disruption of lipid bilayers are not only applicable

to plasma membrane translocation but also to endosomal escape. A mechanism that has been proposed to explain how CPPs could translocate across the plasma membrane of cells involves the negatively charged phospholipid phosphatidylserine (Ptd-Ser). Positively charged CPPs are known to bind negatively charged phospholipids such as Ptd-Ser[141, 142]. This phospholipid is, however, found mainly in the inner leaflet of the plasma membrane of mammalian cells (**Figure 1-1**)[143]. The outer leaflet of the plasma membrane bilayer is, in contrast, composed of zwitterionic phospholipids for which CPPs have little affinity[144, 145]. Nevertheless, it was proposed that CPPs and Ptd-Ser, positioned on either side of the lipid bilayer, might together form the equivalent of a membrane capacitor. This capacitor theoretically generates a membrane potential high enough to create a reversible electropore on a membrane[146]. This model also agrees with experimental data that has found a relatively enhanced ability of oligoarginine peptides to deliver cargo molecules across membranes when compared to oligolysine peptides[73]. The membrane capacitor model suggests that oligoarginines could bind the negatively charged phosphate groups in phospholipids better than oligolysines and form a more stable CPP-Ptd-Ser capacitor. Because the Ptd-Ser lipid asymmetry is presumably maintained within the endocytic pathway, such mechanisms could take place inside endosomes[143]. If this is true, a key question lies in determining how a CPP might permeabilize an endosome without acting first on the plasma membrane. A possible answer to this question could involve the difference in how CPPs access these different bilayers. As previously stated, positively charged CPPs interact with HSPGs present on the cell surface (**Figure 1-1**)[147]. The abundance of HS at the plasma membrane might therefore contribute to reducing the

concentration of CPP directly in contact with lipids. During endocytosis, HSPGs are presumably internalized with CPPs (**Figure 1-1**)[80, 148]. HSPGs therefore continue to have an inhibitory effect on the membrane disruption activity of CPPs[149]. However, HSPGs are gradually hydrolyzed during maturation within the endocytic pathway (**Figure 1-1**)[150]. HS hydrolysis and release from the membrane of endosomes could in turn favor the interaction between CPPs and endosomal lipid bilayers [30].

Several lines of evidence suggest that CPPs could disrupt the lipid bilayer of endocytic organelles more readily than that of the plasma membrane. For instance, positively charged CPPs preferentially bind negatively charged phospholipids over neutral ones[151]. Interestingly, the intraluminal lipid bilayers of late endosomes appear to be uniquely enriched in the negatively-charged phospholipid bis(monoacylglycero)phosphate (BMP), also known as lysobisphosphatidic acid (LBPA) (**Figure 1-1**)[152, 153]. Recently, TAT was shown to induce the leaky fusion of liposomes containing BMP[131]. TAT induces lipid mixing and membrane leakage in a BMP concentration-dependent manner and these activities were also greater at pH 5.5 than at physiological pH. This is important because pH 5.5 is characteristic of the acidic pH found in the lumen of late endosomes. The involvement of BMP in CPP-mediated delivery has not been demonstrated yet. However, cellular assays in which progression through the endocytic pathway is blocked with dominant negative Rab proteins have also suggested that TAT and polyarginine peptides only escape from the endocytic pathway upon reaching late endosomes[103]. Together, these results strongly suggest that BMP is a target

for CPPs and that fusion between the limiting membrane of late endosomes and that of intraluminal vesicles is involved in the escape of CPP-cargo to the cytosolic space of cells.

## 1.4 Tools to improve CPP endosomal escape

### 1.4.1 pH dependent membrane active peptides (PMAPs)

PMAPs have been used in combination with CPPs to increase the endosomal escape of various cargos (**Figure 1-3**). This strategy is attractive because PMAP-CPP fusions can be genetically encoded or easily synthesized by SPPS. Chimeric hybrids of PMAPs and CPPs can therefore be readily obtained. HA2 derivatives are typically attached to the N-terminus of CPPs because HA2 requires a free N-terminal glycine for full membrane activity[154, 155]. It has been shown that TAT-mediated delivery of cell-impermeable cargos into cells is enhanced by conjugation to PMAPs[156]. HA2-TAT and its derivatives have been attached to quantum dots, and such conjugates have been shown to stimulate macropinocytosis and endosomal escape in cultured cells[157]. Protein cargo delivery can also be enhanced by this method, and has potential for therapeutic applications. HA2 fused to the tumor suppressor protein p53 containing the poly-arginine CPP R11 (HA2-

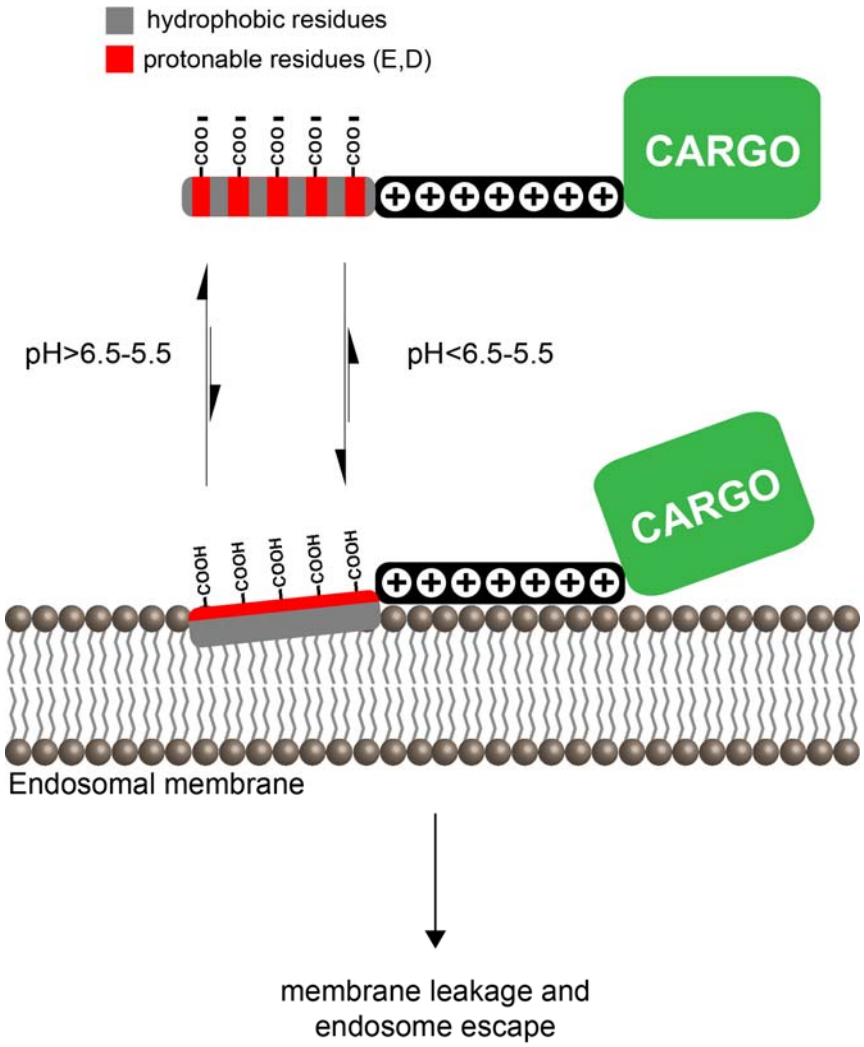


**Figure 1-3. Mechanism of PMAPs-mediated endosomal escape.** PMAPs undergo conformational change upon acidification. This typically involves a shift from a random coil to an ordered conformation such as a helix, in which hydrophobic moieties are on one face while the ionizable moieties are on the other. This ordered conformation leads to membrane binding, and brings conjugated CPPs and cargos into close proximity to the membrane. At sufficient concentrations, this binding eventually leads to lysis or membrane fusion resulting in cargo release.

p53-R11) was, for instance, more efficient in abrogating cancer cell growth than p53-R11 alone[158]. While HA2 can be directly connected to the cargo, HA2-TAT has also been used in trans to increase the delivery of cargos co-incubated with cells. The principle is that HA2-TAT and a TAT-labeled cargo will accumulate together inside the endocytic pathway. HA2-TAT can then induce the endosomal escape of a TAT-cargo that would be present in the lumen of the same organelles. For example, a retro-inverso HA2-TAT, which is less susceptible to degradation within the cell, has been used to increase the delivery of TAT-Cre recombinase[156].

Interestingly, HA2-TAT derivatives can also increase the delivery efficiency of proteins that are not labeled by TAT or other CPPs. For instance, the derivative HA2E5-TAT has been used to deliver fluorescent proteins not labeled with a CPP to the cytosol of cells by simple co-incubation[159]. The apoptosis-inducing peptide PAD was also delivered to cells efficiently when co-incubated with cells, and successful cytosolic delivery was assessed by induction of cellular apoptosis. Amiloride inhibited PAD-mediated cell death in the presence of HA2E5-TAT, suggesting that HA2E5-TAT induces uptake of soluble cargo by macropinocytosis[159]. The strategy is therefore to take advantage of the fact that TAT can induce pinocytic uptake of cargo molecules that do not necessarily interact with cells but are simply present in the extracellular milieu. These cargo molecules, despite not containing TAT, also accumulate in the lumen of endocytic organelles that contain HA2-TAT.

### 1.4.2 Limitations and future challenges

Ideally, PMAPs should only become active at acidic pH so as to prevent disruption of the plasma membrane or membranes of intracellular organelles once cytosolic delivery has been achieved. However, PMAPs exist in equilibrium between protonated and deprotonated forms at any pH (**Figure 1-3**)[160]. This can be illustrated by a modified version of the Henderson Hasselbach equation:

$$pH = pKa + \log (\text{inactive peptide/active peptide})$$

where inactive and active peptide is protonated and deprotonated, respectively. At any given pH a defined fraction of the peptides will be active. Thus, even at neutral pH, a sufficiently high concentration of total peptide can lyse RBCs[145, 161]. Concentrations above ~5 μM HA2E5-TAT has been shown to be toxic to HeLa cells[161]. CPPs might, however, contribute to modulating the toxicity associated with PMAPs. As previously mentioned, CPPs can interact with HSPGs[162, 163]. Heparan, an HS analogue that binds to CPPs such as TAT (**Figure 1-1**), has been shown to inhibit the binding of HA2E5-TAT to RBCs and concomitantly inhibit hemolysis. The effect of heparan on HA2E5 mediated hemolysis is, on the other hand, negligible[145]. It is therefore interesting to speculate that interactions between HA2E5-TAT and HSPGs could reduce access of HA2E5–TAT to the plasma membrane lipid bilayer. These interactions could therefore protect cells from the lytic activity of the PMAP-CPP conjugate. On the other hand, interactions between HA2E5-TAT and HS within the lumen of endosomes could inhibit endosomolysis.

PMAPs can be readily conjugated to CPPs as well as cargo proteins (**Figure 1-3**). In principle, they interact with membranes in a pH-dependent manner, allowing them to

disrupt endosomal membranes only at appropriate concentrations. While they can enhance CPP-mediated delivery, PMAP-CPP conjugates present several challenges. How to incorporate PMAP-CPPs to achieve optimal delivery and minimal toxicity remains to be further explored. As illustrated before, how cargo conjugation affects PMAP-CPP activity remains in particular unclear. Endosomal retention of cargo fused to the PMAP-CPP construct, even after endosomal lysis, is a concern. This phenomenon seems to indicate that preferable designs should include cleavable linkers between PMAP-CPPs and their cargos. Such designs would, in principle, increase endosomal escape and cytosolic delivery. Finally, difficult handling of hydrophobic/amphipathic PMAPs and aggregation in aqueous solutions remains a problem.

### 1.4.3 Photochemical internalization

In 2004, two groups made the observation that fluorescently labeled CPPs could escape from endosomes upon irradiation with visible light (**Figure 1-4**). Arginine-rich CPPs labeled with fluorescein were released from endocytic compartments upon irradiation with laser light at 488 nm. Similar endosomal release was observed when the peptide was labeled with Alexa-Fluor 633, incubated with cells and irradiated with 633 nm laser light[164]. This phenomenon has also been demonstrated when the CPPs are conjugated to proteins (**Figure 1-4**). For instance, the protein p53 labeled with the CPP R11 and with the fluorophore FITC was observed to accumulate in endosomes upon

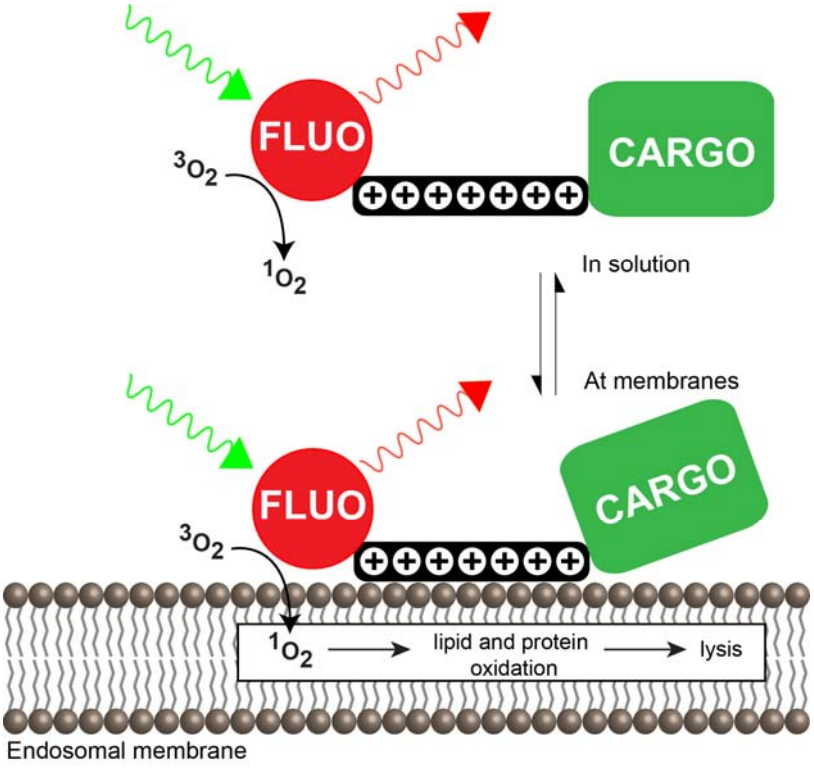


**Figure 1-4. Model for fluorophore-CPP mediated PCI.** The Fl-CPP conjugates exist in equilibrium in a membrane bound and unbound state due to the membrane-targeting role of the peptide moiety. Upon light irradiation, the fluorophore moiety of the conjugate produces singlet oxygen by transfer of energy from its triplet state to molecular oxygen. When present in solution, the Fl-CPP conjugate is innocuous. But, in its membrane bound state, the singlet oxygen produced by the fluorophore reacts with membrane biomolecules and disrupts the membrane, causing release of endosomal contents.

incubation with cells. Repeated fluorescence imaging at 480 nm by confocal laser scanning microscopy, however, led to a redistribution of the FITC conjugate into the cytosolic and nuclear compartments of cells[165]. The use of fluorescently labeled CPPs for PCI has been extended to the cytosolic delivery of RNA molecules. Ohtsuki and co-workers have fused an RNA binding protein U1A to the TAT peptide. This TatU1A construct was labeled with Alexa Fluor 546 or cyanine fluorophores at its C-terminus. The fluorescently labeled TatU1A construct could bind small hairpin RNA (shRNA) containing a U1A binding sequence and carry its cargo into the endocytic pathway of cells. Irradiation with light corresponding to the excitation wavelength of the fluorophores led to release of shRNA from endosomes into cytosol as measured by the cytosolic redistribution of fluorescence as well as by gene silencing mediated by the delivered shRNA. It was therefore shown that gene expression could be spatially and temporally controlled using light irradiation[166].

In addition to the fluorophores cited previously (i.e. xanthenes, Alexa fluor dyes, cyanines), CPP-photosensitizer conjugates have also been tested. For instance, aluminum phthalocyanine (AlPcS) has been attached to TAT to photo-induce endosomal release and cytosolic delivery[167]. Better uptake of the photosensitizer 5-[4-carboxyphenyl]-10,15,20-triphenyl-2,3-dihydroxychlorin (TPC) was also seen when conjugated to oligoarginine R7[168]. The irradiation wavelength required to induce endosomal escape has to match the excitation spectra of the fluorophore and so far, light in the range of 480 to 670 nm has been successfully used[164, 169-174]. When irradiation is performed on a confocal laser scanning microscope, the fluorophores have to be subjected to multiple light exposures to

achieve significant endosomal release. Consequently, cytosolic redistribution typically happens on a time scale of minutes. In contrast, irradiation on an epifluorescence instrument can lead to cytosolic redistribution within milliseconds[175]. This has, for instance, been observed with TAT labeled with the fluorophore tetramethylrhodamine irradiated at 560 nm[175]. Presumably, these differences are due to the fact that while the whole cell is exposed to light when using epifluorescence, only small subcellular areas are exposed to light at once when a scanning laser is used. Together, these results nonetheless suggest that light can be dosed and that, unlike with other methods, endosomal release can in principle be precisely controlled. In addition, it appears that most if not all endocytic organelles containing Fluorophore-CPP conjugates lyse if sufficient light exposure is applied. The overall yield of cytosolic delivery using this methodology can therefore be very high.

### 1.4.4 Limitations and future challenges

A potential limitation of PCI and CPP-mediated PCI in particular, is the photo-toxicity associated with these methodologies. The photosensitizers used for PCI can cause cell death when exposed to sufficient light[176]. The light dose applied to achieve endosomal release must therefore carefully be controlled so as to avoid cell death during delivery[176]. Several reports have shown that CPP-mediated PCI can be accomplished without killing cells[164, 177]. However, R7-TPC causes apoptosis and necrotic cell damage at low and high concentrations, respectively[168]. Recently, rapid cell death was also found to occur during PCI with TMR-TAT. In particular, plasma membrane permeabilization and blebbing were

observed shortly after endosomal escape of TMR-TAT was initiated with light[178]. It is clear that delivering photolytic agents into the cytosol of cells can potentially have detrimental effects. One can imagine how a photolytic Fluorophore-CPP could, upon endosomal escape, reach the membrane of other intracellular organelles, damage these membranes during irradiation, and cause cell death. However, TMR-TAT is not phototoxic when directly microinjected into the cell's cytosol[178]. Instead, endosomal lysis itself has been implicated in the cell death that accompanies PCI with TMR-TAT. In particular, irradiation causes the endosomal release of not only TMR-TAT but also of other molecules present in the lumen of these organelles[178]. The release of toxic material such as lysosomal hydrolases[179] or iron[180] might in principle take place. Recently, the release of calcium from endocytic vesicles photolysed with TMR-TAT has been implicated in cell-death. Release of calcium into the cytosol was followed by accumulation of calcium in the mitochondria, activation of the mitochondrial permeability transition pore (MPTP), and subsequent cell death[178]. Consequently, in tissue culture assays, rapid cell death was abolished with ruthenium red or cyclosporine A, inhibitors of mitochondrial calcium transport or of the MPTP, respectively[178].

In principle, CPP-mediated PCI could be used *in vivo* to deliver drugs to diseased cells by shining light only on selected tissues. PCI is particularly attractive for such applications because of the temporal and spatial control that it provides[166]. The *in vivo* potential of PCI has been demonstrated with photosensitizers[181-183]. However, CPP-mediated PCI has never been tested *in vivo* to my knowledge. Yet, one can envision how CPP-based agents might be complementary to other PCI photosensitizers. While peptides are prone to rapid

degradation *in vivo* and *in cellulo*, retro-inverso (ri) peptides can be used to extend the half-life of Fluorophore-CPPs. It has been observed that endocytosed TMR-TAT loses its photo-endosomolytic activity after only a few hours of incubation, presumably because of proteolytic degradation of the peptide within endocytic organelles[184]. In contrast, TMR-riTAT remains active even after 8 h of incubation[175]. Another important issue for *in vivo* applications is related to the fact that visible light does not penetrate tissues deeply[185]. It is reported that red and near-infrared light penetrates tissues more deeply than light of shorter wavelengths[185]. Chromophores that absorb light above the 600 nm range should therefore be preferable for *in vivo* procedures. However, Fluorophore-CPPs conjugates containing Cy5, Cy5.5, Alexa 660, and Alexa 680 were reported to be dramatically less efficient at inducing the endosomal release of shRNA than fluorophores with shorter excitation wavelength[166]. Whether Fluorophore-CPP can be performed with red or near-infrared chromophores therefore remains to be established.

## 1.5 Multivalent CPPs for delivery of macromolecules inside live cells: another class of endosomolytic agents with potential improved features

### 1.5.1 Multivalency: Concept and rationale for the increase of CPPs activity

One way to increase the endosomolytic activity of CPPs is to create multivalent CPPs. This approach consists of presenting multiple copies of a CPP on a delivery vector so as to increase the local concentration of the CPP where the peptide interacts with cellular components. Several multivalent CPPs have been reported (**Figure 1-5).**

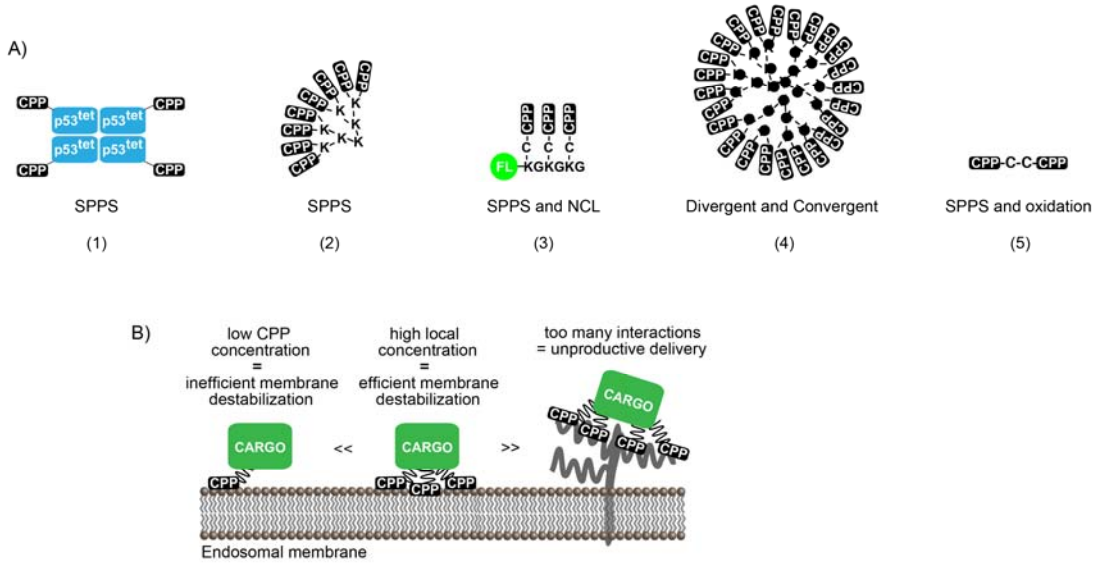


**Figure 1-5. MCPP systems and their interactions with membranes.** (a) Strategies used to generate MCPPs. From left to right: (1) The p53tet-CPP system involves connecting the tetramerization domain from the human tumor repressor protein p53 to a CPP. The peptide sequence is generated using SPPS. After purification of the peptide sequence, p53tet selfassembles into a tetramer producing a tetravalent CPP. (2) Loligomers are a "squid-like" MCPP system. The CPP is attached on the surface of a polylysine branch scaffold. The scaffold and the peptide are generated using SPPS. The number of branches of this MCPP system will depend on the number of Lys coupling steps. (3) The branched CPP system involves the generation of a peptide scaffold of Lys(ε-NH-Cys)Gly repeats to which a CPP-thioester is added using native chemical ligation (NCL). The peptides were generated using SPPS although production of recombinant peptide or protein thioesters is possible using intein fusions. A fluorophore was added on the *N*-terminal end of the scaffold peptide to serve as both an imaging agent and a small model cargo. (4) Dendrimers are MCPPs having a "tree-like" shape and are usually generated using divergent or convergent methods. CPPs have been attached to the surface of polyamidoamine (PAMAM), polypropylenimine (PPI) or polyethylenimine (PEI) dendrimers. The number of CPPs on dendrimers is among the highest observed for MCPPs. (b) A possible model for the mode of action of CPPs versus that of MCPPs. In this example, a CPP-cargo is present at the membrane of endosomes at a low local concentration, leading to poor endosomolytic activity. In contrast, a MCPP-cargo displays multiple copies of the CPP. This leads to efficient membrane interactions and a possible enhancement in membrane disruption. In some cases however, too many CPP copies might cause unproductive membrane interactions such as tight binding to HSPGs. This in turn might lead to poor cellular penetration.

Here, I survey the protocols used to generate multivalent CPPs and discuss the evidence suggesting that multivalent CPPs escape from endosomes more efficiently than their monomeric counterparts.

### 1.5.2 Strategies to generate multivalent CPPs

Multiple synthetic protocols have been used to create multivalent CPPs (**Figure 1-5a).** One strategy involves attaching a protein oligomerization domain to CPPs. For instance, the tetramerization domain of the human tumor suppressor p53 (p53tet), corresponding to amino acids 325–355, has been attached to the CPPs decaarginine and decalysine by solid phase peptide synthesis (SPPS)[186, 187]. The p53tet domain self-assembles in solution and tetrameric CPP constructs were therefore obtained (**Figure 1-5a (1)**). Notably, these compounds delivered DNA into cells more efficiently than decaarginine and decalysine alone. Multivalent CPPs have also been generated by attachment of the peptides to dendrimers[74, 188-191]. Dendrimers are highly branched molecules that display a tree-like shape (**Figure 1-5a (2)**)[192]. The branches of dendrimers can be functionalized and, therefore, dendrimers can serve as a scaffold onto which CPPs can be chemically conjugated. Related approaches consist of attaching CPPs to peptide scaffolds. Branched "squid-like" peptide constructs known as loligomers have, for instance, been reported (**Figure 1-5a (3)**)[193-195]. Loligomers containing eight CPP copies have been assembled by SPPS on branched polylysine scaffolds[196]. TAT has also been assembled on a peptide scaffold consisting of Lys(ε-NH-Cys)Gly repeats (**Figure 1-5a (4)**). In this example, TAT was functionalized with a C-terminal thioester and conjugated

to the cysteine residues of the scaffold by native chemical ligation[197, 198]. The MCPPs generated displayed 2, 3, and 4 TAT copies. Finally, CPPs containing cysteine residues have been dimerized by the straightforward formation of disulfide bridges (**Figure 1-5a (5)**)[199-201]

### 1.5.3 Delivery of cargos using multivalent CPPs

How the extracellular and intracellular behavior of multivalent CPPs compares to that of their monomeric counterparts is not clear. There is certainly growing evidence that multivalent CPPs transduce cargos into cells more efficiently than CPPs. The multivalent CPPs described in the previous paragraph have, for instance, been reported to deliver molecules such as DNA, proteins, peptides, polysaccharides or small organic fluorophores to a higher degree than CPPs[198, 200-204]. However, in the case of DNA transfection experiments, improvements in cytosolic delivery can be difficult to interpret. Positively-charged multivalent CPPs form complexes with DNA that might be significantly different than those formed with CPPs. As a matter of fact, it has been proposed that branched CPPs might be more capable of "multitasking", with a few branches of multivalent CPPs being in complex with its DNA cargo while other branches might interact with cellular components[203]. In contrast, a positively charged and monomeric CPP bound to negatively charged DNA might not be able to interact with other molecules as readily. Taking the example of DNA transfection again, multivalent CPPs/DNA complexes are typically endocytosed at higher levels than CPPs/DNA particles[186, 193, 202]. Since more multivalent CPPs and more DNA accumulate inside endosomes, more DNA is delivered into the

cytosol and nucleus of cells. This would presumably happen even when multivalent CPPs and CPPs might have similar intrinsic endosomal escape activity. It is therefore often difficult to determine whether increased delivery by multivalent CPPs is due to enhanced endocytosis, enhanced endosomal release, or both.

### 1.5.4 Limitations and future challenges

Multivalent CPPs show great potential as endosomolytic compounds. However, several limitations of this class of compounds can be expected. First, synthesis protocols are often complex and multivalent CPPs cannot be generated as easily as their monomeric counterparts. In addition, convenient protocols for the conjugation of these systems to various cargos remain to be established. The *in vivo* utility of multivalent CPPs inside cells is also uncertain because of the potential immunogenicity of branched peptides in general. The possibility that CPPs might act as immunogens has already been discussed in the literature[205, 206]. Notably, multivalent CPPs share close structural resemblance with multiple antigenic peptides (MAPs)[207]. MAPs are known to induce strong immune responses in part because of enhanced molecular recognition by immune cells[208]. The latter is a result of the display of multiple short antigenic peptides in a polylysine dendrimer scaffold. The use of multivalent CPPs could therefore produce a non-desired cellular immune response due to the display of multiple, possibly immunogenic CPPs. One of the challenges ahead consists in understanding how multivalent CPPs mediate better delivery than monomeric peptides. To date, how the number of CPP copies impacts activity remains uncertain. As indicated in **Figure 1-5b**, few CPP branches might not

induce enough activity while too many might cause unproductive behavior. The effect of cargo conjugation also remains to be explored. It is, for instance, possible that the number of CPP branches required for optimal delivery depends on the types of cargo used. Structure-activity relationship studies should also reveal how the architecture of multivalent CPPs affects their interactions with lipid bilayers, their trafficking inside cells, and their endosomolytic activity. The mechanism of multivalent CPPs endosomal escape remains unknown. It is possible that displaying multiple copies of a CPP would change how the peptide is uptaken by cells (direct plasma translocation or endocytosis) and, if endocytosed, how does it escape from the endocytic pathway, when compared to its monomeric counterpart. Mechanistic studies using DN-Rab proteins and endocytosis inhibitors should help decipher the route that multivalent CPPs utilize to penetrate cells. This in turn, could allow the development of more efficient delivery agents.

### 1.6 The goal of my study

Although previous studies showed that multivalent CPPs display an enhanced delivery of multiple different types of cargos, relative to their monomeric counterparts, very little is known about how they penetrate cells. Furthermore, the synthesis of multivalent CPPs and conjugation of cargos to these delivery vectors is complex. In order to establish the mechanism involved in multivalent CPPs penetration, I will utilize cells and liposomes as complementary models. A simple and controllable *in vitro* model, like liposomes, will allow me to study how multivalent CPPs interact with membranes that resemble different lipid bilayers that multivalent CPPs may encounter in a cell. Moreover, I will be able to

study the ability of multivalent CPPs to disrupt these membranes. This will allow me to establish, in a controlled environment, insights involved in multivalent CPPs cell penetration. Yet, liposomes fail to reproduce the activity displayed by multivalent CPPs in cells. To solve this problem, I will use living cells to look at the delivery activity of multivalent CPPs. Furthermore, with the help of cellular and molecular biology tools I will perform mechanistic studies using multivalent CPPs. The *in cellulo* studies will then complement the *in vitro* ones. Together, these will allow me to establish the mechanism of multivalent CPP cell penetration. Finally, my work will also focus on developing new simple and convenient strategies to generate multivalent CPPs, as well as, establishing new protocols for efficient and simple delivery of cargos. Altogether, the knowledge I will acquire will lay a solid foundation for the design of improved delivery agents with high therapeutic potential that can also prove to be very useful to study cellular processes in living cells.

# 2. GENERATION OF MULTIVALENT BRANCHED ENDOSOMOLYTIC REAGENTS OF THE PROTOTYPICAL CELL-PENETRATING PEPTIDE TAT: TOOLS FOR THE INTRACELLULAR DELIVERY OF BIOLOGICALLY ACTIVE COMPOUNDS TO LIVE CELLS IN CIS (COVALENT CONJUGATION) OR TRANS (SIMPLE CO-INCUBATION)*[198]

## 2.1 Introduction

In this chapter, I describe the synthesis and cellular delivery properties of multivalent and branched delivery systems consisting of the prototypical CPP TAT assembled onto peptide scaffolds using native chemical ligation. I test the hypothesis that branched multivalent TAT molecules would display an enhanced endosomolytic activity when compared to TAT and that these delivery agents could induce the release of cell-impermeable macromolecules trapped inside endocytic organelles into the cytosolic space of live cells. This is based on the principle that multivalency results in an increase of the CPP's local concentration at the sites where the peptide interacts with cellular components (avidity effect) (**Figure 1-5b**)[209, 210]. It has been clearly established that such an approach can increase the endocytic uptake of cationic peptides, and that branched molecules can function and multitask in ways their linear homologues cannot[186, 187, 203]. Herein I show that upon displaying three TAT copies, this trimeric delivery agent (Fl-$TAT_3$) escapes from the endocytic pathway. Moreover, Fl-$TAT_3$

*This chapter is reprinted with permission from "Generation of endosomolytic reagents by branching of cell-penetrating peptides: tools for the delivery of bioactive compounds to live cells in cis or trans" by Ángeles-Boza, A.$^{+}$;Erazo-Oliveras, A.$^{+}$; Lee, Y.-J. and Pellois, J.-P. *Bioconjugate Chemistry* **2010**, 21 2164-2167. doi: 10.1021/bc100130r. $^{+}$authors contributed equally. Copyright (2010) by American Chemical Society.

seems to possess an endosomolytic activity much greater that its monomeric and dimeric counterparts (Fl-TAT and Fl-$TAT_2$) and do not appear to show the unproductive membrane binding displayed by its tetrameric counterpart (Fl-$TAT_4$). Moreover, I show that Fl-$TAT_3$ can be utilized to deliver the small cargo fluorescein (Fl) in cis and two different cargos in trans, a fluorescently-labeled dextran (Dextran-tetramethylrhodamine) and a bioactive cell-impermeable peptide (pro-apoptotic domain, PAD). However, the mechanism of multivalent CPP endosomal escape remains unknown.

## 2.2 Results

### 2.2.1 Synthesis and purification of Fl-$TAT_n$ peptides

My synthetic approach consists of assembling multiple CPPs onto scaffold peptides using native chemical ligation (NCL)[197]. The scaffold peptides contain several lysines that have been modified at the ε $NH_2$ with a cysteine residue[211]. Each cysteine is available to react with a TAT peptide containing a C-terminal thioester (TAT-thioester) to generate branched multivalent species. The scaffold peptides were synthesized by solid-phase peptide synthesis (SPPS) using standard Fmoc protocols (**Figure 2-1**). N number of lysine residues bearing methyl-trityl (Mtt) protecting groups at the ε $NH_2$ were incorporated onto the Rink amide resin and separated by glycine residues to reduce steric hindrance during synthesis and NCL. The lysine side chains protecting groups were removed orthogonally with 2 % trifluoroacetic acid (TFA) and Boc-Cys(tButhio)-OH was coupled onto the exposed ε $NH_2$. This was followed by removal of the N-

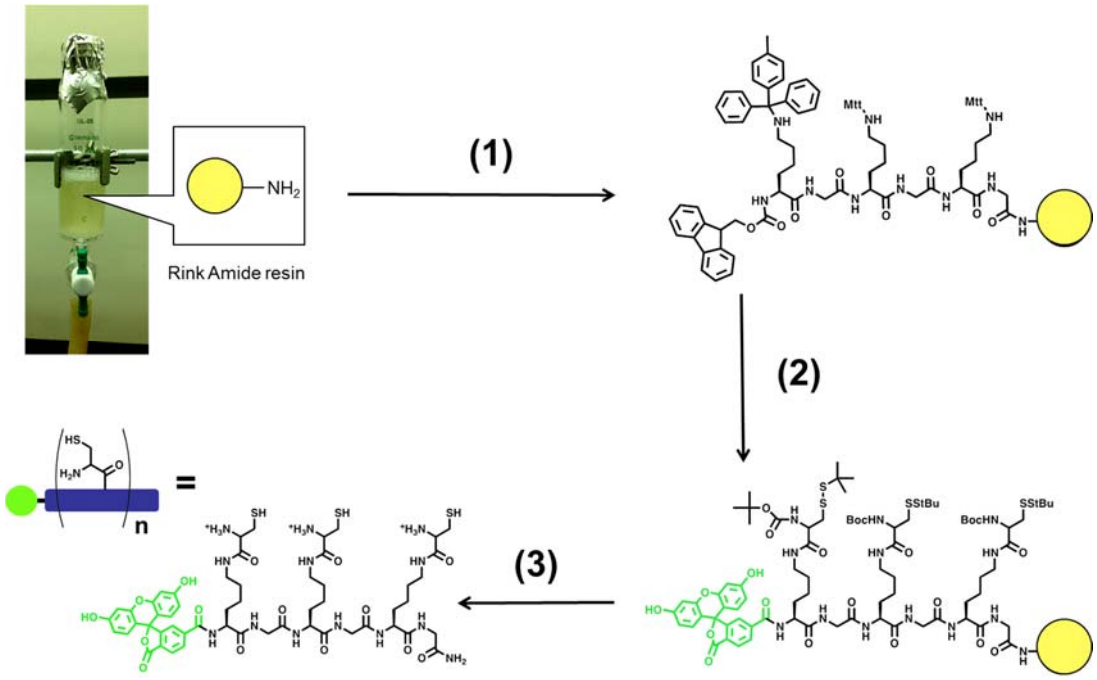


**Figure 2-1. Synthesis scheme of the scaffold peptides using SPPS.** Synthesis is performed in house using a glass vessel connected to a $N_2$ line (providing agitation). Before step 1, the Rink amide resin is swollen in DMF and deprotected (Fmoc removal). In step 1, Fmoc-Gly-OH, HBTU and DIEA are added to the resin to couple the first amino acid to the resin. After coupling, the resin is washed thoroughly, deprotected and Fmoc-Lys(Mtt)-OH is coupled to the resin as before. After coupling, the resin is washed and deprotected. The previous steps are repeated until the desired number of Gly and Lys are added to the resin. In step 2, Mtt (side chain protecting group) is selectively removed with 1 % TFA in DCM, the amino acid Boc-Cys(Stbu)-OH is added, the resin is deprotected and the fluorophore is conjugated to the resin. In step 3, the StBu (side chain protecting group) is removed and the peptide is cleaved from the resin. This last step leads to the generation of the free scaffold peptide.

terminal Fmoc group and subsequent coupling of 5(6)-carboxyfluorescein (Fl) to the free amino group on the scaffold. TFA cleavage and preparative scale reverse phase high-performance liquid chromatography (HPLC) purification afforded the scaffold peptides containing n sites for NCL. The products identity was confirmed using matrix-assisted laser desorption ionization time of flight (MALDI-TOF) mass spectrometry. TAT-thioester was obtained by SPPS on a sulfamylbutyryl resin using reported protocols (**Figure 2-2**)[212]. The branched multivalent TAT compounds were obtained by reacting the scaffold peptides containing n cysteines with 3n equivalents of TAT-thioester at room temperature in aqueous buffer at pH 7.5. Formation of the products, Fl-$TAT_n$, was detected by HPLC as early as 1 h, and the reactions were complete in less than 12 h (**Figure 2-3**). The crude products were purified by preparative scale reverse phase HPLC and their identity was confirmed using MALDI-TOF (**Figure 2-4, 2-5 and 2-6**).

### 2.2.2 Translocation of Fl-$TAT_n$ peptides into live cells

The cellular import of the multivalent compounds (Fl-$TAT_n$) was first investigated by live-cell fluorescence microscopy. The fluorescein molecule installed at the N-terminus of the peptides was used as both a fluorescent label and a model of a small molecule cargo. A fluorescein labeled TAT (Fl-TAT) was evaluated as a "non-branched" control. Fl-TAT, Fl-$TAT_2$, and Fl-$TAT_3$ were incubated with HeLa cells for 30 min at 1 or 5 μM. These concentrations were chosen because Fl-TAT is known to penetrate cells poorly under a concentration threshold of 5-10 μM[102]. I therefore considered that it would be possible to observe any enhancement of activity by Fl-$TAT_2$

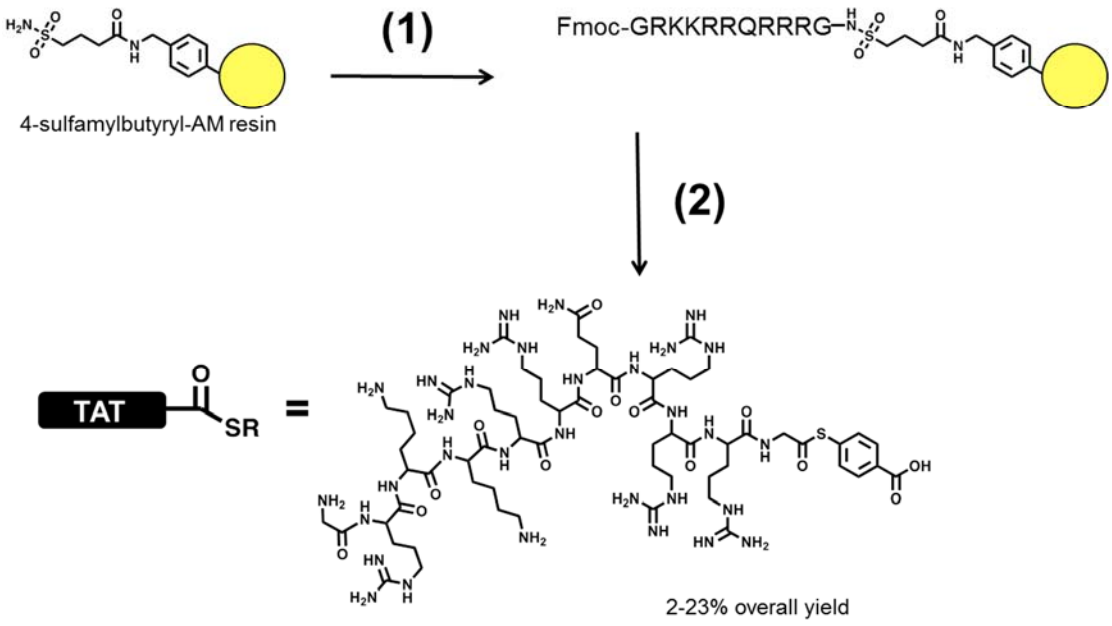


**Figure 2-2. Synthesis scheme of TAT-SR using SPPS.** Synthesis is performed in house using a glass vessel connected to a $N_2$ line (provide agitation). Before step 1, the Rink amide resin is swollen in DMF. In step 1, the resin is activated and the amino acids are coupled using standard SPPS protocols. In step 2, the peptide is cleaved to yield the peptide thioester.

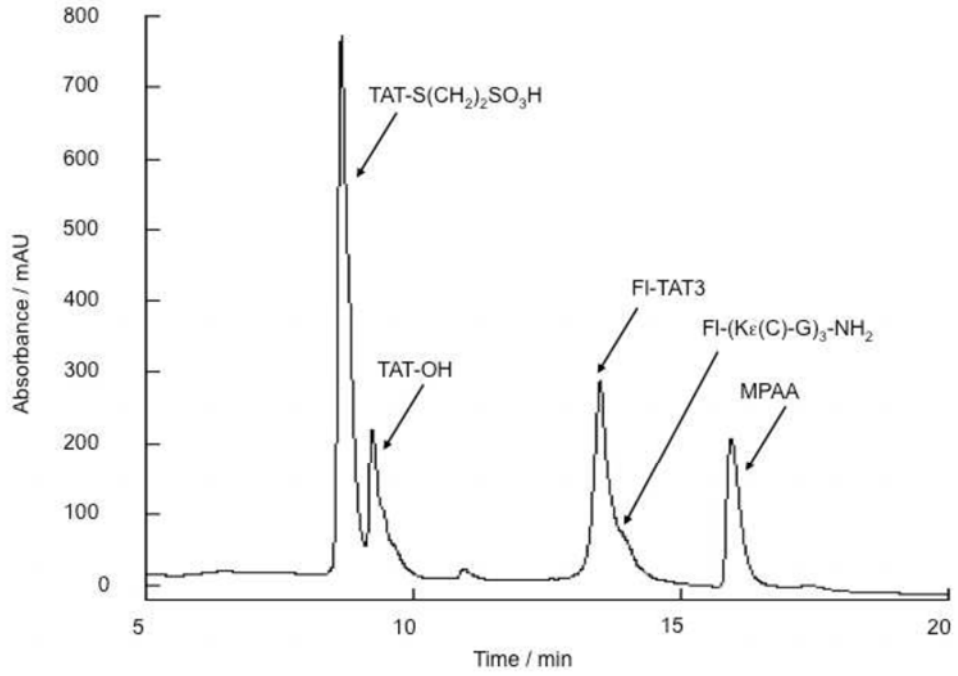


**Figure 2-3 HPLC analysis of the chemical reaction between Fl-(Kε(C)-G)$_3$-NH$_2$ and TAT-thioester.** The species shown here were identified by mass spectrometry.

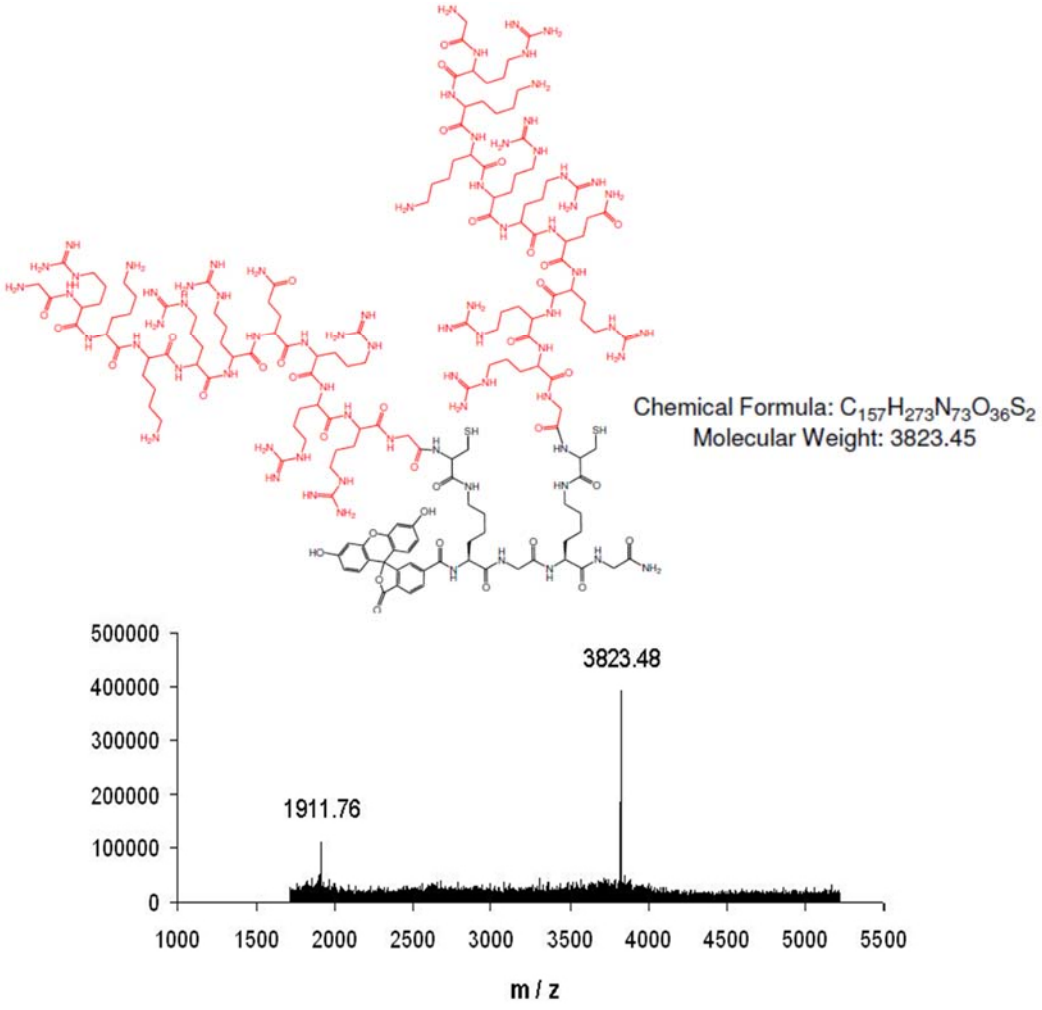


**Figure 2-4 Characterization of Fl-TAT$_2$.** Chemical structure and expected molecular weight of Fl-TAT$_2$ (top) and MALDI-TOF mass spectrum of Fl-TAT$_2$ (bottom). The peak at 1911.76 corresponds to the doubly charged product.

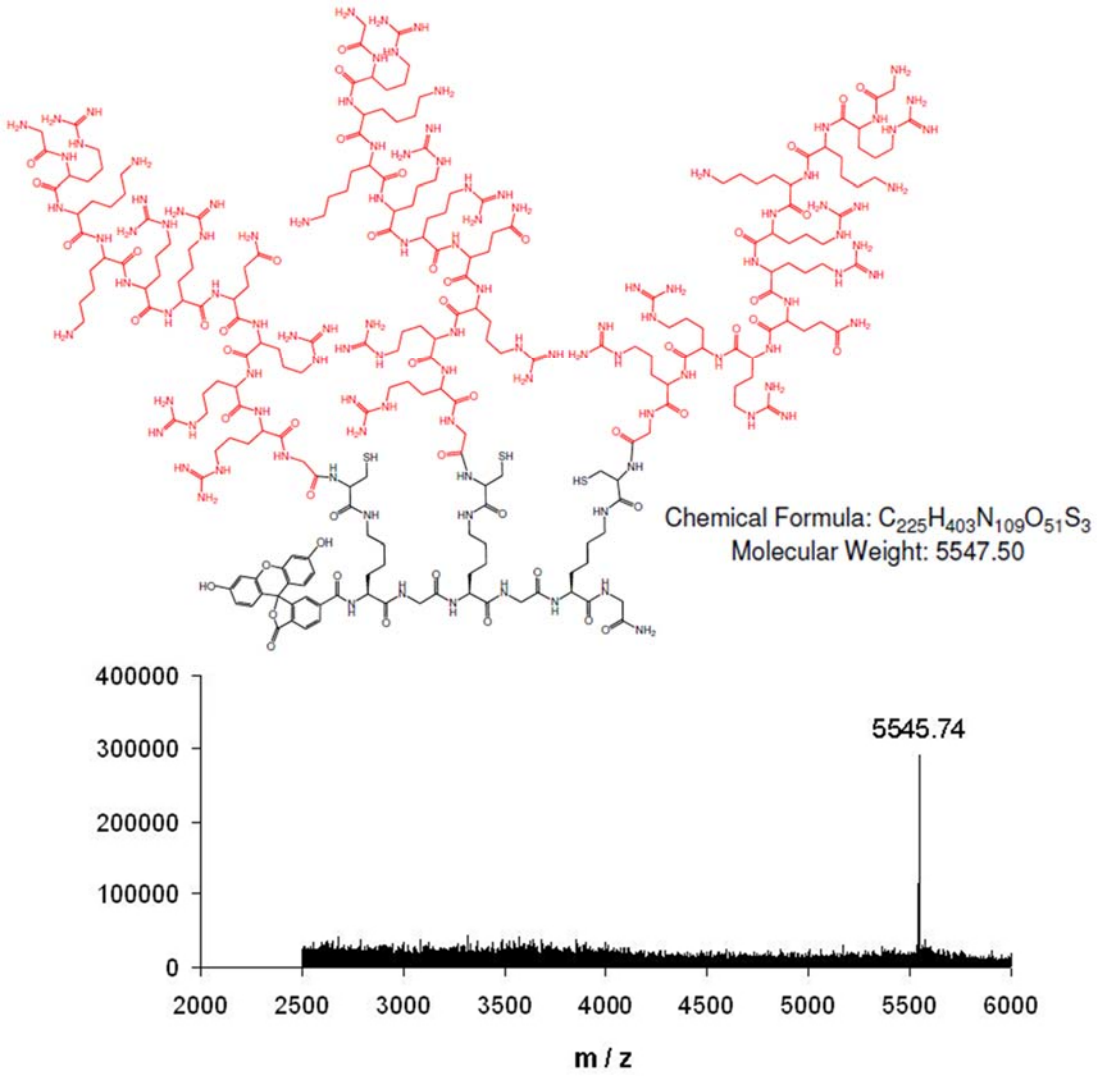


**Figure 2-5 Characterization of Fl-TAT$_3$.** Chemical structure and expected molecular weight of Fl-TAT$_3$ (top) and MALDI-TOF mass spectrum of Fl-TAT$_3$ (bottom).

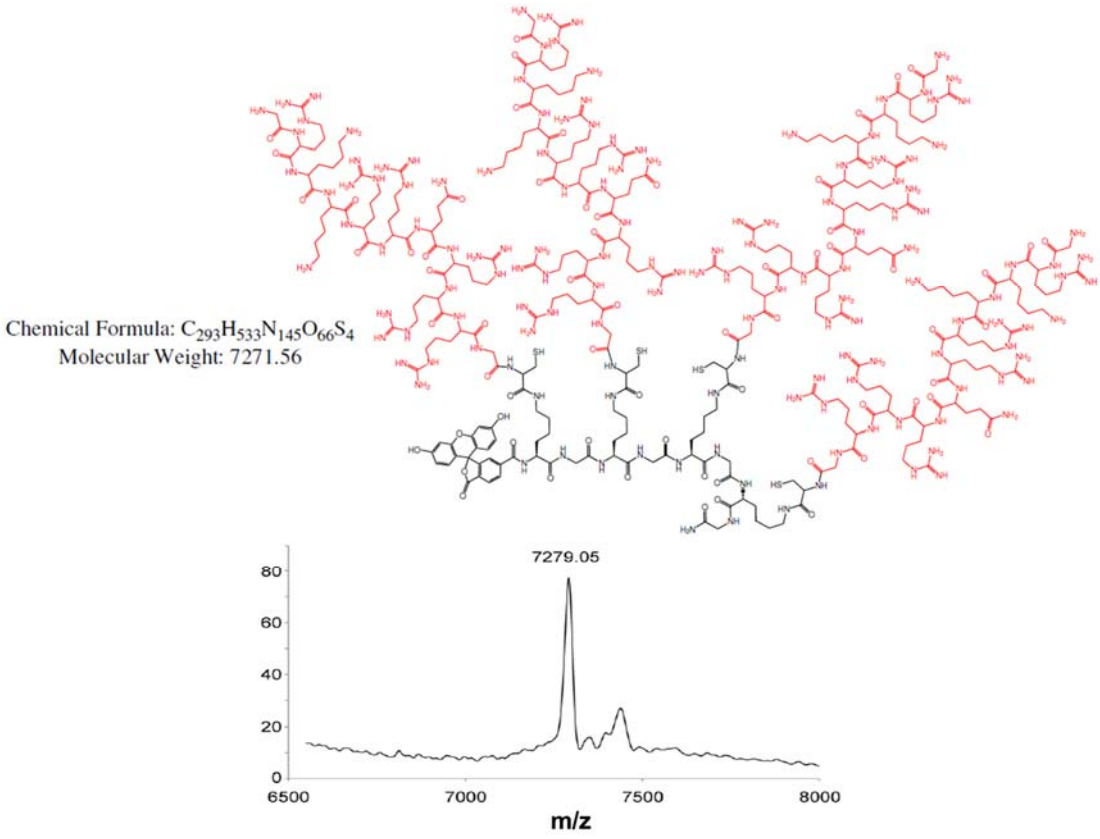


**Figure 2-6 Characterization of Fl-TAT$_4$.** Chemical structure and expected molecular weight of Fl-TAT$_4$ (top) and MALDI-TOF mass spectrum of Fl-TAT$_4$ (bottom).

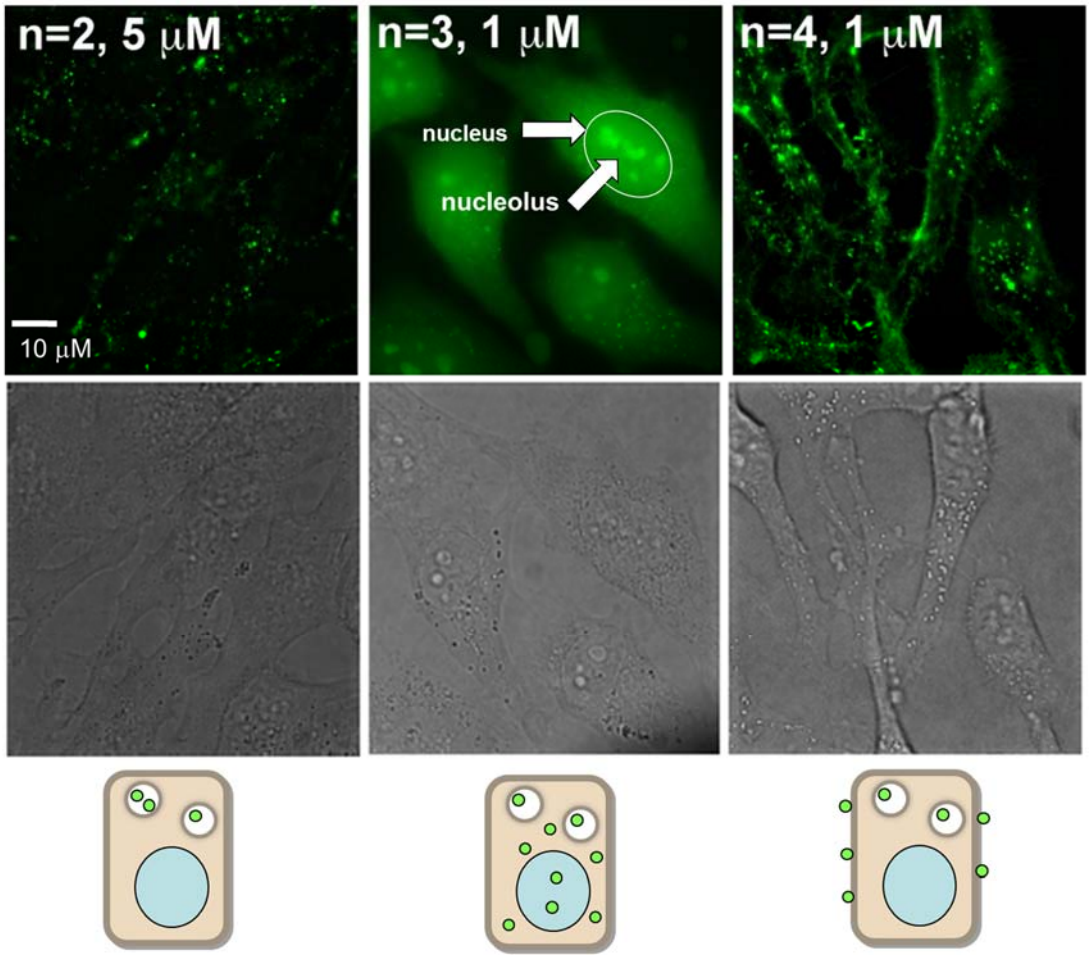


**Figure 2-7 Fluorescence and bright field images of HeLa cells incubated with Fl-$TAT_n$ (n=2,3 and 4).** After incubation with cells, Fl-TAT2 is trapped inside endocytic organelles (punctate distribution (shown in scheme below image), 5 $\mu$M; same results were obtained for Fl-TAT at 5 $\mu$M) but Fl-TAT3 released into the cytosolic space (diffuse distribution in cytosol and nucleus.) at only 1 $\mu$M. Fl-$TAT_4$ is bound to the plasma membrane. Some Fl-$TAT_3$ remains inside endosomes, as shown in scheme but when it reaches the cytosolic space, Fl-$TAT_3$ accumulates in the nucleolus. This is further evidence supporting that the peptide escaped from the endocytic pathway and is indeed inside cells.

and Fl-$TAT_3$ as compared to Fl-TAT under conditions where the monomeric peptide shows low activity. After washing the cells with fresh media, cells were imaged by fluorescence confocal microscopy. In the case of Fl-TAT and Fl-$TAT_2$, a punctate distribution consistent with accumulation of the compounds inside endocytic organelles was observed at both concentrations (1 and 5 μM) (**Figure 2-7**). No accumulation of the peptides in the cytosolic space of cells was detected. In contrast, Fl-$TAT_3$ exhibited a clear diffuse and cytosolic distribution at 1 or 5 μM indicative of an increase in the translocation efficiency as compared to the monomeric and dimeric compounds. Importantly, this was not accompanied by an increase in cytotoxicity of Fl-$TAT_3$ (**see next paragraph and Figure 2-8**). The transport of Fl-$TAT_3$ into the cytosolic space of cells was inhibited by amiloride, an inhibitor of macropinocytosis. These results indicate that Fl-$TAT_3$ is predominantly internalized by macropinocytosis and that it reaches the cytosolic space of cells by escaping from the endocytic pathway. Fl-$TAT_n$ with n = 4, 5 and 6 were also tested but could not be washed from the cell surface to a satisfactory level after incubation and analysis of their transport properties was therefore difficult. These results are consistent with the work of Futaki and coworkers who have reported the synthesis of peptides with four branched chains of the type $(R_n)_4$ (n = 1-6)[213]. $(R_2)_4$ was shown to internalized into cells with an efficiency similar to that of its linear homologue R8 while $(R6)_4$ was found to only accumulate at the plasma membrane without being able to enter cells[214]. Likewise, Fl-$TAT_n$ with n = 4, 5 and 6 (a single TAT peptide copy contains six R residues) might bind to cell-surface components to such an

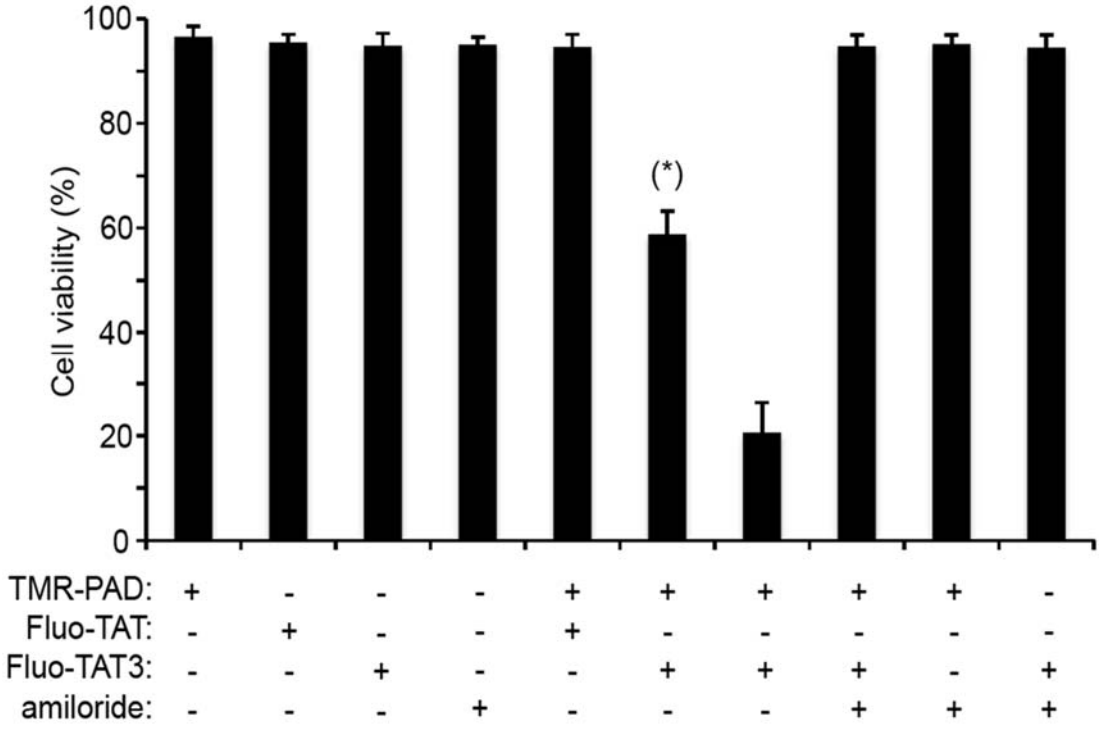


**Figure 2-8 Delivery of TMR-PAD into HeLa cells mediated by Fl-TAT and Fl-TAT$_3$ as measured by a reduction in cell viability.** Fl-TAT (10 $\mu$M) or Fl-TAT$_3$ (1 $\mu$M where highlighted with * or 3 $\mu$M otherwise) were co-incubated with TMR-PAD for 1 h. SYTOX® Blue staining was used to detect dead or dying cells 240 min after incubation with the peptides. Amiloride was used to inhibit macropinocytosis. Cell viability is expressed in % in comparison to an untreated sample. As observed, Fl-TAT and TMR-PaD co-incubation did not lead to a significant change in cell viability. In the contrary, Fl-TAT$_3$, when co-incubated with TMR-PAD, led to a 40 % and 80 % reduction in cell viability when present in the media at 1 μM and 3 μM, respectively. These results represent the average cell viability and corresponding standard deviation from three experiments.

extent that, in this case, it leads to a membrane-bound state that is not productive. Accordingly, these reagents were not considered further in my experiments.

### 2.2.3 Delivery of cell-impermeable macromolecules inside live cells using Fl-TAT$_3$

To characterize the delivery activity of Fl-TAT$_3$, I tested whether Fl-TAT$_3$ might be capable of inducing the release of macromolecules from endosomes. This idea is based on the principle that, if Fl-TAT$_3$ and a macromolecule are co-incubated and accumulate together within endocytic vesicles, Fl-TAT$_3$ might cause leakage of the endosomal membrane and release of the macromolecule into the cytosolic space of cells[159]. This was first suggested by the observation that 70 kDa Dextran-tetramethylrhodamine (Dextran-TMR), a marker of pinocytosis that typically accumulates inside endocytic vesicles when co-incubated with cells, was present into the cytosol of cells when co-incubated with Fl-TAT$_3$ (**Figure 2-9**). To test this working hypothesis further and evaluate the delivery of a bioactive macromolecule, the pro-apoptotic peptide KLAKLAKKLAKLAKNH2 (PAD) was used. PAD is cell-impermeable and has a negligible cytotoxicity towards mammalian cells[215]. However, if delivered into the cytosol of cells, PAD permeabilizes the mitochondrial membrane and induces apoptosis[136, 216]. Cell-death was therefore used as an indicator of the efficiency with which Fl-TAT$_3$ might deliver PAD into live cells. PAD labeled with carboxytetramethylrhodamine (TMR-PAD, 10 μM) was co-incubated with Fl-TAT (1 to 10 μM) or Fl-TAT$_3$ (1 to 3 μM) for 30 min. The import of TMR-PAD, Fl-TAT and Fl-TAT$_3$ into cells was monitored by confocal microscopy and cell viability was assessed

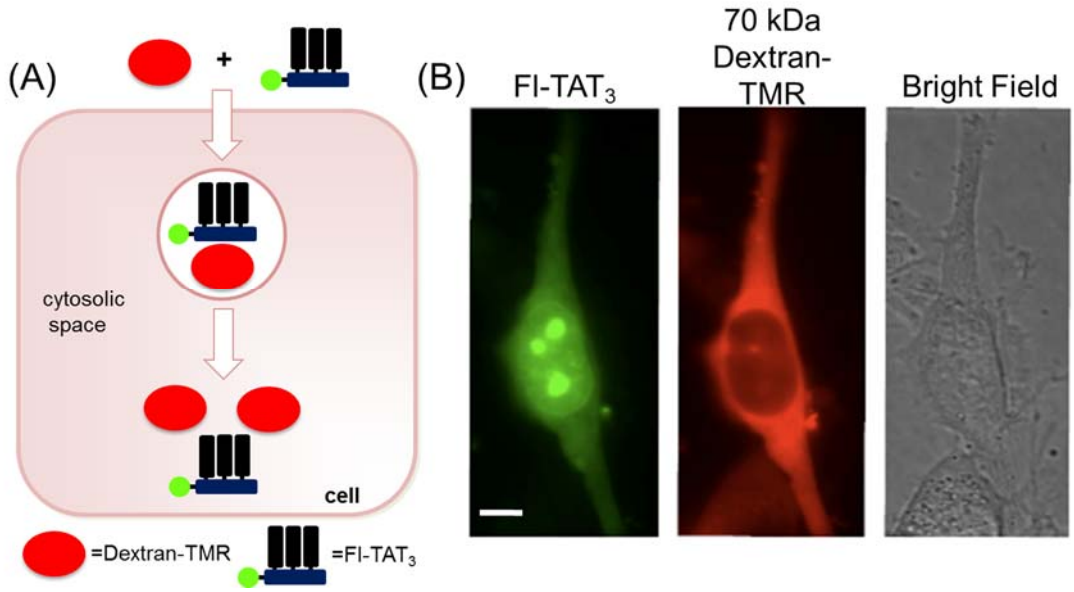


**Figure 2-9 Fluorescence and bright field images of HeLa cells co-incubated with Fl-TAT$_3$ and Dextran-TMR**. (A) Schematic representation of TMR-labeled dextran and Fl-labeled trimeric TAT delivery inside a single cell. (B) Confocal fluorescence microscopy images of HeLa cells incubated with Fl-TAT$_3$ (1 μM) and 70 kDa Dextran-TMR (10 μM), a marker of pinocytosis. As observed, Fl-TAT$_3$ is able to deliver a macromolecule into the cytosolic space of live cells. The cells represented were not stained by SYTOX® Blue. This indicates that the membrane of these cells was not compromised. Scale bar: 10 μm.

by SYTOX® Blue staining. SYTOX® Blue, a high-affinity nucleic acid and cell-impermeable dye, stains the nucleus of apoptotic or necrotic cells with a compromised plasma membrane without staining live cells[217, 218]. When TMR-PAD was co-incubated with Fl-TAT, TMR-PAD was present inside endocytic organelles but did not appear to enter the cytosol of cells (as monitored by TMR fluorescence, data not shown) regardless of the concentration of Fl-TAT used. In addition, the cells' viability was not affected by treatment with these peptides (**Figure 2-8**). These results are consistent with a model where Fl-TAT cannot promote endosomal release of TMR-PAD and, as a result, TMR-PAD is unable to induce cell-death. In contrast, cells incubated with Fl-$TAT_3$ and TMR-PAD showed a diffuse and cytosolic distribution for both TMR-PAD and Fl-TAT3 (**Figure 2-10**). These cells were not stained by SYTOX® Blue 60 min post-incubation (**Figure 2-10 (A)**). However, 40 and 80 % of the cells became SYTOX® Blue positive 240 min post-incubation when 1 or 3 μM Fl-TAT3 were used, respectively (**Figure 2-8 and 2-10 (B)**). Progression to classic morphological changes such as membrane blebbing and nuclear fragmentation further confirmed that cells were undergoing apoptosis. Treatment with amiloride inhibited delivery of Fl-$TAT_3$ and TMR-PAD into cells as well as cell-death (**Figure 2-8 and 2-10 (C)**). These results therefore indicate that the cytotoxicity observed when Fl-$TAT_3$ and TMR-PAD are co-incubated arises from the delivery of TMR-PAD by Fl-$TAT_3$ as opposed to cytotoxic effects that might arise when the peptides are combined and not related to the transport of TMR-PAD. Together, these results support a model where Fl-$TAT_3$ and TMR-PAD are first internalized into cells by

endocytic mechanisms and where Fl-TAT$_3$ then releases TMR-PAD into the cytosol of cells.

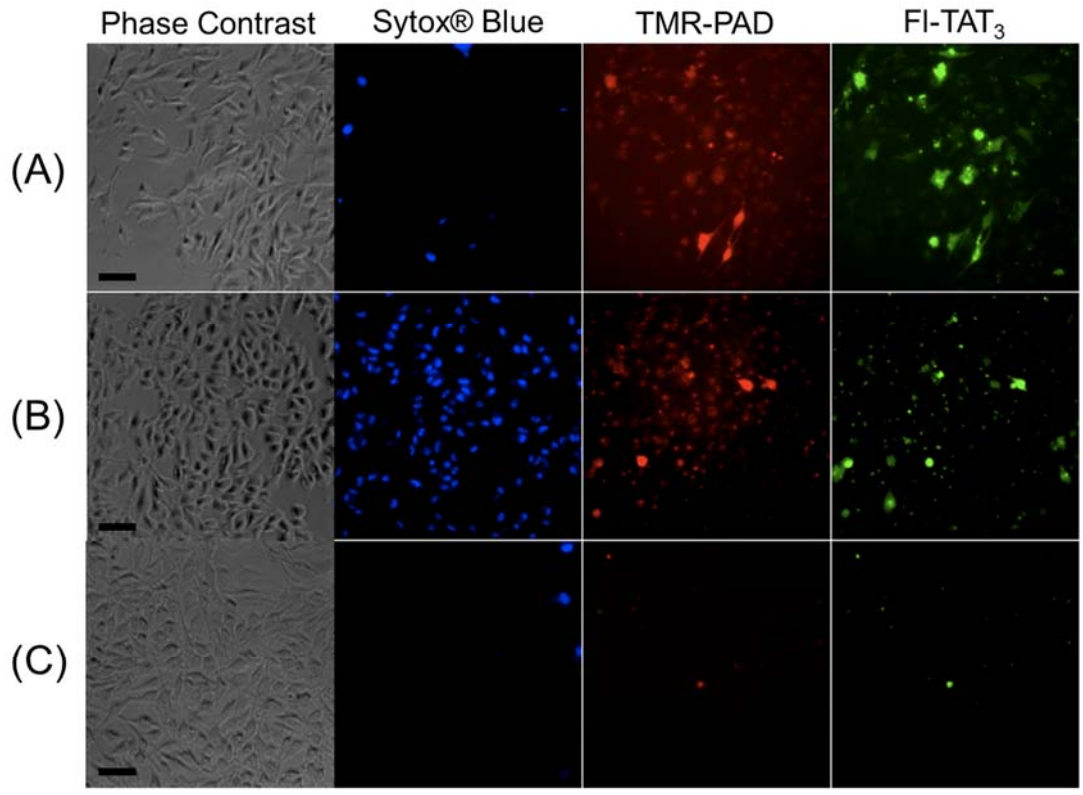


**Figure 2-10 Fluorescence and bright field images of HeLa cells co-incubated with Fl-TAT$_3$ and TMR-PAD**. Cells were incubated with TMR-PAD (10 $\mu$M), Fl-TAT3 (3 $\mu$M), and with or without the macropinocytosis inhibitor amiloride. Cells were incubated with the peptides for 30 min and washed with fresh media, and SYTOX® Blue was added to detect dead cells. Images were acquired 60 or 240 min after addition of SYTOX® Blue. Blue nuclei in the SYTOX® Blue images represent dead or dying cells. Cells containing a cytosolic distribution of both TMR-PAD and Fl-TAT3 can be observed at 60 min. Scale bar: 100 μm.

### 2.2.4 The enhanced delivery activity of Fl-$TAT_3$ is not a result of formation of aggregates containing n ≥ 6 TAT copies

The NCL synthesis scheme that I used in this report generates Fl-$TAT_n$ compounds that contain n free thiols. On one hand, these thiols could be used to attach molecular cargos through a disulfide bond to the multivalent delivery reagents. On the other hand, the thiols, when left unmodified, could promote the aggregation of Fl-$TAT_n$ through the formation of intermolecular disulfide bridges. Such aggregates could participate in the cellular activities observed and lead me to believe that Fl-$TAT_3$ possesses a higher endosomolytic activity when in reality the aggregates with n ≥ 6 TAT copies contribute with most of the observed activity.

To test whether the thiols present in the Fl-$TAT_n$ compounds could lead to aggregate formation through the formation of intermolecular disulfide bridges, the compounds (10 μM in PBS, this concentration reflects the highest concentration used in the cell-based assays) were oxidized by bubbling $O_2$ in the media for 1 hour. Formation of aggregates of higher molecular weights was monitored by HPLC analysis and mass spectrometry (data not shown). The HPLC profiles and mass spectrometry spectra of the oxidized Fl-$TAT_n$ compounds were similar to those presented above and to the samples treated with the reducing agent TCEP (10 mM), indicating that no intermolecular disulfide bridges formed between the Fl-$TAT_n$ molecules. Instead, intramolecular disulfide bridges might have formed. Given the close proximity of the cysteine residues in the Fl-$TAT_n$ compounds, these intramolecular disulfide bonds would have a greater probability of formation than intermolecular disulfide bridges. These intramolecular disulfide bridges

might however not lead to a shift in HPLC retention time. The mass spectrometry analysis was also not accurate enough to unequivocally confirm the loss of 2 H that would accompany the formation of each disulfide bridge.

In the case of Fl-$TAT_2$ and Fl-$TAT_4$, oxidation of the cysteines was confirmed by monitoring the reducing activity of the compounds. Fl-$TAT_2$ and Fl-$TAT_4$ were first reduced with immobilized tris(2-carboxyethyl)phosphine (TCEP) in PBS. The TCEP beads were filtered and the solution was immediately added to a solution of Aldrithiol-2 (2,2'-dithiopyridine, 100 μM). Aldrithiol forms a thiopyridone salt upon reduction and this is accompanied by an increase in absorbance at 350 nm. As expected, the reduced Fl-$TAT_2$ and Fl-$TAT_4$ caused an increase in the absorbance of the solution at 350 nm (data not shown). In a parallel assay, the freshly reduced Fl-$TAT_2$ and Fl-$TAT_4$ were bubbled with $O_2$ as described in the previous paragraph. In this case, addition of Aldrithiol did not cause an increase in the absorbance 350 nm (the absorbance of fluorescein at 490 nm was measured to confirm that the reduced and oxidized Fl-$TAT_n$ compounds were used at the same concentration). These results therefore confirm that the reducing activity of Fl-$TAT_2$ and Fl-$TAT_4$ was abolished after the oxidation step, further confirming that intracellular disulfide bonds are formed.

In the case of Fl-$TAT_3$, one can presume that one intramolecular disulfide bridge might form leaving one cysteine that could potentially form an intermolecular disulfide bond. The fact that I did not detect aggregates of high molecular weight might reflect the fact that intermolecular disulfide bond formation is sterically unfavorable. Indeed, Fl-$TAT_3$ had the ability to reduce Aldrithiol-2 even after the oxidation step, confirming that

a free thiol might remain even after bubbling oxygen (aldrithiol is a small molecule that presumably might have access to this free thiol).

However, to unequivocally confirm that aggregates of the Fl-$TAT_3$ compound were not involved in the unique delivery properties of this compound, the free thiol groups present in the molecule were capped with iodoacetamide. Furthermore, in vitro assays might not reproduce what happens inside cells and it is possible that aggregates form in the lumen of endosomes. To address this issue, the thiols of Fl-$TAT_3$ were blocked with iodoacetamide to form an acetamidated analogue of Fl-$TAT_3$. This product, Fl-$TAT_3$-(S-$CH_2$-CO-$NH_2$)$_3$, cannot form disulfide bonds because the thiols are replaced by thioethers (**Figure 2-11**). To compare the delivery activity of Fl-$TAT_3$-(S-$CH_2$-CO-$NH_2$)$_3$ with that of Fl-$TAT_3$, Fl-$TAT_3$-(S-$CH_2$-CO-$NH_2$)$_3$ (3 μM) and TMR-PAD (10 μM) were co-incubated for 30 min with HeLa cells (**Figure 2-12**) and cell-viability was assessed by microscopy. While incubation with Fl-$TAT_3$-(S-$CH_2$-CO-$NH_2$)$_3$ alone resulted in a cell viability of 90 % (**Figure 2-12 (top panel)**), co-incubation with TMR-PAD resulted in a cell-viability of 25 % 240 min post-incubation (**Figure 2-12 (middle panel)**). Moreover, treatment with amiloride inhibited delivery of Fl-$TAT_3$-(S-$CH_2$-CO-$NH_2$)$_3$ and TMR-PAD into cells as well as cell-death (**Figure 2-12 (bottom panel)**). These results are similar to those obtained with Fl-$TAT_3$. This suggests that the delivery

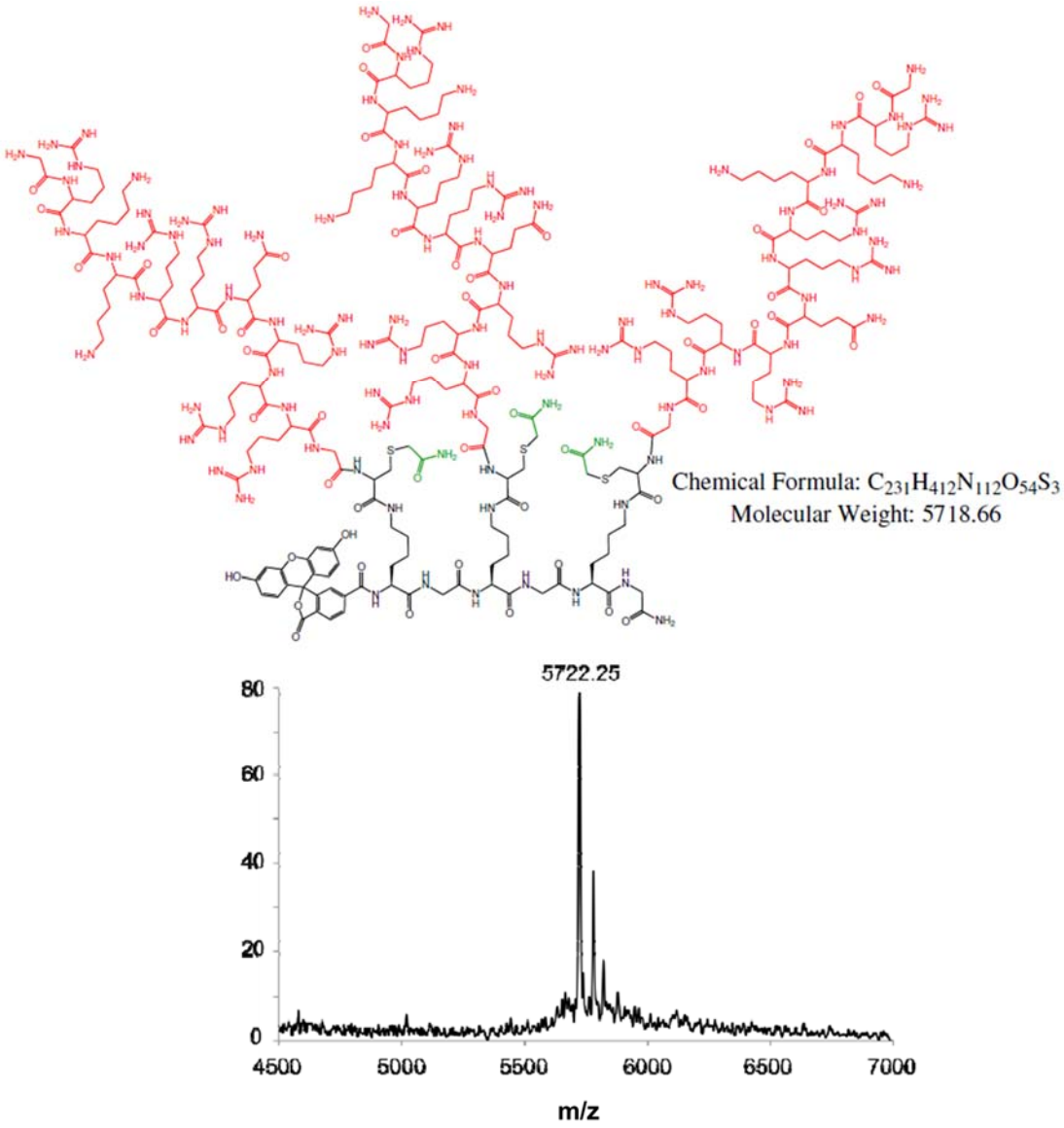


**Figure 2-11 Characterization of Fl-TAT3-(S-CH2-CO-NH2)$_3$.** Chemical structure and expected molecular weight of Fl-TAT$_3$-(S-CH2-CO-NH2)$_3$ (alkyl amide group shown in green) (top) and MALDI-TOF mass spectrum of Fl-TAT$_3$-(S-CH2-CO-NH2)$_3$ (bottom).

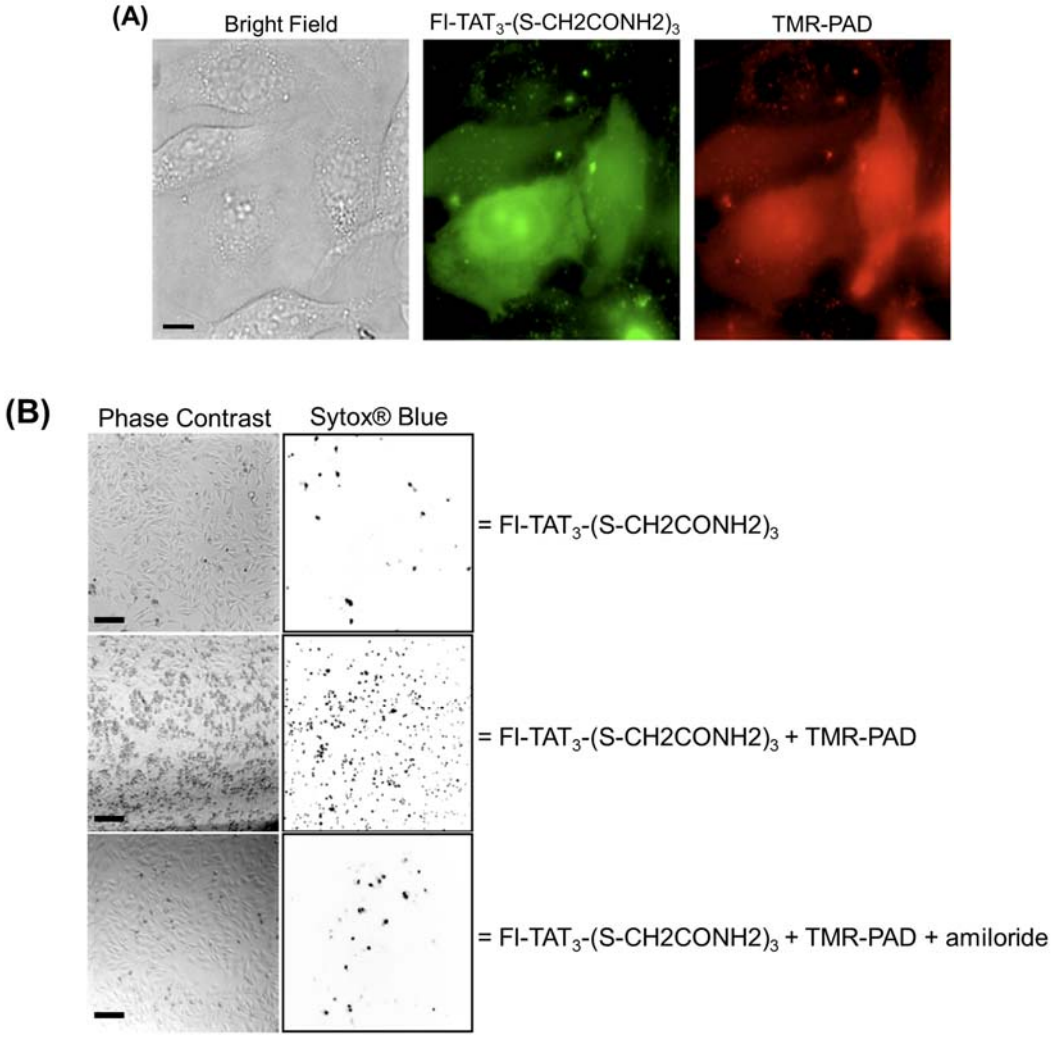


**Figure 2-12 Fluorescence and bright field images of HeLa cells co-incubated with TMR-PAD and Fl-TAT$_3$-(S-CH$_2$-CO-NH2)$_3$.** (A) Cells were treated with Fl-TAT$_3$-(S-CH2-CONH2)$_3$ (3 μM) and TMR-PAD (10 μM) and imaged after a 30 min co-incubation at 37°C (the objective used was 100X). The cells represented were not stained by SYTOX®□Blue at this early timepoint. This indicates that the membrane of these cells was not compromised. Scale bar: 10 μm (B) Cells were incubated with TMR-PAD (10 μM), Fl-TAT$_3$-(S-CH2-CO-NH2)$_3$ (3 μM), and with or without the macropinocytosis inhibitor, amiloride. Cells were incubated with the peptides for 30 min, washed with fresh media, and SYTOX® Blue was added to detect dead cells. Images were acquired 240 min after addition of SYTOX®□Blue. Black nuclei in the SYTOX®□Blue images represent dead or dying cells (images are represented as inverted monochrome). Scale bars: 100 μm.

activity of Fl-$TAT_3$ is not a result of aggregation of the compound and that the presence of the thiols is not necessary to achieve delivery.

## 2.3 Discussion

The trimeric TAT (Fl-$TAT_3$) delivery system is able to deliver cell-impermeable molecules inside cells. Delivery into the cytosolic space is achieved, presumably, by Fl-$TAT_3$-mediated endosomal escape. This is not surprising because it has been known for a long time that TAT monomer, Fl-$TAT_3$ monomeric counterpart, penetrates cells by escaping from endocytic vesicles. Yet, I showed that the ability of Fl-$TAT_3$ to deliver cargos intracellularly is inhibited by amiloride, an inhibitor of macropinocytosis[219]. Similar inhibitory effects have been observed for CPPs that utilize the endocytic pathway to deliver cargos into the cell[220-222].

Fl-$TAT_3$ appears to have an endosomolytic activity much greater than its monomeric and dimeric counterparts without displaying the unproductive membrane binding observed for constructs containing more branches. It was surprising that the delivery activity of these constructs did not follow a constant increase dependent of TAT copies. Work done by Whitesides have shown that polyvalent interactions can be used for the design of inhibitors to block viral and bacterial infections and toxins[209, 223, 224]. The unproductive membrane binding observed could be explain by the presence of multiple simultaneous interactions between Fl-$TAT_n$ ($n > 4$) and HSPGs. Strong interaction between the peptide and HSPGs could block the interaction of the peptide with specific cellular components, lipids for example, required to cause cellular uptake and endosomal

escape. Yet, Fl-$TAT_3$ can deliver the small molecule cargo fluorescein in cis at concentrations much lower than that required for Fl-TAT. In addition, it can also be used to achieve delivery of molecules displaying diverse structures and sizes in trans. Fl-$TAT_3$ delivered a 70-kDa fluorescently-labeled Dextran macromolecule and a bioactive but cell-impermeable peptide. This is important because this demonstrates that a macromolecule does not need to be labeled with an extraneous delivery peptide to be delivered, thereby greatly simplifying delivery protocols for in vitro applications.

The design of Fl-$TAT_3$ used herein allows the delivery of a cargo in cis by covalently attaching a molecule to the N-terminus of the scaffold peptide. Alternatively, delivery of molecules inside cells by linking cargos to the free thiol groups (through disulfide bridges or thioether bond) in Fl-$TAT_3$ could potentially be achieved as well. Interestingly, I show that blocking the free thiols of Fl-$TAT_3$ with iodoacetamide does not affect its delivery activity. Moreover, the alkyl amide in Fl-$TAT_3$-$(S\text{-}CH_2\text{-}CO\text{-}NH_2)_3$ (acetamidated Fl-$TAT_3$) acts as a small model cargo. This delivery system could prove useful for situations that require covalent attachment of the cargo to the delivery system. Furthermore, linking the cargo to Fl-$TAT_3$ through a disulfide bridge would allow cleavage of this bond in the reducing cytosol of cells which would render the cargo unmodified and free of potential interferences from Fl-$TAT_3$ that could affect the cargo bioactivity. Establishing where Fl-$TAT_3$ escapes from the endocytic pathway should also provide valuable insights regarding its endosomolytic activity. Future experiments will also focus on testing the applicability of this delivery method to other macromolecules

and exploring the effect of the structure and spatial orientation of the scaffold peptide on the delivery activity of the TAT trimer.

## 2.4 Materials and methods

### 2.4.1 Peptide synthesis and purification

All amino acids and the Rink amide resin were obtained from Novabiochem (San Diego, CA) and used as received. Peptides were synthesized in-house by SPPS using standard Fmoc protocols. Fmoc-Lys(Boc)-OH, Fmoc-Lys(Mtt)-OH, Fmoc-Gly-OH, Fmoc-Arg(Pbf)-OH, Fmoc-Gln(Trt)-OH, Fmoc-Leu-OH, Fmoc-Ala-OH, and Boc-Cys(StBu) were used to assemble the peptides. Reactions were carried out in SPPS vessels at room temperature using a stream of dry N2 to provide agitation. Fmoc deprotection was performed by addition of piperidine in DMF (20 %, 5 mL) to the protected Fmoc-peptide resin (0.72 mmol). Deprotection was carried out for 1×3 min and 1×10 min. Coupling reactions were carried out for 2 h with a mixture of Fmoc-amino acid (2.88 mmol), HBTU (1.06 g, 2.80 mmol), and DIEA (1.25 mL, 7.2 mmol) in DMF. Upon completion of the reaction, the resin was washed with DMF. The peptides were analyzed and purified by reverse phase HPLC. HPLC analysis was performed on a Hewlett-Packard 1200 series instrument and a Vydac C18 column (5 micron, 4 x 150 mm). Flow rate was 1 mL/min and detection was at 214 nm and 450 nm. Semipreparative HPLC was performed on a Vydac C18 10 × 250 mm column. Flow rate was 4 mL/min and detection was at 214 nm and 450 nm. All runs used linear gradients of 0.1 % aqueous TFA (solvent A) and 90 % acetonitrile, 9.9 % water and 0.1 % TFA (solvent B). The correct identity of the peptides

was confirmed by time-offlight mass spectrometry performed with a Shimadzu/Kratos instrument (AXIMACFR,

Shimadzu, Kyoto).

### 2.4.2 Synthesis of Fl-(Kε(C)-G)$_n$-NH$_2$

The Fl-(Kε(C)-G)n-NH$_2$, n=2-6, peptides were assembled using a standard Fmoc solid phase peptide synthesis strategy. Fmoc-Gly-OH was first coupled to the Rink amide resin (0.72 mmol scale). Fmoc-Lys(Mtt)-OH and Fmoc-Gly-OH were the alternatively coupled to generate the peptides Fmoc-(Kε(Mtt)-G)$_n$-Rink amide. The Mtt protecting groups were cleaved by treating the resin with 2% TFA in DCM for 30 min and Boc-Cys(S*t*Bu)-OH (3 x n equivalents) was coupled onto the exposed ε amino groups in DMF containing DIEA and HBTU (3 x n eq.). This was followed by N-terminal Fmoc deprotection and subsequent overnight coupling of 5(6)-carboxyfluorescein (Fl, 1.1 eq) in DMF containing HBTU (1.1 eq.). The S-StBu groups on the Cys side chains were cleaved on the solid phase using 100 eq of PBu$_3$ and 400 eq of H2O in DMF:DCM for 4 h. The peptides were cleaved from the resin with 92.5 % TFA, 2.5 % TIS, 2.5 % EDT, and 2.5 % H2O. The crude products were precipitated and washed with cold diethyl ether and then lyophilized to yield crude peptide solids that were purified by preparative scale reverse phase HPLC using a water/acetonitrile gradient in the presence of 0.1 % TFA.

### 2.4.3 Synthesis of TAT-thioester

The TAT peptide thioester (GRKKRRQRRRG-thioester) was readily prepared by SPPS on the 4-sulfamylbutyryl-AM resin using reported protocols[212]. The resin was pre-swollen in 10 volumes of dry methylene chloride for 1 h. During this period, Fmoc-Gly-OH (4 equiv) along with 1-methylimidazole (4 equiv) was dissolved in a 4:1 mixture of dry methylene chloride (DCM) and dimethylformamide (DMF) under a blanket of inert gas. N,N-diisopropylcarbodiimide (DIC) was added and the solution was mixed for 5 min at room temperature. This acylation mixture was added to the drained resin. The resin was agitated with a stream of $N_2$ for 18 h at room temperature and then drained. The resin was washed with DCM and DMF. The desired peptide is then formed via standard manual peptide synthesis. Boc-Gly-OH was used in the last coupling. The resin was washed with DMF and DCM. For activation of the resin prior to cleavage, a solution of iodoacetonitrile (25 equiv) and diisopropylethyl amine (10 equiv) in 3 mL of DMF and 1 mL of hexamethylphosphoric triamide was added to the drained resin. The resin was agitated with a stream of $N_2$ for 18 h at room temperature. The solution was drained, and the resin was washed with DMF and DCM prior to immediate cleavage. The peptide was then cleaved from the activated resin with mercaptophenylacetic acid. First, mercaptophenylacetic acid (2.0 mmol for 0.1 mmol resin) was suspended in DCM (10 mL) in a round-bottom flask flushed with argon. The mixture was cooled to 0 °C and DIEA (1.0 mmol) was added dropwise over 5 min. The resin pre-swollen in DCM was drained and treated with the thiol solution. The resin bed was stirred for 18 h at room temperature. The resin was drained and the filtrate collected. The resin was washed with

three additional portions of DCM, these being pooled with the original filtrate. The filtrate was concentrated in vacuo to provide a crude product. The residue was treated with 10 mL of a 95:2.5:2.5 TFA/water/triisopropylsilane (TIS) mixture to remove the side-chain protecting groups. The product was filtered to remove excess insoluble thiol, concentrated in vacuo, and precipitated and washed with cold diethyl ether. The peptide was purified by reversed-phase HPLC and analyzed by mass spectrometry. Expected mass: 1603.9 Da, observed mass: 1603.2 Da.

### 2.4.4 Synthesis of Fl-TAT$_n$

Fl-TAT$_n$ was formed by addition of TAT-MPAA thioester (3 x n equivalents) to Fl-(Kε(C)-G)$_n$-NH2 (1 mM) in 25 mM HEPES, 100 mM MESNa, and 10 mM TCEP at pH 7.5 (TAT-MPAA thioester exchanges to TAT-mercaptoethanesulfonate thioester under these conditions). After 16 hours of reaction at room temperature, the crude product was purified by preparative scale reverse phase HPLC using a water/acetonitrile gradient in the presence of 0.1 % TFA.

### 2.4.5 Synthesis of Fl-TAT

Fl-TAT (GRKKRRQRRRK(Fl)G-$NH_2$) was prepared by SPPS on the Rink amide resin. Fmoc-G-R(Pbf)-K(Boc)-K(Boc)-R(Pbf)-R(Pbf)-Q(Trt)-R(Pbf)-R(Pbf)-R(Pbf)-K(Mtt)-G was first assembled on the resin. The Mtt protecting group was cleaved by treating the resin with 2 % TFA in DCM for 30 min and 5(6)-carboxyfluorescein (Fl, 1.1 eq.) was coupled onto the exposed ε amino groups in DMF containing DIEA and HBTU

(1.1 eq.). This was followed by N-terminal Fmoc deprotection with 20 % piperidine in DMF. The peptide was cleaved from the resin with 92.5 % TFA, 2.5 % TIS, 2.5 % EDT, and 2.5 % $H_2O$. The crude product was precipitated and washed with cold diethyl ether and then lyophilized to yield crude solid that was purified by preparative scale reverse phase HPLC using a water/acetonitrile gradient in the presence of 0.1 % TFA. . Expected mass: 1939.2 Da, observed mass: 1937.2 Da.

### 2.4.6 Synthesis of Cys-PAD (CKLAKLAKKLAKLAK-$NH_2$)

The Cys-PAD (CKLAKLAKKLAKLAK) peptide was assembled using a standard Fmoc solid phase peptide synthesis strategy on a Rink amide resin. The protected peptide was cleaved from the resin with 92.5 % TFA, 2.5 % TIS, 2.5 % EDT, and 2.5 % $H_2O$. The crude product was precipitated and washed with cold diethyl ether. The precipitated peptide was then lyophilized, dissolved in HPLC buffer and purified by preparative scale reverse phase HPLC using a water/acetonitrile gradient in the presence of 0.1 % TFA. Expected mass: 1626.1 Da, observed mass: 1626.6 Da.

### 2.4.7 Synthesis of TMR-PAD (TMR-CKLAKLAKKLAKLAK-$NH_2$)

TMR-PAD (TMR-CKLAKLAKKLAKLAK-$NH_2$) was obtained by reaction between the Cys-PAD peptide and the fluorophore tetramethylrhodamine-5(6)-maleimide. Cys-PAD (0.38 μmol) was dissolved in 25 mM Hepes at pH 7.5, 100 mM MESNa, and 20 mM TCEP (0.38 mM final concentration). To this was added the fluorophore tetramethylrhodamine-5(6)-maleimide (0.38 μmol). After 36 hours at 4 °C,

the reaction was complete and the crude product was purified by preparative scale reverse phase HPLC using a water/acetonitrile gradient in the presence of 0.1 % TFA. Expected mass, 2108.66, observed mass: 2109.40 Da.

### 2.4.8 Oxidation of Fl-TAT$_n$

To test whether the thiols present in the Fl-TAT$_n$ compounds could lead to aggregate formation through the formation of intermolecular disulfide bridges, the compounds (10 μM in PBS, this concentration reflects the highest concentration used in the cell-based assays) were oxidized by bubbling $O_2$ in the media for 1 hour. Formation of aggregates of higher molecular weights was monitored by HPLC analysis and mass spectrometry. The HPLC profiles and MS spectra of the oxidized Fl-TAT$_n$ compounds were similar to those presented above and to the samples treated with the reducing agent TCEP (10 mM), indicating that no intermolecular disulfide bridges formed between the Fl-TAT$_n$ molecules. Instead, intramolecular disulfide bridges might have formed. Given the close proximity of the cysteine residues in the Fl-TAT$_n$ compounds, these intramolecular disulfide bonds would have a greater probability of formation than intermolecular disulfide bridges. These intramolecular disulfide bridges might however not lead to a shift in HPLC retention time. The mass spectrometry analysis was also not accurate enough to unequivocally confirm the loss of 2 H that would accompany the formation of each disulfide bridge. In the case of Fl-TAT$_2$ and Fl-TAT$_4$, oxidation of the cysteines was confirmed by monitoring the reducing activity of the compounds. Fl-TAT$_2$ and Fl-TAT$_4$ were first reduced with immobilized TCEP in PBS. The TCEP beads were

filtered and the solution was immediately added to a solution of Aldrithiol-2 (2,2'-dithiopyridine, 100 μM). Aldrithiol forms a thiopyridone salt upon reduction and this is accompanied by an increase in absorbance at 350 nm. As expected, the reduced Fl-$TAT_2$ and Fl-$TAT_4$ caused an increase in the absorbance of the solution at 350 nm. In a parallel assay, the freshly reduced Fl-$TAT_2$ and Fl-$TAT_4$ were bubbled with $O_2$ as described in the previous paragraph. In this case, addition of Aldrithiol did not cause an increase in the absorbance 350 nm (the absorbance of fluorescein at 490 nm was measured to confirm that the reduced and oxidized Fl-$TAT_n$ compounds were used at the same concentration). These results therefore confirm that the reducing activity of Fl-$TAT_2$ and Fl-$TAT_4$ was abolished after the oxidation step, further confirming that intracellular disulfide bonds are formed. In the case of Fl-TAT3, one can presume that one intramolecular disulfide bridge might form; leaving one cysteine that could potentially form an intermolecular disulfide bond. The fact that I did not detect aggregates of high molecular weight might reflect that fact that intermolecular disulfide bond formation is sterically unfavorable. Indeed, Fl-$TAT_3$ had the ability to reduce Aldrithiol-2 even after the oxidation step, confirming that a free thiol might remain even after bubbling oxygen (Aldrithiol-2 is a small molecule that presumably might have access to this free thiol). However, to unequivocally confirm that aggregates of the Fl-$TAT_3$ compound were not involved in the unique delivery properties of this compound, the free thiol groups present in the molecule were capped with iodoacetamide. These results are described in the next section.

### 2.4.9 Synthesis of Fl-$TAT_3$-$(S\text{-}CH_2\text{-}CO\text{-}NH_2)_3$ (Fl-$TAT_3$ acetamidated with iodoacetamide to block the thiols and prevent disulfide bond formation)

Fl-$TAT_3$-$(S\text{-}CH_2\text{-}CO\text{-}NH_2)_3$ was formed after addition of iodoacetamide (50 mM) to Fl-$TAT_3$ (1.4 mM) in 6 M GnHCl, 25 mM HEPES, and 50 mM TCEP at pH 8.5. The solution was placed on a shaker at room temperature. The reaction was monitored by analytical reversed-phase HPLC and MALDI-TOF. After 24 h, the elution peak corresponding to Fl-$TAT_3$ had completely disappeared to lead to the formation of a single peak corresponding to the product. The product was purified by reverse-phase HPLC. The Aldrithiol test described in the previous section was used to confirm that the compound formed had no reducing activity and therefore no free thiol (Fl-$TAT_3$ was used as a positive control). Yield: 69.3 %. Expected mass: 5718.66 Da, Observed mass: 5722.25 Da.

### 2.4.10 Live-cell imaging experiments

HeLa cells were seeded on 8-well chamber glass slide (Lab-TekTM Cat. No. 177402, 0.8 $cm^2$/well, Nunc International, Naperville, IL) at 3.0 x 104 cells/well in Dulbecco's modified Eagle's medium supplemented with 10 % FBS and incubated for 24 h at 37 °C in a humidified atmosphere containing 5 % $CO_2$. For live-cell imaging, cells were washed and incubated with Leibovitz's L-15 Medium and placed under an inverted epifluorescence microscope (Model IX81, Olympus, Center Valley, PA) equipped with a heating stage maintained at 37 °C. The microscope is configured with a spinning disk unit (DSU, Olympus) to perform both confocal and wide-field fluorescence microscopy. Images were collected using a Rolera-MGI Plus backilluminated EMCCD camera

(Qimaging, Surrey, BC, Canada) mounted on the microscope with UPlanFl 100× / 1.3 NA oil, or LCPlan 20× / 0.4 NA objectives. Images were acquired using phase contrast and three standard fluorescence filter sets: CFP (Ex = 436±20 nm / Em= 480±40 nm), Texas Red (Ex = 560±40 nm / Em= 630±75 nm), and FITC (Ex = 482±35 nm / Em= 536±40 nm). (Semrock, Rochester, NY). Cells were treated with the different peptides in L-15 medium. The concentrations of the peptides were determined by measuring the absorbance of the fluorescein moiety at 492 nm (ε = 56000 M-1 cm-1 at pH 7.4). For macropinocytosis inhibition, cells were first pretreated with 50 μM of amiloride (Sigma*,* MO*)* for 30 minutes, and then with the peptides while keeping amiloride present. After incubation at 37 °C for 30 min, the cells were washed with PBS 5 times and the medium was replaced with fresh L-15. The integrity of the plasma membrane of the cells was determined by addition of the cell-impermeable DNA stain SYTOX® Blue (5 μM, dead cells are stained in less than 5 min at this concentration). Cells were then placed on the microscope and images were acquired in the CFP fluorescence channel for detection of SYTOX® Blue. TMR was detected with the Texas Red filter set and Fl with the FITC filter set. Images were processed using the SlideBook 4.2 software (Olympus, Center Valley, PA). For the delivery of TMR-PAD to live cells reported in Figure 2 and 3, cells were imaged with a 20X objective by phase contrast and fluorescence imaging for up to 4 h. Ten to twenty images were acquired for each experiment. The total number of cells in a given image was determined from the phase contrast image while the number of dead cells was determined by identifying cells containing a blue fluorescent nucleus stained by SYTOX® Blue. Cell viability was determined by first establishing a ratio of dead cells/total number of cells for

each sample (1000 cells were counted in each experiments and each experiments were repeated 3 times).

# 3. CYTOSOLIC DELIVERY OF PROTEINS AND CELL-IMPERMEABLE SMALL MOLECULES INTO LIVE CELLS BY INCUBATION WITH A MULTIVALENT ENDOSOMOLYTIC REAGENT OF THE CELL-PENETRATING PEPTIDE TAT*[225]

## 3.1 Introduction

In this chapter, I describe the synthesis and cellular delivery properties of a multivalent and branched delivery system consisting of a tetramethylrhodamine-labeled dimer of the prototypical CPP TAT, dfTAT. I test the hypothesis that a branched multivalent TAT system, for which its synthesis protocol is very simple, would display an enhanced endosomolytic activity when compared to TAT. Furthemore, I hypothesize that this delivery system could induce the release of cell-impermeable macromolecules trapped inside endocytic organelles into the cytosolic space of live cells. Again, this is based on the principle that multivalency results in an increase of the CPP's local concentration at the sites where the peptide interacts with cellular components (avidity effect)[209, 210, 224, 226]. Here I report that dfTAT penetrates live cells by escaping from endosomes with high efficiency. By mediating endosomal leakage, dfTAT also delivers proteins into cultured cells after a simple co-incubation procedure. I achieved cytosolic delivery in several cell lines and primary cells and observed that only a relatively small amount of material remained trapped inside endosomes. Delivery did not require a binding interaction between dfTAT and a protein, multiple molecules could be delivered

*This chapter is reprinted with permission from "Protein delivery into live cells by incubation with an endosomolytic agent" by Erazo-Oliveras, A.[+]; Najjar, K.[+]; Dayani, L.; Wang, T.-Y.; Johnson, G.A. and Pellois, J.-P. *Nature Methods* **2014**, 11 861-867. doi: 10.1038/nmeth.2998. [+]authors contributed equally. 

simultaneously, and delivery could be repeated. dfTAT-mediated delivery did not noticeably affect cell viability, cell proliferation or gene expression. dfTAT-based intracellular delivery should be useful for cell-based assays, cellular imaging applications and the *ex vivo* manipulation of cells.

### 3.2 Results

Protein transduction strategies are extremely useful for the investigation and manipulation of cellular processes. For example, proteins labeled with fluorophores, stable isotopes or reactive tags and delivered into live cells can, for instance, be used for imaging applications or *in cellulo* structure determination by NMR, respectively[136, 227, 228]. Despite the unique opportunities provided by protein transduction technologies, current protocols are often suboptimal[229, 230]. Proteins fused to a protein transduction domain (PTD) or CPP typically use the endocytic pathway as a route of cellular entry[8]. However, the majority of PTD-protein fusions endocytosed by cells typically remain trapped inside endosomes; as a result, the amount of protein that reaches the cytosol of cells is low, and the biological outcomes achieved are poor[138]. A possible solution to this problem is to increase the ability of proteins to escape from the endocytic pathway. This is possible with membrane-destabilizing agents that disrupt endosomes[222, 231, 232], but to date, the efficiencies of available reagents have remained low[233, 234]. Ideally, a delivery strategy should combine efficient endosomal escape, low cell toxicity and convenience. I aimed to develop an innocuous endosomolytic agent that efficiently delivers protein cargos into cells. Based on the results from chapter two, my working hypothesis is that a trimeric TAT labeled

with the fluorophore tetramethylrhodamine (TMR), which I will call tfTAT for trimeric, fluorescent TAT, might have enhanced endosomolytic activity compared to that of its dimeric and monomeric counterparts, dfTAT and fTAT, respectively. Surprisingly, I show that the dimeric delivery system dfTAT efficiently delivers proteins into live cells in approximately one hour without affecting cell viability or proliferation.

### 3.2.1 Synthesis and purification of dfTAT and its monomeric counterparts

My synthetic approach consists of assembling multiple fluorescently-labeled TAT (fTAT) peptides together by oxidation of free cysteine thiol(s) and formation of disulfide bridges. The design of this multivalent branched delivery system is shown in **Figure 3-1**. It is important to point out that the monomeric and dimeric peptides, fTAT and dfTAT, were generated first since the synthesis protocol for these peptides was much simpler. As a result, I studied their ability to translocate across the plasma membrane and enter the cytosolic space of live cells before assessing the penetration activity of the trimeric peptide tfTAT. To my surprise, the penetration activity of dfTAT was very high and far surpassed my expectations (even expectations for tfTAT). Due to this, the work in this chapter will focus only on studies performed using dfTAT and its monomeric counterparts.

I used TAT as the template for my design of the dimeric delivery vehicle. The fluorescent peptide CK(ε-NH-TMR)-TAT (fTAT) was generated by SPPS using standard Fmoc protocols. I introduced a lysine at the N-terminus of TAT bearing a Mtt protecting group at the ε $NH_2$. The lysine side chain protecting group was removed orthogonally with 2 % trifluoroacetic acid (TFA) and modified with TMR for fluorescence imaging. I

added a cysteine at the N-terminus to permit dimerization by disulfide bond formation (**Figure 3-1 (top)**). Disulfide bonds are relatively stable inside endosomes but are cleaved following endosomal escape and upon entry into the reducing cytosolic space of cells[229, 235, 236]. TFA cleavage and preparative scale reverse phase HPLC purification afforded fTAT (**Figure 3-2 (A)**). Incubation in oxygenated medium and oxidation of the free cysteine thiol of fTAT generated the dimer (CK(ε-NH-TMR)TAT)2 (dfTAT; **Figure 3-2 (B)**). Alternatively, the thiol of CK(ε-NH-TMR)TAT was acetamidated to obtain a peptide (acfTAT) that cannot dimerize (**Figure 3-3**) or was reacted with bis(maleimido)ethane to obtain a nonreducible dimer (nrdfTAT) (**Figure 3-4**). dfTAT, acfTAT and nrdfTAT were purified by HPLC and their identities were evaluated by MALDI-TOF mass spectrometry (**Figure 3-3, 3-4 and 3-5**).

### 3.2.2 dfTAT penetrates the cytosol of live cells efficiently

I incubated fTAT, acfTAT, dfTAT and nrdfTAT for 1 h with HeLa cells, the mouse neuroblastoma cell line Neuro-2a and human primary dermal fibroblasts (HDFs). Internalization was first assessed by fluorescence microscopy. acfTAT (1–20 μM) localized in a punctate distribution consistent with accumulation of the peptide inside endosomes[237] (**Figure 3-6 (A)**). The fluorescence signal of dfTAT was also punctate below 2 μM but became distributed in the cytosolic space and nucleus of an increasing number of cells at higher concentrations (**Figure 3-6 (B) and 3-7**). The overall amount

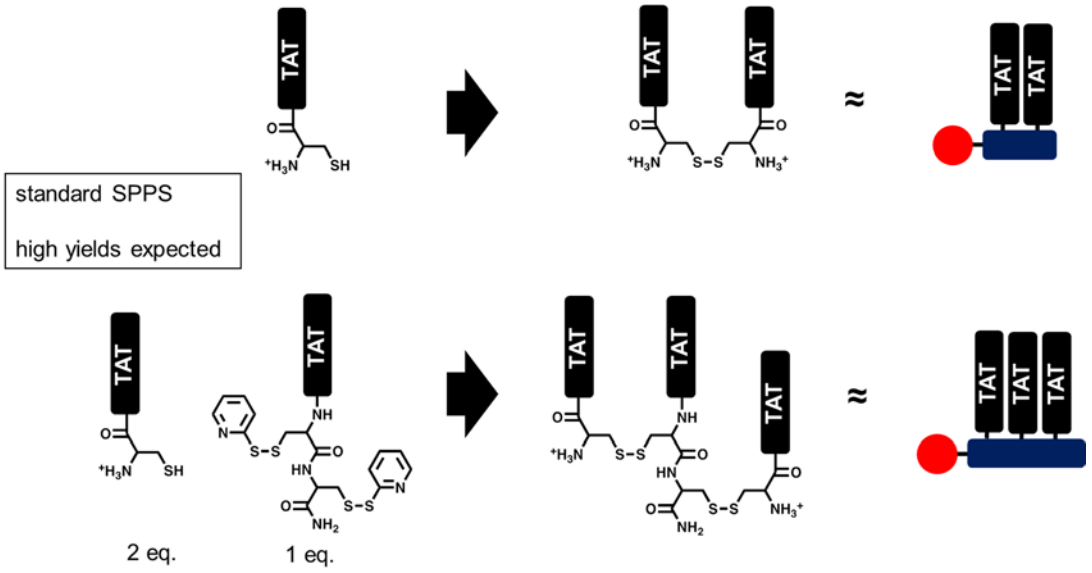


**Figure 3-1 Branched multivalent CPP system using disulfide bonds: 2nd generation.** Peptides will be generated using SPPS, which should allow obtaining higher yields than before. The branched multivalent system will be generated by a simple oxidation step suing a peptide containing one Cys residue (top) or by reacting Aldrithiol-2 with a peptide containing two Cys residues and then allowing the product of that reaction to react with a peptide containing one Cys residue (bottom). As shown, the design of the 2nd generation branched multivalent system was, in part, inspired by the work shown in chapter 2.

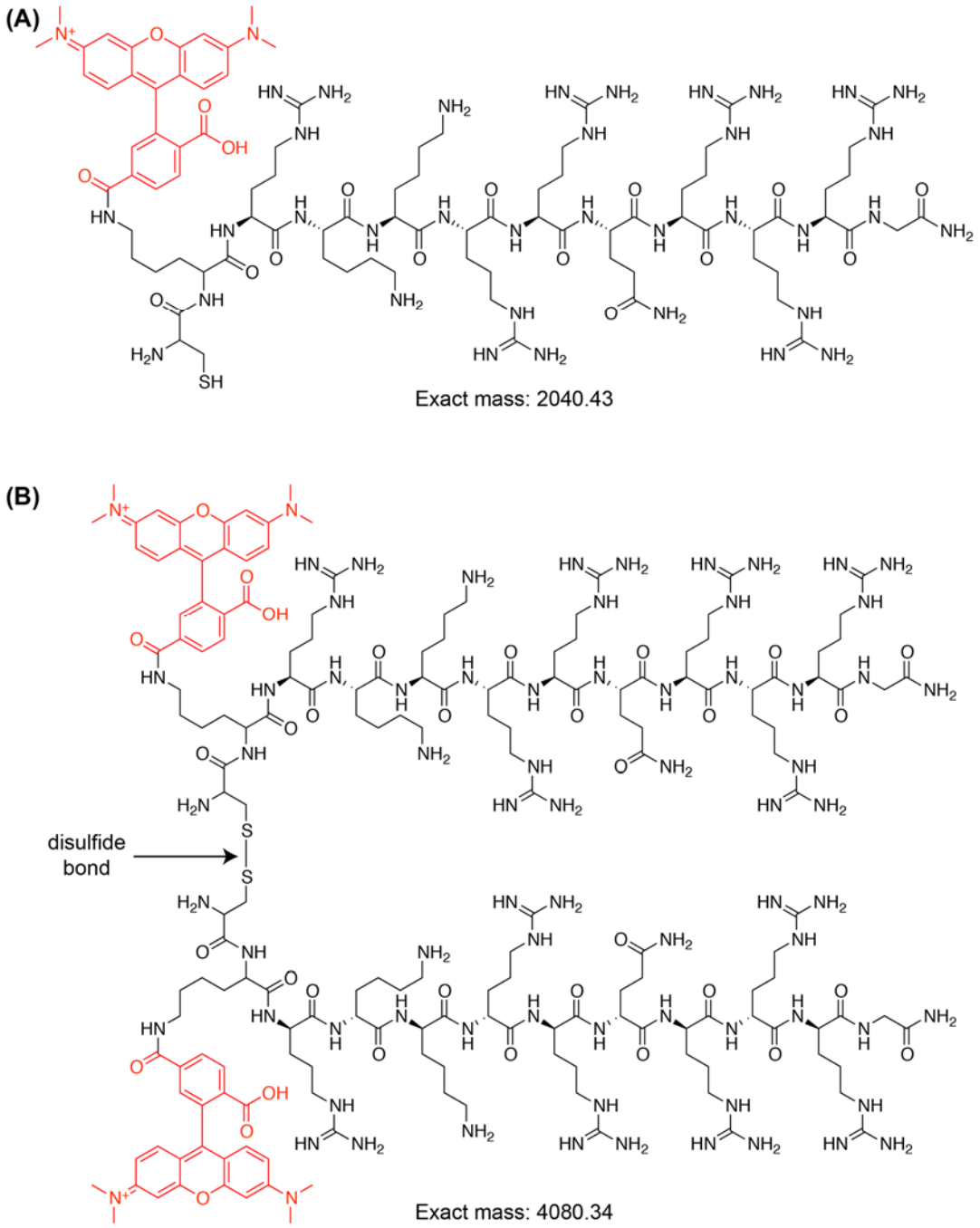


**Figure 3-2 Chemical structure of fTAT and dfTAT.** (A) fTAT contains the TAT sequence, a fluorescently- labeled Lys residue and Cys residue (Lys and Cys were conjugated to the N-terminus of TAT). (B) The thiol group in fTAT is oxidized to form a disulfide bond and generate dfTAT. The exact mass of each peptide is shown.

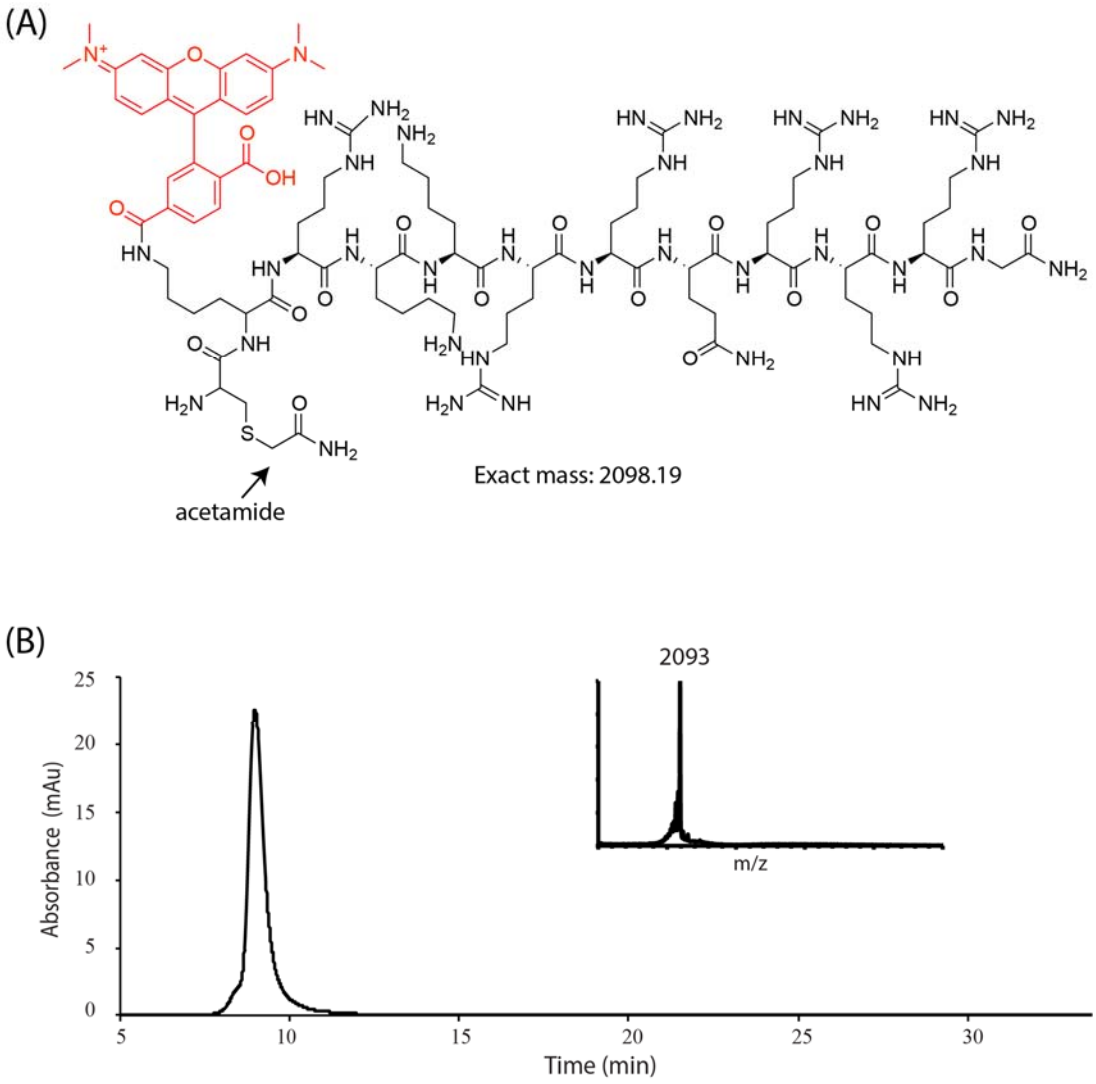


**Figure 3-3 Characterization of acfTAT.** (A) Chemical structure of acfTAT and its exact mass. The alkyl amide group on the peptide prevent dimerization in cells (arrow). (B) HPLC chromatogram of pure acfTAT and MALDI-TOF spectrum.

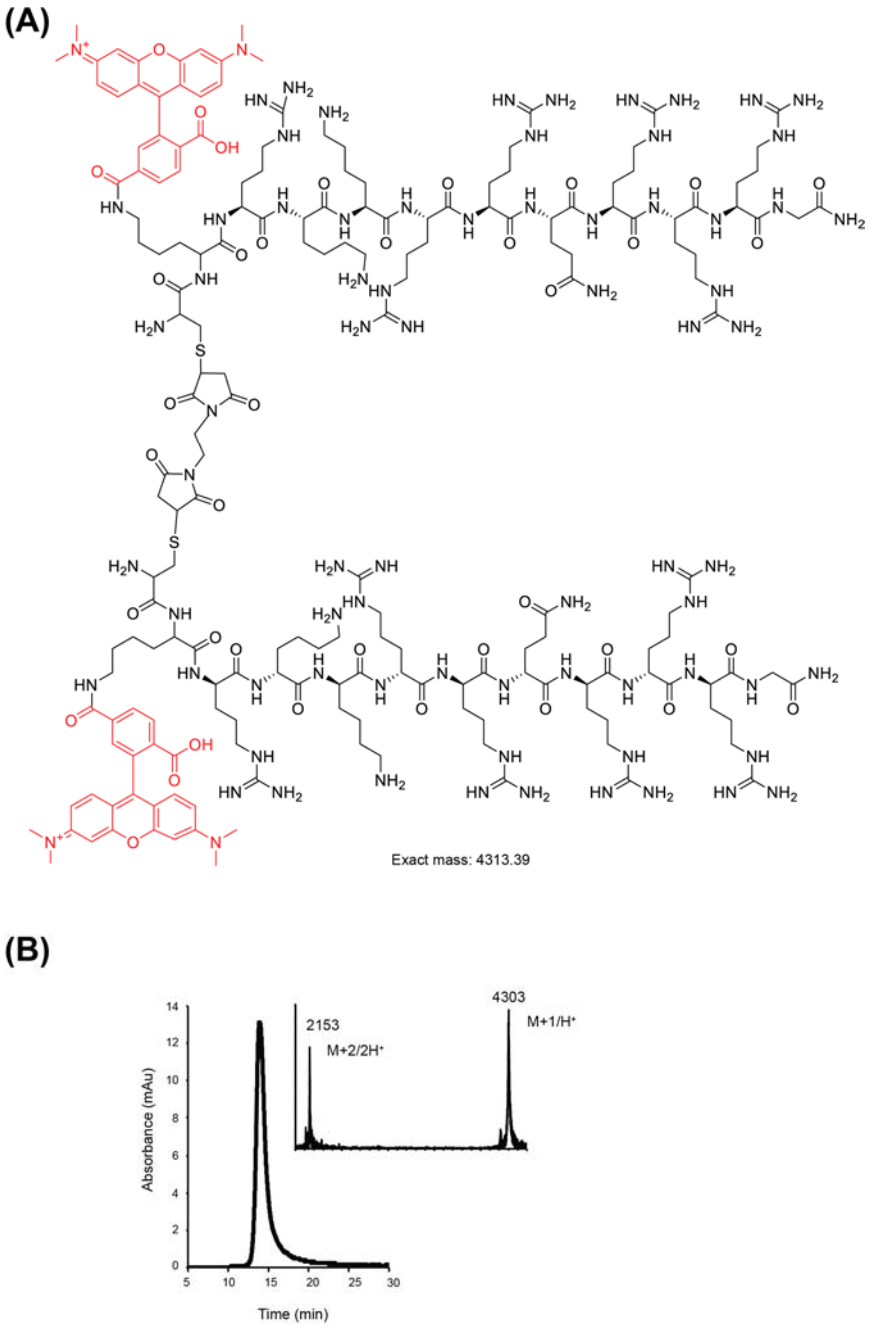


**Figure 3-4 Characterization of nrfTAT.** (A) Chemical structure of nrfTAT and its exact mass. (B) HPLC chromatogram of pure nrfTAT and MALDI-TOF spectrum. The 2153 peak corresponds to doubly charged nrfTAT.

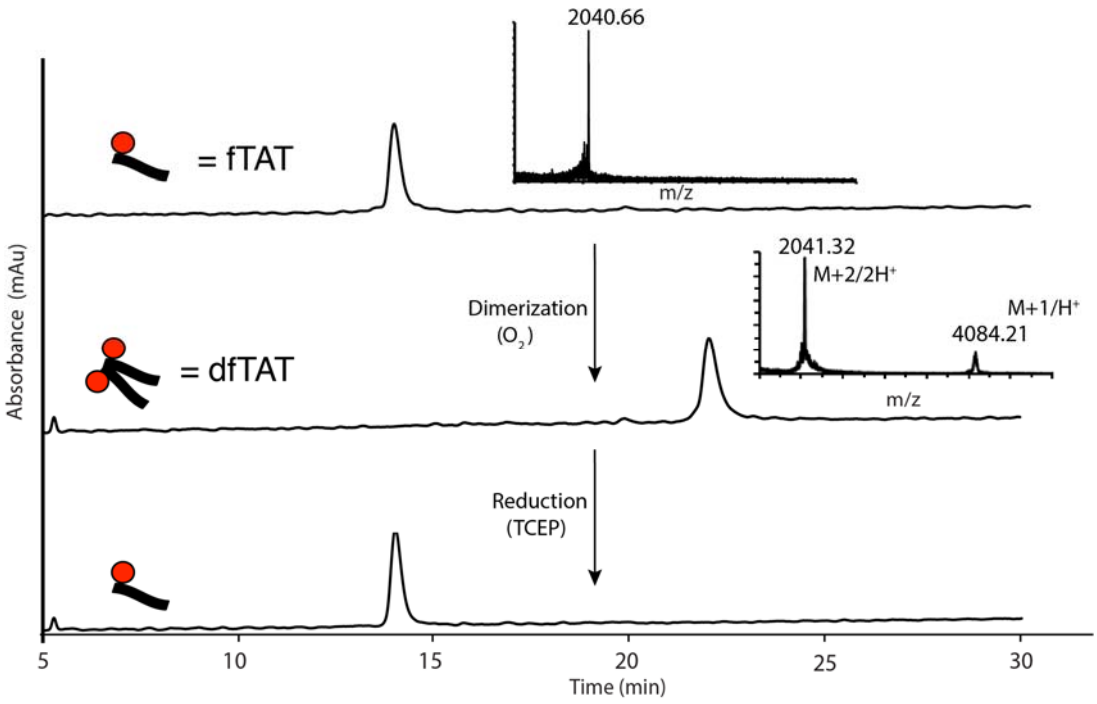


**Figure 3-5 Characterization of dfTAT.** HPLC analysis of reduction reaction of dfTAT after addition of the reducing agent tris(2-carboxyethyl)phosphine (TCEP). Pure dfTAT was mixed with a solution of TCEP (50 mM) in water and allowed to react for 15 min. The HPLC chromatogram shows a peak with rt = 14.3 min and is identical to the retention time of pure fTAT.

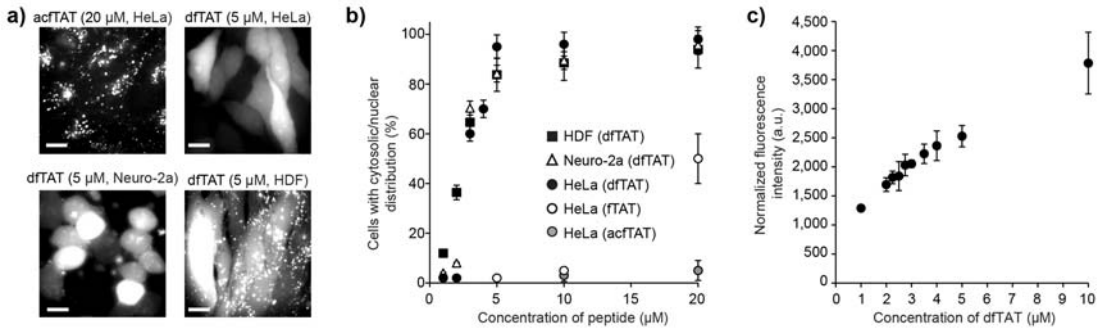


**Figure 3-6 Cytosolic delivery of dfTAT in live cells is efficient.** (a) Cellular localization of acfTAT and dfTAT assessed by fluorescence microscopy. Cells were incubated for 1 h with either acfTAT (20 μM) or dfTAT (5 μM), washed and imaged with a 100× objective. Monochrome images represent the emission of TMR at 560 nm. Scale bars, 10 μm. (b) Comparison of the cytosolic delivery efficiency of acfTAT, fTAT and dfTAT. Cells were incubated with acfTAT, fTAT or dfTAT (1–20 μM) for 1 h. The number of cells with detectable cytosolic and nuclear fluorescence distribution in microcopy images was counted and divided by the total number of cells present (1,000 cells per experiment). (c) dfTAT overall uptake in HeLa cells as a function of the concentration of dfTAT present in the incubation medium. Cells were incubated with dfTAT (1–10 μM) for 1 h, and relative uptake was assessed quantitatively by measuring the bulk fluorescence of cell lysates (300,000 cells per experiment). a.u., arbitrary units. The data in b and c represent the mean of triplicate experiments and the corresponding s.d.

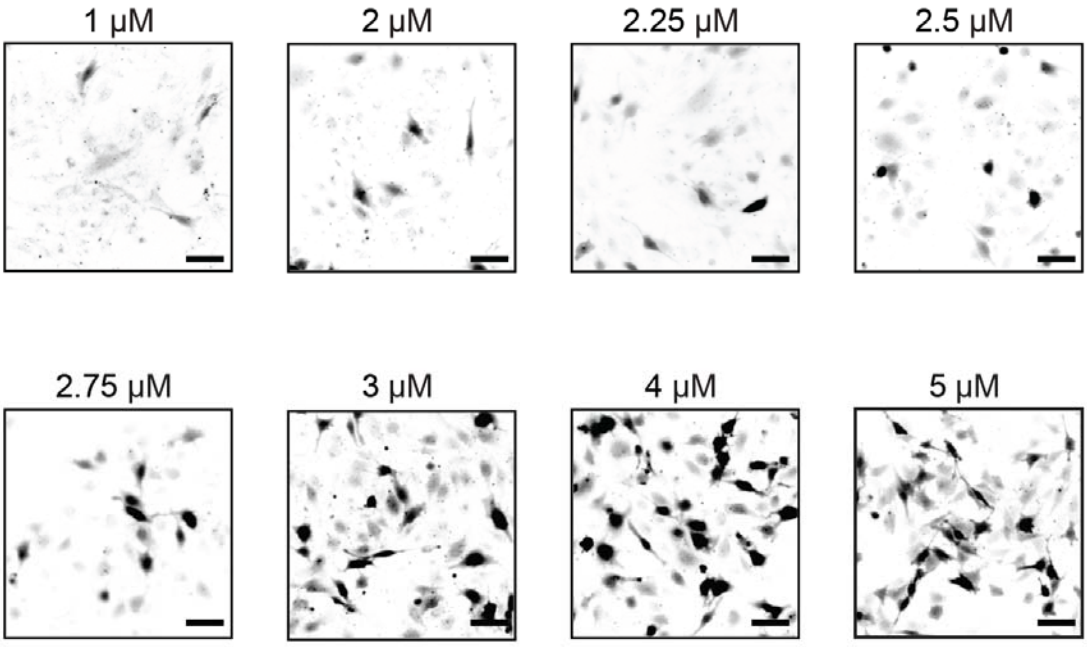


**Figure 3-7 Cytosolic and nuclear fluorescence distribution of dfTAT is concentration dependent.** HeLa cells were incubated with varying concentration of dfTAT (1, 2, 2.25, 2.5, 2.75, 3, 4, 5 µM). Cells were washed and imaged. Inverted monochrome images (20X obkective) show a dramatic increase in the cytosolic delivery of dfTAT between 2-5 µM. Although not shown here, the number of cells in each image is approximately the same as determined by bright field imaging. Cells that display a fluorescence punctate distribution are not clearly visible under these imaging conditions. Further analysis of these cells using 100X objective clearly show a fluorescence punctate distribution indicative of peptide trapped in endosomes. Scale bars: 50 µm

of dfTAT inside cells (in the cytosolic space and endosomes) also increased with the concentration of dfTAT administered extracellularly (**Figure 3-6 (C)**). I delivered dfTAT into the cytosolic space and nucleus of additional cell lines and primary intestinal porcine epithelial cells (**Figure 3-8**). In all cases, cells were not stained with SYTOX® Blue, indicating that their plasma membrane was not compromised and that the cells imaged were alive.

Similarly to acfTAT, fTAT was localized inside endosomes at up to 10 μM. However, at 20 μM, many cells displayed cytosolic fluorescence, indicating that fTAT reproduced some of the activity of dfTAT by possibly dimerizing *in situ* (**Figure 3-9**). Finally, nrdfTAT displayed a cytosolic distribution similar to that obtained with dfTAT (**Figure 3-10**), indicating that the disulfide bond present in dfTAT was not required for cytosolic penetration.

### 3.2.3 dfTAT penetrates cells in a two-step process

To test whether endosomal escape is involved in delivery of dfTAT, I assessed the effects of molecules that influence endocytosis[104, 219, 238, 239]. Whereas filipin and chlorpromazine (inhibitors of caveolae- and clathrin-mediated endocytosis) had little effect, amiloride (inhibitor of macropinocytosis) and bafilomycin (vacuolar $H^+$-ATPase inhibitor) inhibited the delivery of dfTAT, suggesting that macropinocytosis and endosomal acidification are important for cytosolic penetration (**Figure 3-11**). To assess whether endosomal escape could be visualized, dfTAT was incubated with cells for 5 min to permit endocytic uptake; cells were washed and then imaged in a pulse-chase

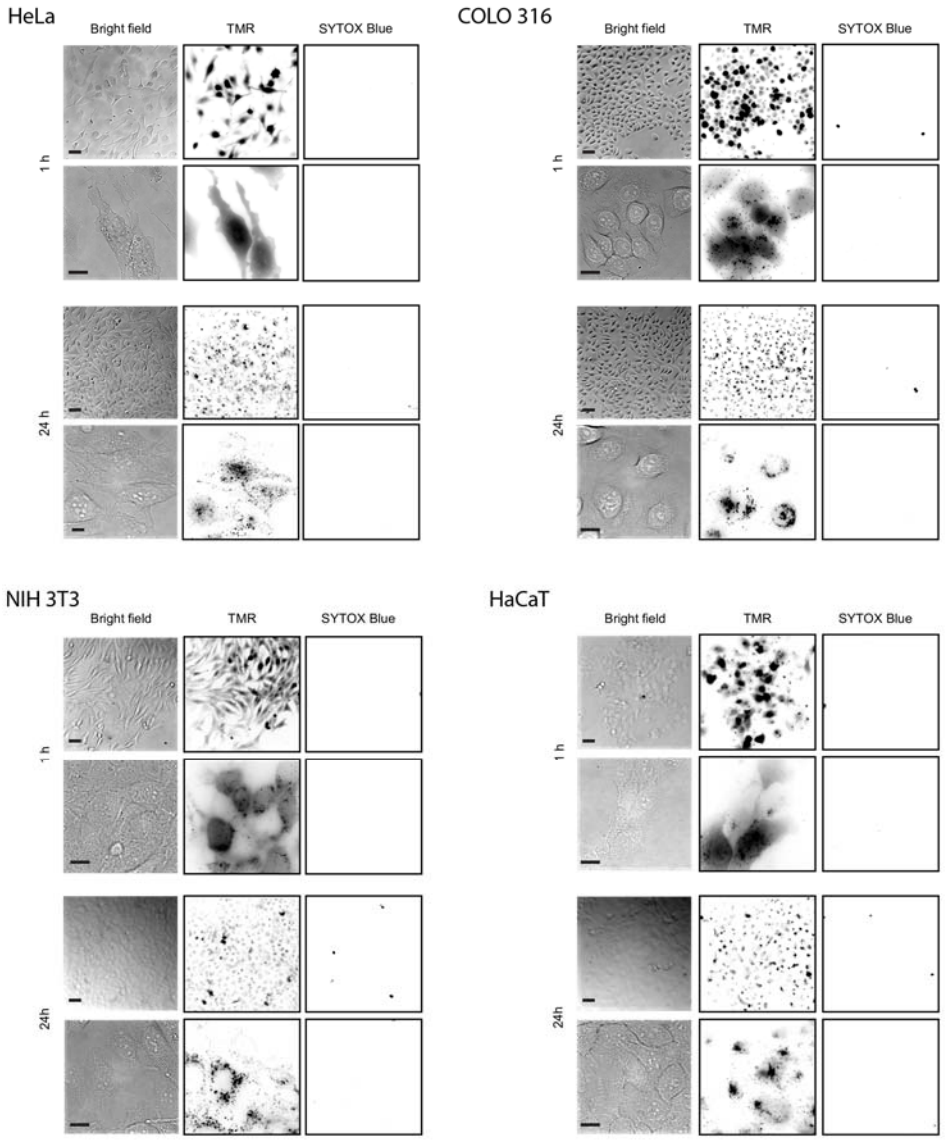


**Figure 3-8 Delivery of dfTAT was achieved in multiple cell types.** HeLa, COLO 316, NIH 3T3, HaCaT, Neuro-2a, MCH58, primary HDF and primary IPEC-1 cells were incubated with 5 μM dfTAT for 1 h, washed and imaged The fluorescence signal detected was in the cytosolic space and nucleus of cells (top panel 100X objective). After imaging cells were incubated in a humidified atmosphere containing 5 % $CO_2$ for 24 h, washed and imaged. (top panel: 20X objective, bottom panel: 100X objective) Cell morphology did not change after 24 h. Cell viability was assessed by exclusion of the cell-impermeable dye SYTOX® Blue after both 1 h and 24 h. The TMR fluorescence at the 24 h time point is different to that obtained at the 1 h time point presumably because of the intracellular degradation of the peptide . Scale bars: 20X objective, 50 μm; 100X objective, 10 μm.

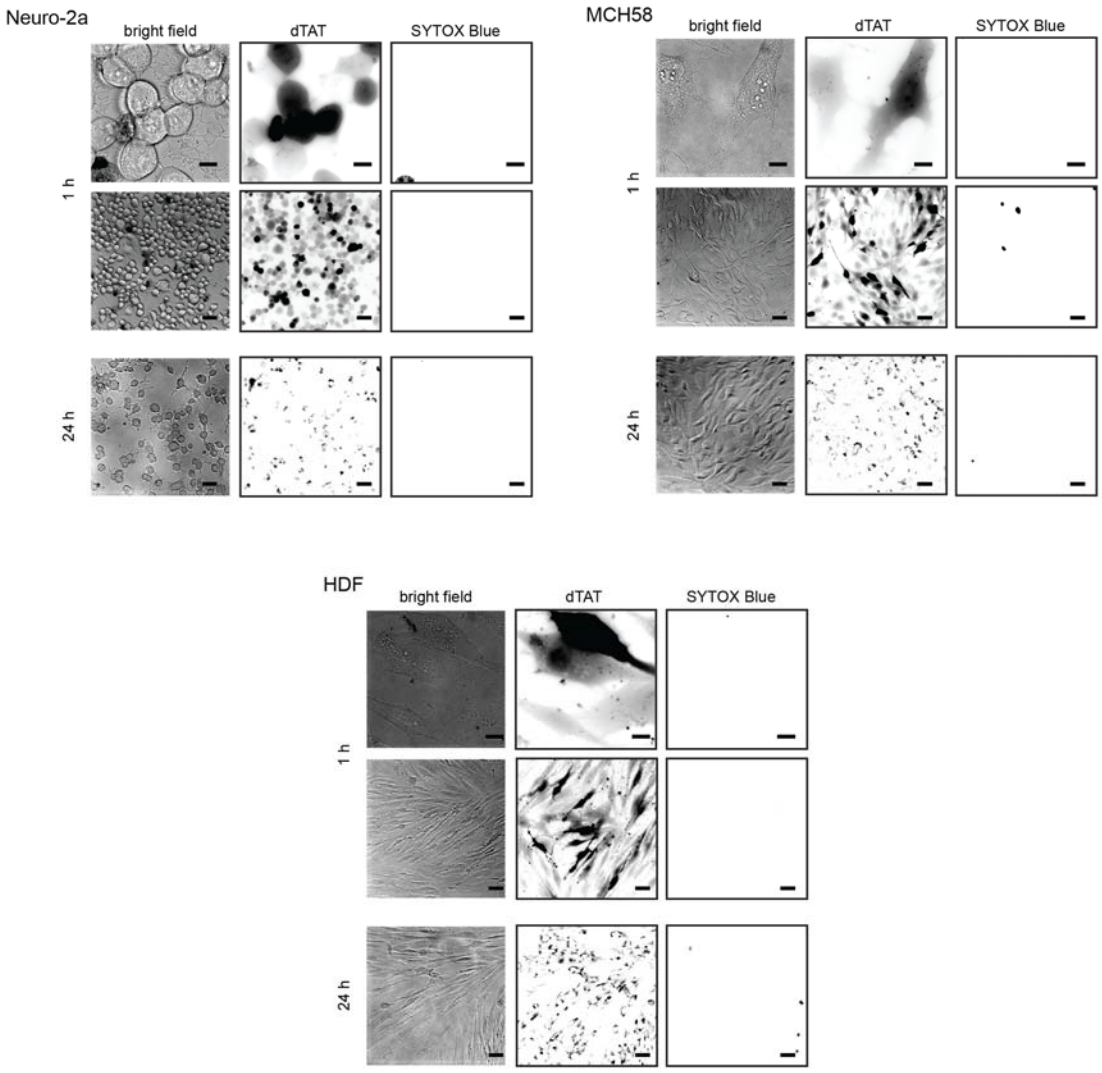


**Figure 3-8** Continued.

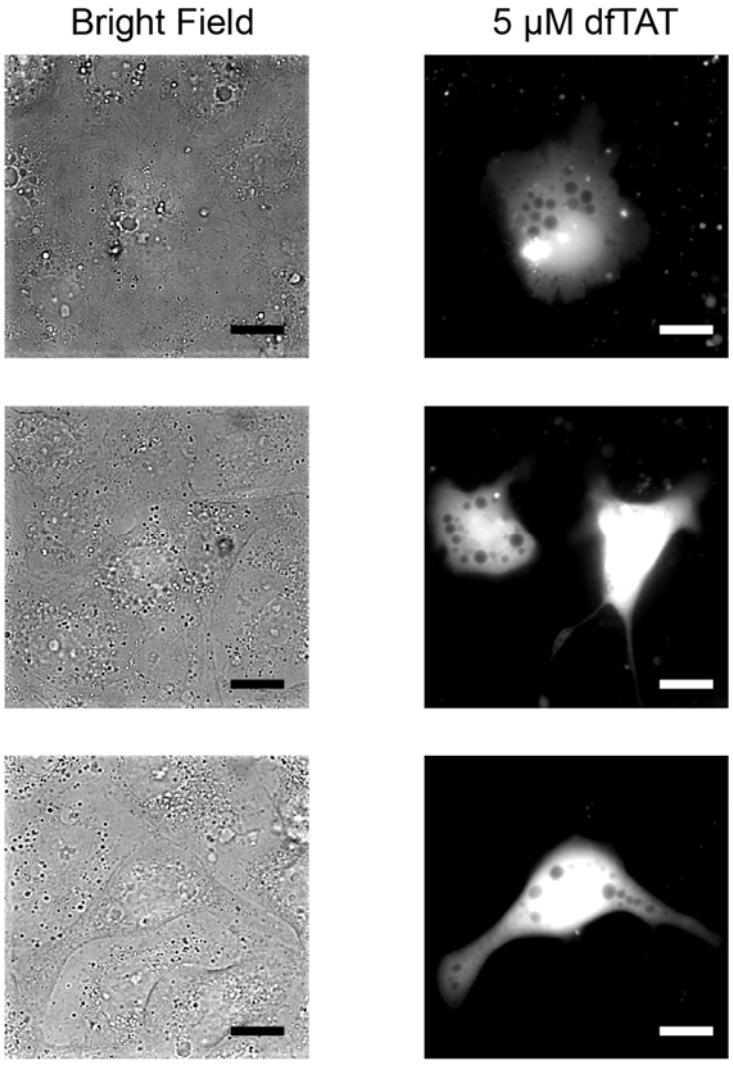


**Figure 3-8** Continued.

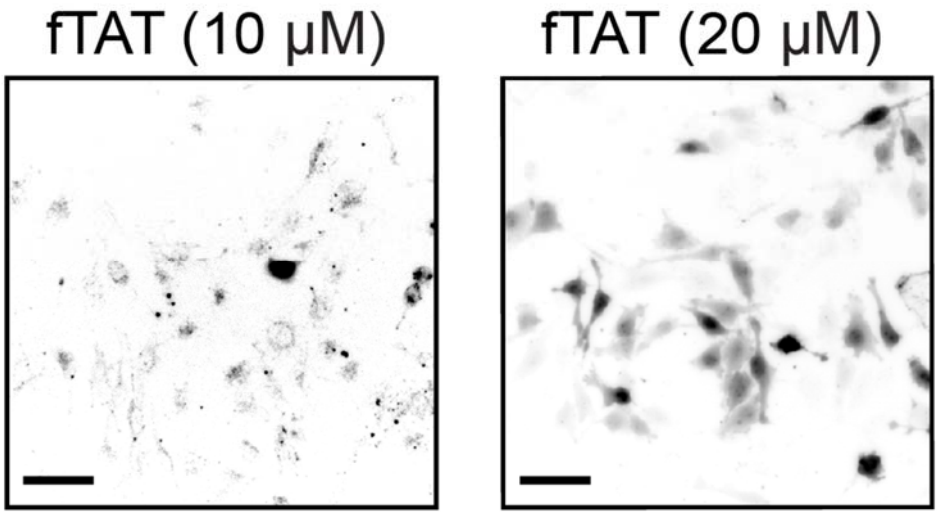


**Figure 3-9 fTAT cellular localization after incubation with live cells depends on its concentration in the extracellular media.** Inverted monochrome (black = fluorescence signal, white = no signal) fluorescence images of HeLa cells incubated with 10 or 20 µM of fTAT for 1 h. fTAT displays at fluorescence punctate distribution at 10 µM fTAT (left panel) while at 20 µM fTAT shows a significant increase in nthe population of cells displaying cytosolic and nuclear fluorescence distribution. Scale bars: 50 µm.

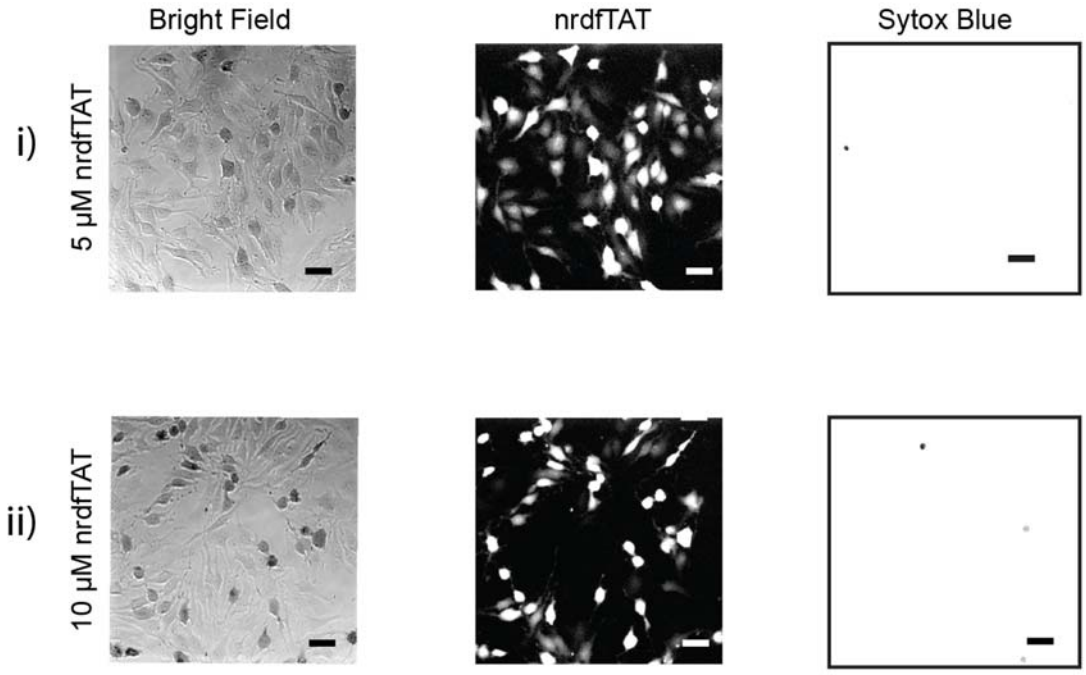


**Figure 3-10 Delivery of nrdfTAT into live cells.** Cells were incubated with nrdfTAT ((i) 2.5–5 μM and (ii) 5-10 μM*) for 1 h. Fluorescence images (monochrome (white = fluorescence signal, black = no signal) 20X image, center panel) show cytosolic delivery of nrdfTAT into HeLa cells at both concentrations. SYTOX® Blue (2 μM) was used as an indicator of cell death. Scale bars: 50 μm (inverted monochrome 20X image).
*The concentration of nrdfTAT was estimated by measuring the absorbance of TMR using a spectrophotometer, as described with other peptides. However, nrdfTAT has two TMR spaced by a 8.0 Å BMOE linker and such close proximity might affect the extinction coefficient of TMR. In order to take this effect into account, a concentration range for nrdfTAT was calculated based on the extinction coefficient of free TMR (91,500 mol-1cm-1) and that of dfTAT (45,500 mol-1cm-1) (dfTAT also has two TMR in close proximity).

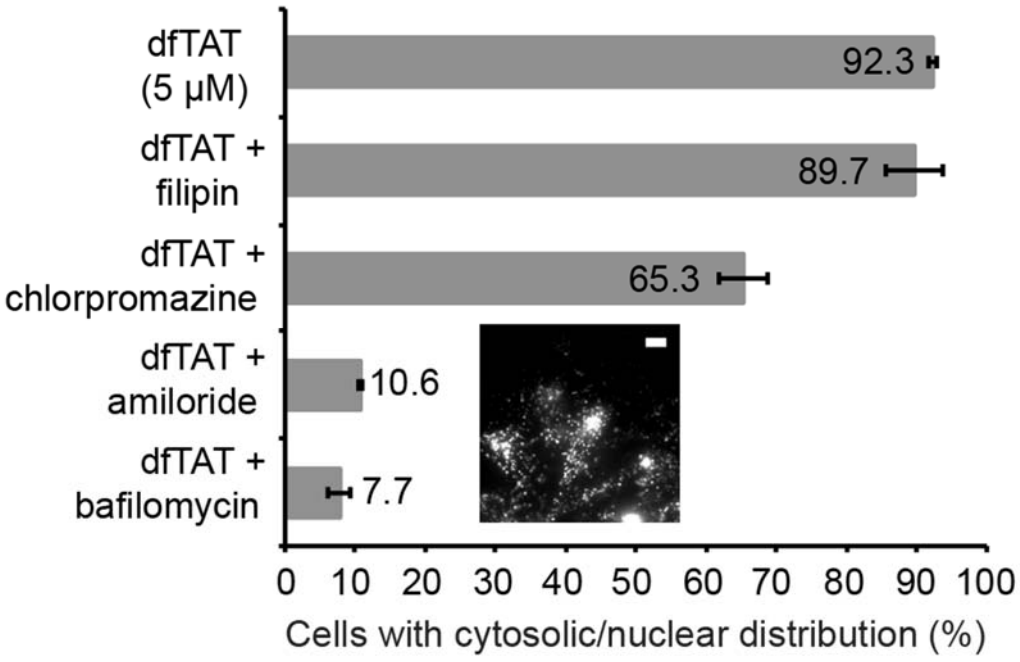


**Figure 3-11 Effect of endocytosis inhibitors on the cellular distribution of dfTAT.** HeLa cells were pretreated with each inhibitor for 20 min, washed and incubated with 5 μM dfTAT and inhibitor for 1 h. The percentage of cells displaying a cytosolic and nuclear fluorescence distribution was quantified as in Figure 3-6 (B). Inset, punctate distribution of dfTAT in the presence of bafilomycin (1,000 cells per experiment, experiments were performed in triplicates, mean ± s.d. represented). Scale bar: 10 μm.

experiment. dfTAT was initially localized in a punctate distribution consistent with that of endosomes (100X objective, data not shown). Yet, an increasing number of cells displayed a cytosolic distribution at later time intervals. When imaged with a 20X objective, cells with a cytosolic distribution were brighter than cells with a punctate distribution (this is consistent with TMR being partially self-quenched when dfTAT is trapped inside endosomes; **Figure 3-12**), and this was used to quantify dfTAT's cytosolic penetration as a function of time. Consistent with the notion that dfTAT penetrates the cytosolic space after endocytic uptake, the percentage of cells with cytosolic fluorescence increased from 4.3 % to 76.9 % over a period of 40 min (**Figure 3-13**). To further test whether dfTAT escapes from endocytic organelles, I incubated cells first with DEAC-K9, a fluorescent peptide that accumulates inside endosomes (**Figure 3-14**)[175]. After washing, cells were incubated with dfTAT. Although only a punctate distribution of fluorescence was observed with cells incubated with DEAC-K9 alone, subsequent addition of dfTAT led to a bafilomycin-dependent redistribution of the DEAC-K9 signal throughout the cytosolic space and nucleus (**Figure 3-15**). These data indicate that dfTAT accumulates inside endosomes already containing DEAC-K9 and that dfTAT endosomal escape is also accompanied by the leakage of luminal DEAC-K9.

### 3.2.4 dfTAT mediated endosomal leakage is very efficient

When endocytosed at similar levels, dfTAT escaped endosomes, whereas acfTAT did not, indicating that dfTAT is greatly more endosomolytic than acfTAT and is active inside endosomes as a dimer rather than as a reduced monomer (**Figure 3-16)**.

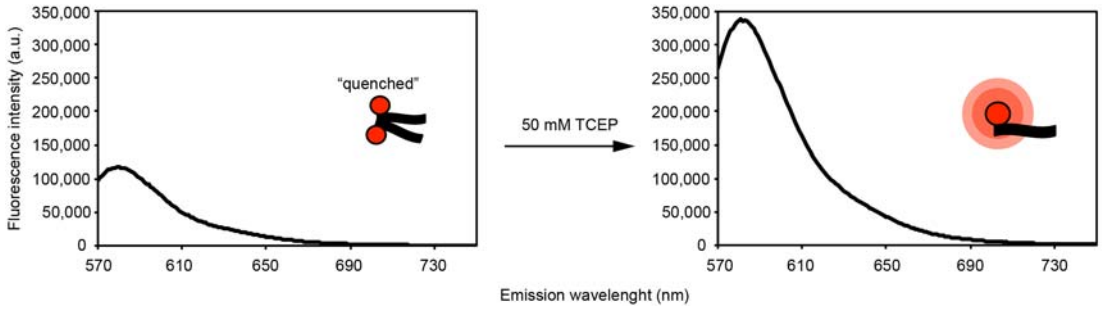


**Figure 3-12 Fluorescence emission spectra of dfTAT (5 µM) before and after reduction with the reducing agent TCEP (50 mM).** The sample was excited at 556 nm and the emission was recorded between 570-750 nm. The emission spectra show that the fluorescence emission of dfTAT increases upon reduction of its disulfide bond. This is indicative of TMR self-quenching in the context of dfTAT. This evidence suggests that TMR fluorescence is quenched inside endosomes where, presumably, the peptide exists as a dimer. This behavior displayed by dfTAT allowed me to design the experiment performed in Figure 3-12.

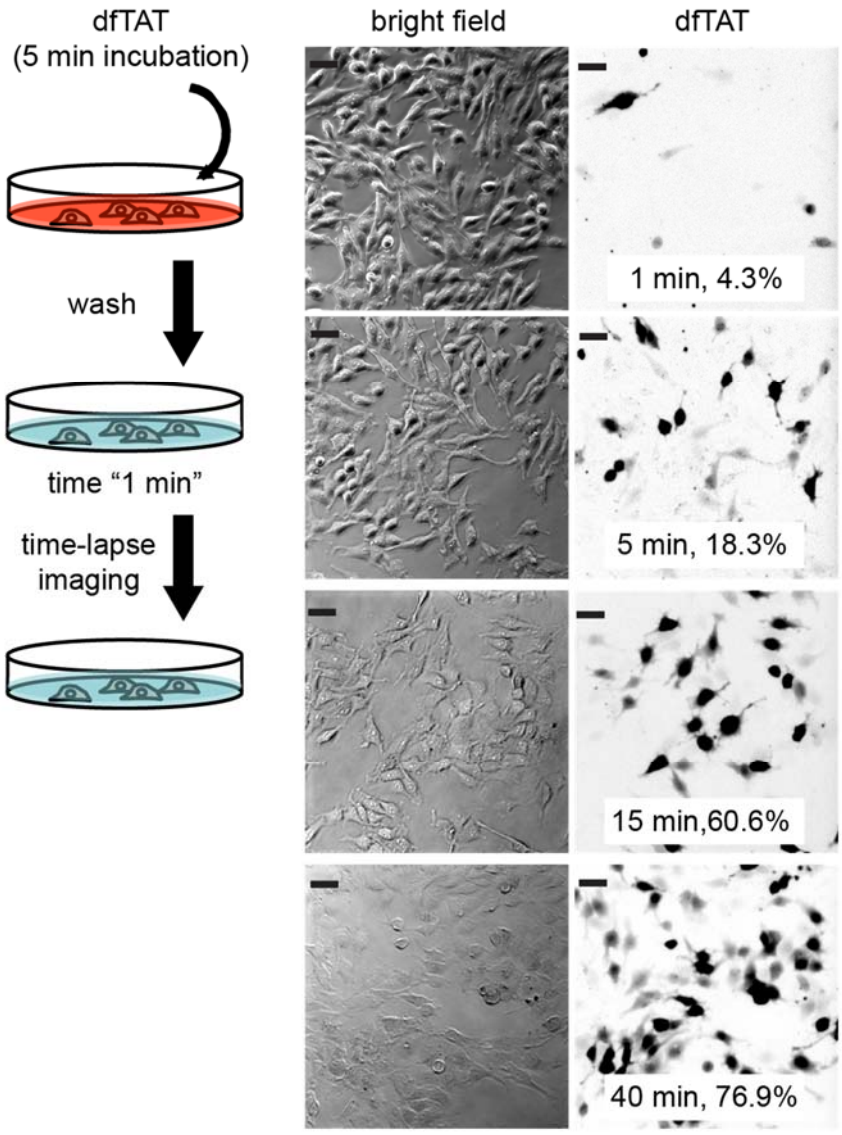


**Figure 3-13 Pulse-chase experiment showing the progressive cytosolic penetration of dfTAT.** HeLa cells were incubated with dfTAT (5 μM) for 5 min, washed and imaged with a 20X objective (TMR fluorescence images are represented as inverted monochrome) (a schematic of the protocol is shown on the left). The imaging intervals and corresponding percentages of cells with a cytosolic signal are represented. Scale bars: 50 μm.

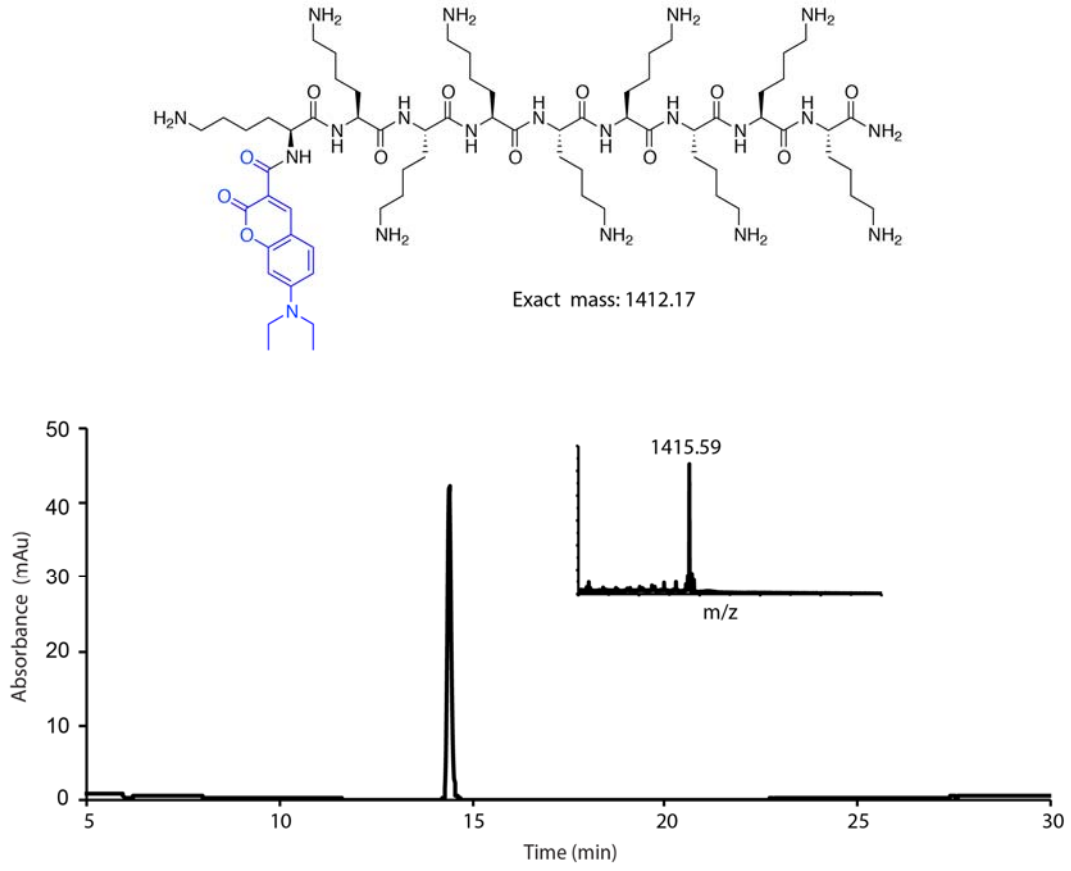


**Figure 3-14 Structure and characterization of DEAC-K9.** Structure and expected mass of DEAC-K9 (top). HPLC analysis and MALDI-TOF mass spectrum of pure DEAC-K9 (rt = 14.4 min) (expected mass: 1412.97, observed mass: 1415.59)

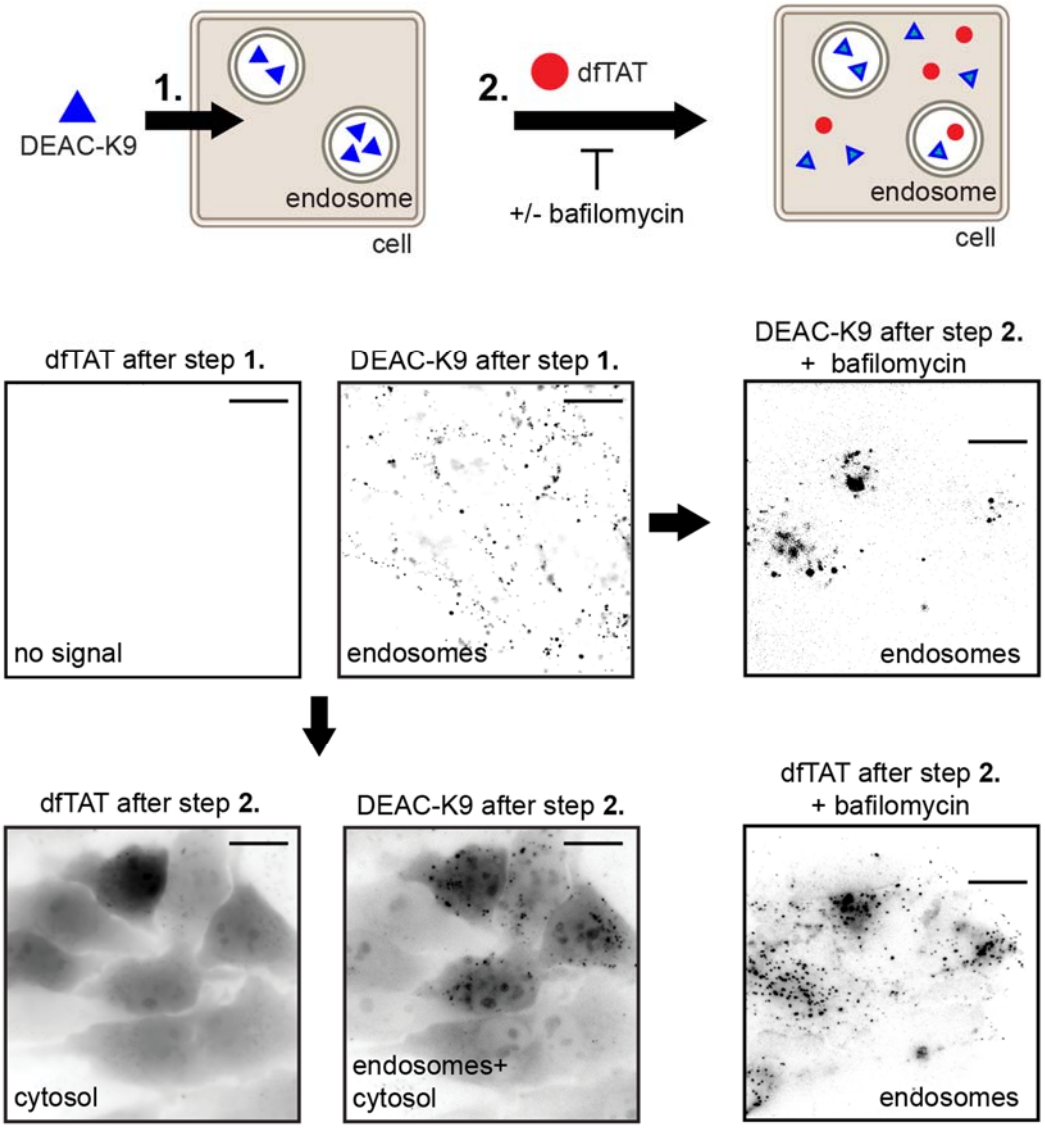


**Figure 3-15 dfTAT causes the cytosolic release of molecules trapped inside endosomes.** Microscopy images showing dfTAT-mediated release of molecules trapped inside endosomes; a schematic of the process is included (top). HeLa cells were incubated with 5 μM DEAC-K9 for 1 h and washed. Cells were subsequently incubated with 5 μM dfTAT for 1 h. Images are represented as inverted monochromes. Scale bars: 10 μm.

**Figure 3-16 dfTAT displays a high endosomolytic activity when compared to acfTAT.** HeLa cells were incubated with dfTAT (5 μM) for 5 min and acfTAT (50 μM) for 1 h. After 1h, the cells were washed with PBS/heparin, imaged and lysed. The lysis buffer used in this experiment contains 2 mM DTT. The bulk fluorescence of cell lysates on a 96-well plate was measured using a plate reader. The fluorescence of each sample was normalized to total protein content in the cell lysate, as determined by a Bradford protein assay. Similarly, the fluorescence of solutions of acfTAT at different concentrations (0.1, 0.5, 1, 5 and 10 μM) was measured using a plate reader. A calibration curve of the peptide fluorescence intensity v.s. peptide concentration was established. These data was used to estimate the average concentration of acfTAT and dfTAT inside cells. Data shows higher fluorescence intensity for acfTAT than dfTAT inside cells. These data suggests that dfTAT is a dimer inside endosomes and that this peptide is more endosomolytic than acfTAT (Model 1).

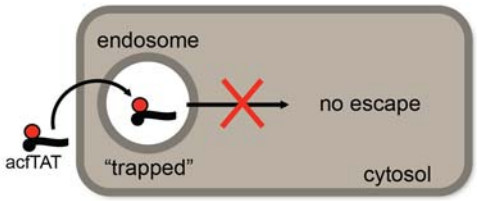


Why does dfTAT penetrate the cytosol of cells when acfTAT and fTAT do not?

Model 1

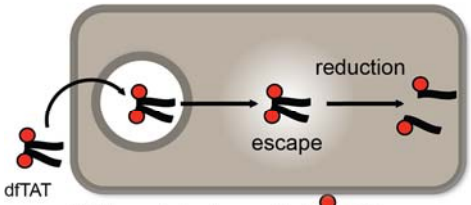


dfTAT penetration is possible if is more endosomolytic than

Model 2

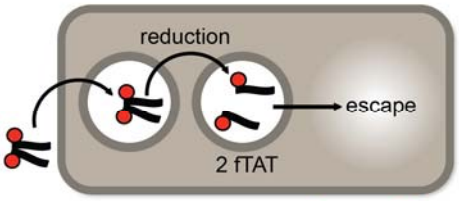


dfTAT penetration is possible if [ ] < [ ]
inside endosomes: reduced dfTAT and acfTAT are equally endosomolytic but the endocytic uptake of dfTAT is such that more peptide accumulates inside endosomes, thereby reaching a "penetration" threshold.

**Design:**

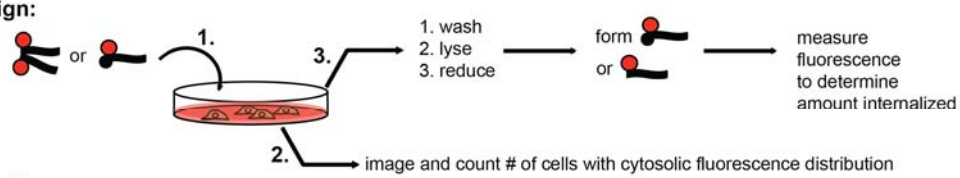


**Results:**

| | peptide in media (μM) | fluorescence intensity of cell lysate (a.u.) | estimated average peptide concentration per cell (mM) | cells with cytosolic fluorescence distribution (%) |
|---|---|---|---|---|
| dfTAT | 5 | 986.8 | 0.65 if or 1.3 if | 76.9 |
| acfTAT | 50 | 1208.4 | 1.6 | 5.6 |

numbers used for calculations: number of cells in sample (measured by flow cytometry) = 80,000
estimated volume of a cell = 2 $10^{-12}$ L (bionumbers.hms.harvard.edu)
calibration with samples of known concentration: fluorescence intensity = 326.5 x [TAT in μM]

**Conclusions:**

When dfTAT is internalized by cells at a lower level then acfTAT (this requires a large concentration of acfTAT in media in comparison to dfTAT), dfTAT penetrates the cytosol of cells but acTAT remains trapped inside endosomes. This is inconsistent with model 2 and instead supports model 1.

Additional information supporting model 1:

1) the number of endosomes present in cells treated with dfTAT (2 μM, below escape threshold) , fTAT, or acfTAT is approximately equal (100-400) based on fluorescence microscopy (this supports the notion that the total amount of peptide internalized by cells can be correlated to the concentration inside endosomes comparably between experiments).

2) nrdfTAT, a dimer that cannot be reduced inside endosomes, has an activity similar to dfTAT.

3) endosomes can be non-reducing (this is cell-type dependent) and disulfide bonds have been demonstrated to be stable inside endocytic organelles of HeLa cells (Lee YJ *et al* J Am Chem Soc. 2008 Feb 27;130(8):2398-9).

However, the cytosolic fluorescence of dfTAT possibly obscures the signal that remains inside endosomes. Under such a scenario, dfTAT endosomal escape would appear more dramatic than it really is. To establish more precisely the efficiency with which dfTAT mediates endosomal leakage, I co-incubated dfTAT with SNAP-Surface, a cell-impermeable green fluorophore that can react with the SNAP protein fusion tag[240]. The experiment was performed in cells expressing a SNAP-H2B histone construct so that SNAP-Surface 488 would label the nucleus of cells upon delivery, deplete the cytosolic signal and reveal the amount of probe remaining trapped inside endosomes. Cells incubated with dfTAT and SNAP-Surface 488 displayed a nuclear staining (**Figure 3-17**), whereas cells incubated with SNAP-Surface 488 alone did not (**Figure 3-18**). Cells with a brightly labeled nucleus also contained only a few dim endosomes. Analysis of the fluorescence signal indicated that 50–90 % of the fluorophore escaped endosomes.

### 3.2.5 dfTAT mediated delivery is not deleterious to cells

By inducing efficient endosomal leakage, dfTAT might negatively affect cell physiology. In addition, endosomal leakage has been previously observed in cells undergoing apoptosis[241]. Endosomal leakage could therefore be either a cause or a consequence of cell death. To address these issues, I treated HeLa, MCH58, HDF and Neuro-2a cells with dfTAT for 1 h and established viability 1 and 24 h after incubation using a SYTOX® Green exclusion assay (**Figure 3-19**). Viability was >95 % after treating cells with 5 μM dfTAT for 1 h—conditions required to achieve cytosolic distribution of dfTAT in >80 % of cells. Cell morphology was also unaffected by dfTAT

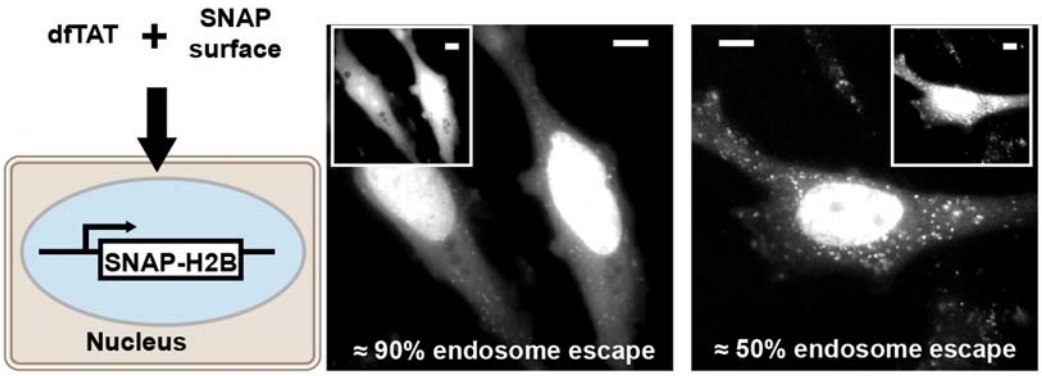


**Figure 3-17 Endosomolytic efficiency of dfTAT.** HeLa cells expressing SNAP-H2B were incubated with 5 μM dfTAT and 5 μM SNAP-Surface 488 (a schematic of the protocol followed is shown on the left). Representative fluorescence images (of 50 total) of SNAP-Surface are shown (dfTAT is in the inset). The SNAP-Surface 488 signal present in the nucleus is indicated as a percentage of the total signal. Scale bars: 10 μm.

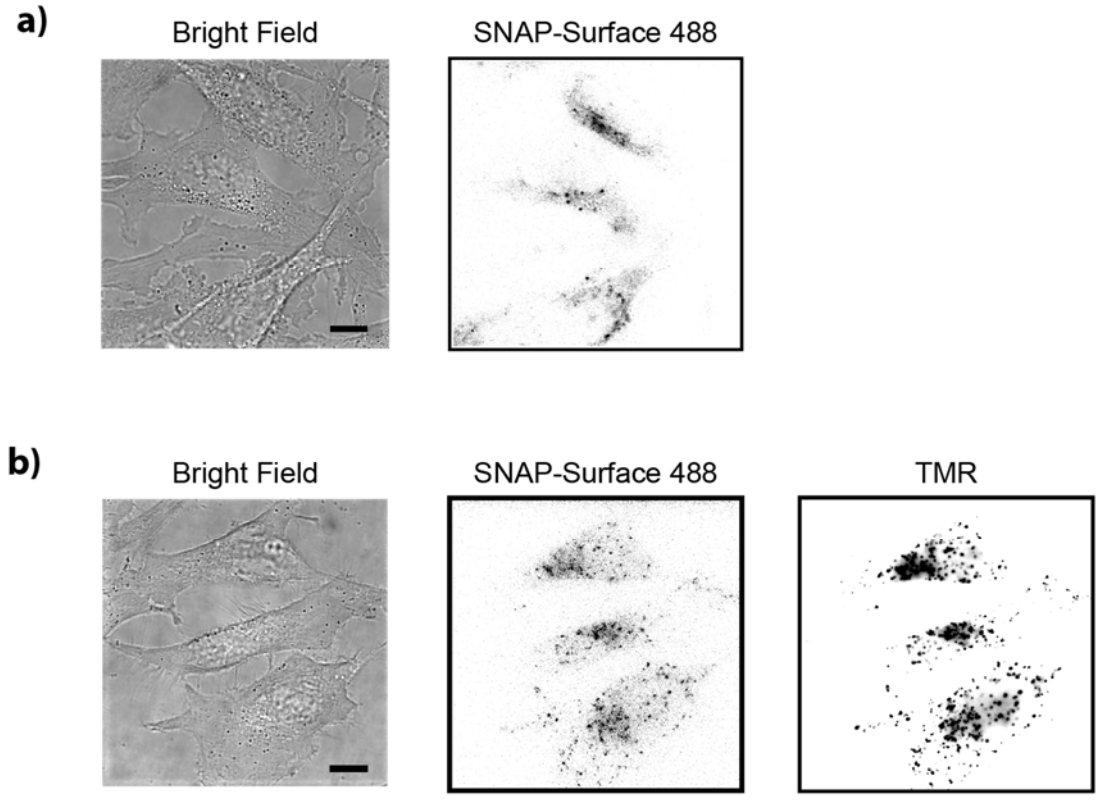


**Figure 3-18 SNAP-Surface 488 enters cells via endocytosis and does not escape endosomes in the absence of dfTAT.** (A) HeLa cells were incubated with 5 μM SNAP-Surface 488 for 1 h, washed and imaged. Inverted monochrome image shows a punctate distribution from SNAP-Surface 488 (right panel). (B) HeLa cells were incubated with 5 μM SNAP-Surface 488 and 2.5 μM dfTAT (a concentration in which dfTAT incubation does not result in significant cytosolic release) for 1 h, washed and imaged. Inverted monochrome images show SNAP-Surface 488 accumulation in endocytic organelles (punctate distribution) (right panel) and colocalization with TMR signal. Bright field images show HeLa cells morphology did not change after uptake of SNAP-Surface 488 and/or dfTAT (right panels). Scale bars: 10 μm.

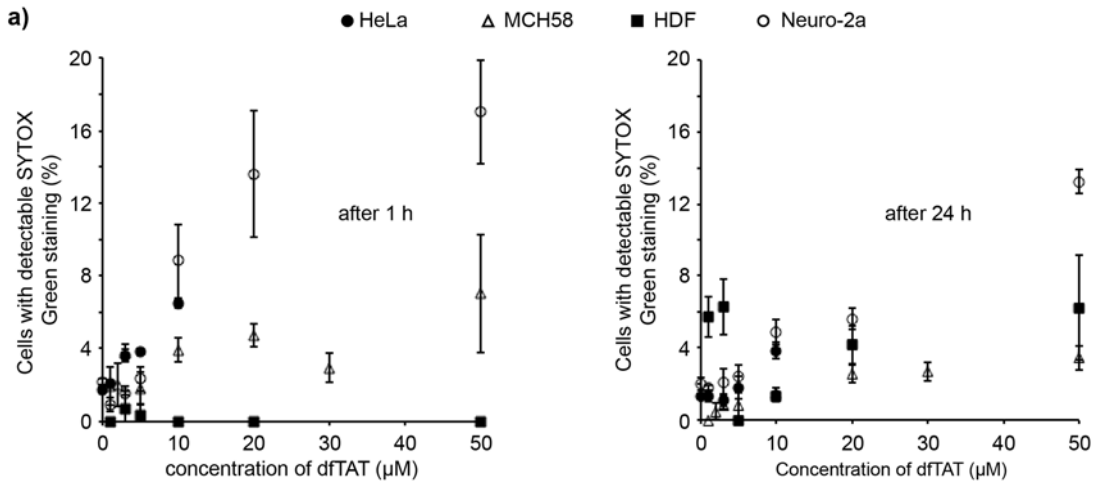


**Figure 3-19 dfTAT is not toxic to cells under conditions where efficient endosomal escape is achieved.** (A) HeLa, MCH58, HDF and Neuro-2a cells were incubated with (1-50 μM) dfTAT for 1 h. Cell viability was assessed by a SYTOX® Green exclusion assay 1, 24, and 48 h (for HeLa) after incubation (1,000 cells/experiment, experiments in triplicates, average and standard deviations represented). (B) Histogram of flow cytometry data. HeLa cells were incubated with 5 μM dfTAT or no peptide (control) for 1h, washed and then incubated in SYTOX® Green (1 μM) for 15 min. Cells were then trypsinized for 5 min, resuspended in a total of 200 μl of nrL-15, and analyzed by flow cytometry (BD Accuri C6 Flow Cytometer). Histograms show that only 2 % and 7.5 % of cells are stained with the cell impermeable dye SYTOX® Green for untreated and treated cells, respectively.

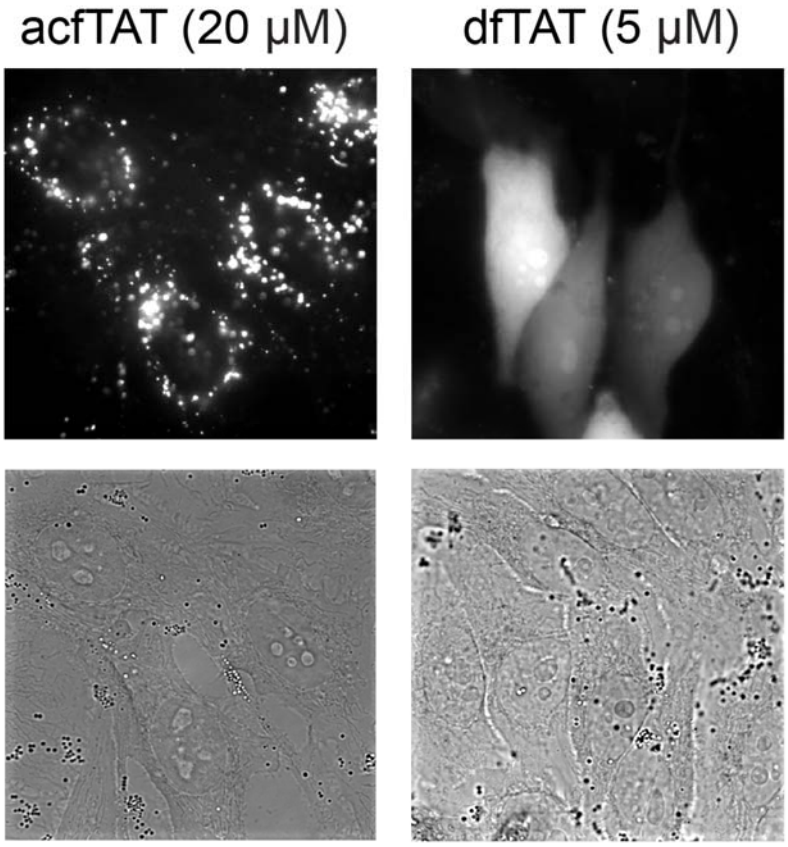


**Figure 3-20 The cellular localization of acfTAT and dfTAT is different after incubation with live cells but cell morphology is not changed.** Fluorescence (monochrome) and bright field images (100X objective) of HeLa cells incubated with 20 μM acfTAT (left panel) and 5 μM dfTAT (right panel). The acfTAT peptide displays a fluorescence punctate distribution while dfTAT exhibits a cytosolic and nuclear fluorescence distribution. Bright field images show no change in HeLa cell morphology upon peptide delivery. Scale bar: 10 μm.

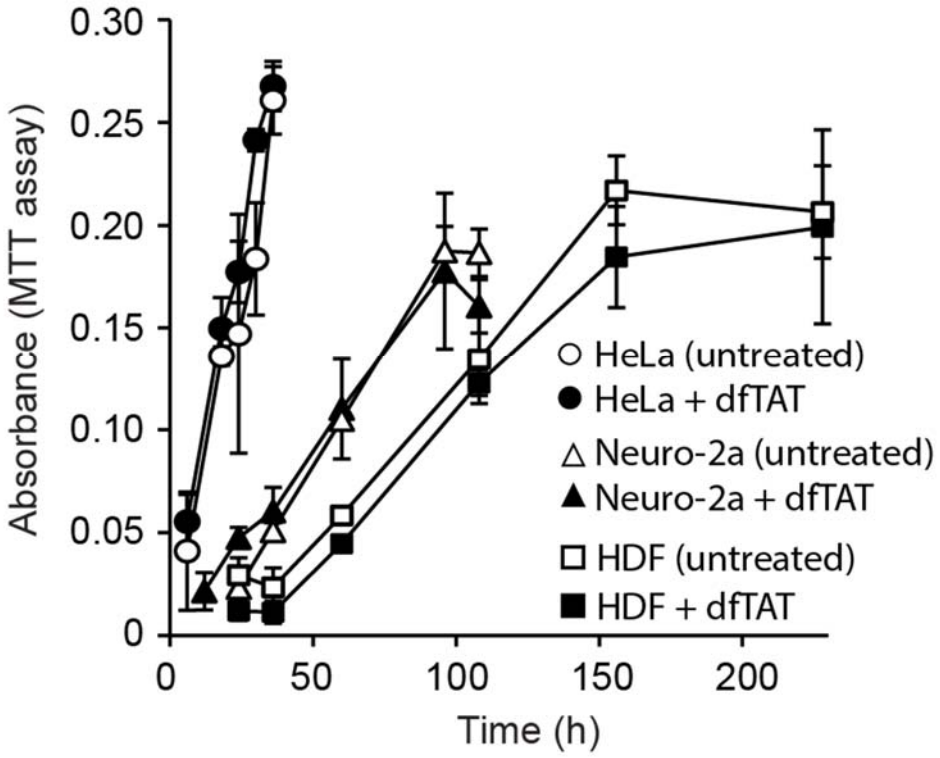


**Figure 3-21 dfTAT-mediated delivery does not significantly affect cell proliferation.** HeLa, Neuro-2a and HDF cells were incubated with 5 μM dfTAT for 1 h or left untreated. Proliferation was assessed using a MTT assay (150,000 cells/experiment, experiments in triplicates, mean and standard deviations represented).

incubation (**Figure 3-20**). Likewise, dfTAT incubation did not affect the proliferation rates of HDF, HeLa or Neuro-2a cells (**Figure 3-21**), and cells containing a cytosolic fluorescence signal indicative of efficient dfTAT endosomal escape were observed to divide normally by microscopy (**figure 3-22**).

To characterize the physiological impact of dfTAT cytosolic penetration in greater detail, I performed transcriptome analysis on HDF cells incubated for 1 h in nrL-15 medium with or without 5 μM dfTAT. Cells harvested immediately after dfTAT incubation showed 11 transcripts up- or downregulated more than twofold compared to those of untreated cells (twofold is used as a significance threshold; 47,321 total transcripts detected; **Figure 3-23**). Only two transcripts were dysregulated in cells incubated in DMEM for an additional 1 h and 24 h after treatment with dfTAT (**Figure 3-23 and 3-24**). Together, these results indicate that dfTAT has a minimal impact on mRNA expression and that cells recover rapidly from dfTAT-mediated endosomal leakage (corroborated by quantitative proteomic profile experiments; **Figure 3-25**).

If dfTAT perturbs many endosomes during a delivery step, I envisioned that endocytic trafficking might be a cellular process likely to be negatively affected following peptide incubation. In particular, I reasoned that dfTAT could cause endosomal leakage after an initial treatment but fail to be endocytosed or remain trapped inside damaged endocytic organelles after a second dfTAT incubation. I therefore tested the stepwise delivery of two different molecules (DEAC-K9 and SNAP-Surface 488). Cells were first incubated with dfTAT (5 μM) and DEAC-K9 (5 μM) for 1 h. As expected, this incubation resulted in the cytosolic distribution of both dfTAT and

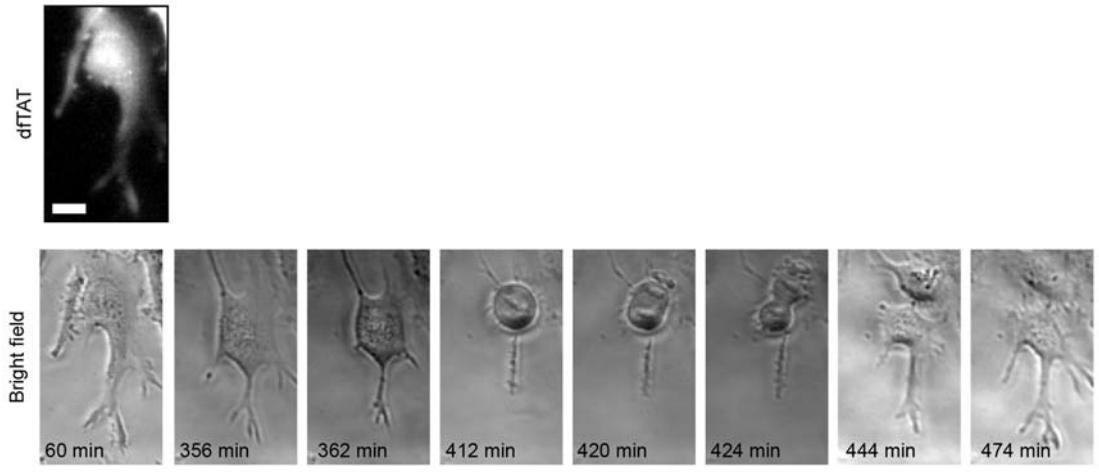


**Figure 3-22 dfTAT-mediated delivery does not significantly affect cell division.** Microscopy imaging showing that cells containing cytosolic dfTAT divide. HeLa cells were incubated with 5 μM dfTAT for 1 h, washed and imaged in a time-lapse experiment. Scale bars, 10 μm

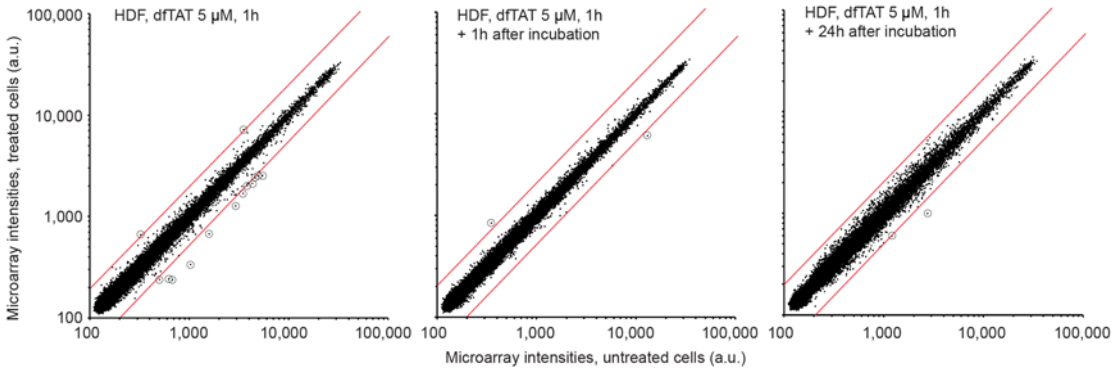


**Figure 3-23 dfTAT-mediated delivery does not significantly affect transcription in primary cells.** Whole-genome microarray analysis of HDF cells treated with dfTAT. HDF cells were treated with 5 µM dfTAT for 1 h and transcriptome analysis was performed immediately, 1 h, or 24 h after dfTAT treatment. The plot displays microarray intensity values of treated vs. untreated (same incubation steps but without peptide) samples. The red lines represent 2-fold intensity change cut-offs and transcripts up or down-regulated above these cut-offs are circled for clarity.

**Figure 3-24 mRNA expression analysis in the presence of staurosporine. (**a) In order to establish a positive control for the microarray analysis, staurosporin was used to induce apoptosis in HDF cells. Cells were treated with staurosporine (0.1 μM) for 1h and mRNA levels were analyzed as described in Figure 3. The identity of transcripts related to apoptosis that were up-regulated (highlighted in red) and down-regulated (highlighted in green) upon treatment with staurosporin are listed. Notably, a total of 1830 transcripts were found to be up-or down-regulated out of 47321 transcripts detected. (b) Analysis of the microarray intensities of untreated HDF cells vs. those of HDF cells treated with staurosporine (0.1 μM) for 1h. The red lines represent the 2-fold cut-offs. (c) Table listing the identity of transcripts that are up-regulated (highlighted in red) and down-regulated (highlighted in green) in HDF cells incubated with dfTAT (5 μM) and analyzed immediately after incubation (1h), or 1h (1h+1h) and 24 h (1h+24h) after incubation. The 11, 2, and 2 transcripts listed represent the total number of transcripts up or down-regulated in the 1h, 1h+1h, and 1h+24h samples, respectively.

a) Staurosporine 1h incubation

| Gene names related to apoptosis | FC | Log2 FC |
|---|---|---|
| Homo sapiens baculoviral IAP repeat-containing 5 (BIRC5), transcript variant 1, mRNA. | 8.67 | 3.12 |
| Homo sapiens cell division cycle 2, G1 to S and G2 to M (CDC2), transcript variant 1, mRNA. | 5.64 | 2.5 |
| Homo sapiens topoisomerase (DNA) II alpha 170kDa (TOP2A), mRNA. | 4.98 | 2.31 |
| Homo sapiens breast cancer 1, early onset (BRCA1), transcript variant BRCA1-delta11b, mRNA. | 2.99 | 1.58 |
| Homo sapiens breast cancer 1, early onset (BRCA1), transcript variant BRCA1-delta14-17, mRNA. | 2.94 | 1.56 |
| Homo sapiens cell division cycle 2, G1 to S and G2 to M (CDC2), transcript variant 1, mRNA. | 2.89 | 1.53 |
| Homo sapiens potassium large conductance calcium-activated channel, subfamily M, alpha member 1 (KCNMA1), transcript variant 2, mRNA. | 2.76 | 1.46 |
| Homo sapiens baculoviral IAP repeat-containing 5 (BIRC5), transcript variant 3, mRNA. | 2.53 | 1.34 |

21 transcripts out of a total 47321 transcripts

| Gene names related to apoptosis | FC | Log2 FC |
|---|---|---|
| Homo sapiens tumor necrosis factor (ligand) superfamily, member 14 (TNFSF14), transcript variant 2, mRNA. | 0.48 | -1.06 |
| Homo sapiens hypoxia-inducible factor 1, alpha subunit (basic helix-loop-helix transcription factor) (HIF1A), transcript variant 2, mRNA. | 0.47 | -1.09 |
| Homo sapiens hypoxia-inducible factor 1, alpha subunit (basic helix-loop-helix transcription factor) (HIF1A), transcript variant 1, mRNA. | 0.47 | -1.09 |
| Homo sapiens BCL2/adenovirus E1B 19kDa interacting protein 3-like (BNIP3L), mRNA. | 0.45 | -1.15 |
| Homo sapiens suppressor of cytokine signaling 2 (SOCS2), mRNA. | 0.41 | -1.29 |
| Homo sapiens msh homeobox 1 (MSX1), mRNA. | 0.36 | -1.47 |
| Homo sapiens DNA-damage-inducible transcript 3 (DDIT3), mRNA. | 0.35 | -1.51 |
| Homo sapiens v-myc myelocytomatosis viral oncogene homolog (avian) (MYC), mRNA. | 0.32 | -1.64 |
| Homo sapiens interleukin 10 (IL10), mRNA. | 0.32 | -1.64 |
| Homo sapiens v-myc myelocytomatosis viral oncogene homolog (avian) (MYC), mRNA. | 0.29 | -1.79 |
| Homo sapiens immediate early response 3 (IER3), mRNA. | 0.28 | -1.84 |
| Homo sapiens cyclin-dependent kinase inhibitor 1A (p21, Cip1) (CDKN1A), transcript variant 2, mRNA. | 0.25 | -2 |
| Homo sapiens heat shock 70kDa protein 5 (glucose-regulated protein, 78kDa) (HSPA5), mRNA. | 0.24 | -2.06 |

b)

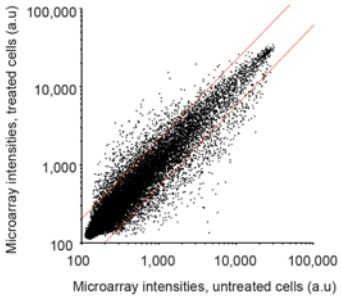


c) dfTAT 5 µM, 1h incubation

| Gene name | Fold change(FC) | Log2 FC |
|---|---|---|
| PREDICTED: Homo sapiens misc_RNA (LOC148430), miscRNA. | 2.04 | 1.03 |
| Homo sapiens ornithine decarboxylase antizyme 2 (OAZ2), mRNA. | 2.04 | 1.03 |
| Homo sapiens immediate early response 3 (IER3), mRNA. | 0.49 | -1.03 |
| Homo sapiens glutaminase (GLS), mRNA. | 0.49 | -1.03 |
| Homo sapiens cDNA FLJ31351 fis, clone MESAN2000167 | 0.48 | -1.06 |
| Homo sapiens early growth response 1 (EGR1), mRNA. | 0.46 | -1.12 |
| Homo sapiens growth differentiation factor 15 (GDF15), mRNA. | 0.43 | 1.21 |
| PREDICTED: Homo sapiens similar to mCG49427 (LOC100129882), mRNA. | 0.42 | -1.25 |
| Homo sapiens microRNA 221 (MIR221), microRNA. | 0.39 | 1.36 |
| Homo sapiens early growth response 2 (Krox-20 homolog, Drosophila) (EGR2), mRNA. | 0.35 | -1.51 |
| Homo sapiens dual specificity phosphatase 6 (DUSP6), transcript variant 2, mRNA. | 0.32 | -1.64 |

11 transcripts out of a total 47321 transcripts

dfTAT 5 µM, 1h + 1h after incubation

| Gene name | FC | Log2 FC |
|---|---|---|
| Homo sapiens FBJ murine osteosarcoma viral oncogene homolog B (FOSB), mRNA. | 2.4 | 1.26 |
| PREDICTED: Homo sapiens misc_RNA (LOC148430), miscRNA. | 0.46 | -1.12 |

2 transcripts out of a total 47321 transcripts

dfTAT 5 µM, 1h+ 24 h after incubation

| Gene name | FC | Log2 FC |
|---|---|---|
| PREDICTED: Homo sapiens similar to aggrecan 1 isoform 2 precursor (LOC649366), mRNA. | 0.5 | -1 |
| Homo sapiens dehydrogenase/reductase (SDR family) member 3 (DHRS3), mRNA. | 0.36 | -1.47 |

2 transcripts out of a total 47321 transcripts

a)

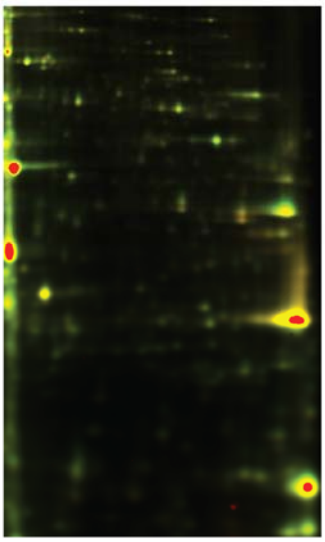

b)

| | 1+0h | 1+1h | 1+24h |
|---|---|---|---|
| | # spots (%) | # spots (%) | # spots (%) |
| Decreased | 29 (6.8%) | 12 (2.3%) | 23 (4.2%) |
| Similar | 391 (91.8%) | 487 (94.9%) | 488 (90%) |
| Increased | 6 (1.4%) | 14 (2.7%) | 31 (5.7%) |
| Total number of spots included | 426 | 513 | 542 |

**Figure 3-25 Differential in gel electrophoresis (DIGE) proteomic analysis of HDF cells treated with dfTAT (5 µM) for 1 h.** (a) Representative green and red fluorescence overlay of 2D gel of cells treated with or without dfTAT for 1h and incubated in fresh media for an additional 1h (1+1h samples, treated sample is labeled with Cy3 and untreated with Cy5). Green and red were used as pseudo colors for Cy3 and Cy5 dyes, respectively, and a yellow color is indicative of equal fluorescence intensities. (b) Table summarizing analysis results obtained from the DIGE using the DeCyder v6.5 suite of software tools (GE Healthcare). Data was obtained using a 2 standard deviation model (95% confidence). Each pair (treated vs. untreated) were individually analyzed based on the normalized volume ratio of each individual protein spot from Cy3- or Cy5- labeled sample.

DEAC-K9 (data not shown). Twenty minutes later, cells were incubated with dfTAT (5 μM) and SNAP-Surface 488 (5 μM) for 1 h. Cells treated with dfTAT using this two-step protocol displayed cytosolic and nuclear fluorescence of both DEAC-K9 and SNAP-Surface 488 (**Figure 3-26**). Delivery of SNAP-Surface 488 did not occur in the absence of dfTAT (**Figure 3-18**) and was inhibited by bafilomycin, consistent with the notion that the second delivery step is also mediated by the endosomolytic activity of dfTAT. Moreover, the fluorescence of SNAP-Surface 488 examined was comparable to that observed when SNAP-Surface 488 was delivered into untreated cells (one-step delivery) or simultaneously with DEAC-K9 (**Figure 3-27**). Together these results establish that dfTAT-mediated delivery can be repeated. This suggests that the endocytic route employed by dfTAT is not dramatically compromised after dfTAT-mediated endosomal leakage.

### 3.2.6 dfTAT delivers proteins by simple co-incubation

To determine whether dfTAT could deliver large proteins into the cytosol of cells, I chose EGFP (26 kDa) as a model cargo. Cells were incubated with EGFP and dfTAT for 1 h and examined by microscopy. EGFP was distributed into the cytosolic space and nucleus in more than 90 % of cells without observable toxicity (**Figure 3-28**). To estimate how much fluorescent and folded protein was delivered, cells were counted, harvested and lysed. The lysate was analyzed by PAGE, and the fluorescence of EGFP was quantified. On the basis of this analysis, approximately 34 μM and 23 μM of EGFP was present per HDF and Neuro-2a cell, respectively (**Figure 3-29**). As imaging

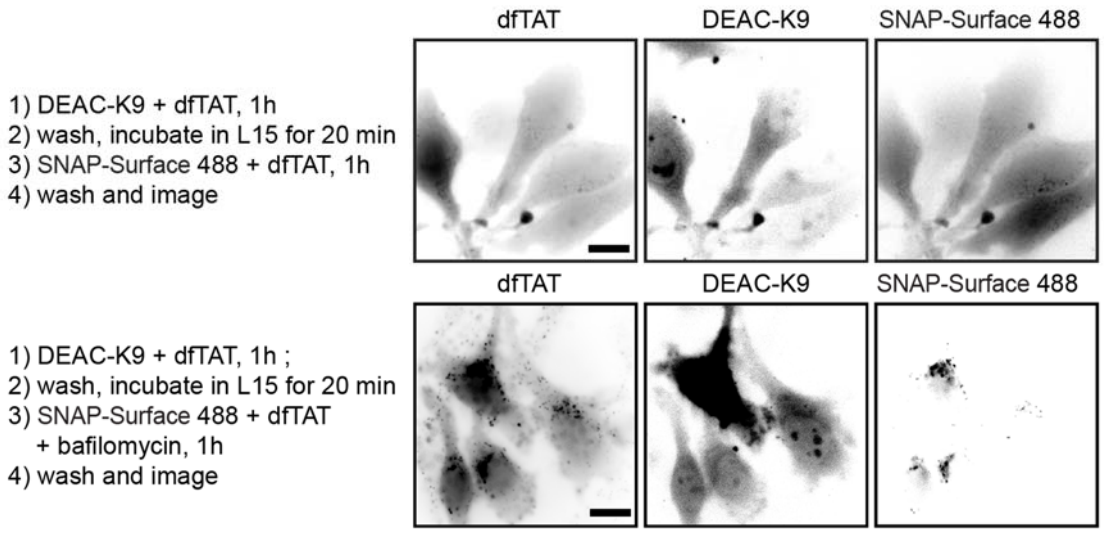


**Figure 3-26 dfTAT-mediated delivery does not significantly affect endocytosis.** Microscopy images showing that dfTAT-mediated endosomal escape can be repeated. HeLa cells were co-incubated with dfTAT (5 μM) and DEAC-K9 (5 μM) for 1 h (step1) (images not shown). After washing, dfTAT (5 μM) and SNAP-Surface 488 (5 μM) were co-incubated in the absence (top panel) or presence (bottom panel) of bafilomycin (200 nM) (step 3). Scale bars: 10 μm.

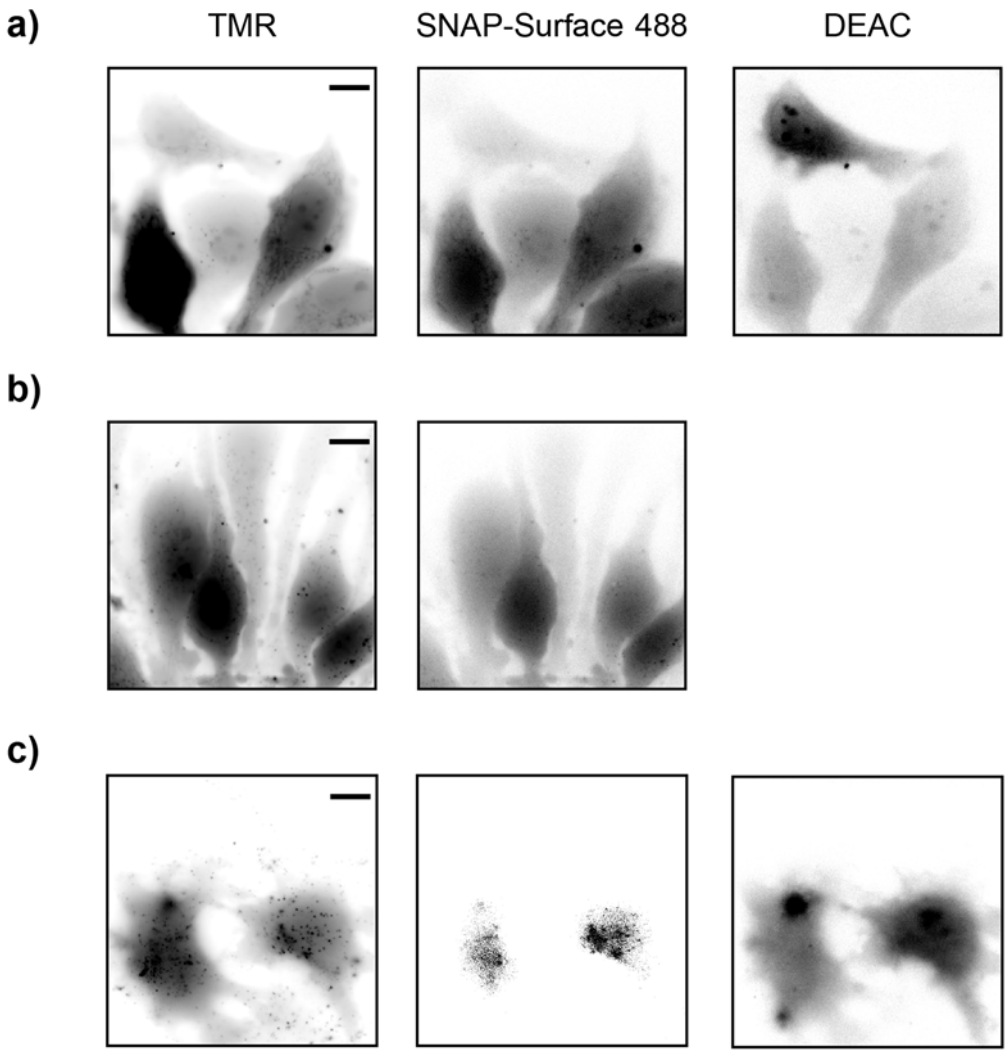


**Figure 3-27 Simultaneous delivery of SNAP-Surface 488 and DEAC inside cells using a one step protocol.** (a) HeLa cells were incubated with 5 µM dfTAT, 5 µM SNAP-Surface 488 and 5 µM DEAC-K9. Inverted monochrome images show cytosolic and nuclear fluorescence localization of dfTAT (red fluorescence), DEAC-K9 (blue fluorescence) and SNAP-Surface 488 (green fluorescence). Scale bars: 10 µm. (b) HeLa cells were incubated with 5 µM dfTAT and 5 µM SNAP-Surface 488. Inverted monochrome images show cytosolic and nuclear fluorescence localization of dfTAT and SNAP- Surface 488. Scale bars: 10 µm. (c) HeLa cells were first incubated with 5 µM dfTAT and 5 µM DEAC-K9 for 1 h. Cells were then washed, incubated with 5 µM SNAP-Surface 488 for 1 h and imaged. In one hand, inverted monochrome images show cytosolic and nuclear localization of TMR and DEAC but, in the other hand, SNAP-Surface 488 display a fluorescence punctate distribution. Scale bar: 10 µm.

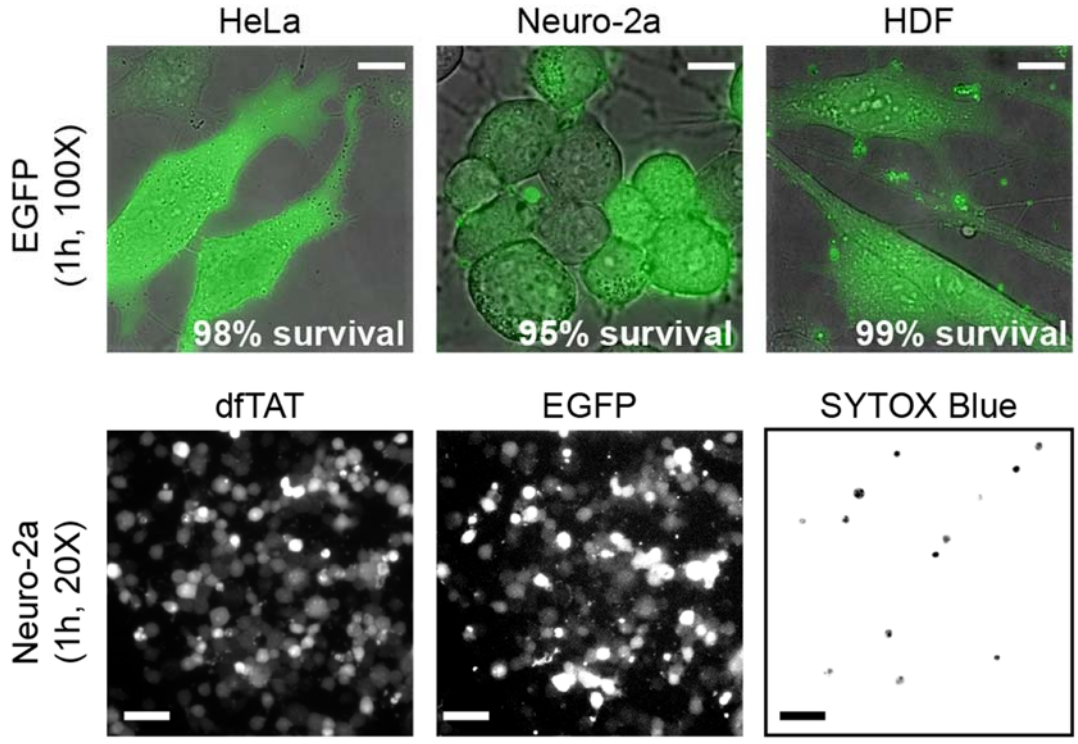


**Figure 3-28 Delivery of intact and functional EGFP using co-incubation with dfTAT.** Microscopy imaging showing that dfTAT delivers EGFP into the cytosol of live cells. HeLa, Neuro-2a and HDF cells were co-incubated with EGFP (10 μM) and dfTAT (5 μM) for 1 h. Scale bars: 100X objective, 10 μm; 20X objective, 100 μm.

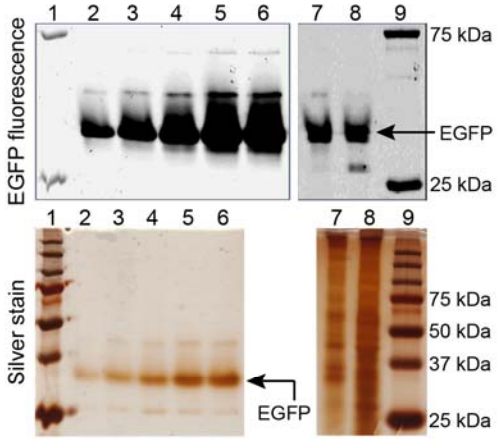


| lane | sample |
|---|---|
| 1 | protein ladder |
| 2 | 100 nM EGFP |
| 3 | 200 nM EGFP |
| 4 | 400 nM EGFP |
| 5 | 800 nM EGFP |
| 6 | 1000 nM EGFP |
| 7 | HDF cell lysate |
| 8 | Neuro-2a cell lysate |
| 9 | protein ladder |

| | EGFP in media (μM) | fluorescence intensity of EGFP band in gel from the cell lysate (a.u.) | amount of EGFP in the cell lysate (nM) | estimated average of EGFP concentration per cell (μM) |
|---|---|---|---|---|
| HDF | 10 | 12100 | 110.2 | 34.6 |
| Neuro-2a | 10 | 3900 | 49.6 | 23.3 |

numbers used for calculation: number of cells in sample (measured by flow cytometry) = 79,600
estimated volume of a cell = 2 $10^{-12}$ L (bionumbers.hms.harvard.edu)

**Figure 3-29 Quantitation of the concentration of EGFP delivered into the cytosol of HDF and Neuro-2a.** HDF and Neuro-2a cells were co-incubated with dfTAT (5 μM) and EGFP (10 μM) for 1 h. After 1 h, cells were washed with PBS/heparin and lysed. The cell lysate was treated with nucleases and an aliquot of 27 μL was analyzed by PAGE (top right panel). Similarly, samples of known EGFP concentrations (determined by measuring absorbance at 488 nm and using an extinction coefficient of 55,000 mol-1cm-1) were analyzed by PAGE (top left panel). A fluorescence imager was used to measure the EGFP fluorescence intensity from the cell lysates and EGFP calibration samples. Silver staining was used to detect all proteins in the lysate. A calibration curve of EGFP fluorescence intensity vs. EGFP concentration was established and used to estimate the average concentration of EGFP in the cell lysates. The data obtained was used to calculate the concentration of EGFP per cell. Important numbers: Cell number on well: 79,600 (determined by flow cytometry); Cell volume: 2000 μm3 (bionumbers.hms.harvard.edu.)

confirmed that a large fraction of EGFP escaped endosomes (**Figure 3-28**), one can expect micromolar concentrations of proteins to be delivered in the cytosolic space of cells. To determine whether dfTAT needs to interact with a particular protein in order to successfully deliver it, I characterized the binding of dfTAT to EGFP. No fluorescence resonance energy transfer (FRET) between dfTAT and EGFP could be detected under conditions used for cellular incubation assays (**Figure 3-30**). Similarly, no interaction between dfTAT and EGFP could be detected by native gel electrophoresis (**Figure 3-31**). In contrast, dfTAT and BSA were found to interact in this assay (presumably through electrostatic interactions). Interestingly, addition of BSA (or fetal bovine serum or heparin) to cell incubation medium reduced the cytosolic penetration of dfTAT in a concentration-dependent manner (**Figure 3-32**).

To further confirm that functional proteins can penetrate cells upon incubation with dfTAT, I tested delivery of Cre recombinase. In this assay, Cre induces recombination of a *loxP*-STOP-*loxP* sequence upstream of the EGFP-encoding gene of a reporter plasmid[156]. Therefore, cells transfected with the reporter plasmid express EGFP when Cre recombinase penetrates cells and excises the STOP signal sequence. Cells treated with TAT-Cre (1 μM) and dfTAT (5 μM) expressed EGFP (**Figure 3-33**), but the percentage of $EGFP^+$ cells was greater in the presence of dfTAT (47 %) than in the presence of fTAT or when TAT-Cre was incubated alone (<5 %).

I also delivered FITC–anti-ATP5A, a fluorescently-labeled antibody that recognizes the α-subunit of the mitochondrial ATP synthase. Cells treated with FITC–anti-ATP5A (20 μg/ml) and dfTAT (5 μM) contained green fluorescent tubular

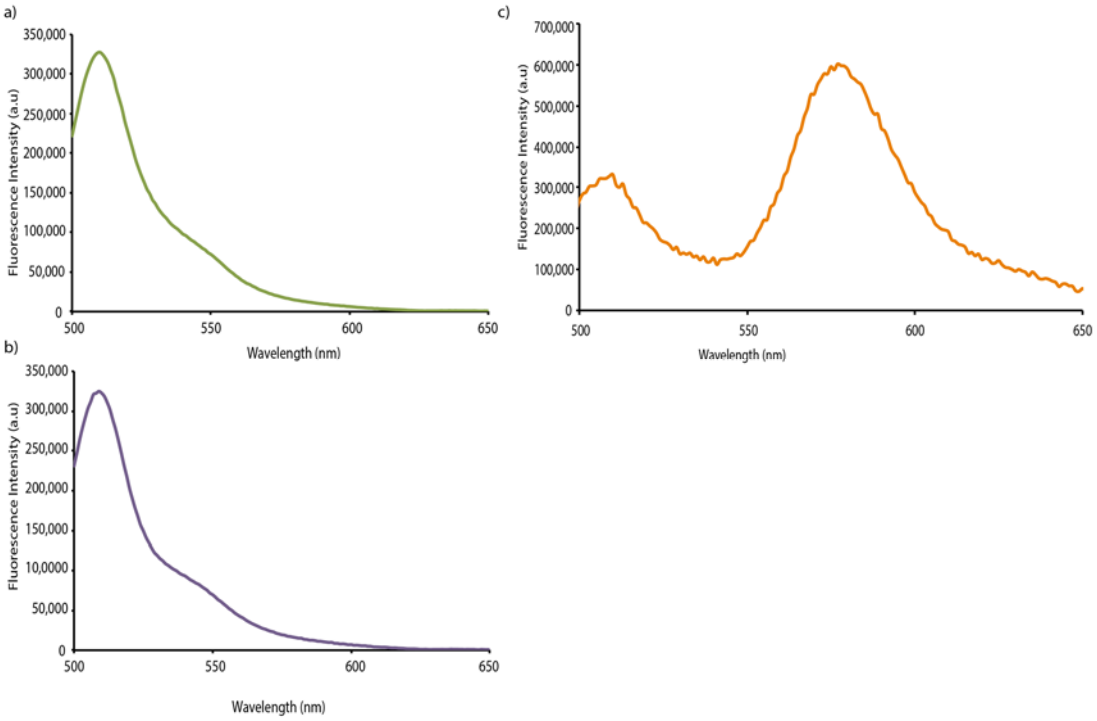


**Figure 3-30 dfTAT and EGFP do not interact when co-incubated.** (a) Fluorescence emission spectrum of EGFP (1 μM) (donor FRET pair) (EGFP, Ex/Em 488/508 nm) excited at 488 nm. The spectrum show an intense emission peak at around 510 nm and a small shoulder peak around 548 nm (b) Fluorescence emission spectrum of a solution of EGFP (1 μM) and dfTAT (5 μM) (acceptor FRET pair) (TMR, Ex/Em 556/580 nm) excited at 488 nm. The spectrum shows an intense emission peak at around 510 nm and a small shoulder peak around 548 nm. The contribution of TMR to the EGFP fluorescence spectrum (crossover fluorescence) was determined by measuring the fluorescence emission of a solution of dfTAT (5 μM) excited at 488 nm (not shown). The spectrum of the solution with EGFP and dfTAT is almost identical to the spectrum of EGFP alone (TMR fluorescence crossover signal was subtracted). (c) Fluorescence emission spectrum of ligated EGFP-CK(TMR). Using expressed protein ligation, EGFP was chemically ligated to CK(TMR) as described to produce EGFP-CK(TMR)7. EGFP-CK(TMR) was used a positive control for the FRET signal. Upon excitation at 488 nm, a dramatic increase in fluorescence between 560-630nm is observed (fluorescence max approximately 580 nm), indicative of a FRET signal due the close proximity between fluorophores. This increase in fluorescence intensity was not observed in the spectrum in part b) (indicative of no interactions between EGFP and dfTAT). Emission of all samples was scanned from 500 to 650 nm.

**Figure 3-31 dfTAT and EGFP do not interact.** (a) Native gel electrophoresis was used to determine binding interaction between dfTAT and EGFP. Samples were prepared by incubating dfTAT (5 μM) with either EGFP (10 μM) or BSA (10 μM, protein with a pI = 4.7, used as a positive control) in nrL-15 for 30 min at 37 °C (pH 7.0, representing the pH of the extracellular milieu of the cell and pH 5.0 representing the lower pH that exists along the endocytic pathway). dfTAT alone, EGFP alone and BSA alone at the same concentration and pH were loaded on the same gel as controls. Fluorescence images of the gel were acquired using a Typhoon scanner. Green fluorescent bands corresponding to EGFP and a red fluorescence band correspond to dfTAT fluorescence. Red fluorescent bands corresponding to both dfTAT and BSA indicated binding between peptide and protein. In contrast, dfTAT fluorescence is not detected in bands corresponding to EGFP, indicating absence of binding. An image of the Commassie stained native gel is also shown (top left corner). (b) Coomassie staining, red fluorescence, and green fluorescence images of samples of dfTAT and EGFP at varying concentration and analyzed by native gel electrophoresis. Similar results were obtained with dmEGFP (EGFP not containing cysteine residues, data not shown).

a)

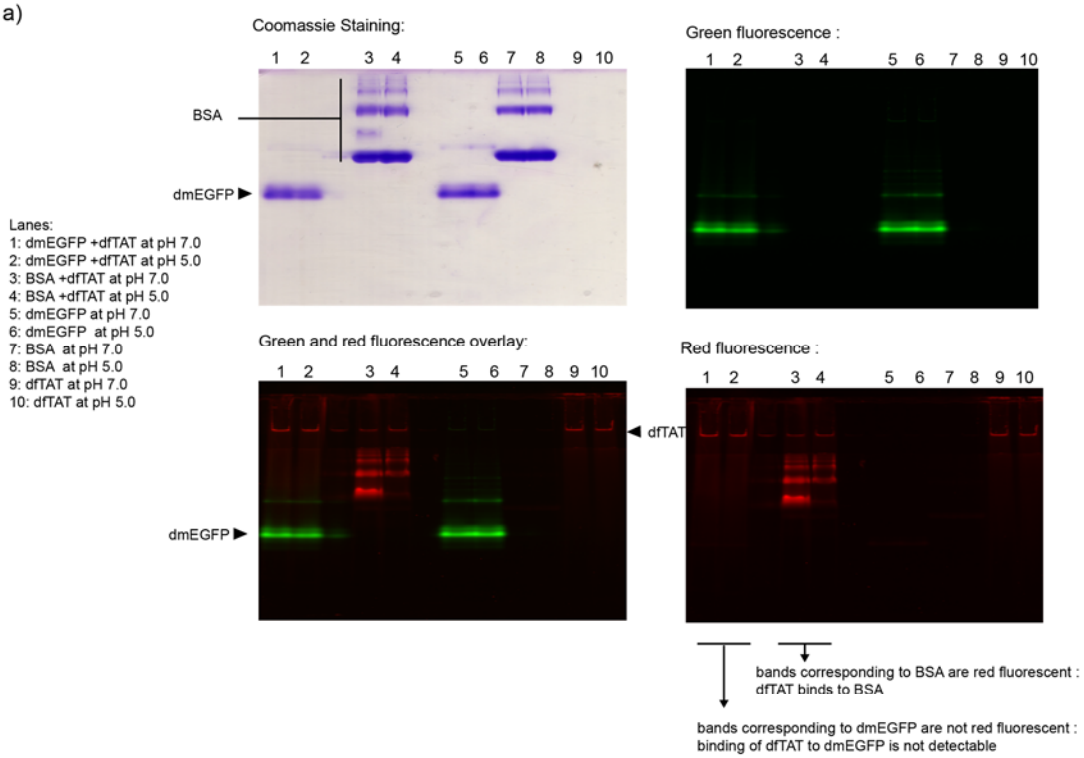


Lanes:
1: dmEGFP +dfTAT at pH 7.0
2: dmEGFP +dfTAT at pH 5.0
3: BSA +dfTAT at pH 7.0
4: BSA +dfTAT at pH 5.0
5: dmEGFP at pH 7.0
6: dmEGFP at pH 5.0
7: BSA at pH 7.0
8: BSA at pH 5.0
9: dfTAT at pH 7.0
10: dfTAT at pH 5.0

b)

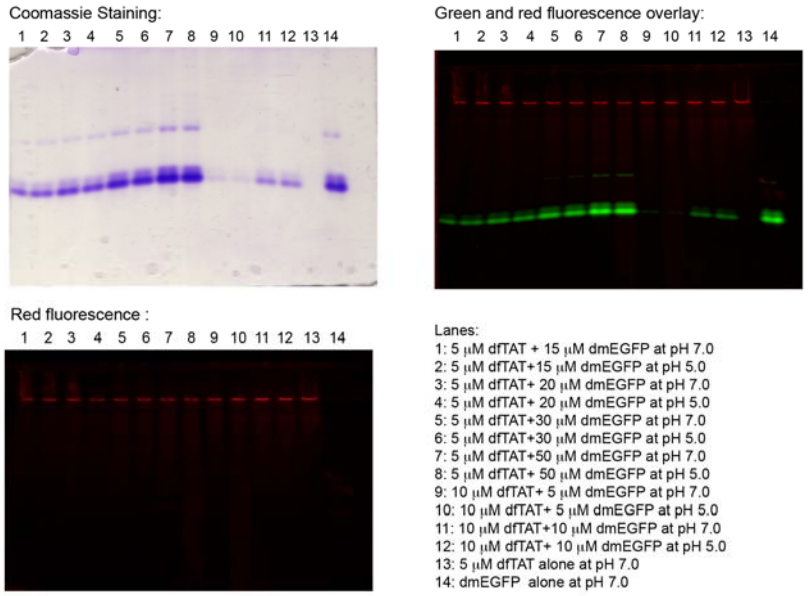


Lanes:
1: 5 μM dfTAT + 15 μM dmEGFP at pH 7.0
2: 5 μM dfTAT+15 μM dmEGFP at pH 5.0
3: 5 μM dfTAT+ 20 μM dmEGFP at pH 7.0
4: 5 μM dfTAT+ 20 μM dmEGFP at pH 5.0
5: 5 μM dfTAT+30 μM dmEGFP at pH 7.0
6: 5 μM dfTAT+30 μM dmEGFP at pH 5.0
7: 5 μM dfTAT+50 μM dmEGFP at pH 7.0
8: 5 μM dfTAT+ 50 μM dmEGFP at pH 5.0
9: 10 μM dfTAT+ 5 μM dmEGFP at pH 7.0
10: 10 μM dfTAT+ 5 μM dmEGFP at pH 5.0
11: 10 μM dfTAT+10 μM dmEGFP at pH 7.0
12: 10 μM dfTAT+ 10 μM dmEGFP at pH 5.0
13: 5 μM dfTAT alone at pH 7.0
14: dmEGFP alone at pH 7.0

**Figure 3-32 Effect of BSA, heparin and FBS on dfTAT cell penetration** (a) Co-incubation of dfTAT with BSA results in a decrease in the percentage of cells displaying cytosolic release of dfTAT. HeLa cells were co-incubated with 5 μM dfTAT and 10 μM BSA for 1h. Cells show a punctate distribution of the peptide (monochrome 100X image) indicative of peptide being trapped in endocytic vesicles. In comparison, HeLa cells incubated with dfTAT (5 μM) alone show a homogenous cytosolic and nuclear distribution of peptide in a majority of cells. (b) Effect of FBS and heparin on dfTAT mediated cellular. HeLa cells were incubated with 5 μM dfTAT and heparin (1-100 μg/mL) or FBS (0.1-10%) for 1 h. Cells were washed and imaged. The % cells with cytosolic and nuclear distribution was calculated as described in Figure 1(b). Scale bars: 10 μm.

a)

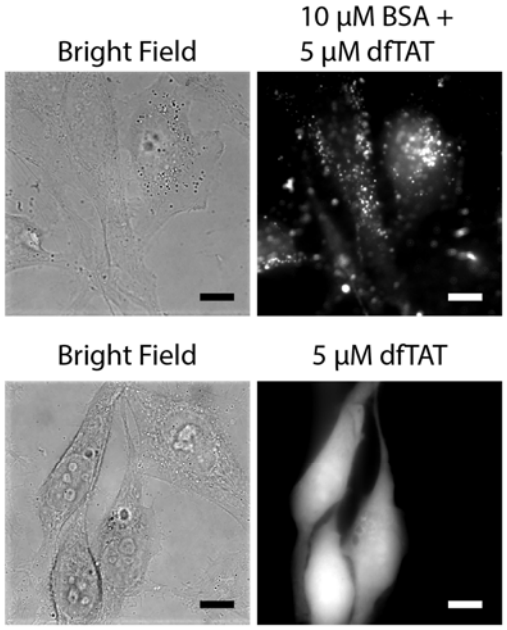
Bright Field
10 μM BSA +
5 μM dfTAT
Bright Field
5 μM dfTAT

b)

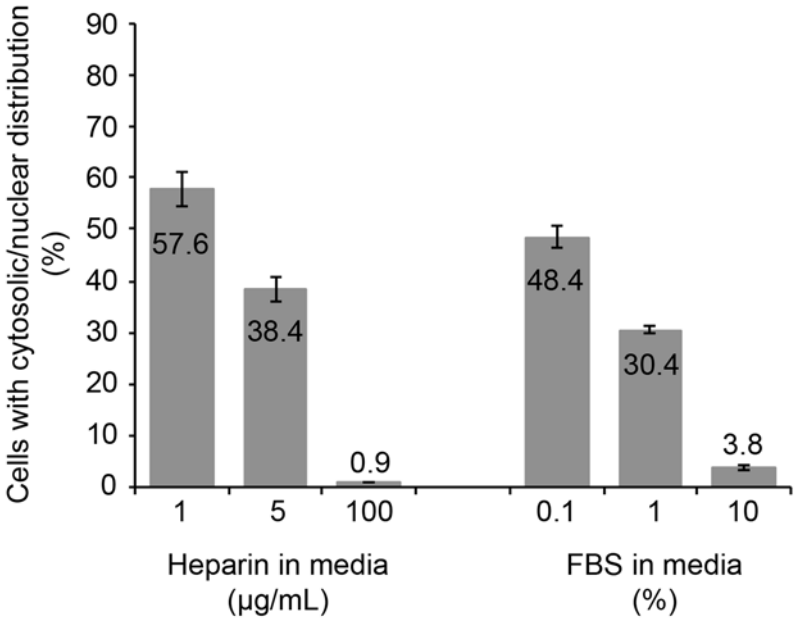
Cells with cytosolic/nuclear distribution (%)
90
80
70
60
50
40
30
20
10
0
57.6
38.4
0.9
48.4
30.4
3.8
1
5
100
0.1
1
10
Heparin in media (μg/mL)
FBS in media (%)

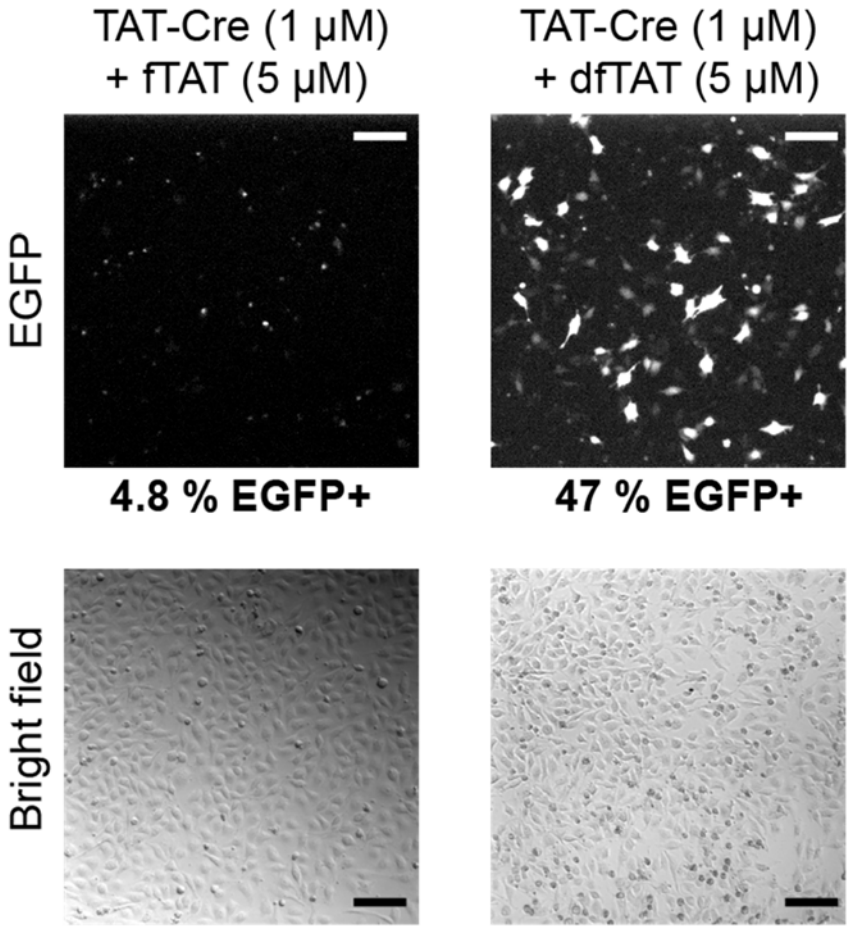


**Figure 3-33 Delivery of intact and functional Cre-recombinase using co-incubation with dfTAT.** Assay showing that dfTAT improves the delivery of TAT-Cre. HeLa cells transfected with a plasmid containing egfp upstream of a loxP-STOP-loxP sequence were incubated for 1 h with either fTAT (5 μM) or dfTAT (5 μM) in the presence of TAT-Cre (1 μM). $EGFP^+$ cells that result from successful TAT-Cre delivery were visualized and counted by microscopy (confirmed by flow cytometry). Scale bars: 100 μm.

structures (**Figure 3-34**). Colocalization with the blue fluorescent mitochondrial marker pTagCFP-mito confirmed that these structures were mitochondria (**Figure 3-35 (A)**). Cells treated with FITC–anti-IgG, an antibody that does not target mitochondria, did not stain tubular structures (**Figure 3-35 (B)**). These experiments confirmed that dfTAT can deliver a functional antibody into live cells.

The transcription factor HOXB4 can penetrate cells, activate transcription and induce hematopoietic stem cell expansion, either by itself or when fused to $TAT^{242-244}$. I was therefore interested in determining whether dfTAT, by promoting cytosolic delivery, would enhance the transcriptional activity of this protein. NIH 3T3 cells were transfected with a vector containing the luciferase gene under a HOXB4-inducible promoter and with a β-galactosidase reporter as internal control. Cells were incubated with HOXB4 or TAT-HOXB4, in the absence or presence of dfTAT, for 1.5 h. I assessed the expression of luciferase by measuring the luminescence of cell lysates (normalized to β-galactosidase activity, luciferase induction represents a ratio of treated versus untreated cells). HOXB4 and TAT-HOXB4 (200 nM) alone induced a 2.2- and 5.0-fold increase in luciferase activity, respectively (**Figure 3-36**). In contrast, addition of dfTAT (3 μM) led to 53.1- and 307.4-fold luciferase induction, respectively. Neither dfTAT alone nor dfTAT incubated with TAT-mCherry led to the induction of luciferase, indicating that luciferase expression was dependent on the presence of HOXB4.

Although increasing the transcriptional output of HOXB4 is valuable, precisely controlling the level and activity of HOXB4 inside cells is important to achieve desirable biological outcomes[245]. Because dfTAT appears to act independently of the molecules

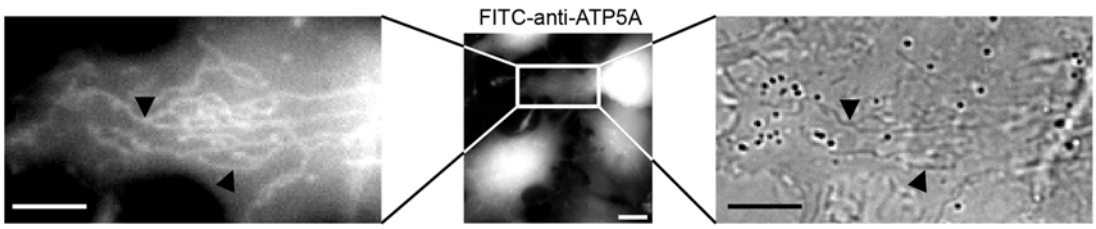


**Figure 3-34 Delivery of an intact and functional antibody using co-incubation with dfTAT.** Microscopy imaging showing that dfTAT mediates the delivery of an antibody. HeLa cells were co-incubated with FITC-anti-ATP5A (20 μg/mL) and dfTAT (5 μM) for 1 h. FITC-anti-ATP5A (green) is delivered in the cytosol of cells and stains tubular mitochondria (more clearly visible in zoomed-in image). Absence of SYTOX® Blue staining indicates that the cells imaged do not have a compromised plasma membrane. Black arrows point to tubular mitochondria. Scale bars: 100X objective, 10 μm; zoomed-in image, 2 μm.

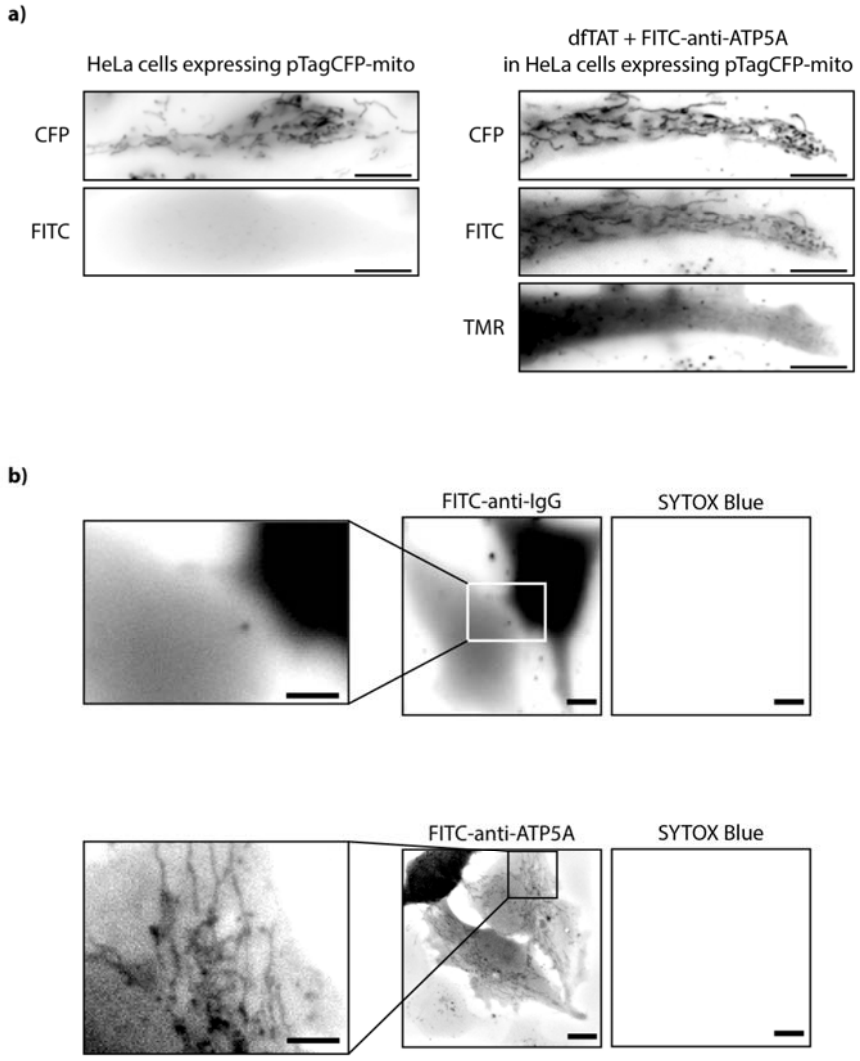


**Figure 3-35 The FITC-anti-ATP5a antibody co-localizes with a fluorescently labeled mitochondrial protein expressed in live cells after dfTAT-mediated delivery.** (a) Cells expressing TagCFP-mito (left) were imaged using the FITC and CFP filters. Tubular mitochondria were clearly observed only in the CFP channel. In a separate experiment, dfTAT (5 μM) and FITC-anti-ATP5A (20 μg/mL) were incubated for 1 h with cells expressing TagCFP-mito. The inverted monochrome images show co-localization of FITC-anti-ATP5A (FITC channel) and TagCFP-mito (CFP channel). Scale bars: 2 μm. (b) To confirm that the mitochondrial staining is specific to FITC-anti-ATP5A, an antibody without an intracellular epitope, FITC-anti-IgG, was delivered with dfTAT. FITC-anti-IgG (20 μg/mL) and dfTAT (5 μM) were incubated with cells for 1 h. Inverted monochrome images show a homogenous cytosolic fluorescence distribution (top). In contrast, cells that were incubated with FITC-anti-ATP5A show fluorescence in tubular structures (bottom). Scale bars: zoom-in image, 2 μm; 100X objective, 10 μm.

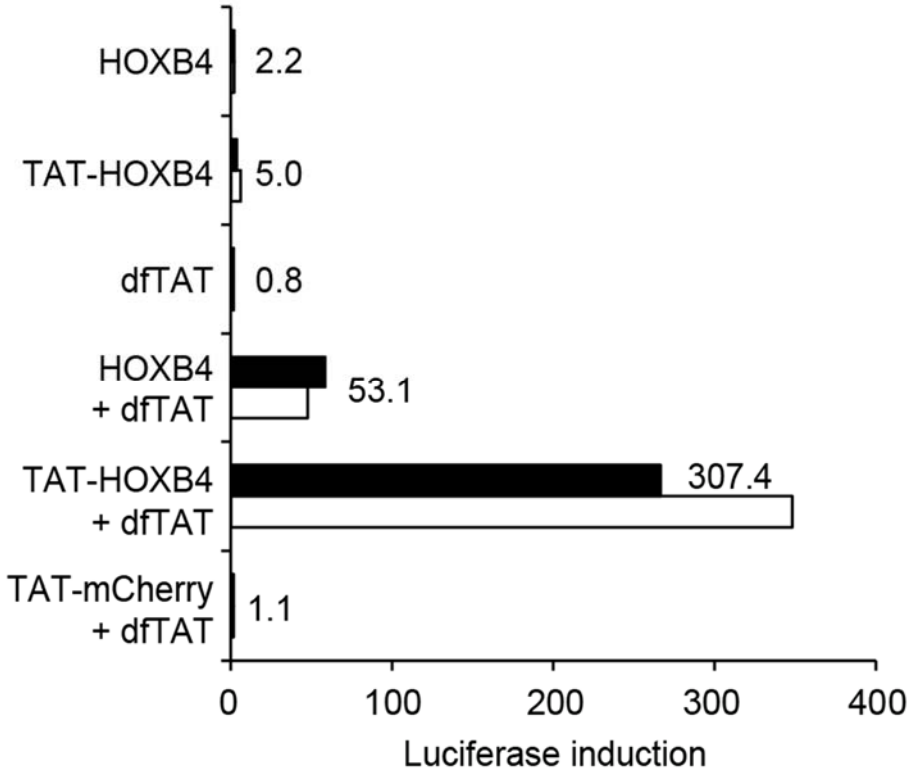


**Figure 3-36 dfTAT mediated delivery of HoxB4 and TAT-HoxB4 improves the expression of a luciferase reporter.** NIH 3T3 transfected with a HoxB4-dependent luciferase reporter were incubated for 1.5 h with either HoxB4 or TAT-HoxB4 (200 nM) in presence or absence of dfTAT (3 μM). TAT-mCherry (200 nM) and dfTAT (3 μM) serve as negative controls (400,000 cells/experiment, experiments in duplicate).

used for co-incubation in my assays, I hypothesized that it might be possible to titrate the amount of protein that penetrates cells by varying the protein concentration in the medium while keeping dfTAT concentration constant. Under this scenario, the efficiency of endosomal escape should remain unaffected, but the amount of material released from endosomes should change. Initial experiments with DEAC-K9 showed that the amount of fluorescent peptide delivered inside cells could be titrated using this protocol (**Figure 3-37 and 3-38**). Consistent with these results, luciferase induction was proportional to the concentration of HOXB4 in the medium (**Figure 3-39**).

### 3.3 Discussion

By mediating endosomal leakage, dfTAT is remarkably efficient at delivering proteins and peptides into the cytosol of cells. Delivery is efficient because the amount of material that reaches the cytosol is substantial and the amount trapped inside endosomes is relatively low, and because cytosolic delivery occurs in most cells present in a sample. Endosomal escape appears to take place in most cells once dfTAT, which is intrinsically more endosomolytic than monomeric TAT, reaches a threshold concentration within endosomes. Future studies aimed at establishing the roles played by the two copies of the peptide TAT and of the fluorophore TMR, as well as their respective arrangement, should provide more molecular details about the activity of dfTAT. Establishing where dfTAT escapes from the endocytic pathway should also provide valuable insights regarding its endosomolytic activity, which will be the focus of my next chapter. Notably, the membrane of endosomes can be lysed by fluorescently

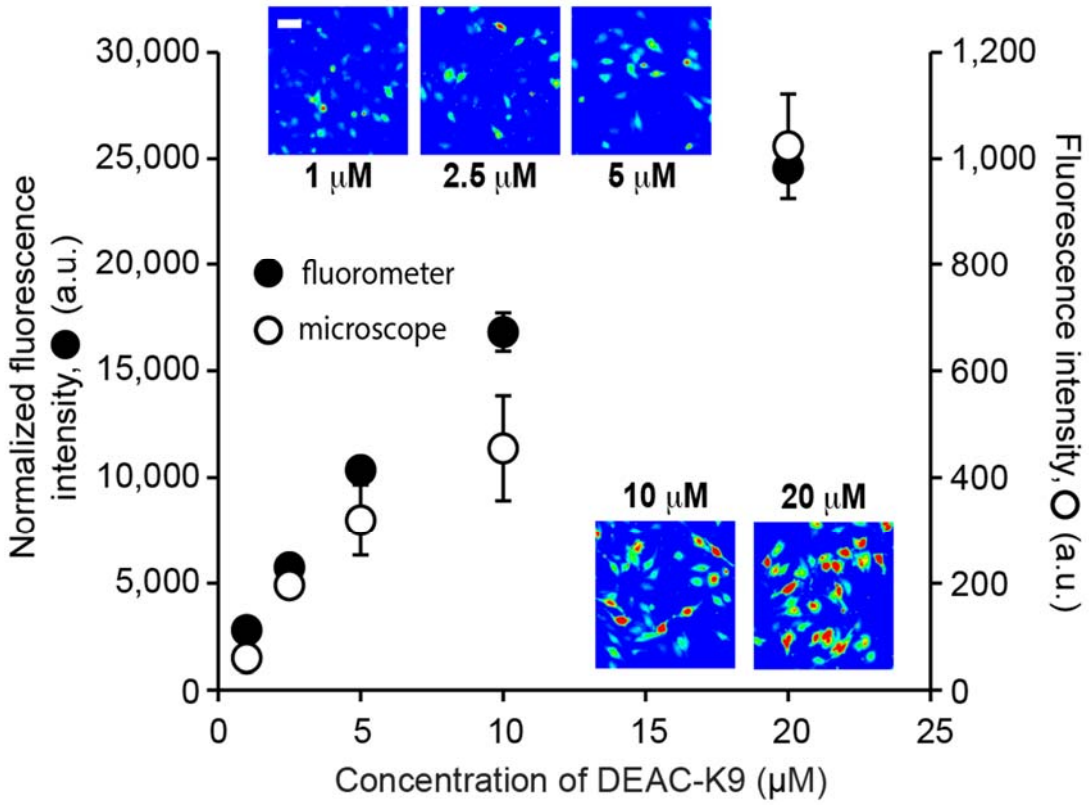


**Figure 3-37 The amount of DEAC-K9 delivered in the cytosol and nucleus of live cells can be titrated.** HeLa cells were incubated with dfTAT (5 μM) and increasing amounts of DEAC-K9 (1, 2.5, 5, 10, 20 μM). The fluorescence intensity of cells displaying cytosolic release was assessed by microscopy (representative 20X images are shown using a pseudocolored colorscale: blue=lowest intensity, red=highest intensity) and by measuring to the bulk fluorescence of cell lysates (microscope: 1,000 cells/experiment, fluorometer: 300,000 cells/experiment; experiments in triplicates, average and standard deviations represented). Scale bars: 10 μm

a)

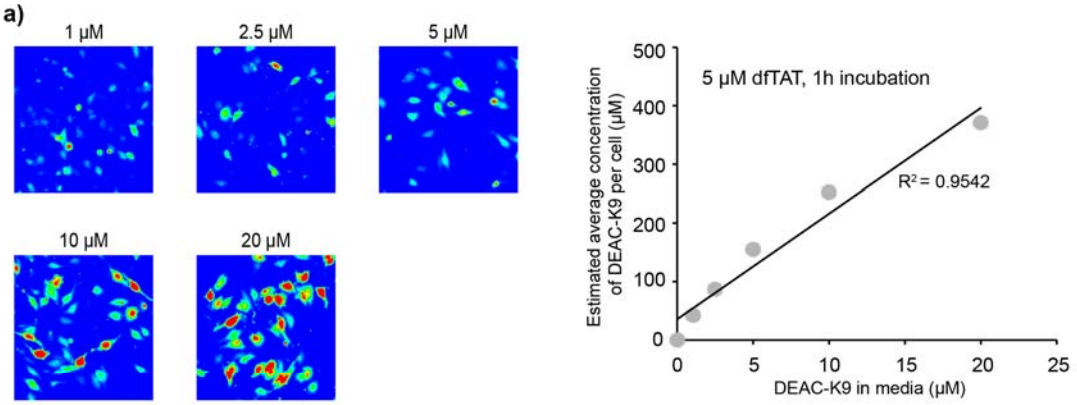


b)

| peptide in media (µM) | fluorescence intensity of cell lysate (a.u.) | DEAC-K9 concentration in the cell lysate (nM) | estimated average concentration of DEAC-K9 per cell (µM) |
|---|---|---|---|
| 1 | 2793.4 | 67.1 | 42.1 |
| 2.5 | 5745.9 | 138.0 | 86.6 |
| 5 | 10352.8 | 248.6 | 156.0 |
| 10 | 16817.2 | 403.9 | 253.4 |
| 20 | 24544.1 | 589.5 | 369.9 |

**Figure 3-38 Determination of the amount of DEAC-K9 delivered into cells.** HeLa cells were incubated with dfTAT (5 µM) and different concentrations of DEAC-K9 (1, 2.5, 5,10 and 20 µM) for 1 h. Cells were washed with PBS/heparin, imaged and lysed. The bulk fluorescence of cell lysates containing DEAC-K9 was measured using a fluorometer. Similarly, the fluorescence of solutions of DEAC-K9 at different concentrations (0.01. 0.1, 1, 10 and 100 µM) was measured using a fluorometer. A calibration curve of DEAC-K9 intensity vs. DEAC-K9 concentration was established. These data was used to estimate the average concentration of DEAC-K9 inside cells. Data shows a linear increase in the amount of DEAC-K9 delivered inside cells (top right panel). Consistent with these data, fluorescence images that show an increase in the fluorescence signal in the cytosol cells with increasing concentrations o DEAC-K9 incubated in the media (top left panel, and Figure 3-37).

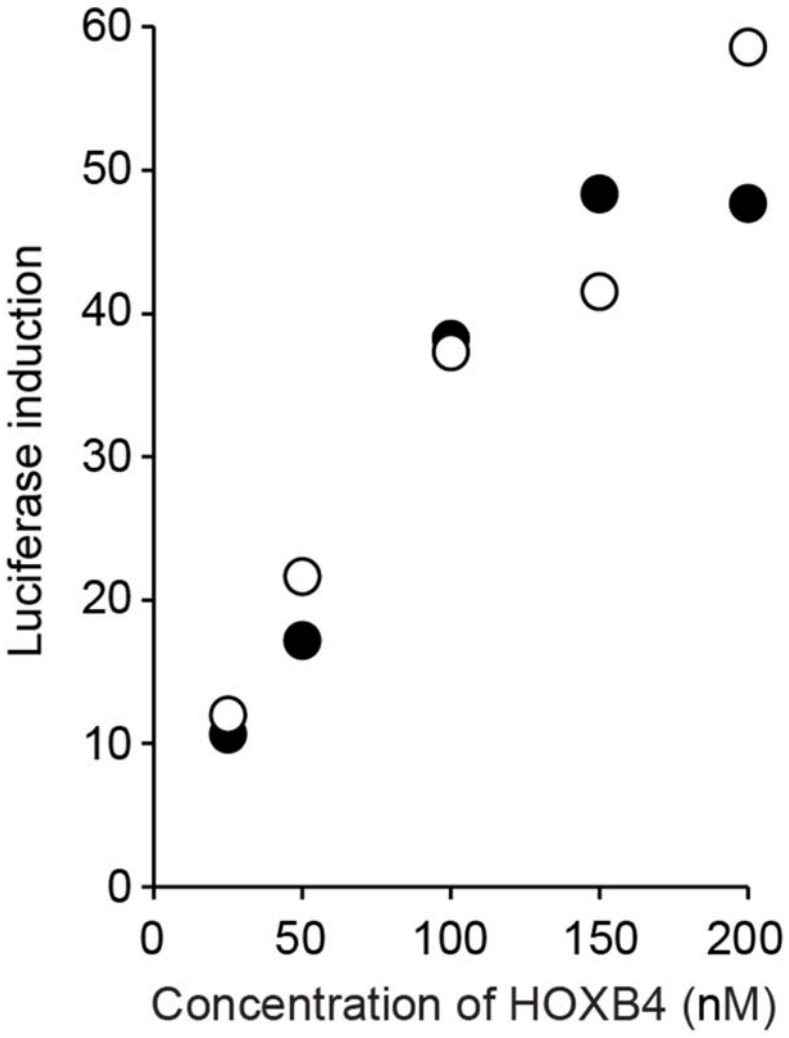


**Figure 3-39 The induction of luciferase expression by dfTAT-medited delivery of HoxB4 into cells can be controlled.** NIH 3T3 cells were co-incubated with HoxB4 (25-200 nM) and dfTAT (3 μM) and luciferase induction was measured as described in a (400,000 cells/experiment, experiments in duplicate).

labeled cell-penetrating peptides upon light irradiation[175, 246]. dfTAT trapped inside endosomes (for example, after incubation at 2 μM) can indeed leak out of endosomes when TMR is continuously excited for several seconds (data not shown). Yet, all delivery experiments reported herein were performed in a dark room with a dim red light. The excitation of dfTAT, when required for fluorescence microscopy, was also minimized to less than 300 ms in all images shown. Overall, I conclude that the endosomal leakage mediated by dfTAT is light independent.

A remarkable aspect of dfTAT-mediated delivery is the minimal cellular responses associated with the efficient endosomal leakage observed. This is surprising because endosomal lysis can be extremely toxic by causing the rapid release of calcium into the cytosol of cells[178]. In addition, the leakage of endolysosomal proteases could contribute to toxicity[247-250]. Yet, I observed that cells were not only viable but also healthy. These results are presumably valid for only the one hour dfTAT incubation used in my assays. Continuous endosomal leakage induced by particulate wear debris induces inflammatory responses and apoptosis[251]. dfTAT could therefore promote similar effects if administered to cells for long incubation times. Notably, membrane repair mechanisms have also been shown to mask the effect of debris-induced endosomal leakage[251]. This, in turn, could also explain why dfTAT-mediated delivery is relatively innocuous under the conditions tested.

dfTAT delivers cell-impermeable molecules displaying diverse structures and properties. DEAC-K9, like dfTAT, is highly positively charged, and the isoelectric points (pI) of Cre (9.4), and HOXB4 (9.8) are also not suggestive of favorable electrostatic interactions with dfTAT. EGFP, a protein with a lower pI (6.2), does not appreciably

interact with dfTAT *in vitro*. It is therefore likely that dfTAT does not need to interact with a given protein outside the cell or within the lumen of endosomes to achieve cytosolic delivery of that protein. Instead, interactions that occur between dfTAT and a protein with low pI such as BSA are inhibitory. Similar inhibitory effects between arginine-rich cell-penetrating peptides and negatively charged species have been observed[203, 252].

The co-incubation protocol used herein allows several cargos to be delivered simultaneously. Alternatively, delivery can be performed in successive steps, without complex sample preparations and, as exemplified by the delivery of SNAP-Surface 488 or FITC–anti-ATP5A, is ideally suited for imaging applications. In addition, co-incubation provides the opportunity to titrate the extracellular concentration of target molecules independently of dfTAT. The amount of protein delivered to the cytosol and the biological output achieved can in turn be modulated. Although my approach is likely not optimal for *in vivo* delivery of biologics, it could offer several advantages over existing reagents for delivery to tissue cultures and the *ex vivo* manipulation of cells.

## 3.4 Materials and methods

### 3.4.1 Peptide design, synthesis and purification

All peptides were synthesized in-house on the rink amide MBHA resin (Novabiochem) by solid-phase peptide synthesis (SPPS) using standard Fmoc protocols. Fmoc-Lys(Mtt)-OH, Fmoc-Lys(Boc)-OH, Fmoc-Gly-OH, Fmoc-Arg(Pbf)-OH, Fmoc-Gln(Trt)-OH and Fmoc-Cys(Trt)-OH (Novabiochem) were used to assemble the peptides. Reactions were carried out in a SPPS vessel at room temperature using a stream of dry

$N_2$ to provide agitation. Fmoc deprotection was performed by addition of piperidine in dimethylformamide (DMF) (Fisher) (20 %, 10 mL) to the Fmoc-peptide resin (0.30 mmol). Deprotection reactions were carried out once for 5 min (1 × 5 min) and 1 × 15 min with a washing step in between reactions. Amino acid coupling reactions were carried out for 4 h with a mixture of Fmoc-amino acid (1.2 mmol), HBTU (Novabiochem) (0.44 g, 1.1 mmol) and di-isopropylethylamine (DIEA) (Sigma) (0.51 mL, 3.0 mmol) in DMF. Upon completion of the reactions, the resin was washed with DMF and dichloromethane (DCM) (Fisher). For DEAC-K9, the DEAC fluorophore (AnaSpec) was coupled to the N terminus of the peptide after coupling of the ninth Fmoc-Lys(Boc)-OH using a mixture of DEAC, HBTU and DIEA (4, 3.9 and 10 molar equivalents (eq) with respect to the peptide) in DMF. The reaction was carried out overnight using a stream of dry $N_2$ to provide agitation. For CK(ε-NH-TMR)TATG (fTAT), the Mtt protecting group at the ε-amino group of Lys on CK(ε-NH-Mtt)TATG was cleaved with 2 % trifluoroacetic acid (TFA) (Fisher) and 2 % tri-isopropylsilane (TIS) (Sigma) in DCM, and the resin was washed with DCM and DMF. A mixture of TMR, HBTU and DIEA (4, 3.9 and 10 eq with respect to the peptide) in DMF was added to the resin, and the reaction was carried out overnight using dry $N_2$ to provide agitation. Following Fmoc-deprotection and peptide assembly, the resin was washed with DCM and dried *in vacuo*. The resin was then treated with TFA containing 2.5 % $H_2O$, 2.5 % TIS and 2.5 % ethanedithiol (EDT) (Sigma) for 3 h at room temperature to achieve global deprotection and cleavage from the resin. The crude peptide products were precipitated and washed with cold anhydrous $Et_2O$ (Fisher). The precipitates were resuspended in water and lyophilized. The products obtained were then

resuspended in 0.1 % aqueous TFA/acetonitrile. The peptides were analyzed and purified by reverse-phase HPLC. HPLC analysis was performed on a Hewlett-Packard 1200 series instrument and an analytical Vydac C18 column (5-μm particle size, 4 mm × 150 mm). The flow rate was 1 mL/min, and detection was at 214 nm and 550 nm. Semi-preparative HPLC was performed on a Vydac C18 10 × 250–mm column. The flow rate was 4 mL/min, and detection was at 214 nm and 550 nm. All runs used linear gradients of 0.1% aqueous TFA (solvent A) and 90% acetonitrile, 9.9 % water and 0.1% TFA (solvent B). The correct identity of the peptides was confirmed by MALDI-TOF performed with a Shimadzu/Kratos instrument (AXIMA-CFR). fTAT expected mass was 2,041.17; observed mass was 2,040.66. DEAC-K9 expected mass, 1,412.97; observed mass, 1,415.59.

### 3.4.2 Synthesis of acetamidated C(S-$CH_2CONH_2$)K(ε-NH-TMR)TATG (acfTAT)

C(S-$CH_2CONH_2$)K(ε-NH-TMR)TATG was formed after addition of iodoacetamide (Sigma) (0.275 mg, 1.49 μmol) to CK(ε-NH-TMR)TATG (148 μg, 0.074 μmol) in 25 mM HEPES, pH 7.5, under an atmosphere of $N_2$. The product was purified using analytical reverse-phase HPLC. Expected mass (MALDI-TOF), 2,098.19; observed mass, 2,096.31.

### 3.4.3 Generation of dfTAT by dimerization of CK(TMR)TATG (fTAT)

dfTAT was formed by dissolving (0.3 mg, $1.5 \times 10^{-4}$ mmol) fTAT in aerated phosphate buffer saline (PBS), pH 7.4 (5 mL). Oxygen dissolved in the buffer acted to

oxidize the thiol groups on the peptides and form a disulfide bond. The reaction was allowed to react overnight until completion (100 % yield according to HPLC analysis). The product was purified using analytical reverse-phase HPLC. Expected mass (MALDI-TOF), 4,080.34; observed mass, 4,084.21.

### 3.4.4 Generation of nrdfTAT using fTAT

Two fTAT peptides linked by the bis(maleimido)ethane (BMOE) (Pierce) linker (nrdfTAT) was formed by reacting pure fTAT (0.202 mg, 0.099 μmol) with BMOE (0.011 mg, 0.0496 μmol) for 3 h in PBS buffer, pH 7.2, under an atmosphere of $N_2$. The product was purified using analytical reverse-phase HPLC. Expected mass (MALDI-TOF), 4,313.39; observed mass, 4,303.

### 3.4.5 Cloning, overexpression and purification of TAT-Cre, TAT-mCherry, HOXB4 and TAT-HOXB4

The pTriEx-HTNC plasmid encoding His-tagged TAT-NLS-Cre (TAT-Cre) protein was purchased from Addgene. The TAT-Cre gene was then cloned into pTXB1 vector and transformed into *Escherichia coli* BL21 (DE3) cells (Agilent Technologies). The protein was expressed and purified as described[253]. Briefly, TAT-Cre was expressed with 1 mM IPTG at 37 °C for 3 h. TAT-Cre was then purified to homogeneity using a Ni-NTA resin (Qiagen) and cation-exchange chromatography (HiTrap SP HP) (GE Healthcare).

pTXB1-TAT-mCherry was obtained by inserting the TAT DNA sequence into the pTXB1-mCherry plasmid. The oligonucleotides with sequences 5′-TAT GGG TCG TAA AAA ACG TCG TCA GCG TCG TCG TGG TCA-3′ and 3′-ACC CAG CAT TTT TTG CAG CAG TCG CAG CAG CAC CAG TAT-5′ (Integrated DNA Technologies) coding for the TAT sequence, which contain NdeI sites, were annealed to generate dsDNA. The pTXB1-mCherry plasmid was cut with NdeI (New England Biolabs) and ligated with TAT dsDNA. The pTXB1-TAT-mCherry plasmid was transformed into BL21 (DE3) cells, and protein expression was induced with 1 mM IPTG at 16 °C for 24 h. Cells were harvested and resuspended in lysis buffer containing 20 mM Tris-Cl (pH 7.5) and 200 mM NaCl. After cell lysis by sonication and high-speed centrifugation at 15,000 r.p.m. (rotor radius: 23 cm) for 1 h, the soluble fraction was applied to chitin resin (New England Biolabs) pre-equilibrated with lysis buffer and incubated overnight at 4 °C (the protein contains a C-terminal intein-chitin binding domain purification tag). The resin was washed with ten column volumes of lysis buffer. The protein was cleaved from the resin by incubating the beads with 1 column volume of cleavage buffer supplemented with 100 mM 2-mercaptoethanesulfonic acid and for 24 h at 4 °C. The protein was further purified using cation-exchange chromatography.

EGFP was cloned, expressed and purified as previously described[254]. The double-mutant EGFP (dmEGFP) was obtained by introducing the mutations (C49S, C71V) in the EGFP plasmid using site-directed mutagenesis. Because dmEGFP does not contain any Cys residue, this protein is unable to form a disulfide bond with fTAT. In all assays, results

obtained with EGFP were similar to those obtained with dmEGFP. In the text, both EGFP and dmEGFP are therefore referred to as EGFP for simplicity.

The pTAT-HA-HOXB4 vector was generously provided by G. Sauvageau (Montreal University). $His_6$-HOXB4 was produced by cloning the *HOXB4* gene into pET-28a. Briefly, the *HOXB4* cDNA was first amplified from pTAT-HA-HOXB4 by using primers designed to introduce the NdeI and XhoI sites at the 5′ and 3′ ends, respectively (5′-GGC ATT CAT ATG GCT ATG AGT TCT TTT TTG ATC AAC TCA- 3′; 5′-GGT CAG TCT CGA GCT AGA GCG CGC GGG G-3′) (IDT). The PCR fragment was then inserted into the corresponding NdeI and XhoI sites of the 6xHis-tag vector, pET-28a. The fidelity of the reading frame was confirmed by sequencing. The procedure for the purification of both TAT-HOXB4 and HOXB4 is similar and has been previously described[244]. Briefly, BL21 (DE3) cells were transformed with either pTAT-HA-HOXB4 or pET28a-HOXB4 and induced at 37 °C for 5 h with 1 mM IPTG. The pelleted cells were lysed by sonication in buffer A (8 M urea, 20 mM HEPES, 200 mM NaCl, pH 8.0). Lysates, which were obtained via high-speed centrifugation (14,000 r.p.m., 30 min at 22 °C), were then adjusted to 10 mM imidazole and incubated with Ni-NTA agarose beads for 60 min at room temperature. The nickel beads were then washed with buffer A containing 20 mM and 40 mM imidazole to eliminate the presence of any nonspecific products, and bound proteins were subsequently eluted with 100 mM and 250 mM imidazole in buffer A. Eluates from both concentrations of imidazole containing the proteins of interest (i.e., TAT-HOXB4 or HOXB4) were loaded on a HiTrap SP HP column at 4 °C in buffer B (4 M urea, 20 mM HEPES, 50 mM NaCl, pH 6.5) and eluted

on the FPLC in a single-step at 4 °C with buffer C (20 mM HEPES, 1 M NaCl, pH 8.0). Both proteins were immediately desalted by diluting with 20 mM HEPES (pH 8.0) and concentrated using centrifugal filter units with 10K MWCO (EMD Millipore), divided into aliquots and flash frozen at –80 °C. Protein concentrations were determined using the Bradford protein assay (Bio-Rad).

### 3.4.6 Cell lines

HeLa (ATCC CCL-2), HaCat[255] (obtained from J. Massagué, Memorial Sloan-Kettering Cancer Center), NIH 3T3 (ATCC CRL-1658), COLO 316[256] (obtained from R. Burghardt, Texas A&M University), HDF (ATCC PCS-201-010), Neuro-2a (ATCC CCL-131) and MCH58[257] (obtained from E. Shoubridge, Montreal Neurological Institute and Hospital) were grown in Dulbecco's minimum essential medium (DMEM) (Fisher) supplemented with 10% fetal bovine serum (FBS) (Fisher) and 1× penicillin/streptomycin (P/S) (Fisher) and kept at 37 °C in a humidified atmosphere containing 5 % $CO_2$. Intestinal porcine epithelial cells (IPEC-1, obtained from G. Wu, Texas A&M University) were cultured in growth medium containing DMEM, 10 % FBS, insulin (5 μg/mL; Sigma), hydrocortisone (1 μg/mL; Sigma), EGF (5 ng/mL; BD Biosciences) and 1× P/S and kept at 37 °C in a humidified atmosphere containing 5% $CO_2$[258]. Cultures were tested for *Mycoplasma* contamination using the PCR Mycoplasma Test Kit II (PromoKine). HeLa cells were profiled using STR, by ATCC before purchase, but other cell lines were not.

### 3.4.7 Delivery of peptides inside live cells

Cells were seeded in eight-well dishes so that the cells were 80–90 % confluent after 48 h. Each well was washed three times with PBS and Leibovitz's L-15 medium that did not contain the amino acid cysteine (nonreducing L-15, nrL-15). The medium (nrL-15) used for incubation lacks cysteine to avoid reduction of the disulfide bond of dfTAT. Cells were then incubated with different concentrations of the acfTAT, fTAT, dfTAT or nrdfTAT at 37 °C for 5–60 min. Cells were washed three times with PBS and nrL-15 and placed on an inverted epifluorescence microscope (Model IX81, Olympus) equipped with a heating stage maintained at 37 °C. Images were collected using a Rolera-MGI Plus back-illuminated electron-multiplying charge-coupled device (EMCCD) camera (Qimaging). Images were acquired using bright-field imaging and three standard fluorescence filter sets: CFP (excitation (Ex) = 436 ± 10 nm/emission (Em) = 480 ± 20 nm), RFP (Ex = 560 ± 20 nm/Em = 630 ± 35 nm) and FITC (Ex = 488 ± 10 nm/Em = 520 ± 20 nm). The fluorescence intensities of different cells were measured with the SlideBook 4.2 software (Olympus), and the average fluorescence intensity was determined for each condition. Our laboratory has previously reported that cell-penetrating peptides labeled with fluorophores such as TMR can photosensitize membranes and cause endosomal leakage upon light irradiation[175, 246]. To minimize the role played by light irradiation in the activities reported herein, I performed all delivery experiments under conditions of minimal light irradiation (dark room with dim red light). When fluorescence imaging was required, probes (for example, SNAP-Surface 488 and EGFP) were imaged before dfTAT images were acquired. dfTAT was also excited for only a maximum of 300 ms. In contrast, the light

dose required to observe light-induced endosomal leakage was typically 10- to 20-fold greater than that used for imaging. For experiments performed with Cre and HOXB4, cells were not imaged and not exposed to light during delivery (cells incubated with HOXB4 were never exposed to light, and cells incubated with Cre were imaged 12 h after incubation).

### 3.4.8 Delivery of peptides and proteins inside live cells by co-incubation with dfTAT

HeLa, HDF and Neuro-2a cells were seeded in eight-well dishes, grown and washed as described in the prior section. Cells were then co-incubated with 5 μM delivery peptide and with the cargo at the corresponding concentration for 1 h at 37 °C. Cells were washed three times with PBS and nrL-15 and placed on the microscope. Images were acquired as described before. For transfection and expression of SNAP-H2B and TagCFP-mito, plasmids were mixed with Lipofectamine 2000 reagent in opti-MEM medium and incubated at room temperature for 30 min. The DNA complex was added to previously seeded HeLa cells (80 % confluent) on an eight-well dish, and cells were kept at 37 °C for 24 h. After 24 h, the wells were washed three times with PBS and nrL-15 before performing the delivery experiments using the SNAP-Surface 488, FITC goat anti-mouse IgG (Life Technologies, Cat. No. F2761) or mouse monoclonal FITC–anti-ATP5A (Abcam ab119688). The SNAP-Surface 488 fluorescence is known to be quenched (80 %) before reacting with the SNAP fusion tag[240]. Consequently, I considered the signal of SNAP-Surface 488 to be 80 % quenched when the molecule is trapped inside endosomes or distributed in the cytosol of cells, but fully fluorescent when localized in the nucleus of

cells (where it reacts with SNAP-H2B). To estimate the amount of SNAP-Surface 488 that escapes from endosomes after dfTAT-mediated delivery, I analyzed the SNAP-Surface 488 fluorescence signal obtained after imaging using the SlideBook software. The total signal intensity of the cytoplasmic region was multiplied by 5 and compared to the total signal intensity of the nuclear region.

### 3.4.9 Quantitative determination of peptide and macromolecule uptake inside cells

HeLa cells were seeded in a 48-well dish, grown and washed as described above. For the peptide uptake experiment, each well was incubated for 1 h with varying concentration of acfTAT, fTAT or dfTAT (range: 5–25 μM peptide concentration). For the titration experiment, cells were incubated with dfTAT (5 μM) and varying concentration of DEAC-K9 (range: 1–20 μM) or EGFP (10 μM) for 1 h. Cells were then washed with PBS with heparin (1 mg/mL) and nrL-15 and imaged. To lyse cells, I removed nrL-15 from the wells, and a total of 100 μl of lysis buffer (50 mM Tris, pH 7.5, 2 mM EDTA, 2 mM DTT, 0.1 % Triton X-100) were incubated with cells for 5 min (alternatively, cells were trypsinized and counted as described in the flow cytometry section). Cells were scraped off the dish, and the cell lysate was pipetted into a 1.5-mL microcentrifuge tube and centrifuged at 13,000 r.p.m. for 25 min (rotor radius: 8.4 cm). For uptake measurement, 70 μl of supernatant were collected and placed in a 96-well plate. The fluorescence emission intensity was measured using a plate reader equipped with a fluorescence module (Ex = 525 nm, Em = 580–640 nm) (GloMax-Multi+ Detection System, Promega). Alternatively, 80 μL of supernatant were diluted to a total volume of

100 µl, and the bulk fluorescence was measured using a SLM-8000C fluorometer (Ex = 435 nm, Em = 465–475 nm) (SLM Instruments). Fluorescence intensities were normalized to total protein concentration in each well (determined by Bradford protein assay, wherein 10 µl of each cell lysate is added to 200 µl of a 1× protein assay reagent and then incubated at room temperature for 30 min; absorbance at 600 nm is measured using the plate reader). To determine the amount of EGFP uptake, I mixed cell lysates (27 µl) with 3 µl of 5× SDS-PAGE loading buffer lacking DTT and analyzed them by SDS-PAGE (the sample was not boiled so as to avoid EGFP unfolding; SDS-PAGE does not unfold EGFP, as described in 259 ; DTT was not included to avoid cleavage of the disulfide bond that might form between fTAT and EGFP). Calibration curves were established for EGFP and DEAC-K9 by analyzing samples of known concentrations using SDS-PAGE gel and fluorescence, respectively. All experiments were performed in triplicate.

### 3.4.10 Quantitative analysis of TAT-HOXB4 and HOXB4 delivery with fTAT and dfTAT using a luciferase reporter

The murine fibroblast cell line (NIH 3T3, stably transfected with the E2A-PBX vector), the luciferase reporter vector, pML (5xHOX/PBX; contains a promoter with binding sites for HOXB4 and PBX) and the β-gal internal control vector used in the following studies were kindly provided by P. Zandstra (University of Toronto). The cells were initially cultured in 100-mm dishes at 37 °C with 5 % $CO_2$ in DMEM supplemented with 10% FBS. For experimental purposes, however, cells were seeded in 24-well plates at a density of $5 \times 10^4$–$6 \times 10^4$ cells per well for 24 h. Subsequently, cells were

cotransfected with 0.8 μg/ml of pML (5xHOX/PBX) and of the β-gal internal control vector using Lipofectamine 2000. Twelve hours post transfection, cells were washed and incubated with TAT-HOXB4 or HOXB4 (both at 200 nM, unless, otherwise noted; see below) with or without fTAT or dfTAT in nrL-15 for 90 min. Some cells were also incubated with TAT-mCherry (200 nM) with and without the peptides. After incubation, all cells were washed with PBS and lysed according to the manufacturer's protocol for the reporter lysis buffer (RLB) (Promega). For titration experiments, the same protocol was followed, with the exception that HOXB4 concentrations were varied (25, 50, 100, 150 and 200 nM). In order to quantitate the luciferase reporter activity, I added 100 μl of luciferase assay reagent (Promega) to 20 μl of cell lysate and bioluminescence was immediately measured using a SpectraMaxL luminometer (Molecular Devices). For the purposes of measuring transfection efficiency, 180 μl of β-gal assay buffer were mixed with 20 μl of cell lysate in a 96-well plate and incubated at 37 °C for 30 min. The β-gal assay buffer is composed of 75 % 0.1 M sodium phosphate, pH 7.5, 24 % *o*-nitrophenyl β-D-galactopyranoside (ONPG made at a concentration of 4 mg/mL in 0.1 M sodium phosphate) (Sigma) and 1% 100-fold solution (10 % 1 M magnesium chloride solution, 32 % β-mercaptoethanol and 58 % distilled water). Absorbance was then measured at 450 nm using the plate reader. As the absorption spectrum of the chromophore (TMR) conjugated to the peptide used in this study overlaps with that of β-gal, 20 μl of cell lysate containing the peptide were also diluted with 180 μl of the lysis buffer, and absorbance values obtained at 450 nm were subtracted from those of the β-gal. The luciferase activity of all samples was determined as a ratio of the luciferase activity to the β-gal activity, and

the fold-increase in luciferase activity was established by normalizing the luciferase activity of each sample to that of cells, which were transfected but had no protein delivered.

### 3.4.11 Cell viability assays

In order to determine cells that had compromised plasma membranes, I treated cells with SYTOX® green (SYTOX® blue in some cases) and Hoechst (Invitrogen). SYTOX® dyes are cell impermeable and stain the DNA of cells with compromised plasma membranes. The Hoechst dye is cell permeable and stains the DNA of all cells. Images were acquired using the green and blue filter. The green and blue images were used to count cells with a blue- or green-stained nucleus. ImageJ was used to count the dead (green) and total cells (blue). Cytotoxicity was determined from the ratio of SYTOX® green–positive cells/total number of cells. An MTT (3-(4,5-dimethylthiazol-2-yl)-2,5-diphenyltetrazolium bromide) assay was performed to determine the effect of the peptide on cell proliferation. Cells were seeded in a six-well dish, grown and washed as described above. One well from the dish was incubated with 5 μM dfTAT at 37 °C for 1 h. A second well was left untreated and served as control. Cells were washed three times with PBS and nrL-15. Cells were trypsinized and seeded into 96-well dishes containing 200 μl of DMEM. The cells were then allowed to attach to the bottom of the dish for 12 h. The MTT assay was then performed at specific time points to measure cell proliferation. The DMEM was removed and replaced with 100 μl of nrL-15, and 10 μl of a 12 mM MTT stock solution were added to the wells. The 96-well dish was incubated at 37 °C for 4 h. After

the incubation, 100 µl of a 10 mM SDS-HCl solution were added to each well. The solution was mixed thoroughly by pipetting up and down and was incubated for 13 h. After the incubation each sample was mixed, and the absorbance at 600 nm was measured. Controls included a negative control where 10 µl MTT was added to 100 µl of nrL-15 alone (no cells). A second control consisted of cells treated with the delivery peptide but to which no MTT was added to subtract the contribution of TMR from the measured absorbance. The absorbance of the negative control was subtracted from all samples. The final time point measurement for each cell type corresponded to 100 % cell confluency.

### 3.4.12 Whole-genome microarray analysis

HDF cells were cultured in 24-well dishes and incubated with nrL-15 (untreated cells), nrL-15 supplemented with dfTAT (5 µM, treated cells) or nrL-15 supplemented with staurosporine (0.1 µM) for 1 h. Cells were trypsinized immediately after washing with PBS or nrL-15 (1-h time point). Alternatively, cells were trypsinized after 1 h (1 h + 1 h) or 24 h (1 h + 24 h) incubation in 10 % FBS/DMEM. Cells were removed from each well by gentle pipetting and spun down at 12,000 r.p.m. for 4 min at 4 °C. The cell pellets were preserved in 1 mL Trizol (Ambion, Life Technologies) and shipped frozen to the UT Southwestern microarray facility, where total RNA was extracted and analyzed on an Illumina Human HT-12 v4 sequencer using reported protocols (https://microarray.swmed.edu/protocols/protocol/illumina-gene-expression-probe-labeling).

### 3.4.13 Differential in gel electrophoresis (DIGE) proteomic analysis

HDF cells were treated with or without dfTAT as described in the whole-genome microarray analysis assay. A volume of 150 µl of lysis buffer (10 mM Tris, pH 7.5, 1 % CHAPS and 1× protease inhibitor cocktail) was added to each well. After 5 min, the solution was transferred to an Eppendorf tube, and 20 µl of nuclease cocktail were added to the cell lysates and incubated on ice for 30 min. The lysate was spun down at 13,000 r.p.m. for 10 min at 4 °C. The supernatant was saved, and an aliquot was used in Bio-Rad protein assay for quantification of total protein in the cell lysates. Methanol-chloroform precipitation was performed on the remaining sample[260]. All DIGE experiments were performed with pH 3–10 NL gradients. Each sample (~50 µg of protein) was resuspended in 30 µl of labeling buffer (7 M urea, 2 M thiourea, 4 % CHAPS, 30 mM Tris, 5 mM magnesium acetate). All samples were individually labeled with Cy3 or Cy5 (GE Healthcare) for 30 min on ice and in the dark (200 pmol), after which the reaction was quenched by the addition of 10 mM lysine for 10 min followed by the addition of an equal volume of 2× rehydration buffer (7 M urea, 2 M thiourea, 4 % CHAPS, 4 mg/mL DTT). The combined samples were brought up to 250 µl with 1× rehydration buffer (7 M urea, 2 M thiourea, 4 % CHAPS, 2 mg/mL DTT, 0.5 % IPG buffer, pH 3–10). All strips were subjected to isoelectric focusing for 25,000 V h, according to manufacturers' recommendations. DIGE-associated instrumentation was manufactured by GE Healthcare. Electrophoresis instrumentation was from Hoefer. Cy2/3/5-specific 16-bit data files were acquired at 100-µm resolution separately by dye-specific excitation and

emission wavelengths using a Typhoon Trio Variable Mode Imager in a manner that greater than 90% of the proteins were in the linear range of detection.

### 3.4.14 Determination of dfTAT and EGFP interaction by FRET

Fluorescence emission spectra were obtained using an SLM-8000C fluorometer upgraded with the Phoenix package (ISS) and Vinci v.1.6 PC software (ISS). The experiments were conducted using a quartz cuvette at room temperature. The samples were excited at 488 nm (slit width = 1 mm), and the fluorescence emission was scanned from 500 to 650 nm (slit width = 1 mm). All samples (1 μM EGFP or dmEGFP and 5 μM dfTAT) were prepared using nrL-15. A 12% native gel was run using Tris-glycine running buffer at 100 mV for 2 h. Samples containing dfTAT (5 or 10 μM) were co-incubated with either varying concentration of dmEGFP (10–20 μM) or BSA (10 μM) in nrL-15 (pH 5.0 and 7.0) for 30 min at 37 °C before gel loading. Fluorescence images of dfTAT and EGFP bands on the gel were detected using a fluorescence scanner (Typhoon, GE Healthcare). (dfTAT fluorescence detection: Ex, 568 nm; Em, 620 nm. EGFP fluorescence detection: Ex, 488 nm; Em, 525 nm.) Gels were then stained with Coomassie blue.

# 4. dfTAT MEDIATES CYTOSOLIC DELIVERY OF PROTEINS, PEPTIDES AND CELL-IMPERMEABLE SMALL MOLECULES INTO CELLS BY PROMOTING INTRACELLULAR UPTAKE THROUGH ENDOCYTOSIS AND BY MEDIATING ENDOSOMAL ESCAPE FROM LATE ENDOSOMES

## 4.1 Introduction

In chapter two and three I showed that branched and multivalent CPPs of the peptide TAT can penetrate live cells[198]. Furthermore, my results show that, in cases where cytosolic penetration was successful, the multivalent CPPs delivery efficiency was higher than their monomeric counterparts[198, 222]. These improved endosomolytic delivery agents can be used to deliver different cargos such as: antibodies, transcription factors, peptides and cell-impermeable small molecules inside cells. These deliveyr agents, specifically dfTAT, display very high endosomolytic activity. Interestingly and to my surprise, this is not accompanied by high cell toxicity. The molecular details involved in dfTAT penetration and high endosomolytic activity remain unknown.

In this chapter, I describe the mechanism of cell penetration involved in the delivery of cargos into the cytosolic space of cells of a highly endosomolytic branched and multivalent CPP, dfTAT. I test the hypothesis that dfTAT reaches the cytosolic space of cells after dfTAT cellular uptake by endocytosis, trafficking through the endocytic pathway and dfTAT-mediated escape from late endosomes. Futhermore, I hypothesize that dfTAT-mediated endosomal escape depends on the presence of a negatively-charged phospholipid found only in late endosomes inside cells, BMP. I formulated my hypothesis

based on evidence showing that the TAT peptide can bind negatively-charged phospholipids and can cause disruption of membranes containing BMP *in vitro*[72, 131, 141, 142]. Moreover, it has been shown that TAT monomer reaches the cytosolic space after it escapes from endocytic organelles found late in the endocytic pathway[103]. Here I report that dfTAT requires to be transported to endocytic vesicles found late in the endocytic pathway to escape and reach the cytosolic space. I demonstrate that dfTAT does not escape from early endosomes or lysosomes and instead, like TAT, it appears to escape from late endosomes. I achieved cytosolic delivery in cells that were incubated with an inhibitor than blocks transport from endosomes to the trans-Golgi network (TGN), retro-2. This suggests that dfTAT does not reach the cytosolic space via retrograde transport. On the other hand, delivery was blocked by an antibody that accumulates in the lumen of late endosomes and binds BMP, anti-BMP. This result suggests that dfTAT interacts with BMP in order to escape from late endosomes.

## 4.2 Results

### 4.2.1 Transport of dfTAT to endocytic organelles found late in the endocytic pathway is required for endosomal escape

In chapter three I showed that dfTAT penetrates cells via a two-step process. First, dfTAT is taken up by cells by endocytosis (macropinocytosis been the major mechanism). This step leads to entrapment of dfTAT inside endocytic vesicles and trafficking along the endocytic pathway. Subsequently, dfTAT escapes from the endocytic pathway and enters the cytosolic space of cells. The exact exit point where dfTAT escapes remains unknown.

In order to establish where dfTAT escapes from the endocytic pathway, I decided to block endocytic transport at specific points using known molecular biology tools. To do this, I incubated dfTAT with cells expressing dominant negative-Rab5 (DN-Rab5) or dominant negative Rab7 (DN-Rab7). Rab proteins are part of a group of regulators that control endosome biogenesis, endosome maturation and trafficking[261]. Expression of DN-Rab5 and DN-Rab7 arrests transport of cargos at a specific step by blocking the maturation of endocytic vesicles to early endosomes and late endosomes, respectively **(Figure 4-1)**[262-266]. When dfTAT (3 μM) was incubated with cells expressing DN-Rab5 and DN-Rab7 penetration of dfTAT into the cytosolic space was inhibited dramatically. While the population of untreated (non transfected cells, "dfTAT alone") cells showed 57.6 % cytosolic fluorescence distribution, cells expressing DN-Rab5 and DN-Rab7 displayed 8.1 % and 6.9 % cells with cytosolic fluorescence distribution, respectively **(Figure 4-2 and 4-3).** Most cells expressing DN-Rab5 and DN-Rab7 showed a punctate fluorescence distribution consistent with the peptide being trapped inside endosomes **(Figure 4-4).**

Disruption of the endocytic pathway using inhibitors or, as in this case, DN-Rab proteins can cause a negative feedback where uptake/endocytosis is affected. Expression of DN-Rab5 and DN-Rab7 could lead to a decrease of dfTAT intracellular uptake, which in turn can decrease dfTAT endosomal escape due to a decrease in the amount of dfTAT inside endosomes. To confirm that reduction of the % cells with cytosolic dfTAT

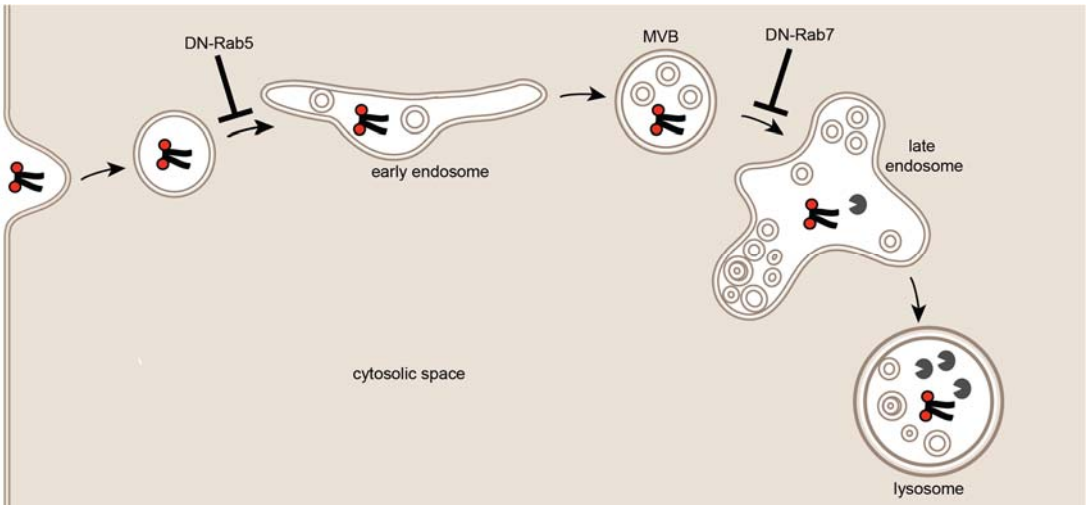


**Figure 4-1 Model of endocytic trafficking and dfTAT inhibition of transport mediated by DN-Rab5 and DN-Rab7.** In principle, dfTAT transport to early endosomes and subsequent vesicles will be blocked by expression of DN-Rab5. On the other hand, transport of dfTAT to late endosomes and lysosomes will be block by expression of DN-Rab7.

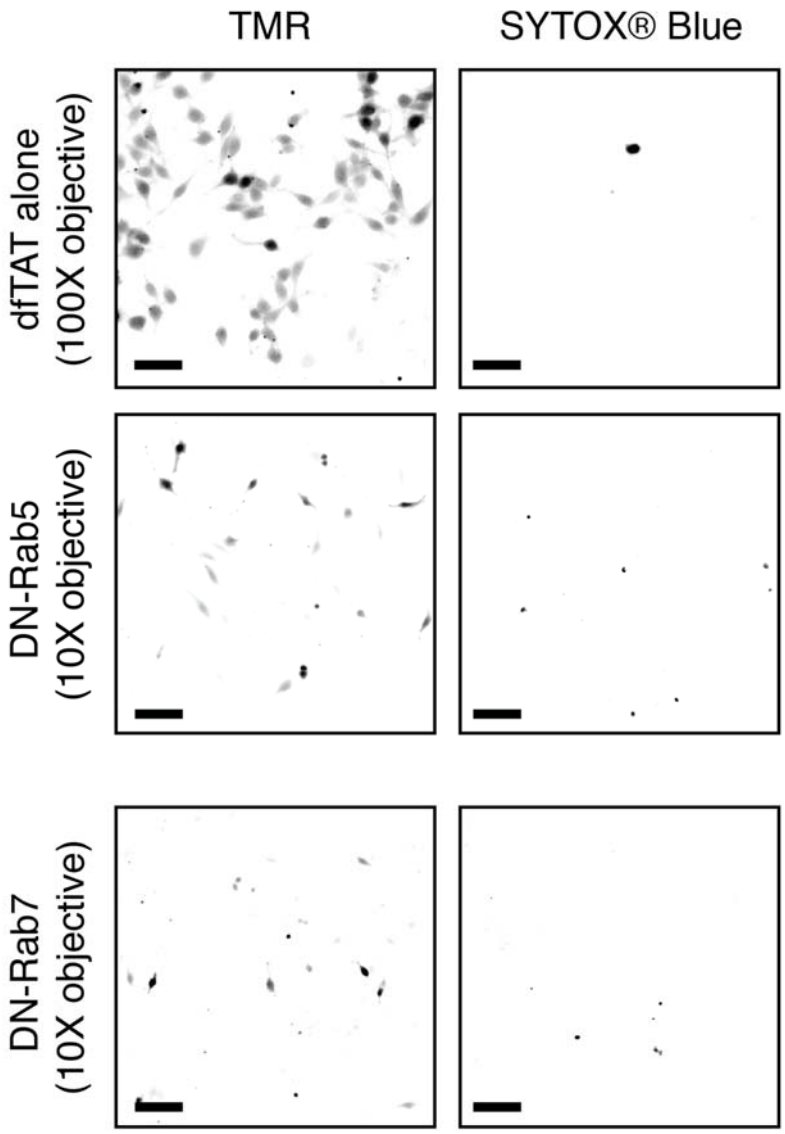


**Figure 4-2 Expression of DN-Rab5 and DN-Rab7 in live cells inhibits dfTAT endosomal escape.** Assay showing that dfTAT endosomal escape is significantly reduced by expression of DN-Rab5 and DN-Rab7. Untreated (dfTAT alone) HeLa cells or transfected cells with a plasmid containing rab5q79l and and rab7q67l genes were incubated for 1 h with dfTAT (3 μM). Cells displaying cytosolic dfTAT fluorescence distribution that result from successful dfTAT delivery were visualized and counted by microscopy. Scale bars: 10X objective, 100 μm.

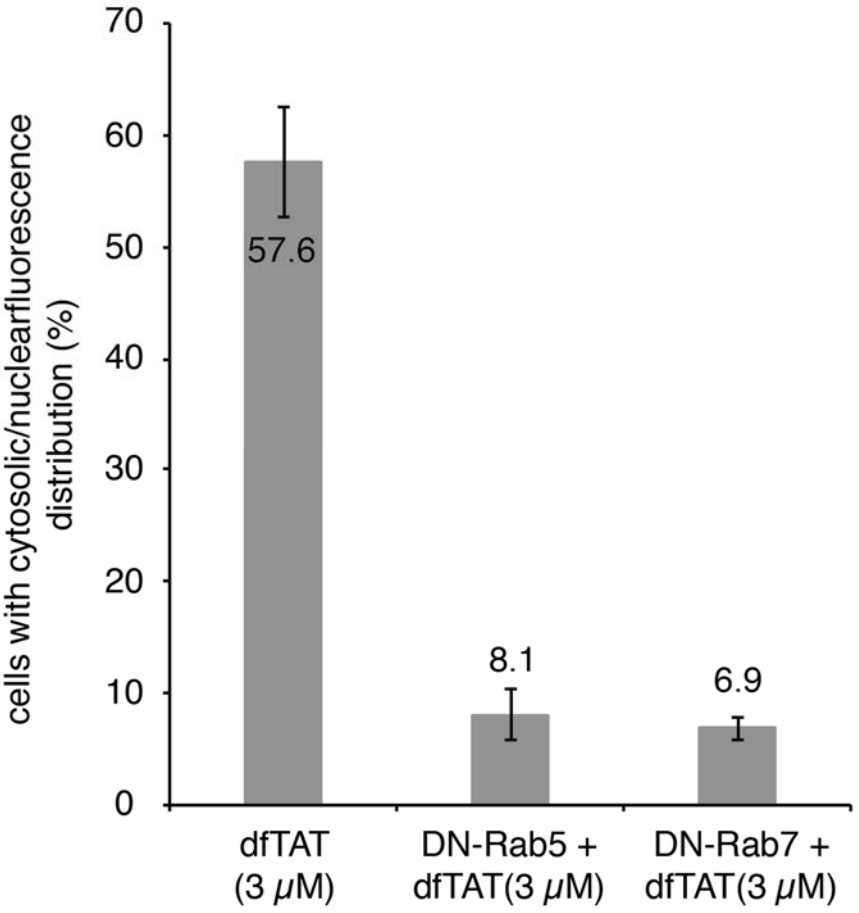


**Figure 4-3 Quantitative analysis of dfTAT penetration in live cells expressing DN-Rab5 and DN-Rab7.** Cells were incubated with dfTAT (3 μM) for 1 h. The number of cells with detectable cytosolic and nuclear fluorescence distribution in microcopy images was counted and divided by the total number of cells present (1,000 cells per experiment).

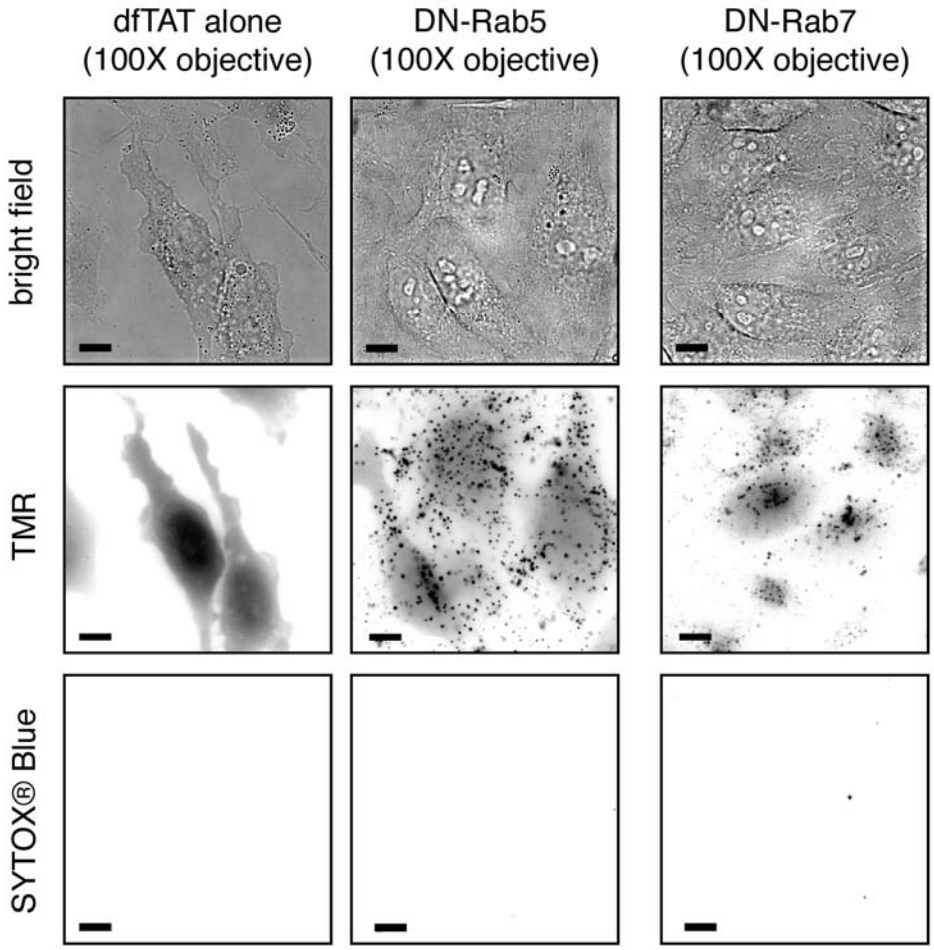


**Figure 4-4 Expression of DN-Rab5 and DN-Rab7 causes dfTAT to remain trapped inside endocytic vesicles.** Untreated (dfTAT alone) HeLa cells or transfected cells with a plasmid containing rab5q79l and and rab7q67l genes were incubated for 1 h with dfTAT (3 μM). Cells were visualized as before. Scale bars: 100X objective, 10 μm

fluorescence distribution was not a consequence of a reduction in the amount of dfTAT endocytosed, I measured dfTAT intracellular uptake. Cells expressing DN-Rab5 and DN-Rab7 did not show a significant difference in the amounts of dfTAT uptake when compared to non transfected cells **(Figure 4-5)**. This confirms that the reduction in the % cells with cytosolic fluorescence distribution is not due to a decrease in dfTAT uptake. These data altogether indicate that dfTAT, after been endocytosed, has to be transported to endocytic organelles found late in the endocytic pathway (late endosomes or lysosomes) to achieve endosomal escape and enter the cytosolic space of cells.

### 4.2.2 dfTAT does not cause leakage of a peptide that accumulates inside lysosomes

At this point, penetration of dfTAT into the cytosolic space of cells appears to require transport into late endosomes or lysosomes or both. These endocytic organelles are two potential candidates for the exit point of dfTAT from the endocytic pathway. To determine if dfTAT can escape from lysosomes, I will test the dfTAT-mediated release of DEAC-K9 into the cytosolic space of cells using fluorescence microscopy (as performed in chapter 3). DEAC-K9 is a fluorescently-labeled cell-impermeable peptide that gets endocytosed by the same pathway as dfTAT[175, 225]. However, unlike dfTAT, DEAC-K9 cannot escape from the endocytic pathway by itself and so it remains trapped inside endosomes after incubation with cells. In chapter 3, I showed that after incubation of cells with DEAC-K9 and a quick wash (1 min), incubation with dfTAT causes leakage of DEAC-K9 from endosomes into the cytosolic space of cells (Figure 3-15). My rationale is that if dfTAT escapes from lysosomes it could mediate the release of

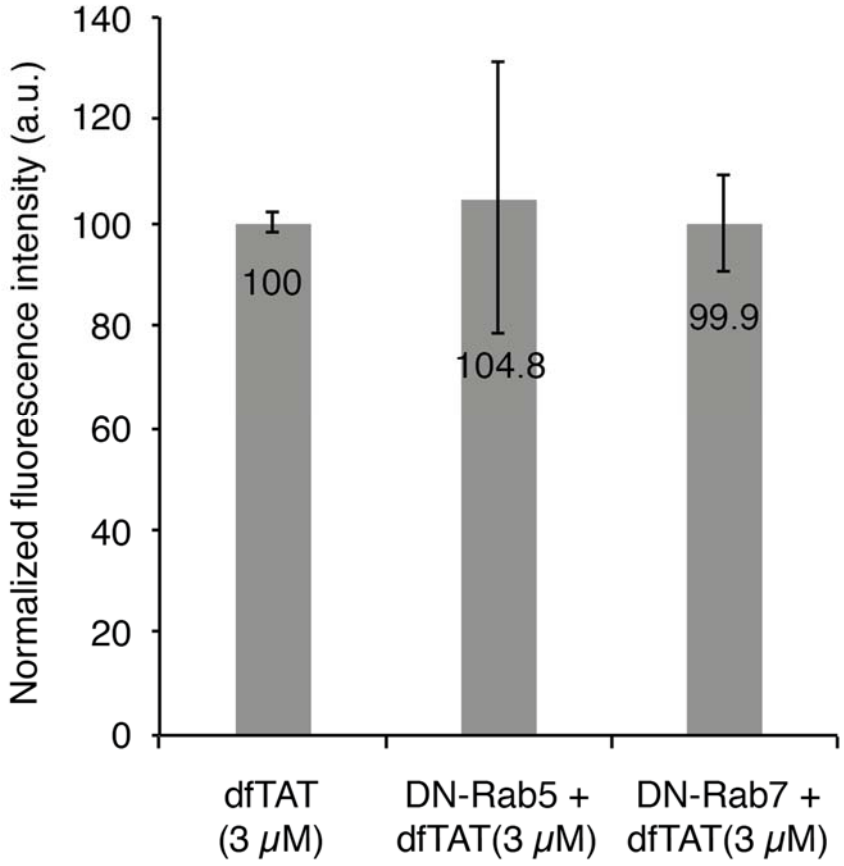


**Figure 4-5 Quantitative analysis of dfTAT intracellular uptake in cells expressing DN-Rab5 and DN-Rab7.** Cells were incubated with dfTAT (3 μM) for 1 h, and relative uptake was assessed quantitatively by measuring the bulk fluorescence of cell lysates (300,000 cells per experiment). a.u., arbitrary units. The data represent the mean of triplicate experiments and the corresponding s.d.

DEAC-K9 from lysosomes to the cytosolic space. Interestingly, I was able to detect co-localization of DEAC-K9 with LysoTracker® Green, a marker of lysosomes, after incubating cells with the peptide (10 μM) for 1 h, washing and imaging after only 30 min (**Figure 4-6**). As observed before, incubation of cells with dfTAT, after a quick wash (1 min), caused leakage of DEAC-K9 from endosomes (**Figure 4-7, left panel**). On the contrary, dfTAT did not cause leakage of DEAC-K9 when the latter was allowed to tr8affic along the endocytic pathway and accumulate inside lysosomes for 2 h following an 1 h incubation and wash (**Figure 4-7, right panel**). Moreover, the punctate fluorescence signal of DEAC-K9 co-localized with LysoTracker® Green (data not shown) suggesting it remained trapped inside endosomes. One possibility is that dfTAT escapes from lysosomes (late endosomes as well, late endosomes being the major exit point) in an inefficient manner, to an extent that cannot be detected from the release of DEAC-K9 by fluorescence microscopy, because most of the peptide is degraded by proteases in lysosomes. To test this possibility, I used a protease-resistant version of dfTAT made out of D-amino acids, D-dfTAT. Like dfTAT, D-dfTAT penetrates cells efficiently (data not sown). Incubation of D-dfTAT with cells that had been pre-incubated with DEAC-K9 did not cause leakage of DEAC-K9 from lysosomes (same protocol used earlier was followed) (**Fig 4-8**). Together, these findings suggest that transport of dfTAT to lysosomes and lysosomal leakage are not required for dfTAT endosomal escape. It is possible that dfTAT reaches this organelle but possibly it is degraded before it can disrupt the membrane of lysosomes.

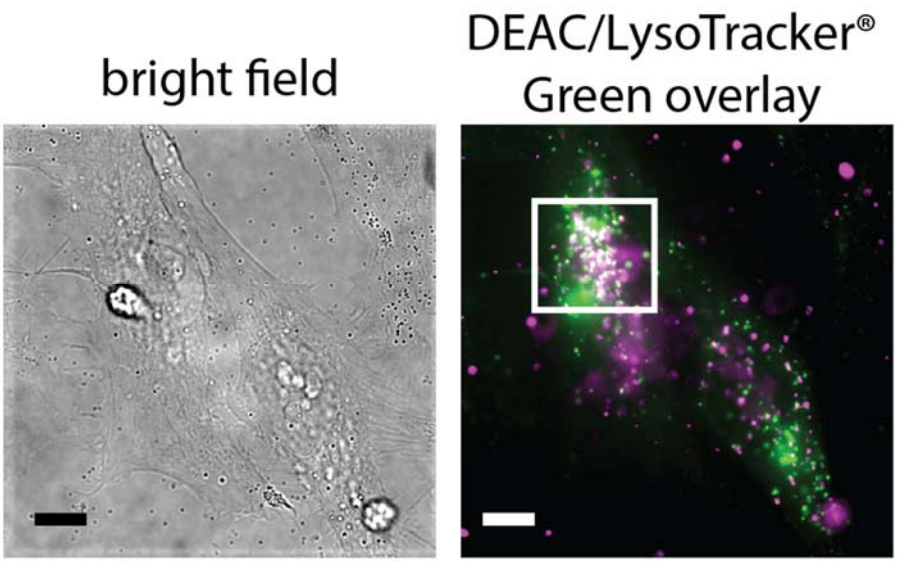


**Figure 4-6 DEAC-K9 cellular localization following cellular uptake and endocytic trafficking.** Cells were incubated with DEAC-K9 (10 μM) for 1 h, washed and imaged after 30 min. DEAC fluorescence signal is shown in magenta and LysoTracker® Green signal is shown in green. Co-localization is displayed as white (highlighted inside square). Scale bars: 10 μm.

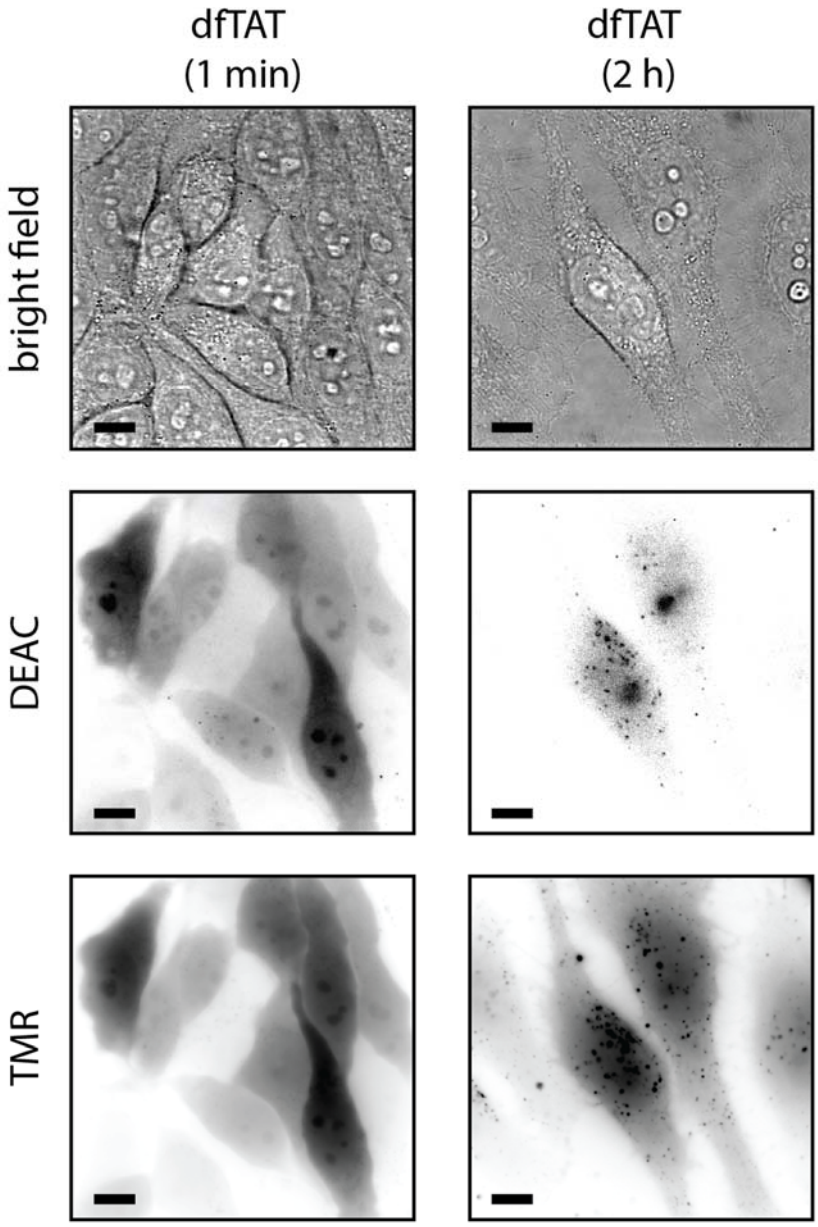


**Figure 4-7 dfTAT does not mediate leakage of DEAC-K9 from lysosomes.** HeLa cells were incubated with 10 μM DEAC-K9 for 1 h and washed. Cells were subsequently incubated with 5 μM dfTAT, after 1 min or 2 h, for 1 h. Images are represented as inverted monochromes. Scale bars: 10 μm.

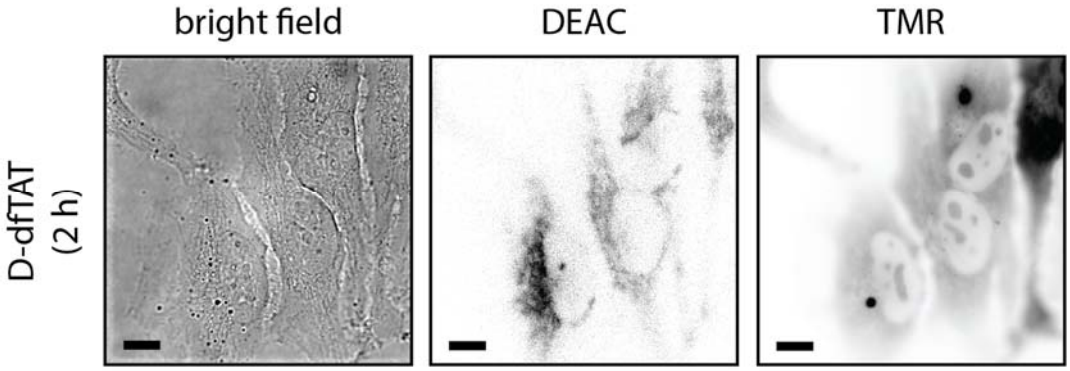


**Figure 4-8 D-dfTAT does not mediate leakage of DEAC-K9 from lysosomes.** HeLa cells were incubated with 10 μM DEAC-K9 for 1 h and washed. Cells were subsequently incubated with 5 μM D-dfTAT, after 1 min or 2 h, for 1 h. Images are represented as inverted monochromes. Scale bars: 10 μm.

### 4.2.3 Retro-2, an inhibitor of retrograde transport, does not block penetration of dfTAT into the cytosolic space of cells

Until this point, penetration of dfTAT into the cytosolic space appears to require transport into late endosomes. dfTAT could be escaping from the endocytic pathway by causing leakage of late endosomes. On the other hand, dfTAT endosomal escape could proceed from the Golgi apparatus (Golgi) or the endoplasmic reticulum (ER) via the TGN after transport of dfTAT to late endosomes[267]. There is evidence showing that toxins and viruses utilize this pathway to reach the cytosolic space of cells[267-269]. Interestingly, both modes of endosomal escape described require transport to late endosomes. To establish if retrograde transport is involved in dfTAT endosomal escape I will block retrograde transport using retro-2. Retro-2 is a molecule known to protect cells against ricin-mediated cell death (ricin transports from early endosomes to the TGN) and infection by viruses like SV40 (SV40 transports from late endosomes to the TGN) by blocking transport from endosomes to the TGN[270, 271]. It is important to mention that retro-2 blocks retrograde transport but not endosome maturation (retro would not block transport to late endosomes)[270]. I pre-incubated cells with retro-2 (20 μM) for 30 min, washed and incubated with dfTAT (3 μM). After incubation, dfTAT escaped from endosomes and showed a cytosolic fluorescence distribution (**Figure 4-9**). Moreover, the % of cells with dfTAT fluorescence distribution did not change when compared to untreated cells (**Figure 4-10**). Furthermore, intracellular uptake of dfTAT was not affected by incubation with retro-2 (**Figure 4-11**). These findings suggest that

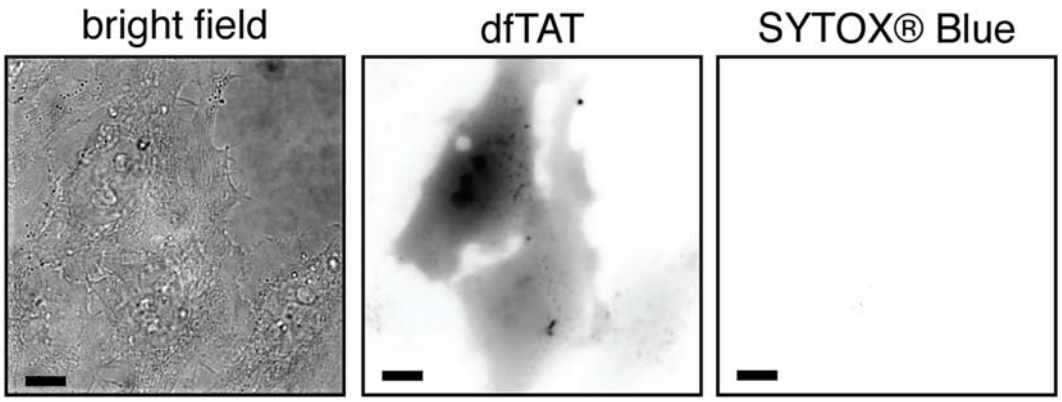


**Figure 4-9 dfTAT does not escape from the endocytic pathway via retrograde transport.** HeLa cells were pre-incubated with 20 μM for 30 min and washed. Subsequently, cells were co-incubated with dfTAT (3 μM) and retro-2 (20 μM) for 1 h washed and imaged. Scale bars: 10 μm.

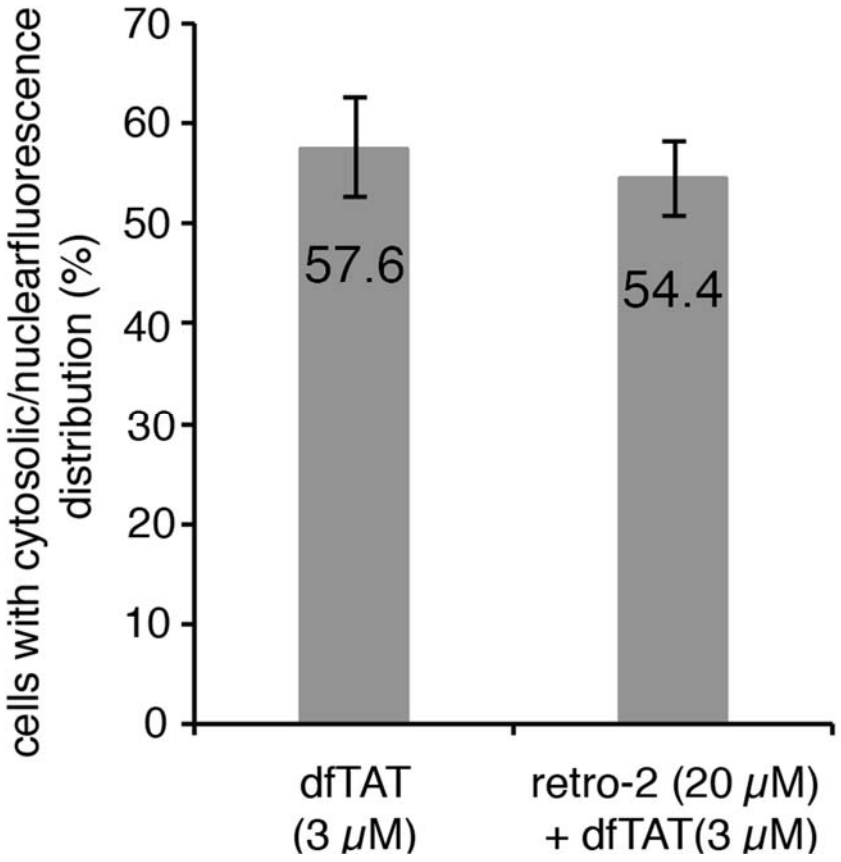


**Figure 4-10 Quantitative analysis of dfTAT penetration in live cells incubated with retro-2, an inhibitor of retrograde transport.** Cells were pre incubated with retro-2 (20 μM) and washed. Subsequently, cells were co-incubated with dfTAT (3 μM) and retro-2 (20 μM) for 1 h. The number of cells with detectable cytosolic and nuclear fluorescence distribution in microcopy images was counted and divided by the total number of cells present (1,000 cells per experiment).

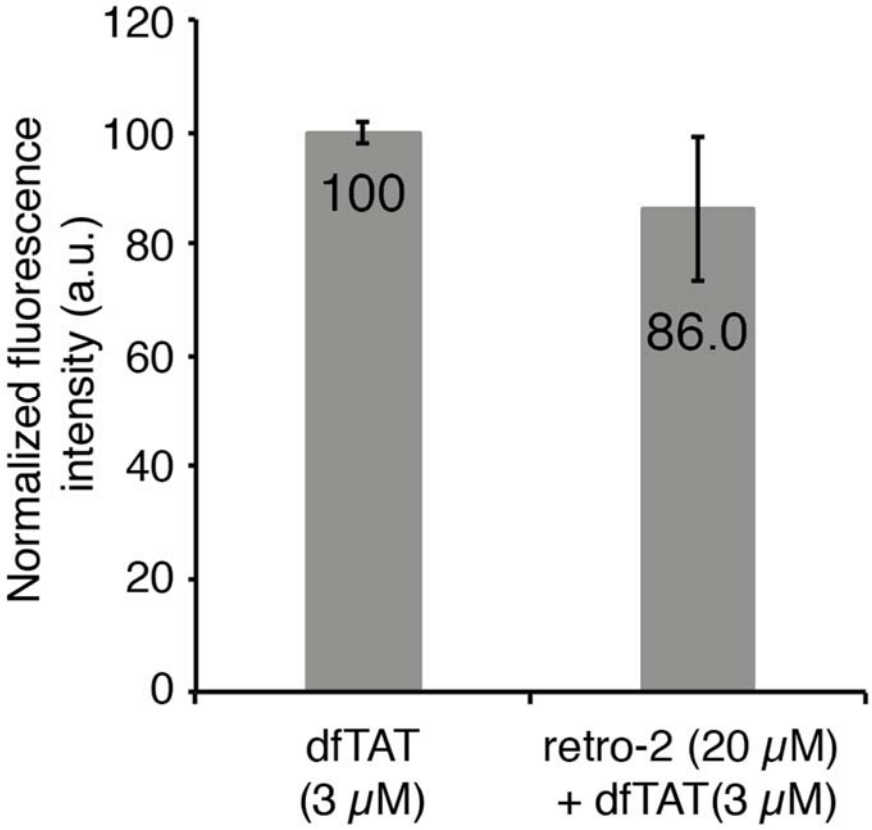


**Figure 4-11 Quantitative analysis of dfTAT intracellular uptake in cells pre-incubated with retro-2.** Cells were pre-incubated with retro-2 (20 μM) and washed. Subsequently, cells were co-incubated with dfTAT (3 μM) and retro-2 (20 μM) for 1 h and relative uptake was assessed quantitatively by measuring the bulk fluorescence of cell lysates (300,000 cells per experiment). a.u., arbitrary units. The data represent the mean of triplicate experiments and the corresponding s.d.

dfTAT does not utilize retrograde transport to escape from the endocytic pathway and enter the cytosolic space of cells.

### 4.2.4 Penetration of dfTAT into the cytosolic space is blocked by an antibody against BMP

So far, all the data I have shown points at late endosomes as the exit point for dfTAT endosomal escape. It is well established that the TAT peptide binds to negatively-charged phospholipids and can disrupt membranes containing phosphatidylserine (Pdt-Ser) and BMP[72, 141, 142]. Moreover, TAT has been shown to cause lipid mixing and leakage of molecules encapsulated in liposomes containing BMP[131]. Late endosomes are enriched with the negatively-charged peptide BMP. Interestingly, BMP is found only in late endosomes inside cells[152, 153]. Therefore, I decided to establish the role of BMP in dfTAT endosomal escape. To do this, I utilized anti-BMP, an antibody known to bind BMP and accumulate in late endosomes after uptake by fluid-phase endocytosis[128, 130, 152, 272]. Anti-BMP has been shown to block infection of vesicular stomatitis virus (VSV), a virus that requires transport to late endosomes to cause infection, presumably by interfering selectively with late endosome/BMP functions[130]. Long pre-incubation of cells with anti-BMP (50 μg/mL, for 18 h) led to a significant decrease in the % of cells with dfTAT cytosolic fluorescence distribution (**Figure 4-12, left panel**). While 57.6 % of untreated cells (dfTAT alone) displayed a cytosolic fluorescence distribution, only 5.2 % of cells pre-incubated with anti-BMP (anti-BMP, 18 h incubation) displayed a cytosolic fluorescence distribution

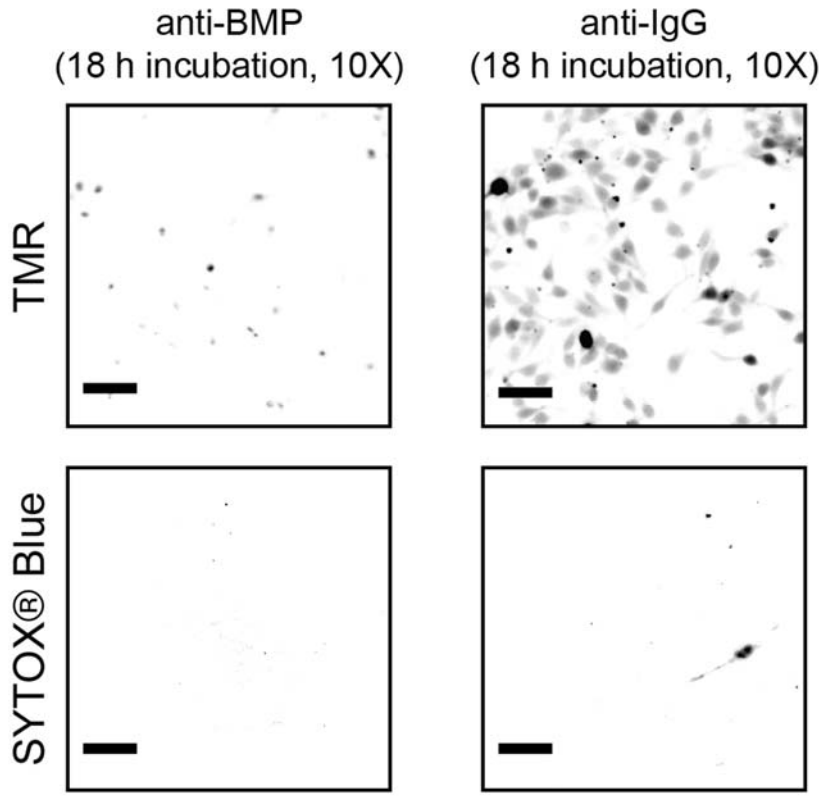


**Figure 4-12 Incubation of live cells with anti-BMP inhibits dfTAT endosomal escape.** Cells were pre-incubated with anti-BMP (50 μg/mL) or anti-IgG (50 μg/mL) for 18 h, washed, co-incubated with anti-IgG (50 μg/mL) or anti-BMP (50 μg/mL) and dfTAT (3 μM) for 1 h. Cells displaying cytosolic dfTAT fluorescence distribution that result from successful dfTAT delivery were visualized and counted by microscopy. Scale bars: 10X objective, 100 μm.

(**Figure 4-13**). Interestingly, the intracellular uptake of dfTAT was not significantly affected by incubation with anti-BMP (**Figure 4-14**) Moreover, the majority of treated cells showed a punctate fluorescence distribution consistent with dfTAT being trapped inside endosomes (**Figure 4-15, left panel**). To show that inhibition was not an indirect effect of antibody incubation, cells were pre-incubated with anti-IgG (50 μg/mL, for 18 h) (anti-IgG has no known effect on endosome/BMP function). Incubation with anti-IgG showed no significant change in the % of cells with dfTAT cytosolic fluorescence distribution when compared to untreated cells (**Figure 4-12 (right panel) and 4-13**). Interestingly, treatments of cells with both, anti-BMP and anti-IgG, did not have a significant effect on intracellular uptake of dfTAT, even though the observe dfTAT penetration activity differed greatly between treatments (**Figure 4-14**). Long incubation with anti-BMP has been shown to affect endosome morphology, endosome dynamics and localization and trafficking of proteins associated with endosome function[128, 153, 273, 274]. To confirm that inhibition of dfTAT penetration was not due to changes in the endocytic pathway, cells were incubated with anti-BMP for only a short time. Similarly as before, incubation with anti-BMP (50 μg/mL, for 30 min) led to a significant decrease in the % of cells with dfTAT cytosolic fluorescence distribution. I observed only 6.6 % of cells showed penetration of dfTAT into the cytosolic space (**Figure 4-13**). Moreover, dfTAT fluorescence signal co-localized with WT GFP-Rab7, a marker of late endosomes[275, 276] (**Figure 4-16**). The latter shows that incubation of anti-BMP does not block transport of dfTAT to late endosomes. Altogether, these data suggests that dfTAT

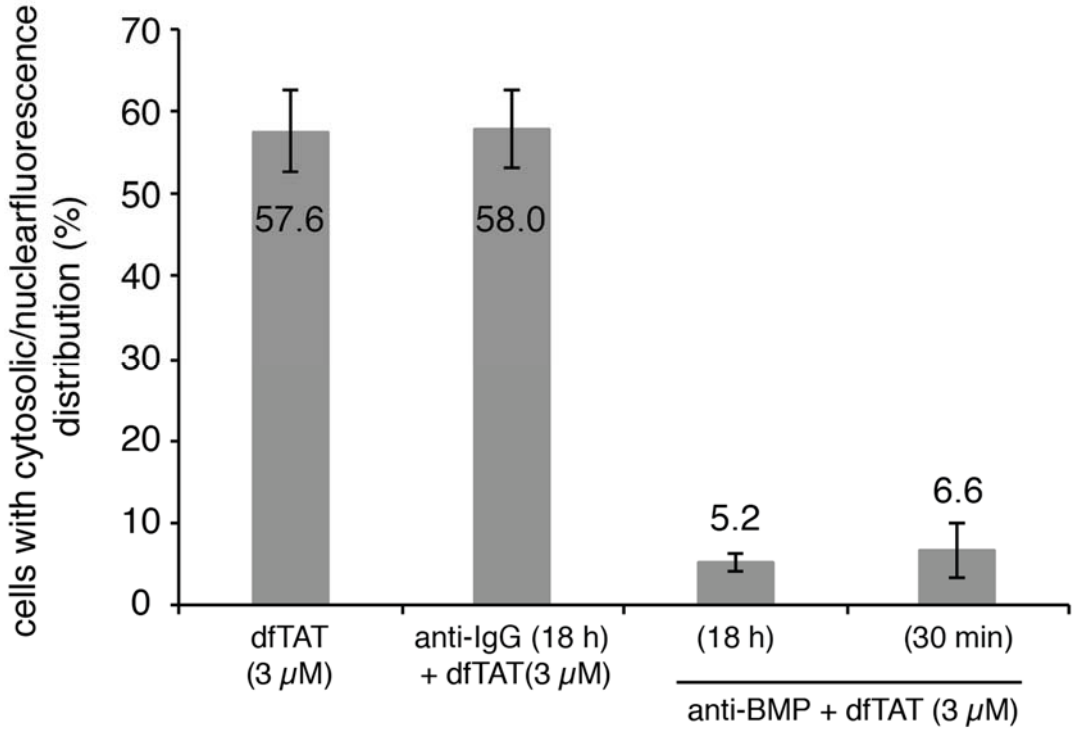


**Figure 4-13 Quantitative analysis of dfTAT penetration in live cells pre-incubated with anti BMP.** Cells were pre incubated with anti-BMP (50 μg/mL) and washed. Subsequently, cells were co-incubated incubated with dfTAT (3 μM) and anti-BMP (50 μg/mL) for 1 h. The number of cells with detectable cytosolic and nuclear fluorescence distribution in microcopy images was counted and divided by the total number of cells present (1,000 cells per experiment).

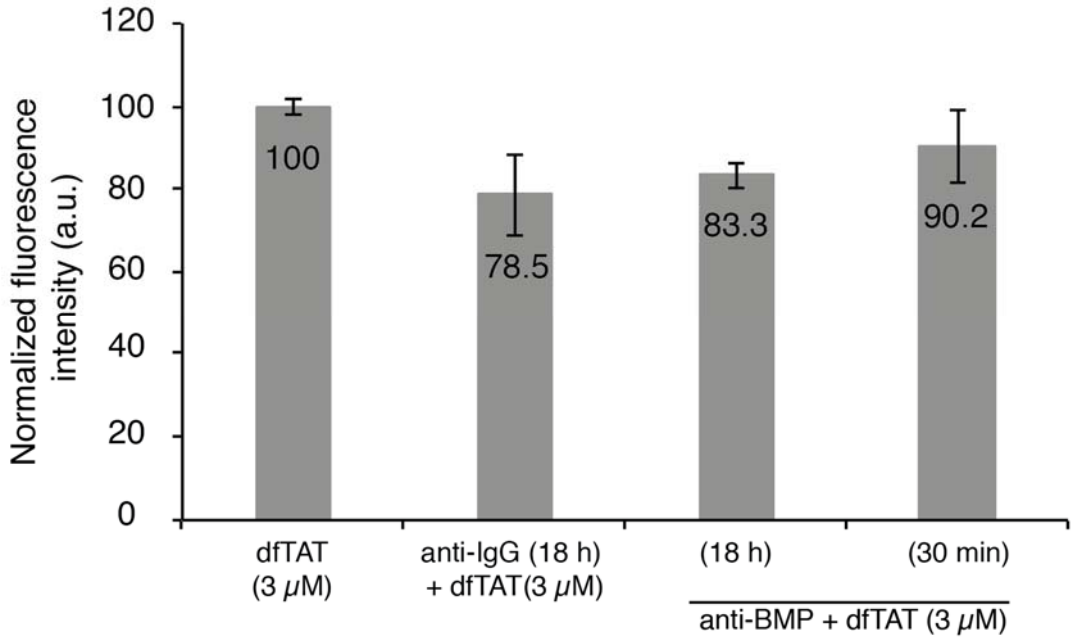


**Figure 4-14 Quantitative analysis of dfTAT intracellular uptake in cells pre-incubated with anti-IgG and anti-BMP.** Cells were pre-incubated with antibodies (50 μg/mL) for the specified time and washed. Subsequently, cells were co-incubated with dfTAT (3 μM) and antibodies (50 μg/mL) for 1 h and relative uptake was assessed quantitatively by measuring the bulk fluorescence of cell lysates (300,000 cells per experiment). a.u., arbitrary units. The data represent the mean of triplicate experiments and the corresponding s.d.

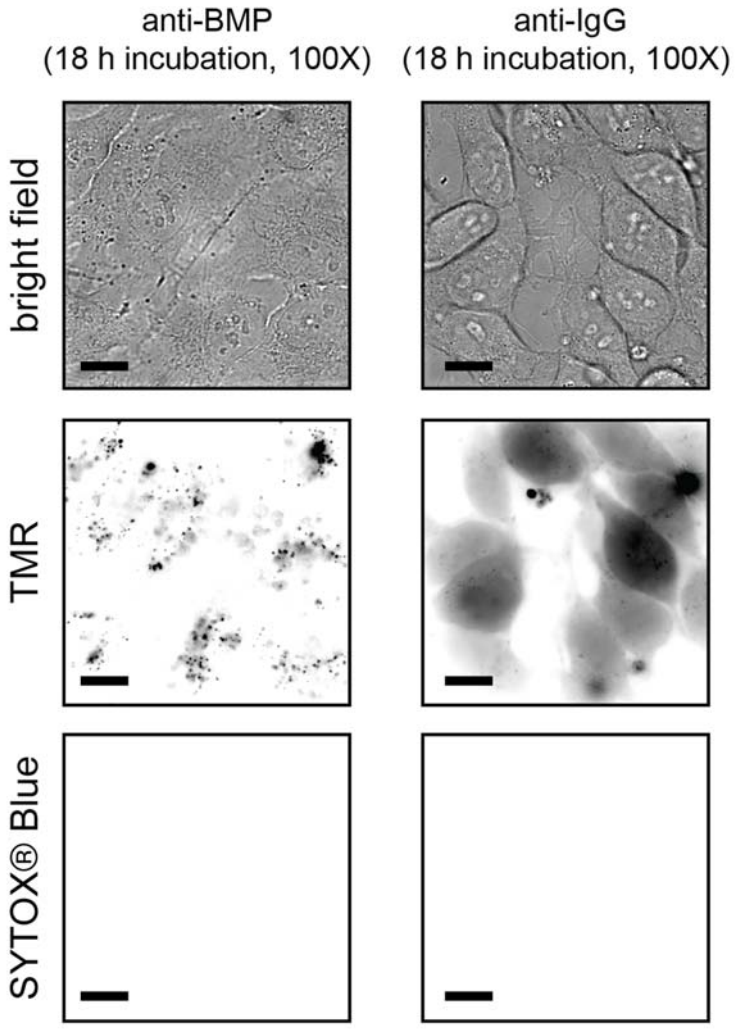


**Figure 4-15 Incubation of cells with anti-BMP causes dfTAT to remain trapped inside endocytic vesicles.** Cells were pre-incubated with anti-BMP (50 μg/mL) or anti-IgG (50 μg/mL) for 18 h, washed, co-incubated with anti-IgG (50 μg/mL) or anti-BMP (50 μg/mL) and dfTAT (3 μM) for 1 h. Cells were imaged as before. Scale bars: 100X objective, 10 μm

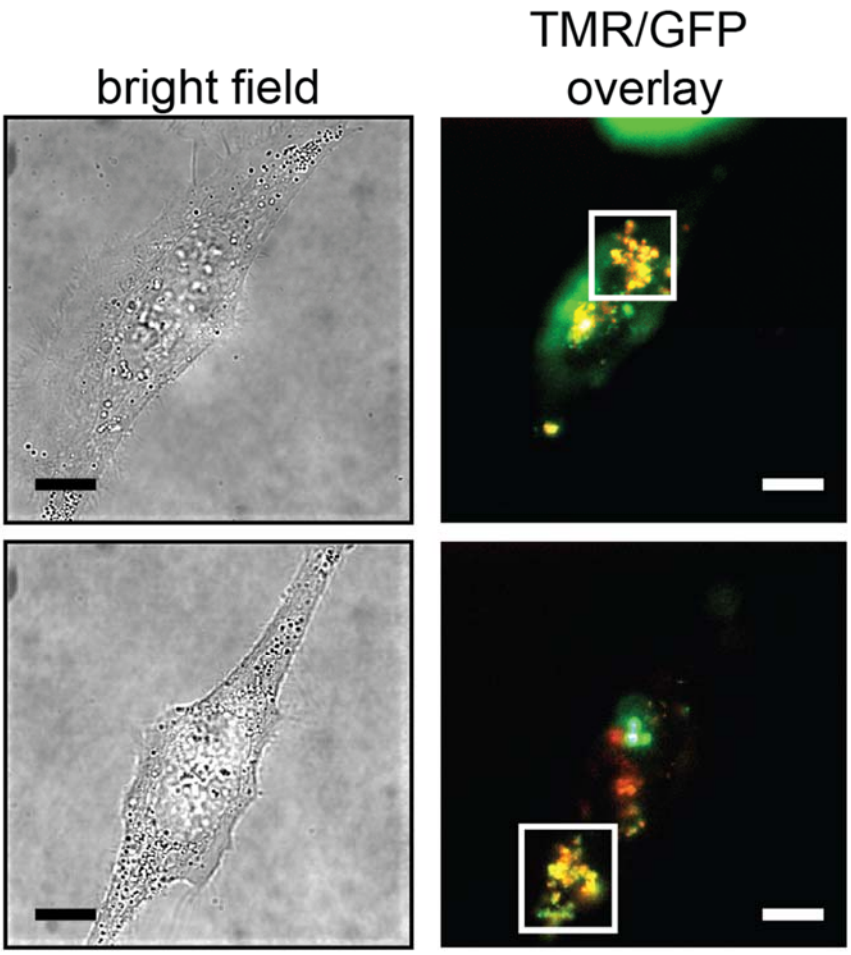


**Figure 4-16 dfTAT cellular localization in cells pre-incubated with anti-BMP.** Cells expressing WT GFP-Rab7 were pre-incubated with anti-BMP (50 µg/mL) for 30 min and washed. Subsequently, cells were co-incubated with dfTAT (3 µM) and anti-BMP (50 µg/mL) for 1 h, washed and imaged after 30 min. dfTAT fluorescence signal is shown in red and GFP-Rab7 signal is shown in green. Co-localization is displayed as yellow (highlighted inside square). Scale bars: 10 µm.

endosomal escape requires transport to late endosomes and productive interactions between dfTAT and BMP.

### 4.3 Discussion

By mediating endosomal leakage, dfTAT escapes from the endocytic pathway after entering cells via macropinocytosis. The ability of dfTAT to escape from endosomes seems to require transport into late endosomes. Disruption of dfTAT transport to late endosomes using DN-Rab5 and DN-Rab7 proved to be effective at inhibiting dfTAT endosomal escape and shows that dfTAT endosomal escape does not take place from early endosomes. The latter phenomenon associated with dfTAT endosomal escape was true even in conditions where the amount of dfTAT endocytosed by cells expressing DN-Rab proteins ("treated cells") was similar than untreated cells. This clearly shows that high peptide cellular uptake is not sufficient to cause endosomal escape. Further suggesting that transport to these vesicles (late endosomes) is a key step in the mechanism of dfTAT cell penetration.

The ability of dfTAT to escape the endocytic pathway was also blocked when anti-BMP, an antibody known to bind and disrupt BMP dynamics, was incubated with cells and allowed to accumulate in late endosomes prior to treatment of dfTAT with cells. Interestingly, transport of dfTAT to late endosomes was detected in cells treated with anti-BMP. Previous data shows that dfTAT endosomal escape requires transport to late endosomes. Furthermore, this evidence hints that once the peptide reaches these BMP-enriched vesicles effective interactions between dfTAT and BMP are required for dfTAT

endosomal escape. This is consistent with evidence showing that TAT can disrupt membranes containing BMP and cause leaky fusion (in a BMP concentration dependent manner) more efficiently than with membranes that do not contain this phospholipid. Future experiments will be performed to investigate, in much more detail, the interactions between dfTAT and BMP and its ability to disrupt membranes that resemble different endocytic organelles including the membranes of intraluminal vesicles found inside late endosomes.

A remarkable aspect of dfTAT-mediated delivery is the minimal effect it has on cellular processes such as: cell division, transcription and endocytosis after achieving efficient endosomal leakage (as discussed before in chapter 3). It is known that endosomal lysis can be extremely toxic, in part, due to rapid release of calcium, from endocytic vesicles, into the cytosol of cells[178]. In addition, the leakage of endolysosomal proteases could contribute to toxicity[247-250]. Interestingly, dfTAT does not cause the release of a cell impermeable peptide, DEAC-K9, which was allowed to accumulate inside lysosomes. The latter suggests that dfTAT does not cause leakage of lysosomes, does not cause leakage of lysosomal proteases into the cytosolic space of cells and does not escape from these vesicles. This evidence could explain, in part, the observation that cells are not only viable but also healthy after dfTAT-mediated endosomolysis. However, these results are presumably only valid for the incubation conditions used in my assays. For example, continuous endosomal leakage induced by particulate wear debris (discussed also in chapter 3) have shown to induce inflammation and apoptosis[251]. Therefore, dfTAT

treatment could be detrimental to cells if administered for long incubation times. Future experiments will be performed to address these concerns.

## 4.4 Materials and methods

### 4.4.1 Peptide design, synthesis and purification

All peptides were synthesized in-house on the rink amide MBHA resin (Novabiochem) by solid-phase peptide synthesis (SPPS) using standard Fmoc protocols. Fmoc-Lys(Mtt)-OH, Fmoc-D-Lys(Dde)-OH, Fmoc-Lys(Boc)-OH, Fmoc-D-Lys(Boc)-OH, Fmoc-Gly-OH, Fmoc-D-Gly-OH, Fmoc-Arg(Pbf)-OH, Fmoc-D-Arg(Pbf)-OH, Fmoc-Gln(Trt)-OH, Fmoc-D-Gln(Trt)-OH, Fmoc-Cys(Trt)-OH and Fmoc-D-Cys(Trt)-OH (Novabiochem) were used to assemble the peptides (D-amino acids were used to generate the D peptide versions). Reactions were carried out in a SPPS vessel at room temperature using a stream of dry $N_2$ to provide agitation. Fmoc deprotection was performed by addition of piperidine in dimethylformamide (DMF) (Fisher) (20 %, 10 mL) to the Fmoc-peptide resin (0.30 mmol). Deprotection reactions were carried out once for 5 min (1 × 5 min) and 1 × 15 min with a washing step in between reactions. Amino acid coupling reactions were carried out for 4 h with a mixture of Fmoc-amino acid (1.2 mmol), HBTU (Novabiochem) (0.44 g, 1.1 mmol) and di-isopropylethylamine (DIEA) (Sigma) (0.51 mL, 3.0 mmol) in DMF. Upon completion of the reactions, the resin was washed with DMF and dichloromethane (DCM) (Fisher). For DEAC-K9, the DEAC fluorophore (AnaSpec) was coupled to the N terminus of the peptide after coupling of the ninth Fmoc-Lys(Boc)-OH using a mixture of DEAC, HBTU and DIEA (4, 3.9 and 10 molar

equivalents (eq) with respect to the peptide) in DMF. The reaction was carried out overnight using a stream of dry $N_2$ to provide agitation. For CK(ε-NH-TMR)TATG (fTAT), the Mtt protecting group at the ε-amino group of Lys on CK(ε-NH-Mtt)TATG was cleaved with 2 % trifluoroacetic acid (TFA) (Fisher) and 2 % tri-isopropylsilane (TIS) (Sigma) in DCM, and the resin was washed with DCM and DMF. For the D version of CK(ε-NH-TMR)TATG (ck(ε-NH-TMR)tatg, D-fTAT), the Dde protecting group at the ε-amino group of Lys on ck(ε-NH-Dde)tatg was cleaved with 2 % hydrazine monohydrate in DMF (25 mL/g of resin). To couple and label the peptides with TMR, a mixture of TMR, HBTU and DIEA (4, 3.9 and 10 eq with respect to the peptide) in DMF was added to the resin, and the reaction was carried out overnight using dry $N_2$ to provide agitation. Following Fmoc-deprotection and peptide assembly, the resin was washed with DCM and dried *in vacuo*. The resin was then treated with TFA containing 2.5 % $H_2O$, 2.5 % TIS and 2.5 % ethanedithiol (EDT) (Sigma) for 3 h at room temperature to achieve global deprotection and cleavage from the resin. The crude peptide products were precipitated and washed with cold anhydrous $Et_2O$ (Fisher). The precipitates were resuspended in water and lyophilized. The products obtained were then resuspended in 0.1 % aqueous TFA/acetonitrile. The peptides were analyzed and purified by reverse-phase HPLC. HPLC analysis was performed on a Hewlett-Packard 1200 series instrument and an analytical Vydac C18 column (5-μm particle size, 4 mm × 150 mm). The flow rate was 1 mL/min, and detection was at 214 nm and 550 nm. Semi-preparative HPLC was performed on a Vydac C18 10 × 250–mm column. The flow rate was 4 mL/min, and detection was at 214 nm and 550 nm. All runs used linear gradients of 0.1% aqueous TFA (solvent A) and 90%

acetonitrile, 9.9 % water and 0.1% TFA (solvent B). The correct identity of the peptides was confirmed by MALDI-TOF performed with a Shimadzu/Kratos instrument (AXIMA-CFR). fTAT and D-dfTAT expected mass was 2,041.17; dfTAT observed mass was 2,040.66. D-fTAT observed mass was 2,042.77 DEAC-K9 expected mass, 1,412.97; observed mass, 1,415.59.

### 4.4.2 Generation of dfTAT and D-dfTAT by dimerization of CK(TMR)TATG (fTAT) or ck(TMR)tatg (D-fTAT)

dfTAT and D-dfTAT was formed by dissolving (0.3 mg, $1.5 \times 10^{-4}$ mmol) fTAT or D-fTAT in aerated phosphate buffer saline (PBS), pH 7.4 (5 mL). Oxygen dissolved in the buffer acted to oxidize the thiol groups on the peptides and form a disulfide bond. The reaction was allowed to react overnight until completion (100 % yield according to HPLC analysis). The product was purified using analytical reverse-phase HPLC. dfTAT and D-dfTAT expected mass, 4,080.34; dfTAT observed mass, 4,084.21; D-dfTAT observed mass 4,078.87

### 4.4.3 Cell lines

HeLa (ATCC CCL-2) were grown in Dulbecco's minimum essential medium (DMEM) (Fisher) supplemented with 10% fetal bovine serum (FBS) (Fisher) and 1× penicillin/streptomycin (P/S) (Fisher) and kept at 37 °C in a humidified atmosphere containing 5 % $CO_2$. Cultures were tested for *Mycoplasma* contamination using the PCR

Mycoplasma Test Kit II (PromoKine). HeLa cells were profiled using STR, by ATCC before purchase.

### 4.4.4 Delivery of peptides inside live cells

Cells were seeded in eight-well dishes so that the cells were 80–90 % confluent after 48 h. Each well was washed three times with PBS and Leibovitz's L-15 medium that did not contain the amino acid cysteine (nonreducing L-15, nrL-15). The medium (nrL-15) used for incubation lacks cysteine to avoid reduction of the disulfide bond of dfTAT or D-dfTAT. Cells were then incubated with dfTAT or D-dfTAT (using a specified concentration) at 37 °C for 1 h. Cells were washed three times with PBS and nrL-15 and placed on an inverted epifluorescence microscope (Model IX81, Olympus) equipped with a heating stage maintained at 37 °C. Images were collected using a Rolera-MGI Plus back-illuminated electron-multiplying charge-coupled device (EMCCD) camera (Qimaging). Images were acquired using bright-field imaging and three standard fluorescence filter sets: CFP (excitation (Ex) = 436 ± 10 nm/emission (Em) = 480 ± 20 nm), RFP (Ex = 560 ± 20 nm/Em = 630 ± 35 nm) and FITC (Ex = 488 ± 10 nm/Em = 520 ± 20 nm). The fluorescence intensities of different cells were measured with the SlideBook 4.2 software (Olympus), and the average fluorescence intensity was determined for each condition. Our laboratory has previously reported that cell-penetrating peptides labeled with fluorophores such as TMR can photosensitize membranes and cause endosomal leakage upon light irradiation[175, 246]. To minimize the role played by light irradiation in the activities reported herein, I performed all delivery experiments under conditions of minimal light irradiation

(dark room with dim red light). When fluorescence imaging was required, probes (for example, DEAC-K9 and LysoTracker® Green) were imaged before dfTAT and D-dfTAT images were acquired. dfTAT and D-dfTAT were also excited for only a maximum of 300 ms. In contrast, the light dose required to observe light-induced endosomal leakage was typically 10- to 20-fold greater than that used for imaging.

### 4.4.5 Determination of dfTAT cell localization and quantitative determination of dfTAT endosomal escape in cells expressing DN-Rab5 and DN-Rab7

HeLa cells were seeded in eight-well dishes, grown and washed as described in the prior section. Cells expressing DN-Rab5 or DN-Rab7 were incubated with 3 μM dfTAT for 1 h at 37 °C. Cells were washed three times with heparin/PBS and nrL-15. Images were acquired as described before. For transfection and expression of DN-Rab5 (Rab5(Q79L)) and DN-Rab7 (Rab7(Q67L)), plasmids (purchased from addgene) were mixed with Lipofectamine 2000 reagent in opti-MEM medium and incubated at room temperature for 30 min. The DNA complex was added to previously seeded HeLa cells (70-80 % confluent) on an eight-well dish, and cells were kept at 37 °C for 18 h. After 18 h, the wells were washed three times with PBS and nrL-15 before performing the delivery experiments using dfTAT. Cells displaying a cytosolic/nuclear fluorescence distribution was established to determine the % of cells with cytosolic/nuclear dfTAT fluorescence distribution and divided by the total number of cells in the well, as determined from bright field images (~2000 cells were counted in each experiments).

### 4.4.6 Delivery of DEAC-K9 inside live cells with dfTAT or D-dfTAT

HeLa were seeded in eight-well dishes, grown and washed as described in the prior section. Cells were incubated with 10 μM DEAC-K9 for 1 h at 37 °C. Cells were washed three times with heparin/PBS and nrL-15 and placed on the heating stage maintained at 37 °C. The delivery peptide was incubated with cells quickly after or 2 h after washing the cells for 1 h at 37 °C. Cells were washed three times with heparin/PBS and nrL-15 and LysoTracker® Green (250 nM) was added. Images were acquired as described before.

### 4.4.7 Quantitative analysis of dfTAT delivery in cells incubated with anti-BMP

HeLa cells were seeded in eight-well dishes, grown and washed as described in the prior section. Cells were incubated with 50 μg/mL purified mouse monoclonal anti-BMP (6C4) (Echelon Biosciences, Cat. No. Z-PLBPA) for 30 min (short incubation) or 18 h (long incubation) at 37 °C. Cells were washed three times with heparin/PBS and nrL-15 and placed on the heating stage maintained at 37 °C. dfTAT (3 μM) was incubated with cells for 1 h at 37 °C. Cells were washed three times with heparin/PBS and nrL-15. Images were acquired as described before. Cells displaying a cytosolic/nuclear fluorescence distribution was established to determine the % of cells with cytosolic/nuclear dfTAT fluorescence distribution and divided by the total number of cells in the well, as determined from bright field images (~2000 cells were counted in each experiments).

### 4.4.8 Quantitative determination of peptide uptake inside cells

HeLa cells were seeded in a 48-well dish, grown and washed as described above. For the DN-Rab5 and DN-Rab7 and anti-BMP or FITC mouse anti-human IgG (Abcam 99772) experiments cells were incubated with dfTAT (specified concentration) after transfection and incubation with antibody, respectively. For the retro-2 experiment, cells were incubated with dfTAT (specified concentration) after incubating cells with retro-2 (20 μM) for 30 min as described before in (270). Cells were then washed with PBS with heparin (1 mg/mL) and nrL-15 and imaged. To lyse cells, I removed nrL-15 from the wells, and a total of 100 μL of lysis buffer (50 mM Tris, pH 7.5, 2 mM EDTA, 2 mM DTT, 0.1 % Triton X-100) were incubated with cells for 5 min. Cells were scraped off the dish, and the cell lysate was pipetted into a 1.5-mL microcentrifuge tube and centrifuged at 13,000 r.p.m for 25 min (rotor radius: 8.4 cm). For uptake measurement, 70 μl of supernatant were collected and placed in a 96-well plate. The fluorescence emission intensity was measured using a plate reader equipped with a fluorescence module (Ex = 525 nm, Em = 580–640 nm) (GloMax-Multi+ Detection System, Promega). Fluorescence intensities were normalized to total protein concentration in each well (determined by Bradford protein assay, wherein 10 μl of each cell lysate is added to 200 μL of a 1× protein assay reagent and then incubated at room temperature for 30 min; absorbance at 600 nm is measured using the plate reader). All experiments were performed in triplicate.

# 5. CONCLUSION

Due to the enhanced functional activity observed from specific molecules that exist in nature (viruses, antibodies), I propose that multivalency can be used to increase the delivery activity of monomeric CPPs. In chapter two, I generated a series of multivalent peptide constructs of the CPP TAT to establish the effect of multivalency in CPP delivery and to study the mechanism of multivalent CPP penetration. I observed a significant increase in the endosomolytic activity of the CPP TAT after conjugating TAT-thioester to a scaffold peptide containing n number of LysGly repeats (n =3) and displaying multiple copies of this CPP. This trimeric endosomolytic agent was able to deliver intact functional molecules into the cytosolic space of live cells, including a bioactive cell-impermeable peptide that can cause apoptosis. Interestingly, a dimeric version of this multivalent peptide construct could not escape from endosomes while a tetrameric version was not able to reach the cytosolic space of cells due to unproductive plasma membrane binding. The results revealed that although multivalency is an effective strategy to increase the endosomolytic activity of CPPs increasing the number of CPP copies display in the delivery agent does not always translate to increase in delivery activity. However, this phenomenon may vary between multivalent CPPs displaying different sequences and structures and might not be true for other multivalent CPPs. Yet, finding just the right number of CPPs that will lead to the highest achievable delivery activity is key to generate improved delivery agents.

The synthesis protocol for these multivalent delivery agents was difficult and produced low yields. Furthermore, the amount of delivery agent required to study and establish the mechanism of penetration involved in multivalent CPP-mediated macromolecule delivery, which was my main goal, was high. For this reason I set out to develop a new delivery agent that displayed highly efficient endosomolytic activity but that, at the same time, was simple to generate in high yields. In chapter three, I observed that a dimeric-branched multivalent delivery agent of the CPP TAT, dfTAT, penetrated live cells by escaping from endosomes with remarkable high efficiency (dfTAT can be produced by simple disulfide bond formation in high yields). Moreover, I found that dfTAT escaped the endocytic pathway and entered the cytosolic space of cells more efficiently that its monomeric counterpart even when both peptides where present inside endocytic vesicles at the same amounts. Consequently, I was able to directly establish for the first time that displaying multiple copies of a CPP can increase its endosomolytic activity. Furthermore, dfTAT delivered different proteins including a fluorescent protein, EGFP, an enzyme, Cre-recombinase, a mitochondrial antibody, anti-ATP5A and a transcription factor, HoxB4 using a simple co-incubation protocol. Delivery was achieved in multiple cell types including primary cells and I observed that only a few molecules remained trapped inside endosomes. Interestingly, I was able to deliver multiple molecules inside cells simultaneously and more than once and the amount of cargo delivered could be controlled. Remarkably, noticeable negative effects on cell viability, cell proliferation or transcription did not accompany the herculean endosomolytic activity displayed by

dfTAT. These results revealed that dfTAT offers several advantages over existing delivery agents.

Throughout my studies, I aimed to better understand the mechanism of multivalent CPP penetration. In chapter four, I observed that dfTAT penetration was blocked after expression of DN-Rab5 and DN-Rab7 in cells. This result revealed that dfTAT does not escape from early endosomes and that it has transport and reach endocytic vesicles found late in the endocytic pathway to escape from endosomes. I found that dfTAT could not cause leakage of DEAC-K9, which accumulates inside lysosomes. This result revealed that dfTAT does not escape from lysosomes. Furthermore, this shows that dfTAT presumably does not cause leakage of lysosomal proteases. This, in part, can explain the observed low cytotoxicity associated with dfTAT endosomolysis. Finally, I showed that dfTAT penetration is blocked by an antibody that accumulates in late endosomes, binds and disrupts BMP dynamics, anti-BMP. This result revealed that both transport to late endosomes and interactions between BMP and dfTAT are necessary for penetration of dfTAT inside live cells. The collective of insights herein provides a basis for the design of improved delivery agents that could prove useful for the delivery of molecules. Moreover, the delivery agents shown here, specially dfTAT, could be very useful for delivery of molecules into tissues, manipulation of cells in a culture (cell reprogramming), the study of cell processes in live cells (cell-based assays) and cell imaging applications.

# REFERENCES


1. Foged, C. & Nielsen, H.M. Cell-Penetrating Peptides for Drug Delivery Across Membrane Barriers. *Expert Opinion on Drug Delivery* 5, 105-117 (2008).

2. Drin, G., Cottin, S., Blanc, E., Rees, A.R. & Temsamani, J. Studies on The Internalization Mechanism of Cationic Cell-Penetrating Peptides. *Journal of Biological Chemistry* 278, 31192-31201 (2003).

3. Torchilin, V. Intracellular Delivery of Protein And Peptide Therapeutics. *Drug Discovery Today: Technologies* 5, e95-e103 (2008).

4. Chakravarty, P., Qian, W., El-Sayed, M.A. & Prausnitz, M.R. Delivery of Molecules Into Cells Using Carbon Nanoparticles Activated by Femtosecond Laser Pulses. *Nat Nano* 5, 607-611 (2010).

5. Kaczmarczyk, S.J., Sitaraman, K., Young, H.A., Hughes, S.H. & Chatterjee, D.K. Protein Delivery Using Engineered Virus-Like Particles. *Proceedings of the National Academy of Sciences* 108, 16998-17003 (2011).

6. Kabouridis, P.S. Biological Applications of Protein Transduction Technology. *Trends in Biotechnology* 21, 498-503 (2003).

7. Morris, M.C., Vidal, P., Chaloin, L., Heitz, F. & Divita, G. A New Peptide Vector for Efficient Delivery of Oligonucleotides Into Mammalian Cells. *Nucleic Acids Research* 25, 2730-2736 (1997).

8. Dietz, G.P.H. & Bδhr, M. Delivery of Bioactive Molecules Into the Cell: The Trojan Horse Approach. *Molecular and Cellular Neuroscience* 27, 85-131 (2004).

9. Patel, L., Zaro, J. & Shen, W.-C. Cell Penetrating Peptides: Intracellular Pathways and Pharmaceutical Perspectives. *Pharm Res* 24, 1977-1992 (2007).

10. Lewis, J.G. et al. A Serum-Resistant Cytofectin for Cellular Delivery of Antisense Oligodeoxynucleotides and Plasmid DNA. *Proceedings of the National Academy of Sciences* 93, 3176-3181 (1996).

11. Suhorutsenko, J. et al. Cell-Penetrating Peptides, PepFects, Show No Evidence of Toxicity and Immunogenicity In Vitro and In Vivo. *Bioconjugate chemistry* 22, 2255-2262 (2011).

12. Rennert, R., Neundorf, I. & Beck-Sickinger, A.G. Calcitonin-Derived Peptide Carriers: Mechanisms and Application. *Advanced Drug Delivery Reviews* 60, 485-498 (2008).

13. Bitler, B.G.a.S., J. A. Anti-Cancer Therapies That Utilize Cell Penetrating Peptides. *Recent Pat. Anticancer Drug Discovery* 5, 99– 108 (2010).

14. Frankel, A.D. & Pabo, C.O. Cellular Uptake of the Tat Protein From Human Immunodeficiency Virus. *Cell* 55, 1189-1193 (1988).

15. Green, M. & Loewenstein, P.M. Autonomous Functional Domains of Chemically Synthesized Human Immunodeficiency Virus Tat Trans-Activator Protein. *Cell* 55, 1179-1188 (1988).

16. Mann, D.A. & Frankel, A.D. Endocytosis and Targeting of Exogenous HIV-1 Tat Protein. *EMBO Journal* 10, 1733-1739 (1991).

17. Vivès, E., Brodin, P. & Lebleu, B. A Truncated HIV-1 Tat Protein Basic Domain Rapidly Translocates through the Plasma Membrane and Accumulates in the Cell Nucleus. *Journal of Biological Chemistry* 272, 16010-16017 (1997).

18. Derossi, D., Joliot, A.H., Chassaing, G. & Prochiantz, A. The Third Helix of the Antennapedia Homeodomain Ttranslocates Through Biological Membranes. *Journal of Biological Chemistry* 269, 10444-10450 (1994).

19. Nishikawa, M. et al. Induction of Tumor-specific Immune Response by Gene Transfer of Hsp70-cell-penetrating Peptide Fusion Protein to Tumors in Mice. *Mol Ther* 18, 421-428 (2009).

20. Deshayes, S., Morris, M.C., Divita, G. & Heitz, F. Interactions of Amphipathic CPPs With Model Membranes. *Biochimica et Biophysica Acta (BBA) - Biomembranes* 1758, 328-335 (2006).

21. Pooga, M., Hällbrink, M., Zorko, M., Langel, U. Cell Penetration by Transportan. *The FASEB Journal* 12, 67-77 (1998).

22. Matsushita, M. et al. A High-Efficiency Protein Transduction System Demonstrating the Role of PKA in Long-Lasting Long-Term Potentiation. *The Journal of Neuroscience* 21, 6000-6007 (2001).

23. Morris, M.C., Depollier, J., Mery, J., Heitz, F. & Divita, G. A Peptide Carrier For The Delivery of Biologically Active Proteins Into Mammalian Cells. *Nat Biotech* 19, 1173-1176 (2001).

24. Montrose, K., Yang, Y., Sun, X., Wiles, S. & Krissansen, G.W. Xentry, A New Class of Cell-Penetrating Peptide Uniquely Equipped For Delivery of Drugs. *Sci. Rep.* 3 (2013).

25. Crombez, L. et al. A New Potent Secondary Amphipathic Cell-penetrating Peptide for siRNA Delivery Into Mammalian Cells. *Mol Ther* 17, 95-103 (2008).

26. Lorents, A. et al. Cell-penetrating Peptides Split into Two Groups Based on Modulation of Intracellular Calcium Concentration. *Journal of Biological Chemistry* 287, 16880-16889 (2012).

27. Munyendo, W.L., Lv, H., Benza-Ingoula, H., Baraza, L.D. & Zhou, J. Cell Penetrating Peptides in the Delivery of Biopharmaceuticals. *Biomolecules* 2, 187-202 (2012).

28. El-Andaloussi, S., Holm, T. & Langel, U. Cell-Penetrating Peptides: Mechanisms and Applications. *Current Pharmaceutical Design* 11, 3597-3611 (2005).

29. El-Andaloussi, S., Johansson, H.J., Holm, T. & Langel, U. A Novel Cell-penetrating Peptide, M918, for Efficient Delivery of Proteins and Peptide Nucleic Acids. *Mol Ther* 15, 1820-1826 (2007).

30. Johnson, R., Harrison, S. & Maclean, D. in Cell-Penetrating Peptides, Vol. 683. (ed. Ü. Langel) 535-551 (Humana Press, 2011).

31. Wagstaff, K.M. & Jans, D.A. Protein Transduction: Cell Penetrating Peptides and Their Therapeutic Applications. *Current Medicinal Chemistry* 13, 1371-1387 (2006).

32. Phelan, A., Elliott, G. & O'Hare, P. Intercellular Delivery of Functional p53 by the Herpesvirus Protein VP22. *Nat Biotech* 16, 440-443 (1998).

33. Snyder, E.L., Meade, B.R., Saenz, C.C. & Dowdy, S.F. Treatment of Terminal Peritoneal Carcinomatosis by a Transducible p53-Activating Peptide. *PLoS Biol* 2, e36 (2004).

34. Michl, J. et al. PNC-28, a p53-Derived Peptide That is Cytotoxic To Cancer Cells, Blocks Pancreatic Cancer Cell Growth In Vivo. *International Journal of Cancer* 119, 1577-1585 (2006).

35. Takenobu, T. et al. Development of p53 Protein Transduction Therapy Using Membrane-permeable Peptides and the Application to Oral Cancer Cells. *Molecular Cancer Therapeutics* 1, 1043-1049 (2002).

36. Pooga, M. et al. Cell Penetrating PNA Constructs Regulate Galanin Receptor Levels and Modify Pain Transmission In Vivo. *Nat Biotech* 16, 857-861 (1998).

37. Schwarze, S.R., Ho, A., Vocero-Akbani, A. & Dowdy, S.F. In Vivo Protein Transduction: Delivery of a Biologically Active Protein Into the Mouse. *Science* 285, 1569-1572 (1999).

38. Dash-Wagh, S. et al. Intracellular Delivery of Short Interfering RNA in Rat Organ of Corti Using a Cell-penetrating Peptide PepFect6. *Mol Ther Nucleic Acids* 1, e61 (2012).

39. Mo, R.H., Zaro, J.L. & Shen, W.-C. Comparison of Cationic and Amphipathic Cell Penetrating Peptides for siRNA Delivery and Efficacy. *Molecular Pharmaceutics* 9, 299-309 (2011).

40. Meade, B.R. & Dowdy, S.F. Exogenous siRNA Delivery Using Peptide Transduction Domains/Cell Penetrating Peptides. *Advanced Drug Delivery Reviews* 59, 134-140 (2007).

41. Davidson, T.J. et al. Highly Efficient Small Interfering RNA Delivery to Primary Mammalian Neurons Induces MicroRNA-Like Effects before mRNA Degradation. *The Journal of Neuroscience* 24, 10040-10046 (2004).

42. Sharma, G. et al. Cell Penetrating Peptide Tethered Bi-Ligand Liposomes for Delivery to Brain In Vivo: Biodistribution and Transfection. *Journal of Controlled Release* 167, 1-10 (2013).

43. Sayers, E.J., Cleal, K., Eissa, N.G., Watson, P. & Jones, A.T. Distal Phenylalanine Modification for Enhancing Cellular Delivery of Fluorophores, Proteins and Quantum Dots by Cell Penetrating Peptides. *Journal of Controlled Release*.

44. Deshayes, S., Morris, M.C., Divita, G. & Heitz, F. Cell-Penetrating Peptides: Tools for Intracellular Delivery of Therapeutics. *CMLS, Cell. Mol. Life Sci.* 62, 1839-1849 (2005).

45. Berry, C.C. Intracellular Delivery of Nanoparticles Via the HIV-1 Tat Peptide. *Nanomedicine* 3, 357-365 (2008).

46. Liu, B.R., Huang, Y.-w., Winiarz, J.G., Chiang, H.-J. & Lee, H.-J. Intracellular Delivery of Quantum Dots Mediated by a Histidine- and Arginine-Rich HR9 Cell-Penetrating Peptide Through the Direct Membrane Translocation Mechanism. *Biomaterials* 32, 3520-3537 (2011).

47. Denicourt, C. & Dowdy, S.F. Protein Transduction Technology Offers Novel Therapeutic Approach for Brain Ischemia. *Trends in Pharmacological Sciences* 24, 216-218 (2003).

48. Richard, J.P. et al. Cell-penetrating Peptides: A Reevaluation of the Mechanism of Cellular Uptake. *Journal of Biological Chemistry* 278, 585-590 (2003).

49. Fuchs, S.M. & Raines, R.T. Pathway for Polyarginine Entry Into Mammalian Cells†. *Biochemistry* 43, 2438-2444 (2004).

50. Al-Taei, S. et al. Intracellular Traffic and Fate of Protein Transduction Domains HIV-1 TAT Peptide and Octaarginine. Implications for Their Utilization as Drug Delivery Vectors. *Bioconjugate chemistry* 17, 90-100 (2005).

51. Nishi, K. & Saigo, K. Cellular Internalization of Green Fluorescent Protein Fused with Herpes Simplex Virus Protein VP22 via a Lipid Raft-mediated Endocytic Pathway Independent of Caveolae and Rho Family GTPases but Dependent on Dynamin and Arf6. *Journal of Biological Chemistry* 282, 27503-27517 (2007).

52. Gillmeister, M.P., Betenbaugh, M.J. & Fishman, P.S. Cellular Trafficking and Photochemical Internalization of Cell Penetrating Peptide Linked Cargo Proteins: A Dual Fluorescent Labeling Study. *Bioconjugate chemistry* 22, 556-566 (2011).

53. Turner, J.J., Arzumanov, A.A. & Gait, M.J. Synthesis,Cellular Uptake and HIV-1 Tat-Dependent Trans-Activation Inhibition Activity of Oligonucleotide Analogues Disulphide-Conjugated to Cell-Penetrating Peptides. *Nucleic Acids Research* 33, 27-42 (2005).

54. El-Sayed, A., Futaki, S. & Harashima, H. Delivery of Macromolecules Using Arginine-Rich Cell-Penetrating Peptides: Ways to Overcome Endosomal Entrapment. *AAPS J* 11, 13-22 (2009).

55. Vivès, E., Schmidt, J. & Pèlegrin, A. Cell-Penetrating and Cell-Targeting Peptides in Drug Delivery. *Biochimica et Biophysica Acta (BBA) - Reviews on Cancer* 1786, 126-138 (2008).

56. Guterstam, P. et al. Elucidating Cell-Penetrating Peptide Mechanisms of Action for Membrane Iinteraction, Cellular Uptake, and Translocation Utilizing the Hydrophobic Counter-Anion Pyrenebutyrate. *Biochimica et Biophysica Acta (BBA) - Biomembranes* 1788, 2509-2517 (2009).

57. Rydström, A. et al. Direct Translocation as Major Cellular Uptake for CADY Self-Assembling Peptide-Based Nanoparticles. *PloS one* 6, e25924 (2011).

58. Madani, F. et al. Mechanisms of Cellular Uptake of Cell-Penetrating Peptides. *Journal of Biophysics* 2011 (2011).

59. Trabulo, S., Cardoso, A.L., Mano, M. & De Lima, M.C.P. Cell-Penetrating Peptides—Mechanisms of Cellular Uptake and Generation of Delivery Systems. *Pharmaceuticals* 3, 961-993 (2010).

60. Madani, F. et al. Modeling the Endosomal Escape of Cell-Penetrating Peptides Using a Transmembrane pH Gradient. *Biochimica et Biophysica Acta (BBA) - Biomembranes* 1828, 1198-1204 (2013).

61. Qian, Z. et al. Early Endosomal Escape of a Cyclic Cell-Penetrating Peptide Allows Effective Cytosolic Cargo Delivery. *Biochemistry* 53, 4034-4046 (2014).

62. Magzoub, M., Gr, auml & slund, A. Cell-Penetrating Peptides: Small from Inception to Application. *Quarterly Reviews of Biophysics* 37, 147-195 (2004).

63. Säälik, P. et al. Penetration Without Cells: Membrane Translocation of Cell-Penetrating Peptides in the Model Giant Plasma Membrane Vesicles. *Journal of Controlled Release* 153, 117-125 (2011).

64. Yandek, L.E. et al. Mechanism of the Cell-Penetrating Peptide Transportan 10 Permeation of Lipid Bilayers. *Biophysical Journal* 92, 2434-2444 (2007).

65. Derossi, D., Chassaing, G. & Prochiantz, A. Trojan Peptides: Tthe Penetratin System for Intracellular Delivery. *Trends in Cell Biology* 8, 84-87 (1998).

66. Su, Y., Doherty, T., Waring, A.J., Ruchala, P. & Hong, M. Roles of Arginine and Lysine Residues in the Translocation of a Cell-Penetrating Peptide from 13C, 31P, and 19F Solid-State NMR. *Biochemistry* 48, 4587-4595 (2009).

67. Console, S., Marty, C., García-Echeverría, C., Schwendener, R. & Ballmer-Hofer, K. Antennapedia and HIV TAT 'Protein Transduction Domains' Promote Endocytosis of High Mr Cargo Upon Binding to Cell Surface Glycosaminoglycans. *Journal of Biological Chemistry* (2003).

68. Sun, D., Forsman, J., Lund, M. & Woodward, C.E. Effect of Arginine-Rich Cell Penetrating Peptides on Membrane Pore Formation and Life-Times: A Molecular Simulation Study. *Physical Chemistry Chemical Physics* 16, 20785-20795 (2014).

69. Deshayes, S., Konate, K., Aldrian, G., Heitz, F. & Divita, G. in Cell-Penetrating Peptides, Vol. 683. (ed. Ü. Langel) 41-56 (Humana Press, 2011).

70. Räägel, H., Säälik, P. & Pooga, M. Peptide-Mediated Protein Delivery—Which Pathways Are Penetrable? *Biochimica et Biophysica Acta (BBA) - Biomembranes* 1798, 2240-2248 (2010).

71. Khalil, I.A., Kogure, K., Akita, H. & Harashima, H. Uptake Pathways and Subsequent Intracellular Trafficking in Nonviral Gene Delivery. *Pharmacological Reviews* 58, 32-45 (2006).

72. Chen, X., Sa'adedin, F., Deme, B., Rao, P. & Bradshaw, J. Insertion of TAT Peptide and Perturbation of Negatively Charged Model Phospholipid Bilayer Revealed by Neutron Diffraction. *Biochimica et Biophysica Acta (BBA) - Biomembranes* 1828, 1982-1988 (2013).

73. Tünnemann, G. et al. Live-Cell Analysis of Cell Penetration Ability and Toxicity of Oligo-Arginines. *Journal of Peptide Science* 14, 469-476 (2008).

74. Wender, P.A., Galliher, W.C., Goun, E.A., Jones, L.R. & Pillow, T.H. The Design of Guanidinium-Rich Transporters and Their Internalization Mechanisms. *Advanced Drug Delivery Reviews* 60, 452-472 (2008).

75. Futaki, S. Arginine-Rich Peptides: Potential for Intracellular Delivery of Macromolecules and The Mystery of the Translocation Mechanisms. *International journal of pharmaceutics* 245, 1-7 (2002).

76. Rothbard, J.B. et al. Arginine-Rich Molecular Transporters for Drug Delivery: Role of Backbone Spacing in Cellular Uptake. *Journal of Medicinal Chemistry* 45, 3612-3618 (2002).

77. Åmand, H.L. et al. Cell Surface Binding and Uptake of Arginine- and Lysine-Rich Penetratin Peptides in Absence and Presence of Proteoglycans. *Biochimica et Biophysica Acta (BBA) - Biomembranes* 1818, 2669-2678 (2012).

78. Tumova, S., Woods, A. & Couchman, J.R. Heparan Sulfate Chains from Glypican and Syndecans Bind the Hep II Domain of Fibronectin Similarly Despite Minor Structural Differences. *Journal of Biological Chemistry* 275, 9410-9417 (2000).

79. Poon, G.M. & Gariepy, J. Cell-Surface Proteoglycans as Molecular Portals for Cationic Peptide and Polymer Entry Into Cells. *Biochemical Society Transactions* 35, 788-793 (2007).

80. Richard, J.P. et al. Cellular Uptake of Unconjugated TAT Peptide Involves Clathrin-Dependent Endocytosis and Heparan Sulfate Receptors. *Journal of Biological Chemistry* 280, 15300-15306 (2005).

81. van der Voort, R., Keehnen, R.M.J., Beuling, E.A., Spaargaren, M. & Pals, S.T. Regulation of Cytokine Signaling by B Cell Antigen Receptor and Cd40-Controlled Expression of Heparan Sulfate Proteoglycans. *The Journal of Experimental Medicine* 192, 1115-1124 (2000).

82. Haupt, L.M. et al. The Heparan Sulfate Proteoglycan (HSPG) Glypican-3 Mediates Commitment of MC3T3-E1 Cells Toward Osteogenesis. *Journal of Cellular Physiology* 220, 780-791 (2009).

83. Echtermeyer, F. et al. Delayed Wound Repair and Impaired Angiogenesis in Mice Lacking Syndecan-4. *The Journal of Clinical Investigation* 107, R9-R14 (2001).

84. Bishop, J.R., Schuksz, M. & Esko, J.D. Heparan Sulphate Proteoglycans Fine-Tune Mammalian Physiology. *Nature* 446, 1030-1037 (2007).

85. Coppi, A. et al. Heparan Sulfate Proteoglycans Provide a Signal to Plasmodium Sporozoites to Stop Migrating and Productively Invade Host Cells. *Cell Host & Microbe* 2, 316-327 (2007).

86. Fuki, I.V., Iozzo, R.V. & Williams, K.J. Perlecan Heparan Sulfate Proteoglycan: A Novel Receptor that Mediates a Distinct Pathway For Ligand Catabolism. *Journal of Biological Chemistry* 275, 25742-25750 (2000).

87. Argyris, E.G. et al. The Perlecan Heparan Sulfate Proteoglycan Mediates Cellular Uptake of HIV-1 Tat Through a PathwayResponsible for Biological Activity. *Virology* 330, 481-486 (2004).

88. ZIMMERMANN, P. & DAVID, G. The Syndecans, Tuners of Transmembrane Signaling. *The FASEB Journal* 13, 91-100 (1999).

89. Lambaerts, K., Wilcox-Adelman, S.A. & Zimmermann, P. The Signaling Mechanisms of Syndecan Heparan Sulfate Proteoglycans. *Current Opinion in Cell Biology* 21, 662-669 (2009).

90. Beckett, K., Franch-Marro, X. & Vincent, J.-P. Glypican-Mediated Endocytosis of Hedgehog has Opposite Effects in Flies and Mice. *Trends in Cell Biology* 18, 360-363 (2008).

91. Flannagan, R.S., Jaumouillé, V. & Grinstein, S. The Cell Biology of Phagocytosis. *Annual Review of Pathology: Mechanisms of Disease* 7, 61-98 (2012).

92. Watts, C. & Marsh, M. Endocytosis: What Goes In and How? *Journal of Cell Science* 103, 1-8 (1992).

93. Lim, J.P. & Gleeson, P.A. Macropinocytosis: An Endocytic Pathway for Internalising Large Gulps. *Immunol Cell Biol* 89, 836-843 (2011).

94. Lamaze, C. & Schmid, S.L. The Emergence of Clathrin-Independent Pinocytic Pathways. *Current Opinion in Cell Biology* 7, 573-580 (1995).

95. Nabi, I.R. & Le, P.U. Caveolae/Raft-Dependent Endocytosis. *The Journal of Cell Biology* 161, 673-677 (2003).

96. McMahon, H.T. & Boucrot, E. Molecular Mechanism and Physiological Functions of Clathrin-Mediated Endocytosis. *Nat Rev Mol Cell Biol* 12, 517-533 (2011).

97. Abes, S. et al. Endosome Trapping Limits the Efficiency of Splicing Correction by PNA-Oligolysine Conjugates. *Journal of Controlled Release* 110, 595-604 (2006).

98. Jones, A.T. Macropinocytosis: Searching for an Endocytic Identity and Role in the Uptake of Cell Penetrating Peptides. *Journal of Cellular and Molecular Medicine* 11, 670-684 (2007).

99. Nakase, I. et al. Cellular Uptake of Arginine-Rich Peptides: Roles for Macropinocytosis and Actin Rearrangement. *Mol Ther* 10, 1011-1022 (2004).

100. Jiyoon, R., Kyuhyung, H., Jinseu, P. & Soo Young, C. Enhanced Uptake of a Heterologous Protein with an HIV-1 Tat Protein Transduction Domains (PTD) at Both Termini. *Mol. Cells* 16, 385-391 (2003).

101. Mäger, I., Langel, K., Lehto, T., Eiríksdóttir, E. & Langel, Ü. The Role of Endocytosis on the Uptake Kinetics of Luciferin-Conjugated Cell-Penetrating Peptides. *Biochimica et Biophysica Acta (BBA) - Biomembranes* 1818, 502-511 (2012).

102. Duchardt, F., Fotin-Mleczek, M., Schwarz, H., Fischer, R. & Brock, R. A Comprehensive Model for the Cellular Uptake of Cationic Cell-penetrating Peptides. *Traffic* 8, 848-866 (2007).

103. Appelbaum, Jacob S. et al. Arginine Topology Controls Escape of Minimally Cationic Proteins from Early Endosomes to the Cytoplasm. *Chemistry & Biology* 19, 819-830 (2012).

104. Vercauteren, D. et al. The Use of Inhibitors to Study Endocytic Pathways of Gene Carriers: Optimization and Pitfalls. *Mol Ther* 18, 561-569 (2010).

105. Fotin-Mleczek, M. et al. Cationic Cell-Penetrating Peptides Interfere with TNF Signalling by Induction of TNF Receptor Internalization. *Journal of Cell Science* 118, 3339-3351 (2005).

106. Rinne, J. et al. Internalization of Novel Non-Viral Vector TAT-Streptavidin Into Human Cells. *BMC Biotechnology* 7, 1 (2007).

107. Gump, J.M., June, R.K. & Dowdy, S.F. Revised Role of Glycosaminoglycans in TAT Protein Transduction Domain-mediated Cellular Transduction. *Journal of Biological Chemistry* 285, 1500-1507 (2010).

108. Marsh, M. & McMahon, H.T. The Structural Era of Endocytosis. *Science* 285, 215-220 (1999).

109. Swanson, J.A. & Watts, C. Macropinocytosis. *Trends in Cell Biology* 5, 424-428 (1995).

110. Bryant, D.M. et al. EGF Induces Macropinocytosis and SNX1-Modulated Recycling of E-Cadherin. *Journal of Cell Science* 120, 1818-1828 (2007).

111. Grimmer, S., van Deurs, B. & Sandvig, K. Membrane Ruffling and Macropinocytosis in A431 Cells Require Cholesterol. *Journal of Cell Science* 115, 2953-2962 (2002).

112. Gold, S., Monaghan, P., Mertens, P. & Jackson, T. A Clathrin Independent Macropinocytosis-Like Entry Mechanism Used by Bluetongue Virus-1 During Infection of BHK Cells. *PloS one* 5, e11360 (2010).

113. Mishra, A. et al. Translocation of HIV TAT Peptide and Analogues Induced by Multiplexed Membrane and Cytoskeletal Interactions. *Proceedings of the National Academy of Sciences* 108, 16883-16888 (2011).

114. Thomas D. Pollard, W.C.E., and Jennifer Lippincott-Schwartz, Vol. 2nd edition Chapter 22 (Elsevier, 2007).

115. Wang, J.T.H., Teasdale, R.D. & Liebl, D. Macropinosome Quantitation Assay. *MethodsX* 1, 36-41 (2014).

116. Swanson, J.A. Shaping Cups Into Phagosomes and Macropinosomes. *Nat Rev Mol Cell Biol* 9, 639-649 (2008).

117. Stoorvogel, W., Oorschot, V. & Geuze, H.J. A Novel Class of Clathrin-Coated Vesicles Budding From Endosomes. *The Journal of Cell Biology* 132, 21-33 (1996).

118. Fridolfsson, H.N., Roth, D.M., Insel, P.A. & Patel, H.H. Regulation of Intracellular Signaling and Function by Caveolin. *The FASEB Journal* 28, 3823-3831 (2014).

119. Gruenberg, J. The Endocytic Pathway: A Mosaic of Domains. *Nat Rev Mol Cell Biol* 2, 721-730 (2001).

120. Gorvel, J.-P., Chavrier, P., Zerial, M. & Gruenberg, J. Rab5 Controls Early Endosome Fusion In Vitro. *Cell* 64, 915-925.

121. Huotari, J.H.A. Endosome maturation. *The EMBO Journal* 30, 3481-3500 (2011).

122. Gruenberg, J. & Stenmark, H. The Biogenesis of Multivesicular Endosomes. *Nat Rev Mol Cell Biol* 5, 317-323 (2004).

123. Scheuring, D. et al. Multivesicular Bodies Mature from the Trans-Golgi Network/Early Endosome in Arabidopsis. *The Plant Cell Online* 23, 3463-3481 (2011).

124. Peng, J. et al. Atg5 Regulates Late Endosome and Lysosome Biogenesis. *Sci. China Life Sci.* 57, 59-68 (2014).

125. Stoorvogel, W., Strous, G.J., Geuze, H.J., Oorschot, V. & Schwartzt, A.L. Late Endosomes Derive From Early Endosomes by Maturation. *Cell* 65, 417-427.

126. Humphries, W.H.I.V., Szymanski, C.J. & Payne, C.K. Endo-Lysosomal Vesicles Positive for Rab7 and LAMP1 Are Terminal Vesicles for the Transport of Dextran. *PloS one* 6, e26626 (2011).

127. Vanlandingham, P.A. & Ceresa, B.P. Rab7 Regulates Late Endocytic Trafficking Downstream of Multivesicular Body Biogenesis and Cargo Sequestration. *Journal of Biological Chemistry* 284, 12110-12124 (2009).

128. Kobayashi, T. et al. A Lipid Associated with the Antiphospholipid Syndrome Regulates Endosome Structure and Function. *Nature* 392, 193-197 (1998).

129. Roth, S.L. & Whittaker, G.R. Promotion of Vesicular Stomatitis Virus Fusion by the Endosome-Specific Phospholipid Bis(monoacylglycero)phosphate (BMP). *FEBS Letters* 585, 865-869 (2011).

130. Le Blanc, I. et al. Endosome-to-Cytosol Transport of Viral Nucleocapsids. *Nat Cell Biol* 7, 653-664 (2005).

131. Yang, S.-T., Zaitseva, E., Chernomordik, L.V. & Melikov, K. Cell-Penetrating Peptide Induces Leaky Fusion of Liposomes Containing Late Endosome-Specific Anionic Lipid. *Biophysical Journal* 99, 2525-2533 (2010).

132. Saftig, P. & Klumperman, J. Lysosome Biogenesis and Lysosomal Membrane Proteins: Trafficking Meets Function. *Nat Rev Mol Cell Biol* 10, 623-635 (2009).

133. Lee, Y.-J., Datta, S. & Pellois, J.-P. Real-Time Fluorescence Detection of Protein Transduction into Live Cells. *Journal of the American Chemical Society* 130, 2398-2399 (2008).

134. Burlina, F., Sagan, S., Bolbach, G. & Chassaing, G. A Direct Approach to Quantification of the Cellular Uptake of Cell-Penetrating Peptides Using MALDI-TOF Mass Spectrometry. *Nat. Protocols* 1, 200-205 (2006).

135. Paramelle, D. et al. A Straightforward Approach for Cellular-Uptake Quantification. *Angewandte Chemie International Edition* 49, 8240-8243 (2010).

136. Takeuchi, T. et al. Direct and Rapid Cytosolic Delivery Using Cell-Penetrating Peptides Mediated by Pyrenebutyrate. *ACS Chemical Biology* 1, 299-303 (2006).

137. Medintz, I.L. et al. Intracellular Delivery of Quantum Dot−Protein Cargos Mediated by Cell Penetrating Peptides. *Bioconjugate chemistry* 19, 1785-1795 (2008).

138. Pan, C., Lu, B., Chen, H. & Bishop, C. Reprogramming Human Fibroblasts Using HIV-1 TAT Recombinant Proteins OCT4, SOX2, KLF4 and c-MYC. *Mol Biol Rep* 37, 2117-2124 (2010).

139. Loison, F. et al. A Ubiquitin-Based Assay for the Cytosolic Uptake of Protein Transduction Domains. *Mol Ther* 11, 205-214 (2005).

140. Herce, H.D. & Garcia, A.E. Molecular Dynamics Simulations Suggest a Mechanism for Translocation of the HIV-1 TAT Peptide Across Lipid Membranes. *Proceedings of the National Academy of Sciences* 104, 20805-20810 (2007).

141. Thorén, P.E.G. et al. Membrane Binding and Translocation of Cell-Penetrating Peptides†. *Biochemistry* 43, 3471-3489 (2004).

142. Tiriveedhi, V. & Butko, P. A Fluorescence Spectroscopy Study on the Interactions of the TAT-PTD Peptide with Model Lipid Membranes. *Biochemistry* 46, 3888-3895 (2007).

143. Leventis, P.A. & Grinstein, S. The Distribution and Function of Phosphatidylserine in Cellular Membranes. *Annual Review of Biophysics* 39, 407-427 (2010).

144. Ruzza, P., Biondi, B., Marchiani, A., Antolini, N. & Calderan, A. Cell-Penetrating Peptides: A Comparative Study on Lipid Affinity and Cargo Delivery Properties. *Pharmaceuticals* 3, 1045-1062 (2010).

145. Lee, Y.-J., Johnson, G. & Pellois, J.-P. Modeling of the Endosomolytic Activity of HA2-TAT Peptides with Red Blood Cells and Ghosts. *Biochemistry* 49, 7854-7866 (2010).

146. Cahill, K.E. Molecular Electroporation and the Transduction of Oligoarginines. *Biophysical Journal* 98, 83a.

147. Bernfield, M. et al. Functions of Cell Surface Heparan Sulfate Proteoglycans. *Annual Review of Biochemistry* 68, 729-777 (1999).

148. Rothe, R. et al. Characterization of the Cell-penetrating Properties of the Epstein-Barr Virus ZEBRA Trans-Activator. *Journal of Biological Chemistry* 285, 20224-20233 (2010).

149. Tyagi, M., Rusnati, M., Presta, M. & Giacca, M. Internalization of HIV-1 Tat Requires Cell Surface Heparan Sulfate Proteoglycans. *Journal of Biological Chemistry* 276, 3254-3261 (2001).

150. Belting, M. Heparan Sulfate Proteoglycan as a Plasma Membrane Carrier. *Trends in Biochemical Sciences* 28, 145-151.

151. Magzoub, M., Kilk, K., Eriksson, L.E.G., Langel, Ü. & Gräslund, A. Interaction and Structure Induction of Cell-Penetrating Peptides in the Presence of Phospholipid Vesicles. *Biochimica et Biophysica Acta (BBA) - Biomembranes* 1512, 77-89 (2001).

152. Kobayashi, T., Startchev, K., Whitney Andrew, J. & Gruenberg, J. in Biological Chemistry, Vol. 382 4832001).

153. Matsuo, H. et al. Role of LBPA and Alix in Multivesicular Liposome Formation and Endosome Organization. *Science* 303, 531-534 (2004).

154. Steinhauer, D.A., Wharton, S.A., Skehel, J.J. & Wiley, D.C. Studies of The Membrane Fusion Activities of Fusion Peptide Mutants of Influenza Virus Hemagglutinin. *Journal of Virology* 69, 6643-6651 (1995).

155. Qiao, H., Armstrong, R.T., Melikyan, G.B., Cohen, F.S. & White, J.M. A Specific Point Mutant at Position 1 of the Influenza Hemagglutinin Fusion Peptide Displays a Hemifusion Phenotype. *Molecular Biology of the Cell* 10, 2759-2769 (1999).

156. Wadia, J.S., Stan, R.V. & Dowdy, S.F. Transducible TAT-HA Fusogenic Peptide Enhances Escape of TAT-Fusion Proteins After Lipid Raft Macropinocytosis. *Nat Med* 10, 310-315 (2004).

157. Koshman, Y.E. et al. Delivery and Visualization of Proteins Conjugated to Quantum Dots in Cardiac Myocytes. *Journal of Molecular and Cellular Cardiology* 45, 853-856 (2008).

158. Michiue, H. et al. The NH2 Terminus of Influenza Virus Hemagglutinin-2 Subunit Peptides Enhances the Antitumor Potency of Polyarginine-mediated p53 Protein Transduction. *Journal of Biological Chemistry* 280, 8285-8289 (2005).

159. Lee, Y.J., Erazo-Oliveras, A. & Pellois, J.P. Delivery of Macromolecules Into Live Cells by Simple Co-Incubation With a Peptide. *Chembiochem : a European journal of chemical biology* 11, 325-330 (2010).

160. Zhelev, D.V., Stoicheva, N., Scherrer, P. & Needham, D. Interaction of Synthetic HA2 Influenza Fusion Peptide Analog with Model Membranes. *Biophysical Journal* 81, 285-304 (2001).

161. Lee, Y.-J., Johnson, G., Peltier, G.C. & Pellois, J.-P. A HA2-Fusion Tag Limits the Endosomal Release of Its Protein Cargo Despite Causing Endosomal Lysis. *Biochimica et Biophysica Acta (BBA) - General Subjects* 1810, 752-758 (2011).

162. Hakansson, S., Jacobs, A. & Caffrey, M. Heparin Binding by The HIV-1 Tat Protein Ttransduction Domain. *Protein Science* 10, 2138-2139 (2001).

163. Hakansson, S. & Caffrey, M. Structural and Dynamic Properties of the HIV-1 Tat Transduction Domain in the Free and Heparin-Bound States. *Biochemistry* 42, 8999-9006 (2003).

164. Maiolo, J.R., Ottinger, E.A. & Ferrer, M. Specific Redistribution of Cell-Penetrating Peptides from Endosomes to the Cytoplasm and Nucleus upon Laser Illumination. *Journal of the American Chemical Society* 126, 15376-15377 (2004).

165. Matsushita, M. et al. Photo-Acceleration of Protein Release From Endosome in the Protein Transduction System. *FEBS Letters* 572, 221-226 (2004).

166. Endoh, T., Sisido, M. & Ohtsuki, T. Spatial Regulation of Specific Gene Expression Through Photoactivation of RNAi. *Journal of Controlled Release* 137, 241-245 (2009).

167. Zhao, J.-F., Chen, J.-Y., Mi, L., Wang, P.-N. & Peng, Q. Enhancement of Intracellular Delivery of Anti-cancer Drugs by the Tat Peptide. *Ultrastructural Pathology* 35, 119-123 (2011).

168. Choi, Y., McCarthy, J.R., Weissleder, R. & Tung, C.-H. Conjugation of a Photosensitizer to an Oligoarginine-Based Cell-Penetrating Peptide Increases the Efficacy of Photodynamic Therapy. *ChemMedChem* 1, 458-463 (2006).

169. Berg, K. et al. Photochemical Internalization: A Novel Technology for Delivery of Macromolecules into Cytosol. *Cancer Research* 59, 1180-1183 (1999).

170. Berg, K. et al. in Photodynamic Therapy, Vol. 635. (ed. C.J. Gomer) 133-145 (Humana Press, 2010).

171. Berg, K. et al. in Nucleic Acid Transfection, Vol. 296. (eds. W. Bielke & C. Erbacher) 251-281 (Springer Berlin Heidelberg, 2010).

172. Berg, K. et al. Disulfonated Tetraphenyl Chlorin (TPCS2a), A Novel Photosensitizer Developed for Clinical Utilization of Photochemical Internalization. *Photochemical & Photobiological Sciences* 10, 1637-1651 (2011).

173. Selbo, P.K., Weyergang, A., Bonsted, A., Bown, S.G. & Berg, K. Photochemical Internalization of Therapeutic Macromolecular Agents: A Novel Strategy to Kill Multidrug-Resistant Cancer Cells. *Journal of Pharmacology and Experimental Therapeutics* 319, 604-612 (2006).

174. Mathews, M.S. et al. Photochemical Internalization of Bleomycin for Glioma Treatment. *BIOMEDO* 17, 0580011-0580018 (2012).

175. Srinivasan, D. et al. Conjugation to the Cell-Penetrating Peptide TAT Potentiates the PhotodynamicEffect of Carboxytetramethylrhodamine. *PloS one* 6, e17732 (2011).

176. Oliveira, S., Fretz, M.M., Høgset, A., Storm, G. & Schiffelers, R.M. Photochemical Internalization Enhances Silencing of Epidermal Growth Factor Receptor Through Improved Endosomal Escape of siRNA. *Biochimica et Biophysica Acta (BBA) - Biomembranes* 1768, 1211-1217 (2007).

177. Endoh, T. & Ohtsuki, T. in RNA Interference, Vol. 623. (eds. W.-P. Min & T. Ichim) 271-281 (Humana Press, 2010).

178. Muthukrishnan, N., Johnson, G.A., Lim, J., Simanek, E.E. & Pellois, J.P. TAT-Mediated Photochemical Internalization Results in Cell Killing by Causing the Release of Calcium Into the Cytosol of Cells. *Biochimica et biophysica acta* 1820, 1734-1743 (2012).

179. Selbo, P.K., Høgset, A., Prasmickaite, L. & Berg, K. Photochemical Internalisation: A Novel Drug Delivery System. *Tumor Biology* 23, 103-112 (2002).

180. Saggu, S., Hung, H.-I., Quiogue, G., Lemasters, J.J. & Nieminen, A.-L. Lysosomal Signaling Enhances Mitochondria-Mediated Photodynamic Therapy in A431 Cancer Cells: Role of Iron. *Photochemistry and photobiology* 88, 461-468 (2012).

181. Berg, K., Dietze, A., Kaalhus, O. & Høgset, A. Site-Specific Drug Delivery by Photochemical Internalization Enhances the Antitumor Effect of Bleomycin. *Clinical Cancer Research* 11, 8476-8485 (2005).

182. Nishiyama, N. et al. Light-Induced Gene Transfer from Packaged DNA Enveloped in a Dendrimeric Photosensitizer. *Nat Mater* 4, 934-941 (2005).

183. Selbo, P.K., Sivam, G., Fodstad, Ø., Sandvig, K. & Berg, K. In Vivo Documentation of Photochemical Internalization, a Novel Approach to Site Specific Cancer Therapy. *International Journal of Cancer* 92, 761-766 (2001).

184. van Rossenberg, S.M.W. et al. Targeted Lysosome Disruptive Elements for Improvement of Parenchymal Liver Cell-specific Gene Delivery. *Journal of Biological Chemistry* 277, 45803-45810 (2002).

185. Berg, K. et al. Porphyrin-Related Photosensitizers for Cancer Imaging and Therapeutic Applications. *Journal of Microscopy* 218, 133-147 (2005).

186. Kawamura, K.S., Sung, M., Bolewska-Pedyczak, E. & Gariépy, J. Probing the Impact of Valency on the Routing of Arginine-Rich Peptides into Eukaryotic Cells†. *Biochemistry* 45, 1116-1127 (2006).

187. Hassane, F.S. et al. A Peptide-Based Dendrimer That Enhances the Splice-Redirecting Activity of PNA Conjugates in Cells. *Bioconjugate chemistry* 20, 1523-1530 (2009).

188. Kang, H., DeLong, R., Fisher, M. & Juliano, R. Tat-Conjugated PAMAM Dendrimers as Delivery Agents for Antisense and siRNA Oligonucleotides. *Pharm Res* 22, 2099-2106 (2005).

189. Juliano, R.L. Intracellular Delivery of Oligonucleotide Conjugates and Dendrimer Complexes. *Annals of the New York Academy of Sciences* 1082, 18-26 (2006).

190. Pantos, A., Tsiourvas, D., Nounesis, G. & Paleos, C.M. Interaction of Functional Dendrimers with Multilamellar Liposomes: Design of a Model System for Studying Drug Delivery. *Langmuir* 21, 7483-7490 (2005).

191. Kim, J.-B. et al. Enhanced Transfection of Primary Cortical Cultures Using Arginine-Grafted PAMAM Dendrimer, PAMAM-Arg. *Journal of Controlled Release* 114, 110-117 (2006).

192. Medina, S.H. & El-Sayed, M.E.H. Dendrimers as Carriers for Delivery of Chemotherapeutic Agents. *Chemical Reviews* 109, 3141-3157 (2009).

193. Sheldon, K., Liu, D., Ferguson, J. & Gariépy, J. Loligomers: Design of de Novo Peptide-Based Intracellular Vehicles. *Proceedings of the National Academy of Sciences* 92, 2056-2060 (1995).

194. Singh, D., Kiarash, R., Kawamura, K., LaCasse, E.C. & Gariépy, J. Penetration and Intracellular Routing of Nucleus-Directed Peptide-Based Shuttles (Loligomers) in Eukaryotic Cells†. *Biochemistry* 37, 5798-5809 (1998).

195. Kawamura, K.S. et al. In Vivo Generation of Cytotoxic T Cells from Epitopes Displayed on Peptide-Based Delivery Vehicles. *The Journal of Immunology* 168, 5709-5715 (2002).

196. Singh, D., Bisland, S.K., Kawamura, K. & Gariépy, J. Peptide-Based Intracellular Shuttle Able To Facilitate Gene Transfer in Mammalian Cells. *Bioconjugate chemistry* 10, 745-754 (1999).

197. Dawson, P., Muir, T., Clark-Lewis, I. & Kent, S. Synthesis of Proteins by Native Chemical Ligation. *Science* 266, 776-779 (1994).

198. Angeles-Boza, A.M., Erazo-Oliveras, A., Lee, Y.J. & Pellois, J.P. Generation of Endosomolytic Reagents by Branching of Cell-Penetrating Peptides: Tools for the Delivery of Bioactive Compounds to Live Cells in Cis or Trans. *Bioconjugate chemistry* 21, 2164-2167 (2010).

199. Rudolph, C. et al. Application of Novel Solid Lipid Nanoparticle (SLN)-Gene Vector Formulations Based on a Dimeric HIV-1 TAT-Peptide in Vitro and in Vivo. *Pharm Res* 21, 1662-1669 (2004).

200. Chugh, A., Amundsen, E. & Eudes, F. Translocation of Cell-Penetrating Peptides and Delivery of Their Cargoes in Triticale Microspores. *Plant Cell Rep* 28, 801-810 (2009).

201. Lee, S.-J.Y., S.-H.; Doh, K.-O. Enhancement of Gene Delivery Using Novel Homodimeric Tat Peptide Formed by Disulfide Bond. *J. Microbiol. Biotech.* 21, 802–807. ( 2011).

202. Sung, M., Poon, G.M.K. & Gariépy, J. The Importance of Valency in Enhancing the Import and Cell Routing Potential of Protein Ttransduction Domain-Containing Molecules. *Biochimica et Biophysica Acta (BBA) - Biomembranes* 1758, 355-363 (2006).

203. Tung, C.-H., Mueller, S. & Weissleder, R. Novel Branching Membrane Translocational Peptide as Gene Delivery Vector. *Bioorganic & Medicinal Chemistry* 10, 3609-3614 (2002).

204. Rudolph, C. et al. Oligomers of the Arginine-rich Motif of the HIV-1 TAT Protein Are Capable of Transferring Plasmid DNA into Cells. *Journal of Biological Chemistry* 278, 11411-11418 (2003).

205. Schwarze, S., Ho, A., Vocero-Akbani, A. & Dowdy, S. In Vivo Protein Transduction: Delivery of a Biologically Active Protein Into the Mouse. *Science* 285, 1569 - 1572 (1999).

206. Schwarze, S.R. & Dowdy, S.F. In Vivo Protein Transduction: Intracellular Delivery of Biologically Active Proteins, Compounds and DNA. *Trends in Pharmacological Sciences* 21, 45-48 (2000).

207. Tam, J.P. Synthetic Peptide Vaccine Design: Synthesis and Properties of a High-Density Multiple Antigenic Peptide System. *Proceedings of the National Academy of Sciences* 85, 5409-5413 (1988).

208. Fujita, Y. & Taguchi, H. Current Status of Multiple Antigen-Presenting Peptide Vaccine Systems: Application of Organic and Inorganic Nanoparticles. *Chemistry Central Journal* 5, 48 (2011).

209. Mammen, M., Choi, S.-K. & Whitesides, G.M. Polyvalent Interactions in Biological Systems: Implications for Design and Use of Multivalent Ligands and Inhibitors. *Angewandte Chemie International Edition* 37, 2754-2794 (1998).

210. Krishnamurthy, V.M., Estroff, L.A. & Whitesides, G.M. in Fragment-Based Approaches in Drug Discovery 11-53 (Wiley-VCH Verlag GmbH & Co. KGaA, 2006).

211. Alves, D.A. et al. Synthesis and Use of a Pseudo-Cysteine For Native Chemical Ligation. *Journal of Peptide Science* 9, 221-228 (2003).

212. Szewczuk, L.M. et al. Analysis of Serotonin N-Acetyltransferase Regulation in Vitro and in Live Cells Using Protein Semisynthesis†. *Biochemistry* 47, 10407-10419 (2008).

213. Futaki, S., Nakase, I., Suzuki, T., Zhang & Sugiura, Y. Translocation of Branched-Chain Arginine Peptides through Cell Membranes: Flexibility in the Spatial Disposition of Positive Charges in Membrane-Permeable Peptides†. *Biochemistry* 41, 7925-7930 (2002).

214. Nakase, I. et al. Interaction of Arginine-Rich Peptides with Membrane-Associated Proteoglycans Is Crucial for Induction of Actin Organization and Macropinocytosis†. *Biochemistry* 46, 492-501 (2006).

215. Javadpour, M.M. et al. De Novo Antimicrobial Peptides with Low Mammalian Cell Toxicity. *Journal of Medicinal Chemistry* 39, 3107-3113 (1996).

216. Kwon, M.-K. et al. Antitumor Effect of a Transducible Fusogenic Peptide Releasing Multiple Proapoptotic Peptides by Caspase-3. *Molecular Cancer Therapeutics* 7, 1514-1522 (2008).

217. Yoshida, H. et al. Phosphatidylserine-Dependent Engulfment by Macrophages of Nuclei from Erythroid Precursor Cells. *Nature* 437, 754-758 (2005).

218. Ralston, K.S. et al. Trogocytosis by Entamoeba Histolytica Contributes to Cell Killing and Tissue Invasion. *Nature* 508, 526-530 (2014).

219. Koivusalo, M. et al. Amiloride Inhibits Macropinocytosis by Lowering Submembranous pH and Preventing Rac1 and Cdc42 Signaling. *The Journal of Cell Biology* 188, 547-563 (2010).

220. Li, G.-H., Li, W., Mumper, R.J. & Nath, A. Molecular Mechanisms in the Dramatic Enhancement of HIV-1 Tat Transduction by Cationic Liposomes. *The FASEB Journal* 26, 2824-2834 (2012).

221. Lim, K.J. et al. A Cancer Specific Cell-Penetrating Peptide, BR2, for the Efficient Delivery of an scFv into Cancer Cells. *PloS one* 8, e66084 (2013).

222. Erazo-Oliveras, A., Muthukrishnan, N., Baker, R., Wang, T.Y. & Pellois, J.P. Improving the Endosomal Escape of Cell-Penetrating Peptides and Their Cargos: Strategies and Challenges. *Pharmaceuticals* 5, 1177-1209 (2012).

223. Mourez, M. et al. Designing a Polyvalent Inhibitor of Anthrax Toxin. *Nat Biotech* 19, 958-961 (2001).

224. Liang, M.N. et al. Measuring the Forces Involved in Polyvalent Adhesion of Uropathogenic Escherichia Coli to Mannose-Presenting Surfaces. *Proceedings of the National Academy of Sciences* 97, 13092-13096 (2000).

225. Erazo-Oliveras, A. et al. Protein Delivery Into Live Cells by Incubation With an Endosomolytic Agent. *Nat Meth* 11, 861-867 (2014).

226. Radnai, L. et al. Affinity, Avidity, and Kinetics of Target Sequence Binding to LC8 Dynein Light Chain Isoforms. *Journal of Biological Chemistry* 285, 38649-38657 (2010).

227. Hussain, A.F. et al. Targeted Delivery of Dendritic Polyglycerol–Doxorubicin Conjugates by scFv-SNAP Fusion Protein Suppresses EGFR+ Cancer Cell Growth. *Biomacromolecules* 14, 2510-2520 (2013).

228. Sakakibara, D. et al. Protein Structure Determination in Living Cells by In-Cell NMR Spectroscopy. *Nature* 458, 102-105 (2009).

229. Lee, Y.J., Datta, S. & Pellois, J.P. Real-Time Fluorescence Detection of Protein Transduction Into Live Cells. *Journal of the American Chemical Society* 130, 2398-2399 (2008).

230. Schwarze, S.R., Hruska, K.A. & Dowdy, S.F. Protein Transduction: Unrestricted Delivery Into All Cells? *Trends in Cell Biology* 10, 290-295 (2000).

231. Gratton, J. et al. Cell-Permeable Peptides Improve Cellular Uptake and Therapeutic Gene Delivery of Replication-Deficient Viruses in Cells and in Vivo. *Nat Med* 9, 357 - 362 (2003).

232. Massignani, M. et al. Enhanced Fluorescence Imaging of Live Cells by Effective Cytosolic Delivery of Probes. *PloS one* 5, e10459 (2010).

233. Hoyer, J., Schatzschneider, U., Schulz-Siegmund, M. & Neundorf, I. Dimerization of a Cell-Penetrating Peptide Leads to Enhanced Cellular Uptake and Drug Delivery. *Beilstein Journal of Organic Chemistry* 8, 1788-1797 (2012).

234. Eguchi, A. et al. Efficient siRNA Delivery Into Primary Cells by a Peptide Transduction Domain-dsRNA Bbinding Domain Fusion Protein. *Nat Biotech* 27, 567-571 (2009).

235. Austin, C.D. et al. Oxidizing Potential of Endosomes and Lysosomes Limits Intracellular Cleavage of Disulfide-Based Antibody–Drug Conjugates. *Proceedings of the National Academy of Sciences of the United States of America* 102, 17987-17992 (2005).

236. Dominska, M. & Dykxhoorn, D.M. Breaking Down the Barriers: siRNA Delivery and Endosome Escape. *Journal of Cell Science* 123, 1183-1189 (2010).

237. Puri, V. et al. Cholesterol Modulates Membrane Traffic Along the Endocytic Pathway in Sphingolipid-Storage Diseases. *Nat Cell Biol* 1, 386-388 (1999).

238. Johnson, L.S., Dunn, K.W., Pytowski, B. & McGraw, T.E. Endosome Acidification and Receptor Trafficking: Bafilomycin A1 Slows Receptor Externalization by a Mechanism Iinvolving the Receptor's Internalization Motif. *Molecular Biology of the Cell* 4, 1251-1266 (1993).

239. Rejman, J., Bragonzi, A. & Conese, M. Role of Clathrin- and Caveolae-Mediated Endocytosis in Gene Transfer Mediated by Lipo- and Polyplexes. *Mol Ther* 12, 468-474 (2005).

240. Sun, X. et al. Development of SNAP-Tag Fluorogenic Probes for Wash-Free Fluorescence Imaging. *Chembiochem : a European journal of chemical biology* 12, 2217-2226 (2011).

241. Johnson, J.R., Kocher, B., Barnett, E.M., Marasa, J. & Piwnica-Worms, D. Caspase-Activated Cell-Penetrating Peptides Reveal Temporal Coupling Between Endosomal Release and Apoptosis in an RGC-5 Cell Model. *Bioconjugate chemistry* 23, 1783-1793 (2012).

242. Csaszar, E. et al. An Automated System for Delivery of an Unstable Transcription Factor to Hematopoietic Stem Cell Cultures. *Biotechnology and bioengineering* 103, 402-412 (2009).

243. Amsellem, S. et al. Ex Vivo Expansion ofHuman Hematopoietic Stem Cells by Direct Delivery of the HOXB4 Homeoprotein. *Nat Med* 9, 1423-1427 (2003).

244. Krosl, J. et al. In Vitro Expansion of Hematopoietic Stem Cells by Recombinant TAT-HOXB4 Protein. *Nat Med* 9, 1428-1432 (2003).

245. Will, E. et al. HOXB4 Inhibits Cell Growth in a Dose-Dependent Manner and Sensitizes Cells Towards Extrinsic Cues. *Cell cycle* 5, 14-22 (2006).

246. Muthukrishnan, N., Johnson, G.A., Erazo-Oliveras, A. & Pellois, J.P. Synergy Between Cell-Penetrating Peptides and Singlet Oxygen Generators Leads to Efficient Photolysis of Membranes. *Photochemistry and photobiology* (2012).

247. Marino, J. et al. Lysosomal and Mitochondrial Permeabilization Mediates Zinc(II) Cationic Phthalocyanine Phototoxicity. *The International Journal of Biochemistry & Cell Biology* 45, 2553-2562 (2013).

248. Pourahmad, J., Hosseini, M.-J., Eskandari, M.R., Shekarabi, S.M. & Daraei, B. Mitochondrial/Lysosomal Toxic Cross-talk Plays a Key Role in Cisplatin Nephrotoxicity. *Xenobiotica* 40, 763-771 (2010).

249. Yang, M. et al. Lysosomal Membrane Permeabilization: Carbon Nanohorn-Induced Reactive Oxygen Species Generation and Toxicity by This Neglected Mechanism. *Toxicology and Applied Pharmacology* 280, 117-126 (2014).

250. Bird, P.I., Trapani, J.A. & Villadangos, J.A. Endolysosomal Proteases and Their Inhibitors in Immunity. *Nat Rev Immunol* 9, 871-882 (2009).

251. Scharf, B. et al. Annexin A2 Binds to Endosomes Following Organelle Destabilization by Particulate Wear Debris. *Nat Commun* 3, 755 (2012).

252. Jiang, T. et al. Tumor Imaging by Means of Proteolytic Activation of Cell-Penetrating Peptides. *Proceedings of the National Academy of Sciences of the United States of America* 101, 17867-17872 (2004).

253. Peitz, M., Pfannkuche, K., Rajewsky, K. & Edenhofer, F. Ability of the Hydrophobic FGF and Basic TAT peptides to Promote Cellular Uptake of Recombinant Cre Recombinase: A Tool for Efficient Genetic Engineering of Mammalian Genomes. *Proceedings of the National Academy of Sciences* 99, 4489-4494 (2002).

254. Pellois, J.P. & Muir, T.W. A Ligation and Photorelease Strategy for the Temporal and Spatial Control of Protein Function in Living Cells. *Angewandte Chemie* 44, 5713-5717 (2005).

255. Boukamp, P. et al. Normal Keratinization in a Spontaneously Immortalized Aneuploid Human Keratinocyte Cell Line. *The Journal of Cell Biology* 106, 761-771 (1988).

256. Woods, L.K. et al. Comparison of Four New Cell Lines from Patients with Adenocarcinoma of the Ovary. *Cancer Research* 39, 4449-4459 (1979).

257. Jiang, N., Bénard, C.Y., Kébir, H., Shoubridge, E.A. & Hekimi, S. Human CLK2 Links Cell Cycle Progression, Apoptosis, and Telomere Length Regulation. *Journal of Biological Chemistry* 278, 21678-21684 (2003).

258. Gonzalez-Vallina, R. et al. Lipoprotein and Apolipoprotein Secretion by a Newborn Piglet Intestinal Cell Line (IPEC-1), Vol. 271. (1996).

259. Hunt, M.E., Scherrer, M.P., Ferrari, F.D. & Matz, M.V. Very Bright Green Fluorescent Proteins from the Pontellid Copepod Pontella mimocerami. *PloS one* 5, e11517 (2010).

260. Wessel, D. & Flügge, U.I. A Method for the Quantitative Recovery of Protein in Dilute Solution in the Presence of Detergents and Lipids. *Analytical Biochemistry* 138, 141-143 (1984).

261. Zerial, M. & McBride, H. Rab Proteins as Membrane Organizers. *Nat Rev Mol Cell Biol* 2, 107-117 (2001).

262. Colpitts, T.M., Moore, A.C., Kolokoltsov, A.A. & Davey, R.A. Venezuelan Equine Encephalitis Virus Infection of Mosquito Cells Requires Acidification as well as Mosquito Homologs of the Endocytic Proteins Rab5 and Rab7. *Virology* 369, 78-91 (2007).

263. Bucci, C. et al. Co-operative Regulation of Endocytosis by Three RAB5 Isoforms. *FEBS Letters* 366, 65-71 (1995).

264. Stenmark, H. et al. Inhibition of Rab5 GTPase Activity Stimulates Membrane Fusion in Endocytosis. *EMBO Journal* 13, 1287-1296 (1994).

265. Mainou, B.A. & Dermody, T.S. Transport to Late Endosomes Is Required for Efficient Reovirus Infection. *Journal of Virology* 86, 8346-8358 (2012).

266. Vonderheit, A. & Helenius, A. Rab7 Associates with Early Endosomes to Mediate Sorting and Transport of Semliki Forest Virus to Late Endosomes. *PLoS Biol* 3, e233 (2005).

267. Chia, P., Gunn, P. & Gleeson, P. Cargo Trafficking Between Endosomes and the Trans-Golgi Network. *Histochem Cell Biol* 140, 307-315 (2013).

268. Bonifacino, J.S. & Rojas, R. Retrograde Transport From Endosomes to the Trans-Golgi network. *Nat Rev Mol Cell Biol* 7, 568-579 (2006).

269. Blot, G., Janvier, K., Le Panse, S., Benarous, R. & Berlioz-Torrent, C. Targeting of the Human Immunodeficiency Virus Type 1 Envelope to the trans-Golgi Network Through Binding to TIP47 Is Required for Env Incorporation Into Virions and Infectivity. *Journal of Virology* 77, 6931-6945 (2003).

270. Stechmann, B. et al. Inhibition of Retrograde Transport Protects Mice from Lethal Ricin Challenge. *Cell* 141, 231-242 (2010).

271. Nelson, C.D.S. et al. A Retrograde Trafficking Inhibitor of Ricin and Shiga-Like Toxins Inhibits Infection of Cells by Human and Monkey Polyomaviruses. *mBio* 4 (2013).

272. Rochemonteix, B.G.-d. et al. Interaction of Anti-Phospholipid Antibodies With Late Endosomes of Human Endothelial Cells. *Arteriosclerosis, Thrombosis, and Vascular Biology* 20, 563-574 (2000).

273. Chu, Z., Witte, D.P. & Qi, X. Saposin C–LBPA Interaction in Late-Endosomes/Lysosomes. *Experimental Cell Research* 303, 300-307 (2005).

274. Kobayashi, T. et al. Late Endosomal Membranes Rich in Lysobisphosphatidic Acid Regulate Cholesterol Transport. *Nature Cell Biology* 1, 113-118 (1999).

275. Sugaya, K., Seto, S., Tsujimura, K. & Koide, Y. Mobility of Late Endosomal and Lysosomal Markers on Phagosomes Analyzed by Fluorescence Recovery After Photobleaching. *Biochemical and Biophysical Research Communications* 410, 371-375 (2011).

276. Vitelli, R. et al. Role of the Small GTPase RAB7 in the Late Endocytic Pathway. *Journal of Biological Chemistry* 272, 4391-4397 (1997).